

**LAYERED COMPOSITE THIN FILMS FOR COST  
EFFECTIVE TRANSPARENT ORGANIC SOLAR CELL  
ELECTRODES**

**A DISSERTATION PRESENTED TO THE AFRICAN  
UNIVERSITY OF SCIENCE AND TECHNOLOGY (AUST)**

**IN CANDIDACY FOR THE DEGREE OF DOCTOR OF  
PHILOSOPHY**

**BY**

**Egidius Rutatizibwa Rwenyagila**

**BSc (UDSM - Tanzania), MSc (EPFL – Switzerland)**

**AUST ID. 70053**

**RECOMMENDED FOR ACCEPTANCE  
BY THE DEPARTMENT OF MATERIALS SCIENCE AND  
ENGINEERING**

**ACCEPTING JURY:**

**Prof. Winston Oluwole Soboyejo, Supervisor**

**Prof. Martiale Gaetan Zebaze Kana**

**Prof. Omololu Akin-Ojo**

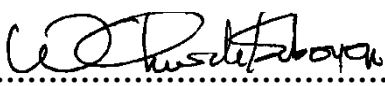
**August 2015  
AUST, Abuja, Nigeria**

Layered Composite Thin Films for Cost Effective Transparent Organic Solar Cell  
Electrodes

By

Egidius Rutatizibwa Rwenyagila

A THESIS APPROVED BY THE MATERIALS SCIENCE AND ENGINEERING  
DEPARTMENT

RECOMMENDED:   
Supervisor, Professor Winston Oluwole Soboyejo



Head, Dept. of Materials Science and Engineering

Approved:   
Vice President, Academics

Date: 25 August, 2015.

## **Dedication**

To Almighty God, the Creator of heaven and earth for enabling everything in my life

To my parents Denis and Leonardina Rwenyagila, who sacrificed a lot to make me the way I am

To my grandfather Emmanuel Mbegu, who survived dreamland glory

To my wife Irene, whose love I honour in my heart

To my daughter Egiline, who I missed since her nativity

May God bless you all

## Abstract

In this dissertation two main themes are explored. In the first part some phenomenologies of light transport across the ZnO/Al/ZnO (ZAZ) thin film multilayer structures are investigated. The multilayered ZAZ thin film composite structures are explored for potential applications as transparent electrodes (TEs) alternatives to the costly transparent indium-doped-tin-oxide (ITO) anodes that are used currently in organic solar cells (OSCs), organic light emitting devices (OLEDs) and variety of other layered optoelectronic structures. The transmission characteristics and the optimum interlayer thicknesses of ZAZ thin film structures were numerically predicted in this part of the project.

Computational modeling and simulations were used successfully to study the transmittances ( $T_s$ ) of the multilayered ZAZ thin film composite stacks with intermediate aluminum (Al) layer thicknesses between  $\sim 1 - 100$  nm. Multilayered ZAZ thin film composite structures with mid-Al layer thicknesses between  $\sim 1 - 10$  nm are shown to have average  $T_s$  between  $\sim 75 - 90\%$ , which decreased further to  $\sim 63$  and  $41\%$  for the mid-layer Al thicknesses of 20 and 40 nm, respectively. A further decrease of the  $T$  values down to  $\sim 35$  and  $15\%$  was observed for the mid-layer Al thicknesses of 50 and 100 nm, respectively.

The actual multilayered ZAZ thin film composite structures were then successfully synthesized with the predicted optimal interlayer thicknesses and tested accordingly. These were produced via radio frequency (RF) magnetron sputtering (MS). Both computational modeling and experimental studies examined the effects of Al nanolayers on the TE properties of ZAZ film composites. The experimental study

clarified the role of the Al mid-layer thickness in a multilayered ZAZ thin film composite with a  $ZnO(25\text{ nm})/Al/ZnO(25\text{ nm})$  structure and an optimum mid-layer Al thickness between  $\sim 1 - 10\text{ nm}$ . Within this range, the numerical simulations are comparable with experimental optical T measurements in multilayered ZAZ thin film composite structures produced with similar ZnO layer thicknesses and the predicted optimum intermediate Al layer thicknesses between  $\sim 1 - 10\text{ nm}$ .

The electrical properties of multilayered ZAZ thin film composite structures were also investigated for structures produced with optimum intermediate Al layer thicknesses. Multilayered ZAZ thin film composite structures, with resistivity values as low as  $\sim 3.62 \times 10^{-4}\ \Omega\text{cm}$  at average Ts between  $\sim 85 - 90\%$  (in the visible region of the solar spectrum), were produced. The results show further that the best multilayered ZAZ thin film composite structures that were produced have the highest Haacke Figure of Merit (HFoM) of  $4.72 \times 10^{-3}\ \Omega^{-1}$  and electrical sheet resistances as low as  $\sim 7.25\ \Omega/\text{sq}$ . These transparent conductive properties of multilayered ZAZ thin film composite structures are shown to be comparable to the performance characteristics of ITO-coated anodes that are used currently in organic solar cells, light emitting devices and other electronics and optoelectronic components in passive and active technological systems.

The highest HFoM above was obtained for a multilayered ZAZ thin film composite structure with an intermediate Al layer thickness of  $\sim 8\text{ nm}$ . Furthermore, the combined apparent optical bandgap energy of the multilayered ZAZ thin film composite structures changed from  $\sim 3.26$  to  $3.85\text{ eV}$ , an increase of  $\sim 0.60\text{ eV}$  for intermediate Al layer thicknesses between  $\sim 1 - 10\text{ nm}$ . This optical bandgap energy widening led to shifts in the optical absorption edges to shorter wavelengths in the solar spectrum. Such

shifts are shown to be in agreement with the Moss-Burstein effect. Generally, the structural, optical and electrical properties of the obtained multilayered ZAZ thin film composite structures revealed realistic physics of TEs. These were also comparably in good agreement with the transparent conductive properties of the standard ITO thin film coated-substrates.

The second theme of the project explores the effects of contact on charge-carrier transport across the interface between the photoactive organic layer and the TE layer of organic photovoltaic (OPV) solar cell systems. The photo-current-density versus voltage (J-V) characteristics of an OSC as function of contact height for different contact lengths were studied by numerical modeling. The obtained results are used to assess the prospects of charge transport and/or collection across the photoactive/TE interfaces of OPV solar cell systems and other electronics/optoelectronic devices and components. The results show that optimum contact length above  $\sim 80\%$  is needed for the organic solar cell to have the performance characteristics that resemble closely to those of organic solar cell systems with perfect planar interfacial/interlayer contacts.

## List of Publications

- **Rwenyagila E. R.**, Agyei-Tuffour B., Onogu K. O., Akin-Ojo O., Zebaze Kana M. G., Alford T. L., and Soboyejo W. O.: *Computational Modeling of Optical Properties in Aluminum Nanolayers Inserted in ZnO for Solar Cell Electrodes*. [Opt. Lett.](#) **40** (16), 3914-3917 (2015).
- Tong T. M., Asare J., **Rwenyagila E. R.**, Anye V. C., Oyewole O. K., Fashena A. A., and Soboyejo W. O.: *A Study of Factors that Influence the Adoption of Solar Powered Lanterns in a Rural Village in Kenya*. [J. PGDT](#) **14** (4), 448-491 (2015).
- **Rwenyagila E. R.**, Agyei-Tuffour B., Zebaze Kana M. G., Akin-Ojo O., and Soboyejo W. O.: *Optical Properties of ZnO/Al/ZnO Multilayer Films for Large Area Transparent Electrodes*. [J. Mater. Res.](#) **29** (24), 2912-2920 (2014).
- Yu D., Oyewole O. K., Kwabi D., Tong T., Anye V. C., Asare J., **Rwenyagila E. R.**, Fashina A., Akogwu, O., and Soboyejo W. O.: *Adhesion in Flexible Organic and Hybrid Organic/Inorganic Light Emitting Device and Solar Cells*. [J. Appl. Phys.](#) **116**, 074506 (2014).
- Agyei-Tuffour B., Annan E., **Rwenyagila E. R.**, Ampaw E., Arthur E., Mustapha K., Kolawole S., Soboyejo O. W., Marinov M. I., Radev D. D.: *Untraditional Synthesis of Ni-based Alloys for Medical Applications*. [J. Eng. Appl. Sci.](#) **8** (4), 270-276 (2013).
- Agyei-Tuffour B., Annan E., **Rwenyagila E. R.**, Ampaw E., Arthur E., Mustapha K., Kolawole S., Soboyejo O. W., Marinov M. I., Radev D. D.: *Untraditional Synthesis of Boron-Containing Superhard and Refractory Materials - A Review*. [GJEDT](#) **2** (1), 21-26 (2013).
- Nyankson E., Agyei-Tuffour B., Asare J., Annan E., **Rwenyagila E. R.**, Konadu D. S., Yaya A., Dodoo-Arhin D.: *Nanostructured TiO<sub>2</sub> and Their Energy Applications – A Review*. [J. Eng. Appl. Sci.](#) **8** (10), 871-886 (2013).

### Book Chapter

- **Rwenyagila E. R.**, B. Agyei-Tuffour, Zebaze Kana M. G., Akin-Ojo O., and Soboyejo W. O., “*Structural and Optical Properties of ZnO Film Precursors for Multilayered Transparent Solar Cell Electrodes*” Textbook Chapter, in “*Advanced Materials for Energy, Biomedical and Multifunctional Structures*” Trans Tech Publications Ltd, Churerstrasse 20, CH-8808 Pfaffikon, Switzerland (Submitted).

## Workshops and Professional Development Courses

- AUST PhD Colloquium, 2015 (AP'Col, 2015), AUST – Abuja, Nigeria, February 22<sup>nd</sup>, 2015, [www.aust.edu.ng/library](http://www.aust.edu.ng/library)
  - *Contribution:* Paper Presentation « Layered Transparent Film Composite Electrodes – Critical Aspects of Numerical Simulations and Verification »
  
- Short Course on Energy Innovation and Sustainability, AUST – Abuja, Nigeria, 13<sup>th</sup> – 24<sup>th</sup> October, 2014
  - *Contribution:* Course tutor « Frontiers of Solar Energy and Maintenance of Photovoltaic Systems »
  
- AUST-2iE Short Course on Renovation and Design, AUST – Abuja, Nigeria, 4<sup>th</sup> – 23<sup>rd</sup> August, 2013
  - *Contribution:* Course tutor « Practical Solar Design, Installation and Maintenance »
  
- AUST-ALOFOS Foundation Workshop on Green Design, Surulere – Lagos, Nigeria, 22<sup>nd</sup> – 26<sup>th</sup> April, 2013
  - *Contribution:* Workshop Instructor « Practical/Laboratory Sessions »

## **Acknowledgements**

This dissertation work was conducted for a period of over three years (between 2012 and 2015) in the Department of Materials Science and Engineering of the African University of Science and Technology (AUST), Abuja, Nigeria. During this time I have acquired an in-depth rewarding experience, both personally and professionally. Also, along this exciting academic way in a foreign country, there were varieties of challenges and adversities. Hence, the results presented in this dissertation would not have been obtained without many-sided support of several talented people. I was, therefore, lucky to receive the assistance of many, some of who I would here express my appreciation and gratitude.

Foremost, I am meekly thankful to Almighty God for offering me the great opportunity of life, for His infinite graces that have enabled me to obtain everything I am/have in my life, and most especially for leading me through this research project, an extremely important milestone in my scholarly and professional career endeavors.

I am sincerely grateful to Prof. Winston Oluwole Soboyejo, my dissertation supervisor, for sharing with me his extremely mighty knowledge with limitless patience and compassion, for the tireless professional discussions and inputs, for the valuable mentor support, guidance and directives during the whole period of the project. I am thankful especially to him, as the President of the African University of Science and Technology, Abuja, for accepting me as Postgraduate Teaching Assistant in his research team, and the assurance that he has put in me to work confidently on one of his interesting research topics. In addition, I am thankful for his full availability and openness to new ideas. His exceptionally human and social relations with me personally,

as well as with the collective materials science and engineering research groups (Solar Energy Materials, Multifunctional Materials and Biomaterials) that he has initiated at AUST, have enabled the most encouraging, interactive and challenging conditions for me to accomplish this study.

I would wish to thank Prof. Martiale Gaetan Zebaze Kana of Materials Science and Engineering Department, Kwara State University, Nigeria, not only for accepting me to spend time with me in his laboratory, but also for his supervision and most especially for providing me with the relevant laboratory environment conditions and the necessary supporting credentials that enabled me to use the Advanced Physics Laboratory at the Sheda Science and Technology Complex (SHESTCO), Abuja, Nigeria. I also appreciate the scientific discussions, constructive criticism and fruitful professional inputs. I wish also to extend my appreciation to Mrs. Keyna Oluchukwu Onogu and Mr. Samuel Oladipupo of Advanced Physics Laboratory, SHESTCO, Nigeria, for their technical assistance with laboratory techniques.

My profound appreciation goes to Prof. Omololu Akin-Ojo from Theoretical and Applied Physics Department of AUST, Abuja, for introducing me to the numerical modeling of semiconductor devices and organic solar cells. I am grateful to him, for sharing with me his huge knowledge of Physics. I am also thankful to him, for his support, guidance, and encouragement, daily discussions in his office and for the wonderful, hilariously charismatic Christmas gifts.

I thank Prof. Terry Lynn Alford from the School for Engineering of Matter, Transport, and Energy, of the Arizona State University, USA, for his fruitful academic, technical and professional contributions. In addition, I am very grateful to him for

agreeing to help as one of my dissertation committee members. I also extend my great appreciation to Prof. Eric Garfunkel from Chemistry and Chemical Biology Department of the Rutgers University, USA, for the honor he has done me by accepting to be part of my dissertation committee.

I would like to express my gratitude to Prof. Joseph Buchweishaija of Chemistry Department, University of Dar es Salaam, Tanzania. I thank him so much not only for linking me with the top scientist of Materials Science and Engineering, Prof. W. O. Soboyejo, who certainly offered me the best for my professional and career advancement, but also for the fruitful friendship, constant academic and professional support that have no limits.

I would want to thank all former and current AUST PhD program-mates for the friendship and help during the entire time of my studies at AUST: Dandogbessi Senakpon Bruno, Benjamin Agyei-Tuffour, Joseph Asare, Vitalis Chioh Anye, Fashina Adebayo Adeboye, Ebenezer Annan, Kwabena Kan-Dapaah, Mustapha Kabiru, Stella Dozie-Nwachukwu, Danyuo Yiporo, Edward Ampaw (Kofi), Emmanuel Kwesi Arthur, Joseph Ani Chukuemeka, Azeko Salifu Tahiru, Emmanuel Vodah (RIP), John David Obayemi, Kolawole Shola Kolade, Ignace Djitog, Onuh Haruna Monday, Diouf Yoro, Opeyemi Aborisade Mayokun, Arreytambe Tabot, Bremang Appah, Abdulmalik Usman Bello, Oyewole Oluwaseun Kehinde, Adedoyin Adegoke, Patrice Ndambomve, Ikechukwu Anthony, Aladeitan Yetunde, Damilola Yusuph, Amarfio Eric Mensah, Angela Nwachukwu Nkechi, Duru Ugochukwu Ilozurike and Fortunatus Jacob. Additionally, I respectfully appreciate the support provided by the general members of the AUST, who

received me warmly as part of their community, and provided me with a highly conducive environment for learning and research.

I wish to thank my wife Irene and my daughter Egiline for their huge sacrifice and support. I am most grateful to them for their encouragement and patience with me over the past more than three and a half year that I have spent away from home. I owe you a lot more than I could ever pay you back.

Finally, my deep gratitude goes to all my family members: my parents Denis and Leonardina Rwenyagila for sacrificing a lot for my education, my brothers Evodius and Diocles, my sisters Evelina, Alistidia, Editha-Demetria, Levina and Belina, and my uncle Methodius and Godeliva Kaiza's family: Margareth, Mwombeki and Benedict. Your cordial support have been of significant assistance in my academic and social endeavors. Without you, my strength is doubtful and our family atmosphere that is relaxing and stimulating has been shoulders I could stand on in good and difficult times. Thank you so much, without your help I would not be here.

I know that many have assisted me but their names are still missing because I am not able to properly remember and recognize everyone here. Although words cannot express the respectful gratitude that I have for all of you, I wish to thank collectively, all the individuals that have helped me in the accomplishment of this project.

May the Almighty God return the favors to everybody!

Egidius Rutatizibwa Rwenyagila  
AUST - Abuja, Nigeria  
Wednesday 5<sup>th</sup> August, 2015

# Table of Contents

Dedication .....	iii
Abstract .....	iv
List of Publications .....	vii
Acknowledgements .....	ix
Table of Contents .....	xiii
List of Figures .....	xvii
List of Tables .....	xxi
1. Chapter One.....	1
Background and Introduction .....	1
1.1 Photovoltaics and the Challenging Energy Supply Context.....	1
1.2 Technologies Alternatives to c-Si PV Solar Cells.....	6
1.2.1 CdTe and CIGS Thin Film PV Generation .....	7
1.2.2 Organic PV (OPV) Solar Cell Generation.....	8
1.2.2.1 Power Conversion Efficiency.....	9
1.2.2.1.1 Optical Losses.....	9
1.2.2.1.2 Electron-Hole Pair Losses .....	10
1.2.2.1.3 Charge carrier transport losses .....	11
1.2.2.1.4 Charge carrier collection losses.....	11
1.2.2.2 Solar Cell Lifetime .....	12
1.2.2.3 OPV Solar Cell Components and Material Costs .....	14
1.3 Background to the Study: Unresolved Issues .....	15
1.3.1 Conceptual Question.....	18
1.3.2 Transparent Conducting Materials Alternatives to ITO .....	18
1.3.3 Motivation of the Study .....	20
1.4 Imperativeness and the Challenging TCO Context of ZnO .....	21
1.4.1 Imperativeness of ZnO as Transparent Electrode.....	21
1.4.2 The Challenging TCO Context of ZnO Films .....	23
1.4.3 The Emerging Layered Thin Film Composite Electrodes.....	24
1.4.4 Materials Selection .....	25
1.5 Research Problem .....	25
1.6 Objectives of the Study.....	26

1.7	General Methodology and Significance of the Work.....	27
1.8	Dissertation Plan.....	28
2.	Chapter Two.....	32
	Literature Review.....	32
2.1	Introduction .....	32
2.1.1	Introduction to PV Technologies.....	33
2.2	PV Solar Cell Operation Principle.....	35
2.2.1	Inorganic PV Solar Cell Systems .....	35
2.2.2	Organic PV Solar Cell Systems.....	40
2.2.2.1	Advances in OPV Technology and OSC Designs .....	42
2.2.2.2	Organic PV Solar Cell Operational Mechanisms.....	45
2.2.2.2.1	Organic BHJ Solar Cell Operation Principles .....	48
2.2.2.2.2	Difference between OPV and Inorganic Solar Cells.....	49
2.2.2.2.3	BHJ Organic PV Solar Cell Structure: How it Works?.....	52
2.3	Transparent Conducting Oxides in OPV Systems.....	52
2.3.1	Doped Transparent Conducting Oxides .....	54
2.3.2	Multilayered Transparent Conducting Films.....	55
2.3.2.1	ITO-based Multilayered Films .....	55
2.3.2.2	Multilayered ZnZ Film Composite Electrodes .....	60
2.3.2.2.1	Design of Multilayered ZnZ Thin Film Composites .....	60
2.3.2.2.2	Prior Work on Multilayered ZnZ Thin Film Composites .....	61
2.3.2.2.3	Multilayered ZnO/Al /ZnO Thin Film Composite Structures .....	67
3.	Chapter Three.....	68
	Numerical Modeling of Multilayered ZAZ Thin Film Composite Structures.....	68
3.1	Introduction .....	68
3.2	Numerical Methods .....	69
3.2.1	Theory of Light Absorption.....	69
3.2.2	Light Reflection and Transmission Model .....	71
3.2.3	Numerical Modeling Tool and Procedure .....	74
3.2.3.1	The Modeling Tool.....	74
3.2.3.2	Numerical Procedure.....	75
3.3	Results and Discussion .....	76
3.3.1	Effects of Al Thickness on the Optical Properties of ZAZ Film.....	76
3.3.2	Effects of ZnO Thickness on the Optical Properties of ZAZ Film .....	79

3.3.3	Average Optical Properties of Model Multilayered ZAZ Films .....	80
3.4	Concluding Remark .....	82
4.	Chapter Four .....	83
	Optical and Electrical Properties of Multilayered ZAZ Thin Film Composites for Applications in Transparent Electrode Coatings .....	83
4.1	Introduction .....	83
4.2	Methods .....	85
4.2.1	Simulations of ZAZ with Ultra-thin Mid-Al Layer Thicknesses .....	85
4.2.2	Experimental.....	85
4.2.2.1	Experimental Procedure .....	85
4.2.2.2	Characterization Techniques .....	88
4.2.2.2.1	The Crystalline Structure of the Obtained ZAZ Multilayer Films .....	88
4.2.2.2.2	Optical Characterization .....	91
4.2.2.2.3	Electrical Characterization .....	92
4.2.2.2.4	Effective Electrical Properties of ZAZ Multilayer Films .....	94
4.3	Results and Discussion .....	97
4.3.1	Crystal Properties of ZAZ Multilayer Film Composites .....	97
4.3.2	Optical Properties of Model ZAZ Multilayer Film .....	100
4.3.2.1	Transmittance of ZAZ Multilayer Thin Film Stacks .....	100
4.3.2.2	Reflectance of Multilayered ZAZ Thin Film Stacks.....	102
4.3.2.3	Comparison of Multilayer ZAZ Simulations with Experiments.....	104
4.3.2.3.1	Effects of Al Thickness on the Optical Bandgap of ZnO Films.....	108
4.3.3	Electrical Properties of ZAZ Multilayer Film Structures .....	112
4.3.4	Comparison of Model ZAZ with other Multilayer Films.....	114
4.3.4.1	Other Multilayered ZAZ Thin Film Stacks.....	114
4.3.4.2	Effects of Mid-Al on the Electrical Properties of ZAZ Film .....	115
4.3.5	Performance of Model ZAZ Multilayer Films .....	117
4.4	Concluding Remarks .....	119
5.	Chapter Five .....	120
	Prospects of Non-ideal Interfacial/Interlayer Contacts in Polymer: Fullerene BHJ Solar Cells.....	120
5.1	Introduction .....	120
5.2	Overview of Organic Solar Cell Models .....	121
5.3	Characterization of Solar Cells via Numerical Modeling .....	123
5.4	Solar Cell Numerical Modeling Approach.....	128

5.4.1	Basic Drift Diffusion Equations .....	129
5.4.1.1	The Poisson's equation.....	129
5.4.1.2	Current Continuity Equations .....	129
5.4.1.3	Boundary Conditions.....	131
5.4.2	Generation-Recombination of Excitons and EHPs .....	131
5.4.3	Generation and Recombination of Charge Carriers .....	132
5.4.4	Solving the 2DG Drift-Diffusion Model .....	135
5.4.4.1	Iteration Scheme.....	135
5.4.5	Discretization of the OSC Device .....	138
5.4.5.1	Discretization of Poisson's Equation .....	139
5.4.5.2	Discretization of Current Densities .....	140
5.4.5.3	Discretized Equations for Charge Carrier Densities .....	142
5.4.6	Modeling of Non-ideal Photoactive-Anode Contacts .....	143
5.5	Results and Discussion .....	145
5.5.1	Effects of contact on the J-V characteristics .....	145
5.5.2	Influence of contact on potential and carrier distributions .....	151
5.5.3	Evaluation of the Numerical Results .....	154
5.5.4	Implications and Concluding Remarks.....	156
6.	Chapter Six .....	158
	Implications, Concluding Remarks and Suggestions for Future Work .....	158
6.1	Implications of the Study.....	158
6.2	Summary and Concluding Remarks .....	160
6.3	Suggestions for Future Work.....	162
6.3.1	The Multilayered ZAZ Thin Film Composite Electrodes .....	163
6.3.2	The Organic Solar Cell .....	164
	References .....	167
	APPENDIX A.....	184
	Program Source Code .....	184
	Electron Mobility .....	191
	Hole Mobility.....	195

## List of Figures

Figure 1.1: Yearly progresses of the different best research solar cell technologies. <sup>[7]</sup> .....	2
Figure 1.2: (a) Yearly contributions by different energy sources to the world energy consumption (b) total energy consumption and the renewable fuel shares in 2013. <sup>[11]</sup> .....	4
Figure 1.3: Schematics of energy level diagram illustrating: (a) desirable and (b) undesirable electronic processes that occur simultaneously in bulkheterojunction (BHJ) organic solar cells. ....	10
Figure 1.4: Yearly developments of laboratory organic solar cell PCEs. <sup>[56,59,60]</sup> .....	12
Figure 1.5: Materials Abundance issues for some selected rare-earth metals. <sup>[69]</sup> .....	14
Figure 1.6: Electro-optical properties of the main transparent conducting oxides prepared by various techniques (shown in brackets) and fluctuations of the properties (indicated by arrow bars) as reported by various researchers. <sup>[68]</sup> .....	19
Figure 1.7: Hexagonal Wurtzite structure of ZnO. <sup>[77]</sup> .....	21
Figure 2.1: Diagrammatic of a typical p-n solar cell operation principle. <sup>[10]</sup> .....	36
Figure 2.2: HOMO and LUMO energy levels (values in unit of eV) of the common OPV solar cell materials (Source: Goswami, <i>et al.</i> Adv. Sol. Ener., Vol. 17, Earthscan London).....	41
Figure 2.3: Schematic diagram of a typical organic BHJ solar cell structure. <sup>[127]</sup> .....	42
Figure 2.4: Absorption coefficients for the commonly used photoactive absorber solar cell materials. <sup>[142]</sup> .....	46
Figure 2.5: Bandgap energies (LUMO-HOMO levels) for several HT/EB layer materials to the left of the absorbers P3HT, Silicon (shown in gray stripe for comparison) and ET/HB layer materials to the right. <sup>[142]</sup> .....	47
Figure 2.6 Mechanistic operational steps for the photo-generation, transportation and collection of free charge carriers in BHJ organic solar cell structures. <sup>[58]</sup> .....	49
Figure 3.1: Schematic illustration of thin film interference. Light wave of intensity, $I_0$ , traveling from a layer of lower refractive index to the layer of higher refractive index automatically undergoes a phase shift of $\pi$ radians upon reflection. The optical path difference (OPD) and wave length, $\lambda$ , of light in a layer, $l$ , of refractive index, $n_l$ , and thickness, $t_l$ , at an angle of refraction, $\theta_l$ , are given by: $OPD = 2n_l t_l \cos\theta_l$ and $\lambda_l = \lambda_{vacuum}/n_l$ , respectively. ....	70

Figure 3.2: Optical T of ZAZ multilayer films with different mid-Al thicknesses between 1 – 100 nm and ZnO double-layers of 50 nm each on transparent glass substrates. .... 77

Figure 3.3: Simulated optical A of multilayered ZAZ thin film composite structures with different captioned mid-layer Al thicknesses and ZnO layers of 50 nm thick each. .... 77

Figure 3.4: Simulations illustrating the dependence of the optical R of multilayered thin film structures with fixed upper and lower ZnO thicknesses of 50 nm and different mid-Al layer thicknesses captioned on each curve..... 78

Figure 3.5: Simulations illustrating the effects of ZnO layer thicknesses between 10 – 100 nm on the optical characteristics of multilayered ZAZ thin film composite structures. Each of the lower and upper ZnO layer thicknesses were varied between 10 – 100 nm with mid-Al layer thickness fixed at 5 nm..... 80

Figure 3.6: Percentage averages of optical A, R and T of multilayered ZAZ thin film composite structures with ZnO double-layers with thicknesses of 50 nm each and mid-layer Al thicknesses varying between ~ 1 – 100 nm. .... 81

Figure 4.1: XRD patterns demonstrating the dependence of crystallinity on thermal annealing conditions for a multilayered ZnO(25 nm)/Al(3 nm)/ZnO(25 nm) thin film composite structures. These were obtained using RF MS deposition power densities of  $2.27 \text{ Wcm}^{-2}$  and  $5.10 \text{ Wcm}^{-2}$  for ZnO and mid-Al layers, respectively..... 87

Figure 4.2: Condition (path-length difference) for the maximum (preferred crystal-orientations) intensity contained in the Bragg's law. The angle of diffraction of x-rays by the crystalline atomic planes gives the structural characteristics of the crystal while the intensity of the scattered radiation signifies the characteristic information or the atomic composition of the crystalline material..... 90

Figure 4.3: Schematic diagram illustrating the operation principle of XRD system.<sup>[198]</sup> As long as the wave length of the x-rays impinging upon the crystal is known, the obtained XRD data allow for the determination of the material crystal structure. If the crystal structure is known, the XRD information allows the identification of the phase composition of a given material..... 91

Figure 4.4: Schematics illustrating the head of a Signatone four-point probe system. .... 92

Figure 4.5: Snapshot of a computer screen showing the cross section of a 2D contour map for sheet resistance of a multilayered ZAZ thin film composite structure with mid-Al layer thickness of 9 nm and ZnO double-layer thickness of 25 nm each. .... 94

Figure 4.6: Schematics of the multilayered ZAZ thin film composite structure with effective sheet resistance,  $R_s$  ( $R_{\text{ZnO/Al/ZnO}}$ ), represented as a parallel combination of sheet resistances of the discrete layers of ZnO and mid-Al in an electric circuitry..... 96

Figure 4.7: XRD patterns of multilayered ZAZ thin film composite structures with ZnO double-layer thicknesses of 25 nm. The inserts indicate the relative dependence of the preferred (002) oriented peak intensity on the different mid-Al layer based on the captioned thicknesses. These patterns were obtained after annealing the multilayered ZAZ thin film composite structures for 90 minutes at 400°C in air. .... 98

Figure 4.8: (a) XRD pattern and (b) optical T profile of a 50 nm thick ZnO thin film deposited on rigid transparent glass after annealing for 90 minutes at 400°C in air. .... 99

Figure 4.9: Solar T curves in the visible region of the spectrum obtained from annealed multilayered ZAZ thin film composite structures with upper and lower ZnO layers, with 25 nm each and mid-Al layer thicknesses captioned in the plots. .... 101

Figure 4.10: Visible R spectra for the annealed multilayered ZAZ thin film composite structures with ZnO layers of 25 nm thick each and mid-layer Al thicknesses based on 0, 5 and 10 nm..... 103

Figure 4.11: Simulated T curves illustrating the dependence of ZnO(25nm)/Al/ZnO(25 nm) multilayered thin film on the thickness of Al interlayer between 3 – 8 nm. .... 104

Figure 4.12: Experimental (solid) and simulated (dash) profiles illustrating the dependence of visible solar T spectra of the multilayered ZnO (25 nm)/Al/ZnO (25 nm) thin film composite structure on different Al interlayer thicknesses based on (a) 3 nm, (b) 4 nm, (c) 5 nm, (d) 6 nm, (e) 7 nm and (f) 8 nm. For comparison, the experimental T spectrum of a 50 nm ZnO film (without mid-layer Al) prepared on glass substrate is also shown as the blue curve in (a)..... 106

Figure 4.13: Average optical properties of ZAZ multilayer film stacks with ZnO double-layers with thicknesses of 25 nm and optimum mid-Al thickness between 1 – 10 nm. . 107

Figure 4.14: Plots of  $(\alpha_s/h\nu)^2$  as function of photon energy,  $h\nu$ , illustrating the dependence of optical bandgap energy of multilayered ZnO (25 nm)/Al/ZnO (25 nm) thin film composite structures on the captioned mid-layer Al thicknesses. .... 109

Figure 4.15: Dependence of optical bandgap energy of ZnO (25 nm)/Al/ZnO (25 nm) on the mid-Al thickness between 0 and 10 nm. .... 110

Figure 4.16: Dependence of the sheet resistance and the effective resistivity of the model multilayered ZAZ thin film composite stack with ZnO-layer thicknesses of 25 nm on the optimum mid-layer Al thicknesses between 1 – 10 nm..... 113

Figure 4.17: Comparison between the Haacke figures of merits for the multilayered ZnO films with mid-layer Al (the ZAZ produced in this work) and those with nanolayers of Au obtained from Ref.<sup>[74]</sup> ..... 118

Figure 5.1: Schematics of typical current-voltage (J-V) characteristics of an illuminated PV solar cell system..... 124

Figure 5.2: Schematics of iterative flow diagram for solving the basic continuum drift-diffusion equations model.....	137
Figure 5.3: Typical 2D finite difference discretization of the OPV solar cell device ....	139
Figure 5.4: Generation rate demonstrating non-ideal contact of arbitrary $L_c$ and $H_c$ .....	144
Figure 5.5: Influence of $H_c$ on J-V curves of a BHJ OSC with $L_C$ of 80%.....	146
Figure 5.6: Influence of $H_c$ on the J-V curves of a BHJ OSC with $L_C$ of 60%.....	146
Figure 5.7: Influence of $H_c$ on the J-V curves of a BHJ OSC with $L_C$ of 40%.....	147
Figure 5.8: Influence of $H_c$ on the J-V curves of a BHJ OSC with $L_C$ of 20%.....	148
Figure 5.9: Influence of contact height, $H_c$ on the J-V curves a BHJ OSC with $L_C$ of 10%. .....	150
Figure 5.10: Evolution of p.d with different contact lengths, $L_c$ , and partial contact, $H_c$ , captioned. ....	153
Figure 5.11: Evolution of charge carrier (p and n) densities with contact length and partial contact height at the photoactive/transparent anode of a BHJ OSC. ....	154
Figure 5.12: Comparison of J-V characteristics of an OPV solar cell system with perfect planar interface with experimental profiles ( <sup>K</sup> ) adapted from Koster <i>et al.</i> <sup>[126]</sup> .....	155

## List of Tables

Table 1.1: Properties of single crystal ZnO at room temperature. <sup>[79]</sup> .....	22
Table 2.1: Electrical resistivity values for the highly conductive metals. <sup>[185]</sup> .....	61
Table 4.1: Process parameters for the deposition of ZAZ multilayer Film stacks .....	88
Table 4.2: List of intermediate layer Al thicknesses used for the RF MS deposition of ZnO (25 nm)/Al/ZnO (25 nm) multilayer thin film composite structures and the corresponding electrical sheet resistances, effective resistivities and HFoMs for structures with conductive nanolayers of Al and Au.....	111

# 1. Chapter One

## Background and Introduction

### 1.1 Photovoltaics and the Challenging Energy Supply Context

Environmentally-benign renewable energy resource must provide a good alternative energy source. Renewable energy is produced from natural resources such as sunlight, wind, rivers, biomass and geothermal sources, which are naturally replenished. Depending on its nature, sunlight is one of the most competitive renewable energy sources. It is a long life, environmentally indisputable energy source that is conveniently accessible from nearly everywhere on earth.

Some evidence based figures to give the novelty of photovoltaic (PV) solar cell technology potentials exist. For example, the total energy consumption on earth in 2009 was  $\sim 5 \times 10^{20} \text{ J}$ ,<sup>[1]</sup> which is equivalent to  $\sim 1$  hour of the annual solar energy supply to the earth. This has been estimated to have a value of  $\sim 2 \times 10^{24} \text{ J}$ .<sup>[1,2]</sup> It has been estimated also that, covering of  $\sim 0.2\%$  of the Earth's land with 10% power conversion efficiency (PCE) solar cells would provide  $\sim 20$  Terawatts of photoelectric power. This is about two times greater than the total fossil fuel consumption of the world including other numerous fuel types.<sup>[3]</sup> The sun is, therefore, a highly abundant source of clean energy.

However, partly due to the high cost, solar energy is not maximally exploited.<sup>[1]</sup> Even though, as shown in Figure 1.1, several PV technologies are available with different characteristics in terms of PCEs, costs, stability, applicability and maturity. These are commonly categorized in three PV generations, namely: generation 1, which involves the mono- and/or poly-crystalline silicon (c-Si) based PV solar cells. Generation 2 includes

thin film solar cell technology, comprising amorphous silicon (a-Si), Copper-Indium-Gallium-Diselenide, Cu(In, Ga)Se<sub>2</sub> (CIGS), cadmium telluride (CdTe) and group III-V compounds (GaAs, GaP, GaSb and so forth). The third generation includes the PV solar cells that are based on dye-sensitised<sup>[4]</sup> and organic (polymer) solar cell technologies.<sup>[5-7]</sup>

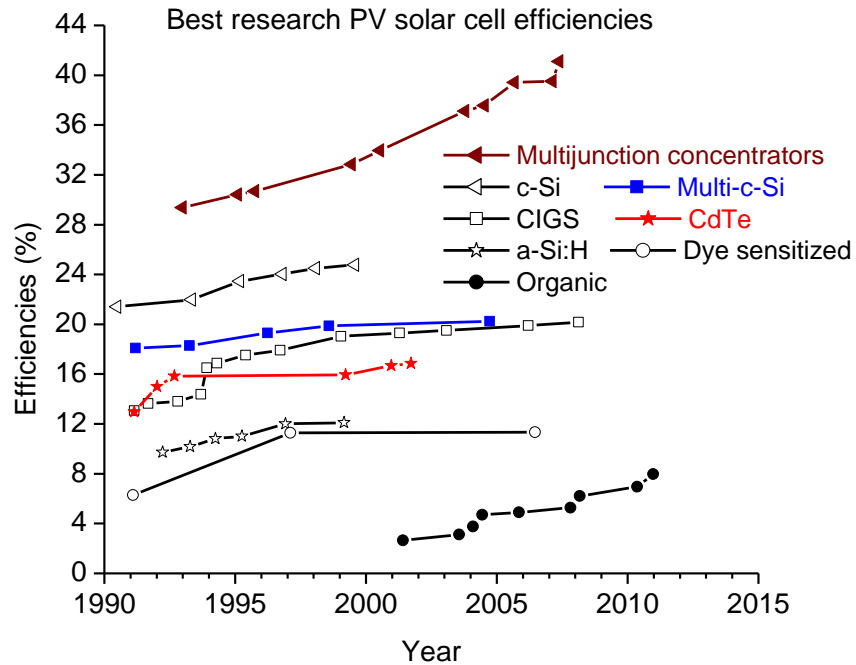


Figure 1.1: Yearly progresses of the different best research solar cell technologies.<sup>[7]</sup>

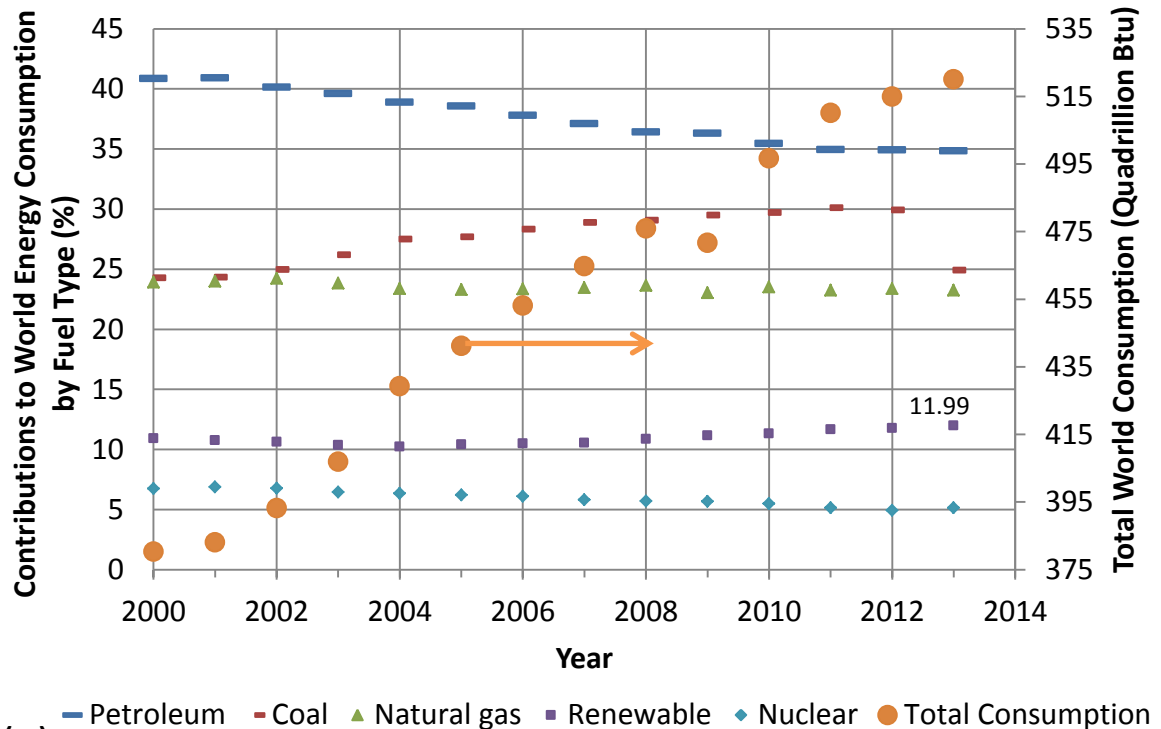
However, owing their attractive combinations of PCE, stability and maturity, solar cell technology involving c-Si are the most widely used and commercially available PV systems. Their superiority over other solar cell technologies has enabled the c-Si based solar cells to dominate the PV industry for a long time. For example, c-Si solar cells accounted for ~ 88% of the global market in 1999,<sup>[8]</sup> about 99% in 2004<sup>[9]</sup> and about 90% of all PV solar cell technology market share in 2008.<sup>[11]</sup>

However, due to the high market demand of c-Si, as principal materials in variety of semiconductor devices and components,<sup>[10]</sup> c-Si has become increasingly expensive,

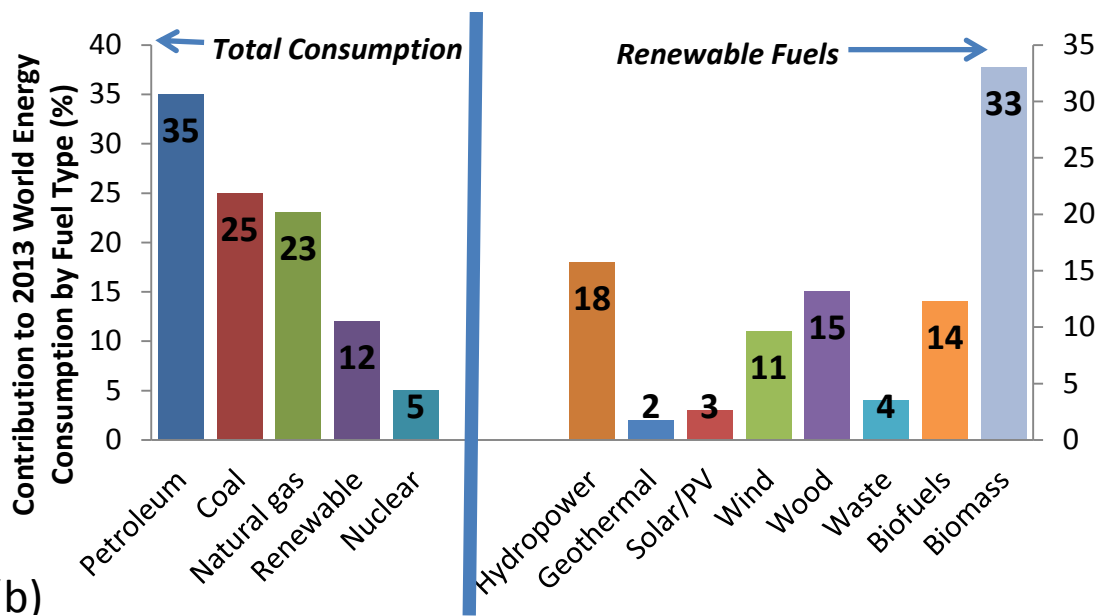
compared to many of the emerging alternatives. Also, the production of electricity from c-Si PV solar cells is based generally on batch-to-batch processing techniques, which are energy intensive and expensive.<sup>[1,8]</sup> As a natural rule, for any of the PV technologies, the solar cell PCE is fundamentally a very important solar cell parameter. However, for economic viability reasons it is desirable to produce solar cells of high PCEs obtained at relatively low costs with low cost-effective materials and processes.

Therefore, some of the present PV solar cell systems, such as c-Si and group III-V compound technologies, are not promising due to their high materials and processing costs. In fact, the cost hurdle has caused the PV technology to remain less competitive in the energy production, compared with the other existing conventional exhaustible fossil fuels. For example, recent reports<sup>[1]</sup> show that, the electricity produced using PV solar cell technologies is of a factor  $\sim 2 - 4$  more expensive than the electricity produced from traditional non-renewable fuel plants.

The above challenges have limited the advancements, distribution and use of PV technologies. Hence, the global share of PV technologies in electricity production still remains marginal today, and is likely to remain this way for a long period of time. Further evidence of the limited global impact of PV is in the increasing market share of fossil fuels in the generation of electricity. Notably, about 65-70% of electricity consumed currently in the global market is derived mainly from exhaustible fossil fuels such as petroleum, coal and natural gas.<sup>[1]</sup> As shown in Figure 1.2, most of the remaining balance is largely derived from other energy resources, such as nuclear, biomass, rivers, geothermal and wind.<sup>[11]</sup>



(a)



(b)

Figure 1.2: (a) Yearly contributions by different energy sources to the world energy consumption (b) total energy consumption and the renewable fuel shares in 2013.<sup>[11]</sup>

Furthermore, due to the strong reliance on non-renewable fossil fuels, the world energy supply system has been experiencing many problems. These include: energy

market instabilities, technical or physical failures/threats that comprise natural disasters and different security sabotages that arise mostly due to strong global dependence on fossil fuel resources, which are concentrated in few countries such as Russia, Iran and Qatar.<sup>[12]</sup> In addition, some of these places are affected by geopolitical problems, as well as socio-economical instabilities.<sup>[12,13]</sup> Moreover, world fossil fuel reserves are unable to follow with the global energy demand, which is rising continually as a result of the effects of human population growth and development (Figure 1.2).

Furthermore, the production of energy from fossil fuels is often toxic to the environment and health.<sup>[14]</sup> It is agreed generally that the increasingly use of hydrocarbon-based fossil fuels (petroleum, coal and natural gas), which represent the main part of the world energy consumptions, is responsible for more than 99% of the greenhouse gas emissions.<sup>[15,16]</sup> It is also generally agreed that greenhouse gases are the main causes of the increasingly world ecosystem instabilities.<sup>[14]</sup> This is proven by the numbers of natural catastrophes that are occurring repeatedly in different areas of the world, mainly as a result of the different adverse effects of climate change.

The above energy and environmental problems that are associated to the use of fossil fuels and the adverse social impacts such as those occurring in hydropower dams<sup>[17]</sup> along with the difficulties in the management of disposals from some of spent fuels such as radioactive wastes from nuclear energy plants.<sup>[18]</sup> These have increased the global interest and concerns about the security, sustainability, reliability and consumption of energy that can be supplied from PV systems. They have also led policymakers, as well as scientists with PV expertise, to propose many strategies, based largely on research and development solutions, that can be used to improve the global PV production and market

penetration. The proposed solutions include the following three important long-term PV objectives:<sup>[1,8]</sup>

- i. Production of high PCE PV solar cell systems.*
- ii. Increasing recourse to alternative low cost PV systems that are based on environmentally harmless solar cell materials and processes.*
- iii. Increasing production, stability, distribution and use of PV systems.*

As mentioned earlier, largely due to high PCEs and maturity, systems that are based on c-Si solar cell technology and processes have dominated the PV industry. The continual use of c-Si based solar cell systems is intended for the enhancement of PV competitiveness in the global energy share and electricity market. However, partly due to high costs of c-Si and the expensive production processes, c-Si solar cells have increased the vulnerability of PV technologies. This has caused some difficulties (technical and practical limitations) in terms of production, distribution and use of PV solar cell technology. It has also impeded the development and implementation of PV technologies in a way that can cover significant share of our electricity and energy needs.

## **1.2 Technologies Alternatives to c-Si PV Solar Cells**

The PV technology challenges above have triggered recent research interest to develop new cost effective solar cell technologies alternatives to the costly c-Si solar cells. Most of these interests are associated to possible mechanisms that can improve PCEs, stabilities and reduce the costs of the non c-Si solar cell systems. So far, several alternative PV technologies (with potentials to compete with and replace c-Si solar cells) have been investigated. These include PV technologies and systems that are based on thin film technologies: CIGS, CdTe and organic or polymer solar cells. The thin film solar

cell technologies are suitable for mass production, mainly due to their promising cost advantages and photo-electric power conversion features. These include:

### **1.2.1 CdTe and CIGS Thin Film PV Generation**

Owing to their good physical properties, CdTe and CIGS compound semiconductors and their related thin film technologies are attractive PV materials, as far as solar cell PCEs and costs are concerned.<sup>[19]</sup> They have large optical absorption coefficients, which minimize their PV solar cell absorber layer thicknesses, while maintaining good electrical and optical stabilities.<sup>[19]</sup> As shown in Figure 1.1, CdTe and CIGS based laboratory solar cells have already reached PCEs of over 15%.<sup>[7]</sup> Additionally, economical fabrication processes of CdTe and CIGS PV systems are already being utilized in large-scale manufacturing.<sup>[3]</sup> Also, their materials bandgap energies are close to the optimum theoretical PCEs and they are not difficult to produce. This is due to good electronic properties of their PV solar cell structures, which are usually easy to optimize via post deposition treatments.<sup>[19]</sup>

However, there are still many drawbacks that must be overcome prior to the widespread use of CdTe and CIGS solar cell technologies. One of the major drawbacks that limit the use of CdTe and CIGS solar cells is their high cadmium content. This gives rise to environmental and health concerns.<sup>[20-22]</sup> In addition, CIGS solar cell structures contain the costly rare earth element, indium, which is the major concern of this dissertation. This makes large scale production of CIGS solar cells expensive. Furthermore, the other materials that are used for the production of CIGS and CdTe solar cells are relatively less abundant. This makes CIGS and CdTe materials less available than those used in silicon or organic solar cells. This ultimately makes CIGS and CdTe

thin film solar cell systems unsustainable technologies in terms of their long-term production at large scales and also in terms of cost effective PV production.

### **1.2.2 Organic PV (OPV) Solar Cell Generation**

Unlike c-Si, CIGS and CdTe solar cell technologies, which are technically mature and widely commercialized, only limited information is known on the fundamental material parameters and operation principles of OPV solar cell technology. Nevertheless, the OPV technology is currently a very promising solar cell technology that allows for the potential use of organic semiconducting polymers as low-cost materials alternatives to c-Si.<sup>[23]</sup> Although OPV technology is still at an early stage of its development, owing to its features of being eco-friendly, mechanical flexibility, vision for mass production and/or large-area fabrication processes (simple roll-to-roll or printing, spin coating, spraying or vaporization), OPVs are considered to be one of the important future sources of energy.<sup>[1,7]</sup>

This makes OPV solar cell technology an important energy source candidate for applications in most of the domestic energy needs (such as lighting) in remote rural places or off-grid urban poor communities. Such places require domestic micro-system energy frameworks and initiatives, which can provide energy solutions that can prove to be more cost-effective (in terms of delivery infrastructure) than extending utility grids from the state agents.<sup>[14]</sup> Furthermore, since organic materials and organic solar cell processes are quite cost effective than traditional inorganic semiconductor (c-Si, CdTe or CIGS) technologies, organic PV is considered to be the appropriate future energy solutions at least for the off-grid poor population.

Notably, in recent years, there have been rapid improvements in the development of organic solar cells in terms of materials and designs.<sup>[4,24-53]</sup> These efforts have raised the performance of organic solar cells to relatively high levels, which few years ago, would have seemed doubtful. For example, the amount of organic semiconductor materials required for the photoactive layers are usually very small. The production potential for a single process line based on printing has been estimated to exceed 1000 m<sup>2</sup> per hour<sup>[54]</sup> and organic solar cells with PCEs between ~ 7 – 10% have been produced.<sup>[7,55,56]</sup> However, it has also become increasingly clear that there remains lots of scope for further improvements to be achieved in terms of the necessary organic solar cell technological requirements that include: materials reliability, solar cell processing and commercialization of the OPV solar cell technology. Most of the improvements are particularly flourished onto the three key challenging contexts of the PV technologies, namely:<sup>[1,8]</sup>

### **1.2.2.1 Power Conversion Efficiency**

Commercial success of any PV technology requires the PCE to be sufficiently high. For organic solar cells, a theoretical PCE of about 20% has been reported.<sup>[57]</sup> However, the actual organic solar cell PCE is generally lower, currently between ~ 1 – 10%. The difference between the theoretical and the generally low experimental (actual) organic solar cell PCEs is attributed to numerous loss factors. These losses include:<sup>[58]</sup>

#### **1.2.2.1.1 Optical Losses**

These occur due to photons losses, which result from incident light reflections at the air/electrode, electrode/organics, organic/organic and organic/inorganic interfaces within organic solar cell structures. Such optical losses may also occur as a result of

unabsorbed sunlight or photons that are being absorbed in organic solar cell materials that are not involved in the photo-generation of free-charge carriers. This decreases the PV effects and reduces the PCEs of organic solar cells.

### 1.2.2.1.2 Electron-Hole Pair Losses

These are losses due to undesirable exciton ( $R_e$ ) and/or polaron ( $R_p$ ) pairs and their recombination events (Figure 1.3). Exciton recombination (which occurs during exciton diffusion, immediately after excitation of donor polymers) annihilates the charge carriers. This prevents excitons from reaching the donor/acceptor (D/A) interfaces for dissociation. Further annihilation of electron-hole (polaron) pairs may occur at or after D/A interfaces. This occurs generally from inefficient charge-carrier dissociation, as a result of unstable polaron-pair separation.

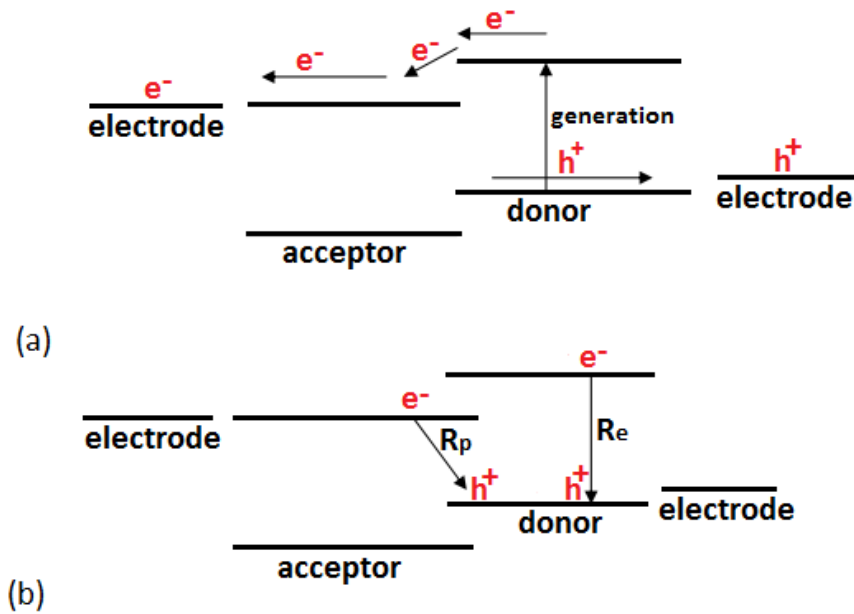


Figure 1.3: Schematics of energy level diagram illustrating: (a) desirable and (b) undesirable electronic processes that occur simultaneously in bulk heterojunction (BHJ) organic solar cells.

### **1.2.2.1.3 Charge carrier transport losses**

These are charge-carrier losses that occur as a result of charge carrier traps. The presence and the subsequent trapping of free charge carriers in donor or acceptor molecular materials limit the photogenerated holes and electrons from reaching their respective electrodes. This prevents them from contributing to the PV effect, thus affecting the overall performance of the solar cell detrimentally.

### **1.2.2.1.4 Charge carrier collection losses**

These involve charge-carrier losses due to the non-ideal interfacial adhesion or poor contacts throughout the solar cell structure. Such interfacial contacts interfere adversely with charge transport mechanisms. This results in inefficient free-charge carrier collections at the anode and cathode of organic solar cells. They, therefore, reduce the PCEs of organic solar cells.

However, global efforts have been made to enhance organic PV solar cell PCEs, stabilities and overall performance. Such efforts have greatly improved organic solar cell PCEs.<sup>[7]</sup> As shown in Figure 1.1, PCEs of organic PV solar cells have been significantly increased over the past ten years. This is further supported by the rapid increase in the amount of publications in the field of organic electronic materials and OPV solar cells.<sup>[56]</sup> Thus, as shown in Figure 1.4, the literature<sup>[56,59,60]</sup> has continually shown increases in organic PV solar cell PCEs, with laboratory solar cell efficiency recently reaching 10%.<sup>[56]</sup>

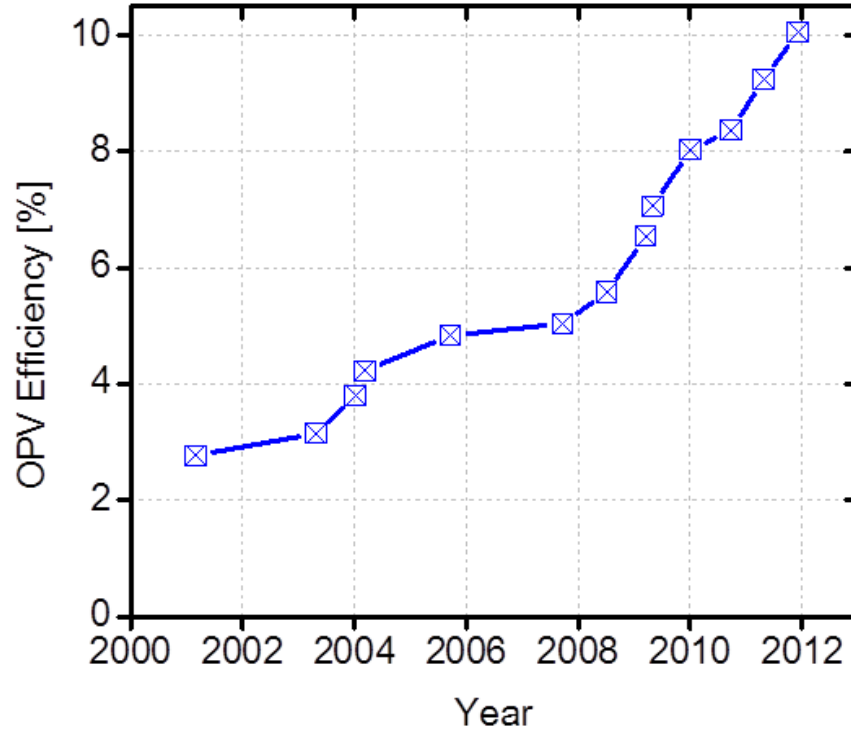


Figure 1.4: Yearly developments of laboratory organic solar cell PCEs.<sup>[56,59,60]</sup>

### 1.2.2.2 Solar Cell Lifetime

Another key challenge that hinders the development and commercialization of organic PVs is their solar cell instabilities. This limits greatly the lifetimes of OPV devices for usage in various environments. Grossiord *et al.*<sup>[1]</sup> have provided an excellent contemporary review of the various degradation mechanisms that occur in organic solar cells. Different research groups<sup>[61-63]</sup> have also reported oxygen and water to be key factors that are responsible for the degradation of organic electronic devices, tested in air. Both water vapour and oxygen can diffuse generally into organic solar cells mainly through the microscopic pores that are present in their back electrode surfaces.<sup>[61-63]</sup>

Generally, the fast degradation or short lifetimes of devices present serious technical concerns for the technological development and commercialization of organic PV devices.<sup>[1]</sup> Such concerns are further increased due mainly to the organic solar cell

stability set-ups and tests, which are often carried out on small laboratory solar cells. Such small solar cells can be fabricated inside the glove boxes with inert environments. The fabrication can usually be followed by immediate encapsulations with impermeable transparent membranes. This is done to increasing the solar cell lifetime by preventing water vapour and oxygenated air from entering the solar cell devices. Unfortunately, large scale production of organic PV systems using glove boxes or inert environments is not economically feasible.

Consequently, processing of large area organic solar cell systems is necessarily done in open atmospheric ambient. This makes the solar cell devices vulnerable to humid oxygenated air and hence acceleration of their degradation mechanisms. Nevertheless, along with enhancements in PCEs, the stabilities and lifetime of organic PV devices have improved greatly over the past years. For example, compared to early organic solar cell systems, which had very short lifetimes in the order of few hours to few days, more stable organic solar cells have been produced in recent years. These include organic solar cell devices with lifetimes of up to  $\sim 10,000$  hours<sup>[64]</sup> or more than a year<sup>[65]</sup> in outdoors test set-ups.

Furthermore, the use of ITO anodes that are coated with some transition metal oxides such as molybdenum oxide ( $\text{MoO}_3$ ) or vanadium oxide ( $\text{V}_2\text{O}_5$ ), as hole transporting layer (HTL) or electron blocking layer (HTL) as alternatives to the conventional poly(3,4-ethylenedioxythiophene): poly(styrene sulfonate) (PEDOT:PSS) have been shown to improve the lifetimes of organic solar cell devices.<sup>[66]</sup> Also, the invention of inverted organic solar cell structures, in which Al backside electrode, the conventionally used cathode material in organic PV devices, is replaced with less reactive

metals such as silver or gold, along with coating of ITO with additional buffer layers of ZnO or TiO<sub>x</sub> (which are more stable than PEDOT: PSS), has been shown to enhance the stability of organic solar cell systems.<sup>[67]</sup>

### 1.2.2.3 OPV Solar Cell Components and Material Costs

The other important hurdle that must be overcome before organic solar cell technology becomes commercially viable is finding low cost-effective materials that can compete with and effectively replace ITO, a standard transparent conducting oxide (TCO) that serves as anode of organic PV devices. In terms of performance characteristics, ITO is a highly effective transparent anode or TE material for applications in organic solar cells<sup>[68]</sup> and many other inorganic and organic optoelectronic devices and components. However, ITO is also surrounded with many drawbacks that hinder its application in large amount. ITO is an expensive material. The high cost of ITO arises primarily from one of its principal element indium. As shown in Figure 1.5, indium is a rare earth metal<sup>[69]</sup>. Hence, it is scarce and very expensive.

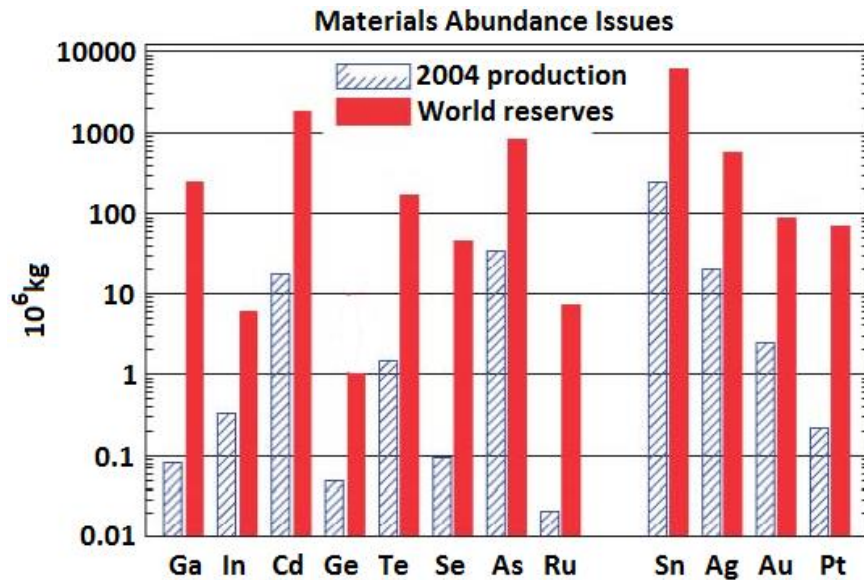


Figure 1.5: Materials Abundance issues for some selected rare-earth metals.<sup>[69]</sup>

Furthermore, the available world reserve of indium of  $\sim 6 \times 10^6$  kg (Figure 1.5), for ITO production will soon be insufficient to meet the global demand based on the anticipated growth in electronic and solar applications. Also, because of its high brittleness, ITO (which is often used as a transparent anode material) cracks easily, thus resulting in PV device failure. This makes it unsuitable for applications in highly flexible organic solar cells or other flexible organic electronic systems, such as organic light emitting diodes (OLEDs).<sup>[70,71]</sup> Therefore, from practical and commercial perspectives, the following two main approaches (long-term objectives) to the development of organic solar cells and light emitting devices are generally agreed upon:

- i. *The first approach is to increase the PCEs as well as the stabilities of OPV systems.*
- ii. *The second one is to reduce the cost of materials that are used in the production of OPV devices. This involves photoactive semiconductor materials, solar cell production processes and other dominant contributors to the overall costs of OPV devices, such as TE materials<sup>[71]</sup> for given OPV solar cell stabilities and PCEs.*

This dissertation deals mainly with the second objective above. It aims at development of multilayered composite transparent conducting thin film structures with improved electro-optical properties. These are explored for potential applications as improved anodes or cost-effective TEs in organic solar cells, light emitting diodes, as well as in other active and passive electronic devices and optoelectronic components.

### **1.3 Background to the Study: Unresolved Issues**

The operation mechanism of organic solar cells (Figure 1.3) requires integration of photoactive organic semiconducting materials with front and backside electrodes. Furthermore, in order to be effective, the front side electrode must be transparent enough

to allow incident photons into the photoactive layer (PAL) of organic solar cell, whereupon the absorption of light results in PV effects. Also, electrodes, the anode and the cathode must be highly conductive in order to collect the photo-generated charge carriers, before passing them to external circuits.

Therefore, effective organic solar cell TEs must possess adequate combination of optical and electrical characteristics. This requires transparent conductive properties that are needed for reasonable operation of organic PV systems and other organic optoelectronic devices. Generally, effective organic solar cell TEs must exhibit two main characteristic features during their processing, and also when in performance within solar cell devices. These are:

- i. High average visible and near infrared solar transparency, since they possess wide bandgap energies, which minimize optical losses in these regions of the spectrum.*
- ii. Low specific sheet resistance or a nearly metallic conductivity that combines with high visible transparency spectral to give an appropriate optoelectronic Haacke figure of merit (HFoM), the practical measure of TE performance.*

It is important to note here that, owing to good electrical property (in the range of  $\sim 5 \times 10^{-4}$  to  $7 \times 10^{-5} \Omega \text{ cm}$ ) and high optical transparencies (above 80%), indium oxide (IO) and ITO are superior over the other transparent conducting thin film coatings.<sup>[68]</sup> This makes them the most widely commercialized materials for applications in TEs in passive or active layered electronics and optoelectronics, such as solar cells, light emitting diodes and other devices.<sup>[68]</sup> Furthermore, the working principle of organic PV devices requires strong electric fields between the front and backside electrodes.<sup>[9]</sup> The field is needed partly for separation of bound polaron-pairs (the short lived charge-

transfer complexes), which are formed immediately following the dissociation of strongly bound organic exciton-pairs.<sup>[9]</sup> The electric field is also important for driving the free charge carriers (Figure 1.3) to their respective electrodes, after successful separation at the D/A interfaces.

The organic solar cell electric field mentioned above is achieved partly by sandwiching the photoactive polymeric materials between two electrodes with relatively larger and smaller work functions,  $\Phi$ .<sup>[1,9]</sup> The commonly used front and backside electrodes involve ITO and Al, respectively, for which the respective work functions in the ranges  $\Phi_{ITO} \sim 4.6 - 4.7 \text{ eV}$ <sup>[72]</sup> and  $\Phi_{Al} \sim 4.28 \text{ eV}$ <sup>[73]</sup> have been reported. So far ITO and Al represent organic solar cell baseline electrode materials that result in organic PV devices with the best optoelectronic properties. These are generally better than performances of the other organic solar cell devices that are fabricated with other TCOs from the toolbox of commercially available electrode materials.

However, as mentioned earlier, ITO is a less abundant and expensive material that is also widely used in a range of electronic structures and components. The scarceness and the high demand for ITO have made it relatively unavailable for applications in large scale electronics and optoelectronic devices,<sup>[69]</sup> such as large area organic solar cells. This has prompted recent research on alternative transparent conducting materials (with much lower resistivities) for potential applications in organic solar cells, light emitting diodes and other optoelectronic devices. Hence, the goal is to increase their future economic viabilities and reliabilities through research.<sup>[74,75]</sup>

However, particular attention must be taken when designing TEs for applications in organic PV solar cells. This is necessary in order to avoid cancelling of the main

advantages of the organic PV technology with limitations and disadvantages of the new TE systems that are being proposed. In other words, important considerations must be paid to the suitability and sustainability of the TE materials that are being explored as alternatives to standard ITO-coated TCO films. There is, therefore, a great need for research on the electro-optical properties of new TE systems. There is also a need to study the optoelectronic characteristics and performances of organic solar cells with improved TE layers and interfacial/interlayer contacts.

### **1.3.1 Conceptual Question**

Hypothetically, it is agreed generally that, integration of new components in an existing device structure would be efficient and sustainable only if the considered new components exhibit comparative engineering properties with respect to the operation mechanism of the system being modified. Therefore, the driving question to this dissertation was to understand how multilayered transparent thin film composite structures that are being explored for applications as host materials alternatives to indium-based TCO films can practically be made suitable in a way that is comparable to the performance characteristics of ITO anodes that are used currently in organic solar cells and organic light emitting devices.

### **1.3.2 Transparent Conducting Materials Alternatives to ITO**

Note that, besides indium based TCOs, which are optoelectronically effective but scarce and expensive (suitable only for applications in sophisticated small area optoelectronic devices), there are other TCO material candidates.<sup>[68]</sup> These include: the group of non-stoichiometric doped thin films of tin, cadmium and zinc oxides, as well as their various blends.<sup>[68]</sup> In fact, for some optoelectronic technologies, modifications and

tests of the electro-optical properties in some of these material systems have already been realized and implemented for TE applications alternatives to ITO or IO thin films.<sup>[68]</sup>

However, cadmium oxide is a toxic material.<sup>[20]</sup> Its use in TEs or solar cells may give raise to difficult disputes. Furthermore, the recycling or disposal of cadmium containing wastes is considered hazardous to health and the environment.<sup>[20]</sup> Hence, mainly due to limited environmental aspects and/or difficult legislatures that are imposed on the use of toxic substances,<sup>[20,21]</sup> cadmium oxide is very far from meeting the requirements of large area TE structures. Figure 1.6 shows the characteristic Ts and sheet resistances for the useful and widely commercialized transparent conducting materials.<sup>[68]</sup>

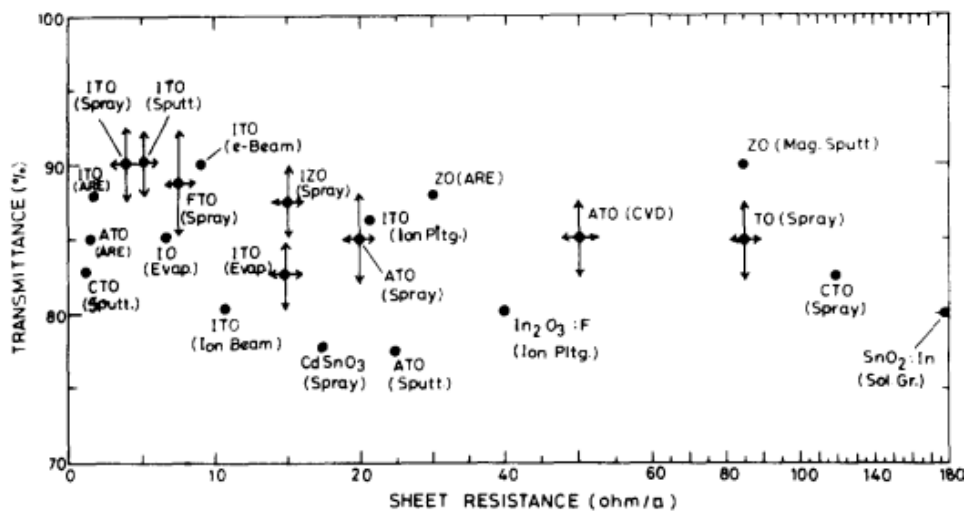


Figure 1.6: Electro-optical properties of the main transparent conducting oxides prepared by various techniques (shown in brackets) and fluctuations of the properties (indicated by arrow bars) as reported by various researchers.<sup>[68]</sup>

The electrical and optical parameters mentioned above are used to define the so called Haacke Figure of Merit (HFoM). The HFoM is used further in the evaluation and selection of TE materials for various optoelectronic applications.<sup>[68,74,75]</sup> Figure 1.6 also shows that, the electro-optical properties of a given transparent conducting material

depend significantly on the preparation techniques that are used. These are also function of the non-ideal preparation conditions of the electrodes. Such conditions may include substrate and annealing temperatures that are used generally for improvements of transparent conductive properties of thin film electrode coatings during their preparation.

### 1.3.3 Motivation of the Study

The superiority of IO and ITO to the other TCOs is also evident in Figure 1.6. This suggests that, for single-layered TCO film coatings, indium containing materials will probably remain the solution for some of the most sophisticated TE applications. However, the motivation of this dissertation is that, effective TEs for applications in large area organic solar cells and other layered electronic structures, such as light emitting devices, can be engineered from indium-free composite thin films that are derived from earth abundant materials. In Figure 1.6, it can be observed also that the optical transmission in optimized thin films of ZnO that are prepared by magnetron sputtering are generally very good comparably exceeding those of ITO-coated optoelectronic substrates.

Furthermore, in terms of organic solar cell operation mechanisms, ZnO compares more favourably than tin oxide. It has an effective work function of  $\sim 4.45 \text{ eV}^{[73]}$ , which is higher than that of Al and very close to that of ITO, which has work function values in the range of  $\sim 4.6 - 4.7^{[72]}$ . This indicates that ZnO should form electric fields that are sufficient for the operation of organic solar cells, comparable to the ITO-coated TCO films. However, the effective electrical sheet resistances of ZnO films are extremely high (see Figure 1.6). This is the most important limitation of ZnO thin films as transparent conducting coating. High sheet resistance hinders ZnO from fulfilling the electrical

requirements that are needed for the effective application as organic solar cell TE thin film coatings.

## 1.4 Imperativeness and the Challenging TCO Context of ZnO

### 1.4.1 Imperativeness of ZnO as Transparent Electrode

ZnO is one of the important semiconducting materials for applications in various electronics, optoelectronic devices and their components.<sup>[76]</sup> It is an inorganic compound, which usually appears as white powder insoluble in water at room temperature. It has a hexagonal Wurtzite structure (Figure 1.7)<sup>[77]</sup> with space group  $p6_3mc$  (186) and lattice constants of  $a \sim 3.25 \text{ \AA}$  and  $c \sim 5.21 \text{ \AA}$ .<sup>[78]</sup> Its  $c/a$  ratio of  $\sim 1.602$  is very close to the ideal value of the hexagonal cell, which has a  $c/a$  value of  $\sim 1.633$ .<sup>[79]</sup> Some of the important physical parameters of ZnO are presented in Table 1.1.<sup>[79]</sup>

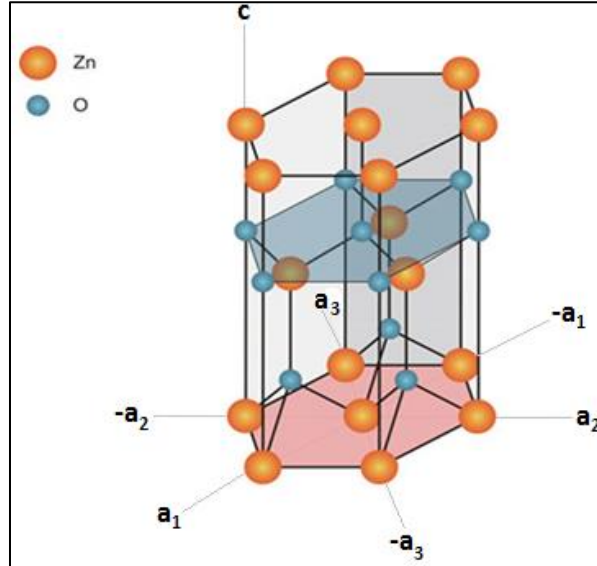


Figure 1.7: Hexagonal Wurtzite structure of ZnO.<sup>[77]</sup>

In its pure form, ZnO usually exhibits n-type conductivity.<sup>[68,80,81]</sup> It also has high melting point of  $\sim 1975 \text{ }^\circ\text{C}$ <sup>[79]</sup> and large intrinsic bandgap energy in the range of  $\sim 3.2 - 3.4 \text{ eV}$ <sup>[74,79-81]</sup> at room temperature. This leaves ZnO with high optical transmission in the

visible region of the solar spectrum.<sup>[79]</sup> Also, mainly due to its large bandgap energy and high melting point, ZnO has a high breakdown voltage. This enables it to sustain large electric fields, high power and high temperature operations.<sup>[79]</sup> Due to these promising functional features above, the thin films of ZnO have been given considerable attention in the literature.<sup>[78,82-85]</sup>

Table 1.1: Properties of single crystal ZnO at room temperature.<sup>[79]</sup>

Property	Value
Lattice parameters at 300 K	
$a$	3.2495Å
$c$	5.2069Å
$c/a$ Crystal structure/Molecular weight	1.602/81.38 amu
Relative density/specific heat	5.606/0.125 cal/gm
Stable phase at room temperature	Wurtzite
Melting point/thermal expansion	1975 °C/ $2.90 \times 10^{-6} \text{ K}^{-1}$
Thermal conductivity	0.6 cal/m/K
Linear expansion coefficient / °C	$a : 6.5 \times 10^{-6}$ $c : 3.0 \times 10^{-6}$
Static dielectric constant	8.656
Refractive index	2.02
Energy gap/Transmission range	3.2 – 3.4 eV, direct/0.4 – 0.6 @ $T > 50\%$ at 2 mm thick
Intrinsic carrier concentration/ maximum doping concentration	$< 10^6 \text{ cm}^{-3}$ / n-type doping $> 10^{20} \text{ cm}^{-3}$ electrons, p-type doping $< 10^{17} \text{ cm}^{-3}$ holes
Exciton binding energy	60 meV
Electron effective mass	0.24
Electron Hall mobility at room temperature	$200 \text{ cm}^2 / Vs$
Hole effective mass	0.59
Hole Hall mobility at room temperature	$5-50 \text{ cm}^2 / Vs$

Furthermore, ZnO is a non-toxic material with flexible hexagonal Wurtzite structure (Figure 1.7). This makes it easy to use ionic substitution and doping to introduce structural phase transformations and conductive free-charge carriers that make it

attractive for the wide range of applications.<sup>[68,76,79,81-87]</sup> Hence, research interest on ZnO thin films goes back many decades.<sup>[76]</sup>

#### **1.4.2 The Challenging TCO Context of ZnO Films**

In recent years, ZnO has been widely explored, as one of the host TCO materials alternatives to ITO for applications in electronics and optoelectronic devices.<sup>[88,89]</sup> The sustained interest in ZnO has been due largely to the high abundance,<sup>[86]</sup> non-toxicity and low cost of ZnO,<sup>[68,74,87]</sup> as well as its stability against hydrogen plasma<sup>[90]</sup> and high temperature processes.<sup>[79,90]</sup> The interest in ZnO is also fueled by its potential for applications as transparent substrates or anodes in large area layered memory devices,<sup>[91]</sup> solar cells, light emitting diodes, flat panel displays<sup>[74]</sup> and in other optoelectronic structures and components.<sup>[68,76]</sup> However, a significant number of practical challenges must be overcome prior to the widespread uses of ZnO. These include the high electrical resistivity of ZnO (Figure 1.6), which prevents its use in TE coatings that require thin films with lower sheet resistances, while retaining good optical transmission properties.

In an effort to overcome the above electrical conductivity challenge, a number of research groups have explored the use of n-type doping with group III elements.<sup>[68,92]</sup> These have been used to enhance the electrical conductivity of ZnO thin films<sup>[68,92]</sup> by intentional doping mainly with Al,<sup>[93]</sup> boron,<sup>[94]</sup> indium<sup>[95]</sup> and gallium.<sup>[96]</sup> Such designs have improved the transparent conductive properties of ZnO thin films to high levels.<sup>[93-97]</sup> For example, a maximum solar T in the range of ~ 85% - 95% and associated electrical resistivities as low as  $\sim 3 \times 10^{-4} \Omega \text{ cm}$ , have been achieved in thin films of ZnO doped with Al.<sup>[98]</sup> Note that these resistivity values compare favourably to those of ITO-coated thin film substrates, for which resistivities of  $\sim 1 \times 10^{-4} \Omega \text{ cm}$  have been

reported.<sup>[89]</sup> However, single layered thin films of doped TCOs have been shown to have limited applications.<sup>[74]</sup> This is partly due to their highly ionized impurity scattering phenomena, which limit their electro-optical properties.<sup>[74]</sup> It is also as a result of their chemical and thermal instabilities in various environments.<sup>[99,100]</sup>

### **1.4.3 The Emerging Layered Thin Film Composite Electrodes**

In an effort to address some of the challenges in the doped thin films of ZnO, multilayered ZnO/metal/ZnO (ZmZ) thin film structures have been proposed for the effective enhancement of the conductivity of ZnO-based thin film electrodes.<sup>[74,90]</sup> The ZmZ thin film structures can be tailored to have low resistivities that are comparable to those of highly conductive intermediate metal layers and high visible region solar transparencies that are needed for applications in solar cells and light emitting diodes.<sup>[101]</sup> They also have the attractive features of low cost and non-toxicity.<sup>[74]</sup> Furthermore, multilayered ZmZ sandwich films have been shown to have good transparent conductive properties and better durability than single layers of doped ZnO and/or metal thin films.<sup>[90,99,101]</sup> Nevertheless, there are relatively few reports of multilayered ZmZ thin film structures.<sup>[101]</sup> Also, there is a great need to develop host TE materials alternatives to ITO-coated TCOs,<sup>[74,101,102]</sup> which are produced from scarce and relatively expensive reserves of indium.<sup>[69]</sup> Therefore, composite TCOs that are based on abundant ZnO and Al thin films are of great interest for potential applications in large area solar cells, light emitting diodes and other opto-electronic devices.

Hence, in recent years, multilayered ZmZ thin film structures<sup>[74]</sup> and the other indium-free transparent conducting sandwiches such as TiO<sub>2</sub>/metal/TiO<sub>2</sub> thin films<sup>[75]</sup> have attracted considerable interest in literature.<sup>[75]</sup> The composite thin film structures are

being explored as host materials for effective low cost TEs<sup>[90]</sup> in electronics and optoelectronic devices. If successful, the composite thin film structures would potentially compete and replace the dominant ITO or ITO/metal/ITO (IMI)<sup>[102-108]</sup> TE systems that contain costly indium, which is not as available as Al and ZnO.<sup>[69]</sup>

#### **1.4.4 Materials Selection**

In terms of materials selection, the family of multilayered ZnZ thin film structures appear to be the most promising composite materials to substitute indium containing transparent conductors. This is due mainly to the high abundance, non-toxicity and low cost of ZnO, as well as the potentially good electro-optical properties (Figure 1.6) and easy fabrication procedure of the multilayers.<sup>[74]</sup> However, the challenges remain to be the realization of the above novel properties of ZnZ multilayers, in a way that can transform those multilayered thin film structures into practical applications in actual organic electronic devices. This is the key question that will be addressed in this dissertation.

### **1.5 Research Problem**

Although the initial idea of composite TEs that are based on multilayered TCO/metal/TCO thin film structures has already been investigated,<sup>[74,90,99,101,109-111]</sup> the concept has not been widely explored. Also, light transport phenomena, the performance characteristics and application of layered thin film structures that are based on TCO/metal/TCO film electrodes in electronic devices are not completely understood. Furthermore, literature reports on multilayered TCO/metal/TCO thin film structures and

their applications, particularly in organic electronic devices such as organic solar cells are still very few, if any.

In addition, mainly due to the generally low PCEs and instabilities of OPVs and organic electronic devices in general, most of the research efforts (in organic PVs) have focused on organic materials for the active layers (Figure 1.4). This has eclipsed the other important interlayers in organic solar cell components, such as the transparent conductors. Nevertheless, such research efforts have greatly improved the organic PV technology (Figure 1.4), making it a more competitive and potentially dependable source of clean renewable energy. This, however, demands for continual enhancements of the organic solar cell materials, components and technological processes that seem to limit the production, large scaling and use of organic electronic devices in future.

## **1.6 Objectives of the Study**

It is against the above background that this research has been carried out. The general objective is, therefore, to produce host organic solar cell transparent thin film composite electrodes (TCEs) alternatives to the ITO based TCOs. In this respect, this work investigates the motivating salient TCE features that are dictated by the recent technological development and operation principles of organic solar cell structures. The features include: structural, electrical and optical properties of multilayered ZmZ thin film sandwiches. This study is particularly important due to the limited abundance and unavailability of indium (used in ITO-coated thin films) for wide range of applications in electronics or optoelectronic structures. In order to execute the study, the general research concept above has been split into the following specific objectives:

- i. *To predict the optimum ZnO/Al/ZnO (ZAZ) interlayer thicknesses from numerical simulations.*
- ii. *To fabricate and test the transparent conductive properties of multilayered ZAZ TCE structures with numerically predicted ZnO and Al interlayer thicknesses.*
- iii. *To itemize on the prospects of including contacts in organic semiconductor BHJ solar cell modeling with special accent on interfaces between photoactive and TE layers.*

## **1.7 General Methodology and Significance of the Work**

So far, little work have been done to investigate and provide understanding on the electro-optical properties and performances of multilayered ZnZ thin film composite structures with reasonable ranges of mid-Al interlayer thicknesses.<sup>[80]</sup> Therefore, this research is carried out to investigate the effects of intermediate layer Al thicknesses on the transparent conductive characteristics of multilayered ZAZ sandwich nano-films. Such multilayered films with nano structures have the potential for applications as improved anodes or TEs in large area organic solar cells and other layered opto-electronic devices and components. Note also that, the proposed multilayered ZAZ thin film TE concept leaves this work with many practical implications, as well as long term technological advantages. These include:

- i. *The TCE materials (ZnO and Al) are both cost-effective and do not cause any harm to health and environment.*
- ii. *Both the TCE and the OSCs are easy to fabricate. They also have low energy payback times since their fabrication do not require expensive purification steps and substantial energy intensive processing methods are always not needed.*

- iii. *Organic PV devices are produced from cheap (mechanically robust) polymeric materials which are easy to recycle. Also, OPV solar cell production by the low-temperature fabrication techniques such as the high-throughput roll-to-roll printing, produces no hazardous wastes and no greenhouse gas emissions such CO<sub>2</sub> are formed. Organic electronics is also a highly versatile and cost-effective solar cell technology. This is due mainly to its non-toxicity and the low consumption (usually few grams per m<sup>2</sup>) of absorber materials, which are also readily available from the highly abundant semiconducting polymers from a large toolbox of synthetic organic chemistry.*
- iv. *OPV solar cell technology allows the production of novel products. These include portable devices and flexible organic solar cells that can be merged with architectural structures, bags and/or cloths. This is possible due mainly to the good mechanical flexibility, low weight and tunability of transparency and aesthetic colour of organic electronic materials.*

## **1.8 Dissertation Plan**

The scope of this study is to develop an understanding that would provide a synergy between cost-effective transparent multilayered ZAZ thin film electrodes and the modern operation of organic PV solar cell structures, which are potentially good semiconductor devices alternatives to the costly c-Si solar cell technology. The idea is that the simplicity and mechanical robustness of organic semiconductor materials will guarantee for the complementarity to achieve the goals of efficient, cost-effective and environmentally indisputable solar cell systems. While the numerical, theoretical and experimental study presented in this report guarantee for the objective of integrating the

cost-effective TCEs with large area organic solar cells, as well as with the other organic or inorganic electronics and optoelectronic structures and components.

The approach of the dissertation and organization of chapters in this report are in line with the progress of the investigations and findings of the research. First, a brief discussion on the generalities, background and problematic of the work is given in this chapter 1. In chapter 2, a brief historical review of the recent development and operation mechanisms of solar cells are presented. This is followed by an up to date literature surveys on TCE concepts, as well as the recent advancement of prototype transparent conducting materials and their properties. This literature survey part is particularly important to clearly highlight and understand the new results and practical uniqueness of the current study. The literature survey is also an important background to the current study.

Chapter 3 presents the numerical prediction of the multilayered ZAZ thin film thicknesses. In this chapter, the basic principles and the associated phenomenological theories of light transport in multilayered thin film structures are presented. The important parameters that are needed for the experimental design and fabrication of the multilayered transparent thin film structures are simulated. The numerical results obtained are carefully evaluated in accordance with the standard requirements for the operation of organic solar cells. The numerically predicted parameters include the optimum mid-layer Al and the embedding ZnO-layer thicknesses. The main characteristics, as well as possible influences of interlayer thicknesses on the electro-optical properties of the model multilayered ZAZ thin film composite structures are also discussed.

Chapter 4 presents the results of a combined theoretical and experimental investigation of the electro-optical properties of multilayered ZAZ composite thin film structures. The experimental and test-setup is selected based on the optimum T results suggested by the optical simulations of the model multilayered ZAZ thin film structures (chapter 3). Therefore, chapter 4 focuses mainly on the classical radio frequency (RF) MS synthesis and characterization of the multilayered ZAZ thin film composite structures. The optimum interlayer thicknesses suggested by the numerical simulations are singled out and studied in experiments on model layered structures. The characterization studies include comprehensive structural, optical and electrical evaluation of synthesized multilayered ZAZ composite thin film structures.

Subsequently, the experimental results obtained are used to test and confirm the validity of the numerical predictions and the practicability of material databases that were used in the simulations. The analyses involve comparisons obtained by fitting some of selected numerical results to the experimental data that were obtained from the multilayered ZAZ composite thin film structures produced with similar interlayer thicknesses. The correlations between the numerical and measured results are carefully analyzed for the validation of the numerical method used and the ZnO and mid-Al interlayer thicknesses that were predicted by numerical procedure in chapter 3.

In chapter 5, the other important factors that affect the performance of organic solar cells are investigated. The chapter is devoted mainly to the numerical investigation of factors that can optimize and/or deter the charge transport and collection in BHJ organic solar cell structures. In other words, this chapter 5 focuses on the understanding of the prospects of interfacial/interlayer contacts that are relevant to charge carrier

transport across photoactive organic layers and TE interfaces in organic semiconductor solar cells. In the first part of the chapter, a finite difference method (FDM) is employed in writing a computer source code that is capable of simulating the relevant characteristics of semiconductor devices with particular accent on organic solar cells.

The code was purposely implemented in Matlab software package. This is due mainly to the well-known strong graphics and the numerical capability of Matlab software program. This enabled numerous random and reasonably easy modifications of source codes to allow for the suitable testing of the different research objectives. The second part of chapter 5 involves the modification of the Matlab code to explore the effects of contact on charge-carrier transport across the organic PALs of organic solar cells and across the TE interface during charge collection. The photo-current-density versus voltage (J-V) characteristics of a BHJ organic solar cell structures with different contact heights and contact lengths are simulated. The obtained results are then used to assess the prospects of charge transport and collection across the interfaces between the photoactive organic layer and TE layer of a BHJ OPV solar cells.

Lastly, in chapter 6, the practicality and limitations of the proposed transparent multilayered ZAZ composite electrodes on the performance of organic solar cells with BHJ structures are discussed. The potential applications of the multilayered ZAZ thin film composite electrodes are also presented in this chapter 6. Finally, the implications of the study are briefly presented before discussing the suggestions for future work and the concluding remarks of the study.

# 2. Chapter Two

## Literature Review

### 2.1 Introduction

For any technological advancement, understanding the device operation mechanism plays a key role in the design and materials development. In PVs, for example, there are so many past examples where the mature inorganic (c-Si, CIGS and CdTe) solar cell technologies blossomed into their present states of development, only when faced with various challenges from their newer generations.<sup>[112]</sup> This appears to be happening in organic PV technology as well. This is motivated further by the fact that knowledge from past studies that may comprise ideas on device designs and technological advancement, allows for further improvements in terms of materials, device structure and characteristic performances. In the case of organic solar cells, for example, this can be used to learn how to improve the PV cell PCE, stability and reduced cost.

This chapter, therefore, attempts to review prior literature on organic electronic structures. The survey focuses on recent knowledge that is relevant to the design and fabrication of organic solar cells. It also reviews some of the concepts developed recently for the synthesis and characterization of TCEs, that make them feasible TCOs appropriate for applications in organic solar cells and other optoelectronic structures and components. The literature on the improvement of organic solar cells is also presented in terms of device configuration and performance characteristics. Finally, the knowledge drawn from literature is analysed for proper design, production, testing and implementation of the main research hypothesis, namely, fabrication of cost-effective TCEs for potential

applications in OSCs and other organic electronics and optoelectronic devices and components.

### **2.1.1 Introduction to PV Technologies**

Historically, the PV effect was discovered in 1839 by Alexandre E. Becquerel at the electrolytic cells laboratories.<sup>[113]</sup> Following this discovery, the interest in solar energy and photoactive semiconducting materials (inorganic and organic) has increased continuously. This has been driven greatly by the increasing global need for clean energy from renewable sources, which is intended to reduce our strong reliance on the diminishing non-renewable fossil fuels, which are also unable to meet increasing energy demands. Furthermore, the excessive use of fossil fuels is believed to play a key role in the climate change.<sup>[14]</sup> The other factors responsible for the increased interest in PV technologies include: the rising human population as well as consumer-producer concerns about modern life and improved living standards. There is also a high desire to save money, by deriving most of our energy consumption from completely clean, cost effective and readily available natural resources (e.g. the Sun). These factors have greatly catalysed the increasing scientific discoveries in PVs and other renewable energy technologies.<sup>[14]</sup>

Following the discovery of the PV effect, the p-n junction was discovered by Shockley *et al.*<sup>[10]</sup> (Nobel prize winners for the transistor in 1956). This further motivated the application of PV effects to the production of electricity, which became increasingly popular around 1950s. The p-n junction was closely followed by the discovery of an inorganic solar cell by Pearson *et al.* in 1953 at the Bell laboratories,<sup>[10]</sup> upon which the first c-Si solar cell was invented. While in the early 1950s, most of the relevant

applications of PV devices were mainly for space propulsions, the terrestrial solar cell modules (with reasonable PCEs as high as ~ 14%) became serious commercial PV contenders in the 1960s.<sup>[56]</sup>

Subsequently, the majority of PV solar cell systems (with significant enhancements in PCEs and stabilities) that are based mainly on inorganic p-n junction have been produced. So far, major improvements in solar cell PCEs and stabilities have routinely been reported.<sup>[9]</sup> The majority of these PV devices are, however, still based on c-Si materials. Some of the improvements that have been achieved in recent years include:

- i. *Demonstration of the first large-area PV solar cells with PCEs between 18 - 19%. The PCEs figures that were hardly achieved only in small-area laboratory PV solar cell systems.*<sup>[112]</sup>
- ii. *An increased recourse in PV solar cell improvements and developments that led to the demonstration of ~ 15 – 20% PCEs in the non-concentrating large area PV solar cell modules.*<sup>[112]</sup>
- iii. *Demonstration of more than 20% PCE PV solar cells. The value that exceeded PCEs that were regarded as practical limits for the non-concentrating crystalline PV solar cell systems.*<sup>[112]</sup>
- iv. *Demonstration of PV solar cell modules with PCEs between 22 – 27.5% for the concentrator PV solar cell systems.*<sup>[112]</sup>

## 2.2 PV Solar Cell Operation Principle

### 2.2.1 Inorganic PV Solar Cell Systems

The PV effect, which is based on the inner photoelectric effect,<sup>[113]</sup> occurs when photons of energy greater than the bandgap energy of a photoactive semiconducting material are absorbed. The absorbed photon energy excites electrons in the valence band. This enables electrons to jump from the valence band into the conduction band, whereupon they become capable of moving freely. With the help of the built-in electric field ( $E_{bi}$ ), near the p-n junction, the freed electrons (in the conduction band) can be swept towards the cathode of the solar cell for collection. Note that, in the case where the energy of the incident photons is smaller than the bandgap energy of the semiconductor, the PV effect will not occur. The electrons in the valence band will not have sufficient energy to enable them jump into the conduction band. In this case, the energy of the photons may be used to increase the kinetic energy of the electrons, thus increasing the temperature of the solar cell system.<sup>[112]</sup>

Figure 2.1 shows a schematic of the basic operation principle of traditional c-Si solar cell system. It generally involves a p-n junction with a heavily doped n-region that is narrower than the p-region. When p-type and n-type semiconductors are placed in contact, electrons (from n-region) and holes (from the p-side) diffuse across the interface of the p-n junction. This phenomenon results in an electric field being created across the junction at equilibrium. The illumination, which enters the solar cell system, helps to generate free charge carriers.

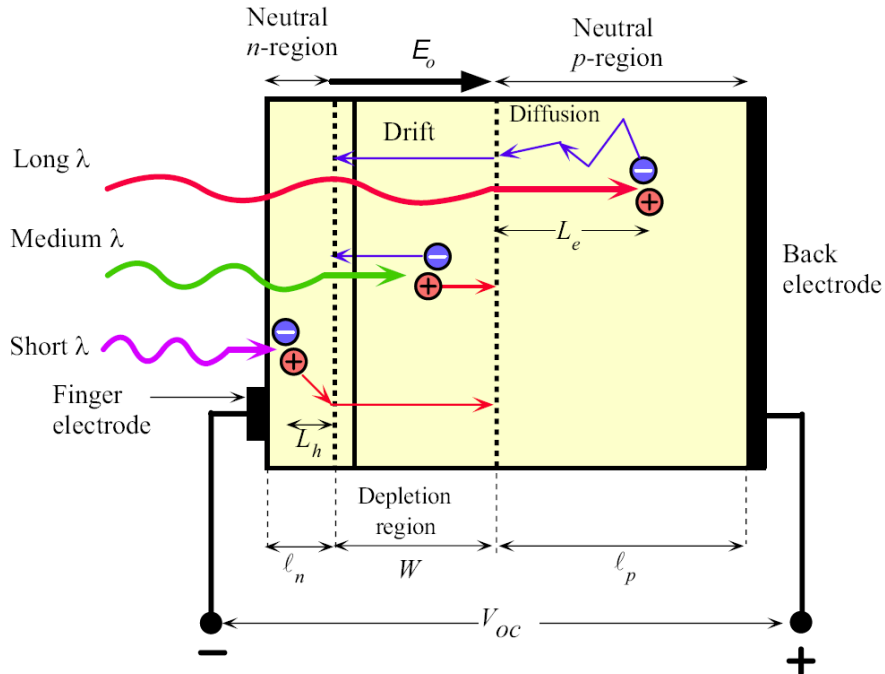


Figure 2.1: Diagrammatic of a typical p-n solar cell operation principle.<sup>[10]</sup>

The  $E_{bi}$ , which is created across the p-n junction boundary (inside a space charge layer (SCL) also known as the depletion layer of width,  $W$  in Figure 2.1 above) is purposely made to extend more into the p-region of the p-n junction.<sup>[10]</sup> Note that, since illumination is generally made through the n-side of the p-n junction, the electrodes that are attached to the n-region must allow sufficient photons to enter photoactive parts of the solar cell. Also, the electrodes must maintain practically high electrical conductivities to ensure a rather low series resistance with other components of the solar cell system. High conductivities are also important to enable the electrodes to be effective in the collection of photo-generated free-charge carriers, before transmitting them to the external circuit for photoelectric power generation.

Furthermore, in inorganic c-Si solar cells, the n-side is typically controlled to be narrower than the p-side of the p-n junction. This is done in order that most of the photons could be absorbed in the depletion layer, as well as within the neutral p-type

region. This results in the creation of electron-hole pairs (EHPs) in those regions of the solar cell system, thereby enhancing the overall electronic performance.<sup>[10]</sup> Generally, the EHPs that are created inside the SCL can be easily drifted apart into free-charge carriers (electrons and holes) by the built-in electric field,  $E_{bi}$ . The separated free-charge carriers are then swept by  $E_{bi}$  to the neutral n-side or p-side of the solar cell system (Figure 2.1).

At the respective electrodes, the free-charge carriers are collected, thus making the electrodes negative (electrons) or positive (holes). This results in an open circuit voltage,  $V_{OC}$ , being created between the positive (anode) and negative (cathode) terminals of the solar cell system (Figure 2.1). However, the EHPs generated deep within the p-type or n-type regions are forced to diffuse around in these layers. Since there is no sufficient electric field to separate them, they are ultimately wasted by recombination. For a given recombination lifetime ( $t_{e,h}$ ) of an electron ( $e$ ) or a hole ( $h$ ), the charge carriers are able to diffuse a mean distance,  $L_{e,h}$ , before they are annihilated by recombination. This length is given by:<sup>[10]</sup>

$$L_{e,h} = \sqrt{2D_{e,h}t_{e,h}} \quad (2.1)$$

where  $D_{e,h}$  is the electron ( $e$ ) or hole ( $h$ ) diffusion coefficient inside the p-type or n-type regions, respectively. The EHPs that are photo-generated within lengths,  $L_{e,h}$  of the depletion region can readily diffuse to reach the built-in field region where they can be separated by the built-in electric field.

Therefore, in the vicinity of the built-in electric field, at the SCL, the electrons and holes of the EHP become separated and these charge carriers migrate to their respective electrodes (holes to anode and electrons to cathode) of the solar cell system. Thus the key role of the built-in electric field is manifest. Without it, no EHPs will be

separated and moved to the electrodes for collection and no accumulation of excess free charge carriers at the electrodes of the solar cell. Ultimately, there will be no possibilities for the PV effect to occur.

In order to minimize losses by the recombination phenomena mentioned above, inorganic c-Si solar cell structures are tailored in a way that enhances the transport of the slowest charge carriers (the holes in this case). This is achieved by making the p-region relatively thicker than the n-region (Figure 2.1). This extends more of the  $E_{bi}$  into the p-region of the device, thus making electrons the minority carriers in that region. Note that, due to differences between mobilities of electrons and holes in c-Si, at particular solar cell conditions, the mean-free path of an electron is generally longer than that of a hole for c-Si materials. In other words, the extension of the  $E_{bi}$  into the p-type region of the solar cell system enhances the creation and collection of free-charge carriers. Ultimately, only the EHPs that are photo-generated within the volume covering:  $L_{e,h} + SCL$  contribute to the PV effect of a given solar cell system.

As mentioned in the previous chapter, the solar cell systems that are based on c-Si materials and technology currently dominate the PV industry. Also, over the years c-Si solar cell systems have improved significantly in terms of reliability, maturity, design, stability and performances, exhibiting PCEs of up to ~ 40% for the tandem concentrator solar cell systems (Figure 1.1).<sup>[7]</sup> Furthermore, the advances in the inorganic thin film solar cell technologies, such as amorphous silicon (a-Si), CdTe and CIGS have led to devices with high PCEs. The overall performances of a-Si, CdTe and CIGS solar cell systems greatly exceed those that can be obtained for organic based PV solar cell systems.

However, the difficulties in processing and the cost burdens associated with the production of inorganic c-Si solar cell systems hinder substantial uses of its solar cell technology and materials. In addition, less material abundance along with the environmental problems that occur during processing and/or use of CdTe and CIGS solar cell systems, as results of the toxicity of their cadmium content<sup>[20,20]</sup> prohibit the widespread uses of these thin film solar cell technologies. These disadvantages, therefore, stimulated recent interest in organic solar cells.

Organic solar cells have the potential of meeting the world's energy needs without the disadvantages listed above for the inorganic PV systems. The large global need for liberalization and deregulation of energy/electricity industry sector is also obvious. It is estimated that currently about 2 billion people in the world have no access to electric power.<sup>[114-117]</sup> The large percentage of this population lives in developing regions that are also too remote to ever receive centralized grid supplies from the state agents.<sup>[117]</sup> Hence, the convenient approach proposed for this population involves complementing any traditional centralized state power plants by small and medium scale distributed electricity generations.<sup>[118]</sup> This approach has recently increased the use of small hydropower,<sup>[119,120]</sup> wind energy,<sup>[121]</sup> biomass<sup>[122]</sup> and solar energy<sup>[14,123]</sup> for provision of electric energy to the off-grid rural and/or urban poor population.

However, the energy solution milestones above require more appropriate energy delivery policies and a more rigorous approach that can prove to be more cost effective than extending state grid utilities to remote rural areas. There is, therefore, a great demand for low cost solar-powered domestic micro-system energy frameworks that can allow the use of relatively cheap locally managed distribution of electricity to serve such

rural and urban poor population.<sup>[117,123]</sup> For this purpose, of the present PV technologies, the OPV appears to be a very promising choice. Furthermore, in terms of materials abundance, only silicon and organic semiconductor materials meet the criteria for the long term and large-scale PV production. Hence, for large scale and cost-effective solar cell production only organic PV technology appears the most appropriate choice.

## 2.2.2 Organic PV Solar Cell Systems

Organic PV technology is a new type of thin film solar cells in the PV industry.<sup>[7]</sup> It involves the use of photoactive organic layers, comprising of chains and bucky-balls of p-type and n-type semiconducting polymers<sup>[124]</sup> or oligomer<sup>[23]</sup> materials. In such polymeric semiconducting materials, the energy levels (Figure 2.2) of the highest occupied molecular orbitals (HOMOs) and lowest unoccupied molecular orbitals (LUMOs) are analogous, respectively to the valence and conduction bands of inorganic semiconductors.

Organic semiconducting materials are thus characterized, selected and/or tailored (through different chemical syntheses) based on the energy gaps between their LUMO and HOMO levels.<sup>[125]</sup> This helps to modify the organic semiconductors in a way controlling their materials electronic mobilities and light absorption characteristics that are relevant to organic PV solar cells and other organic electronic devices. The representative examples of the commonly used photoactive organic semiconducting donor materials (p-type polymers) include: poly-p-phenylenevinylene (PPV), poly(2-methoxy-5-(2-ethylhexyloxy)-1-4-phenylene vinylene) (MEH-PPV), poly[2-methoxy-5-(3',7'-dimethyloctyloxy)]-p-1-4-phenylenevinylene - MDMO-PPV<sup>[126]</sup>, poly(p-phenylene benzobisthiazole) (PBZT) and poly(3-hexylthiophene) (P3HT).<sup>[124]</sup>

In addition, layers of poly(3,4-ethylenedioxythiophene) doped with poly(styrenesulfonate) also known as PEDOT: PSS are usually coated on top of the ITO before deposition of the photoactive organic layers. This PEDOT: PSS layer helps to block electrons (electron-blocking layer, EBL) or to transport holes (hole transporting layer, HTL) to the transparent anode of the organic solar cells, thus enhancing the charge collection of the solar cell system (Figure 2.3).<sup>[127]</sup>

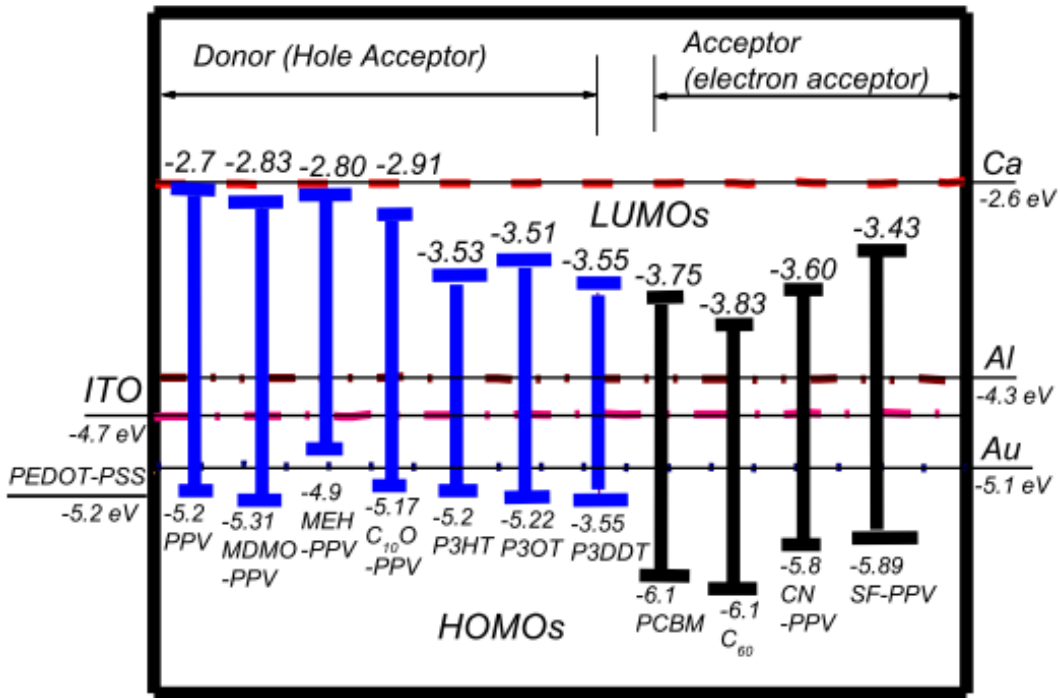


Figure 2.2: HOMO and LUMO energy levels (values in eV) of the common OPV solar cell materials (Source: Goswami, *et al.* Adv. Sol. Ener., Vol. 17, Earthscan London).

The other types of polymer materials that are needed in the fabrication of organic solar cell systems are the so called electron acceptors (n-type) organic semiconductors. The commonly used examples of organic acceptors can be cited from Ref.<sup>[128]</sup> These include: poly(2, 5, 2', 5'-tetraalkoxy-7, 8'-dicyanodi-p-phenylenevinylene) (CN-PPV),

poly(benzamidazobenzophenanthroline) (BBL), [6,6]-phenyl-C<sub>61</sub>-butyric acid methyl ester (PCBM) and poly[2-alkoxy-5-alkanesulfonyl-1-4-phenylene vinylene] (SF-PPV). More examples of semiconducting polymeric donors, acceptors and other baseline materials that are needed generally for the fabrication of organic solar cell systems are summarized in Figure 2.2.

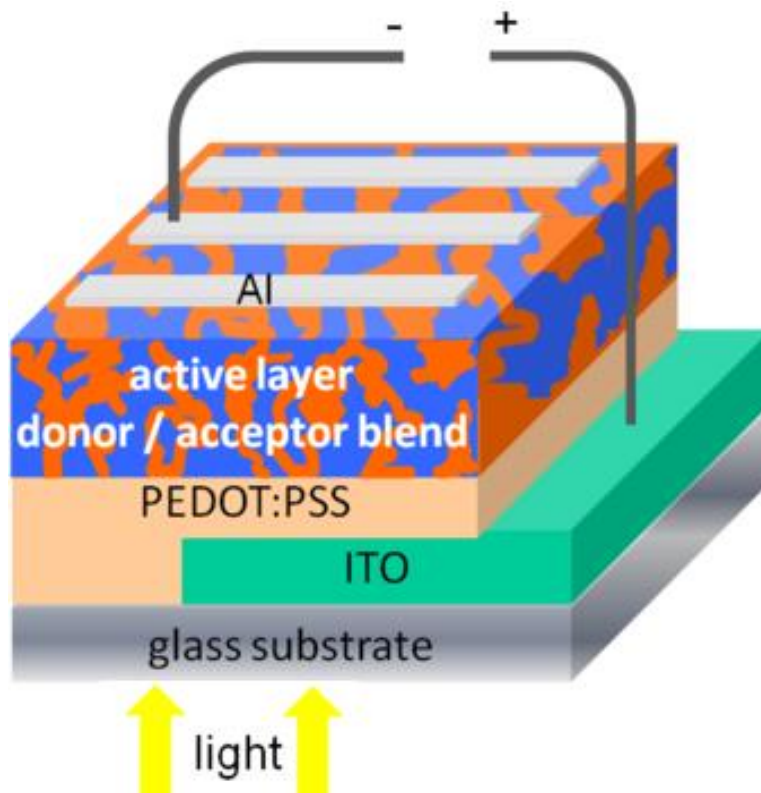


Figure 2.3: Schematic diagram of a typical organic BHJ solar cell structure.<sup>[127]</sup>

### 2.2.2.1 Advances in OPV Technology and OSC Designs

Historically, the first organic solar cell, which was based on anthracene, was reported by Pochettino in 1906.<sup>[9]</sup> Subsequently, after Pochettino's discovery, a number of research efforts have been made to develop high performance semiconducting polymers and enhancement of performances of organic electronic devices. Such devices include: organic solar cells,<sup>[9]</sup> OLEDs<sup>[129]</sup> and layered memory devices.<sup>[91]</sup> Recently, the

OPV technology has evolved from its primitive stage into a relatively reliable source of clean energy. This has led to organic solar cell modules and systems such as chargers of mobile items and flexible organic solar cells that are integrated with portable devices like bags already being produced and commercialized.<sup>[130]</sup> The commonly investigated types of organic solar cell structures include those involving:

- i. Dye-sensitized solar cell systems (DSSCs).<sup>[131]</sup>
- ii. Metal/polymer junction solar cell systems, which however showed very low PCEs that are less than 0.1 %.<sup>[132]</sup>
- iii. Planar organic semiconductor solar cell systems.<sup>[133-135]</sup> These consist of D/A bilayer solar cells and show a relatively low device performance with characteristic PCEs as low as ~ 1%.<sup>[136]</sup>
- iv. BHJ organic solar cell systems; these are characterized by high degree of interaction between their donor and acceptor constituents due mainly to the high interfacial surface area between the two donor and acceptor materials.<sup>[137-140]</sup> BHJ organic solar cells (Figure 2.3) are produced from a solid-state mixed layer of conjugated electron donor polymer such as P3HT and bucky-ball electron acceptor organic molecules such as PCBM. These solar cell structures are fabricated generally by the co-deposition of the two molecules (donor and acceptor) within a thoroughly mixed blend.<sup>[127,139,141]</sup>

Note that, of the organic solar cell structures above, OPV systems with BHJ structures have been shown to result in the most promising solar cell properties in terms of the device PCEs.<sup>[40,41]</sup> This performance is attributed to the proper rationing of the polymeric donor and acceptor molecules within the photoactive blends. The donor and

acceptor materials are chosen and mixed in a way that optimizes the configuration and the local contact area of their final mixture. This blending enhances ultimately the light absorption, exciton/polaron pair dissociation and charge transport, thus improving the PV effect of BHJ organic solar cell structures.<sup>[142]</sup>

In the BHJ organic solar cell structures, the donor and acceptor molecules are very close to each other, typically less than 10 nm apart. Such lengths are within the order of exciton pairs mean free path lengths (the minimum diffusion distance before the exciton is annihilated by recombination). Appropriate rationing of the donor and acceptor blend enables most of the excitons to reach the donor/acceptor interfaces,<sup>[126]</sup> whereupon they dissociate to form loosely bound polaron pairs. Furthermore, BHJ organic solar cell structures have continuous percolated transport pathways through which holes and electrons migrate to their respective anode and cathode electrodes for collection,<sup>[14,143,144]</sup> before their extraction to the external OSC circuitry.

Organic solar cell systems that are based on BHJ structures have been widely studied<sup>[1,9]</sup> and these efforts have enhanced the organic solar cell PCEs to high values of ~ 10% (Figures 1.1 and 1.4),<sup>[56,59,145,146]</sup> the values that were not thought of before. This advancement has fueled further interest in organic PV systems and has also pushed several established companies to turn their focuses on organic solar cell systems and other organic electronic devices and components such as OLEDs. For excellent contemporary reviews on the advances of organic PV systems, please refer to reference numbers one<sup>[1]</sup> and nine.<sup>[9]</sup>

### 2.2.2.2 Organic PV Solar Cell Operational Mechanisms

As mentioned earlier, organic solar cells with BHJ structures have been shown to exhibit good PCEs. This is due partly to high interfacial contact area between the blended donor and acceptor molecules, which enhance the ionization of the strongly bound excitons. It is also due to the increase in charge transporting percolation networks through which the ionized free charge carriers travel, by hopping, to the electrodes. Additionally, studies have shown that, blending of an absorber P3HT<sup>[66]</sup> or MDMO-PPV<sup>[126]</sup> (the donor polymers) with an electron transporting material, PCBM (an acceptor bucky-ball molecule) results in the best organic solar cell structures so far with better PCEs.<sup>[1]</sup> This has been attributed to numerous factors that the blends of P3HT or MDMO-PPV and PCBM have in improving performances of BHJ organic solar cell structures. These potentials include:<sup>[52,137,147-149]</sup>

- i.* Fast free-charge carriers transport of high molecular weight P3HT or MDMO-PPV. This is due to their morphological crystalline chain packing abilities, which enhance the mobilities of holes.<sup>[53]</sup>
- ii.* The side groups in P3HT and MDMO-PPV result in good co-solubility with electron acceptors such as PCBM when they are mixed together inside a well rationed blend. This has been shown to enhance not only the interpenetrability of the D/A blends, but also increasing the interfacial area of BHJ organic solar cell systems, thus increasing the exciton diffusion length and enhancing exciton dissociation.<sup>[150]</sup>
- iii.* Proper rationing of the donor polymer (P3HT or MDMO-PPV) and acceptor PCBM in the mixture results in good overlap between the absorption property of the blend and the solar emission spectrum. For well-prepared blends, the absorption properties have been shown to compare favourably with the absorption characteristics of c-Si

and those of the other inorganic thin film solar cell materials, such as CdTe and CIGS (Figure 2. 4). This makes P3HT or MDMO-PPV the best donor materials so far when blended with PCBM.<sup>[128,142]</sup>

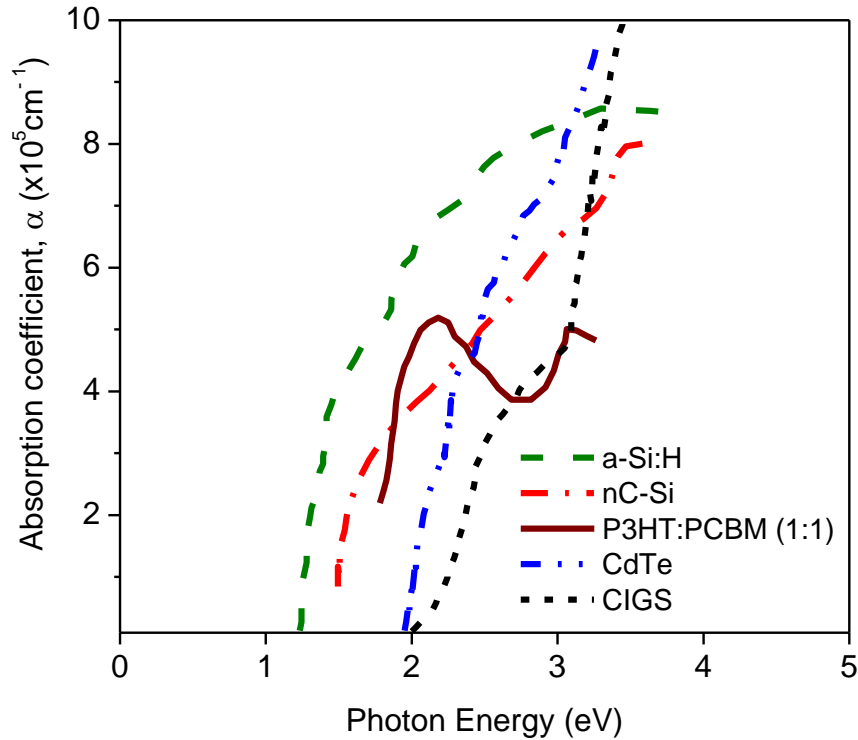


Figure 2.4: Absorption coefficients for the commonly used photoactive absorber solar cell materials.<sup>[142]</sup>

Hence, organic solar cell devices with BHJ structures that are based on substrate/TCO/PEDOT: PSS/(P3HT or MDMO-PPV)/PCBM/Al materials have generally been adopted as baseline organic solar cell structures.<sup>[1,14,126,128,151,152]</sup> These are prepared on top of rigid or flexible substrates. However, poly(styrene sulfonate), PSS, is acidic and hence a strongly hydrophilic material.<sup>[153]</sup> This results to serious organic solar cell problems. The hydrophilicity of PSS is known to accelerate the solar cell degradation

mechanisms. It does so by corroding the TCO layer (usually ITO). This increases the degradation rates of the OPV systems and introduces contaminations into the organic solar cell.<sup>[66,153]</sup> Subsequently, this has hindered the widespread uses of PEDOT: PSS as HTL material.

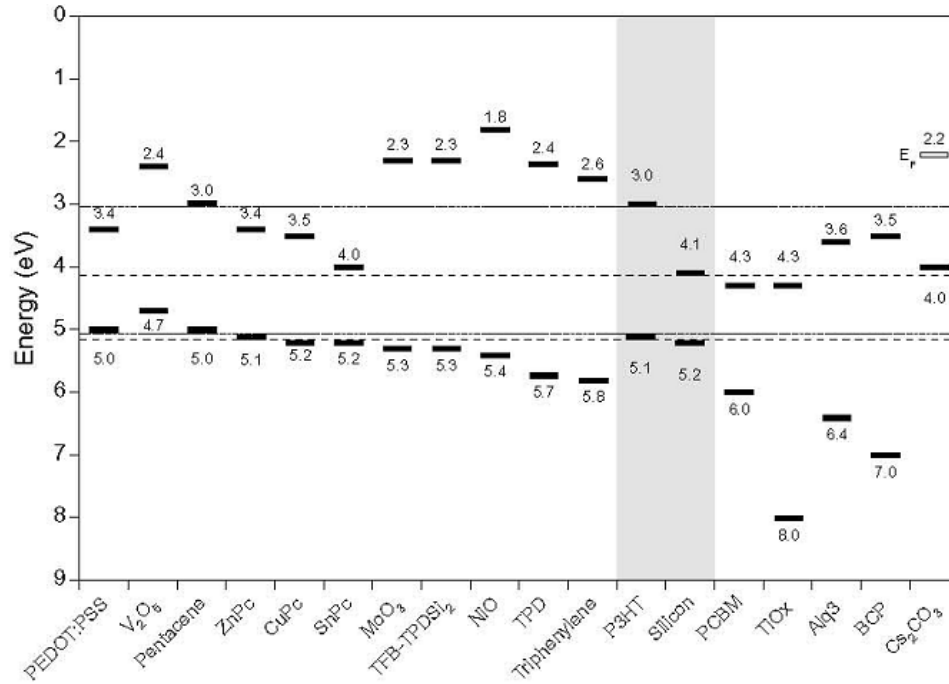


Figure 2.5: Bandgap energies (LUMO-HOMO levels) for several HT/EB layer materials to the left of the absorbers P3HT, Silicon (shown in gray stripe for comparison) and ET/HB layer materials to the right.<sup>[142]</sup>

In an effort to overcome the obstacles above while maintaining practical requirements of the HTL materials, some researchers<sup>[66]</sup> have demonstrated the use of transition metal oxides for effective HT/EB layer materials as alternatives to PEDOT: PSS. These include molybdenum oxide (MoO<sub>3</sub>) and vanadium oxide (V<sub>2</sub>O<sub>5</sub>).<sup>[66]</sup> Such oxides have been shown to prevent most of unwanted chemical reactions and/or corrosion processes between the TCO and photoactive layers of organic solar cells.<sup>[66]</sup> Furthermore, as explained in Ref. 142, the energy levels and work functions of the oxides (V<sub>2</sub>O<sub>5</sub> and

MoO<sub>3</sub>) compare favorably (see Figure 2.5) to those of the baseline materials, shown in Figure 2.2, that are used currently in the operation of BHJ organic solar cell structures.

Furthermore, the use of ITO/MoO<sub>3</sub> coated substrates has been shown<sup>[66]</sup> to result in BHJ organic solar cell devices with good performances that are relatively better than those OPV solar cell systems that are fabricated with traditional PEDOT: PSS buffer layers. Accordingly, in this study, transparent composite thin films are produced and tested for potential application as TEs alternatives to ITO-coated substrates in organic solar cells with BHJ structures. An organic solar cell with a baseline structure of TCO/MDMO-PPV/PCBM/Al materials on top of a rigid glass substrate (with appropriate modification of the TCO layer) will be singled out and studied.

#### **2.2.2.2.1 Organic BHJ Solar Cell Operation Principles**

A general contemporary description of the operating principles of BHJ organic solar cell devices was given by Moliton *et al.*<sup>[58]</sup> This involves sandwiching of a blended photoactive solid-state layer of organic semiconducting materials (donor and acceptor) between a transparent anode (a large work-function electrode material, LWFE) and a cathode (a small work-function electrode material, SWFE). Figure 2.7 presents the summary of the mechanistic steps for the operation of organic solar cell systems with BHJ structures.

This involves the following stages:<sup>[58]</sup> first, the illumination, which is made to enter the solar cell through the transparent anode, is absorbed by the electron donor polymer, such as MDMO-PPV within the photoactive solid-state layer. The absorbed photon energy is then used to excite the MDMO-PPV molecules. The excitation processes remove electrons from the HOMO of the polymer to the LUMO. This creates

the EHPs called exciton-pairs (the *Ex* step in Figure 2.7) with electrons and holes bound together by strong electrostatic bonds.

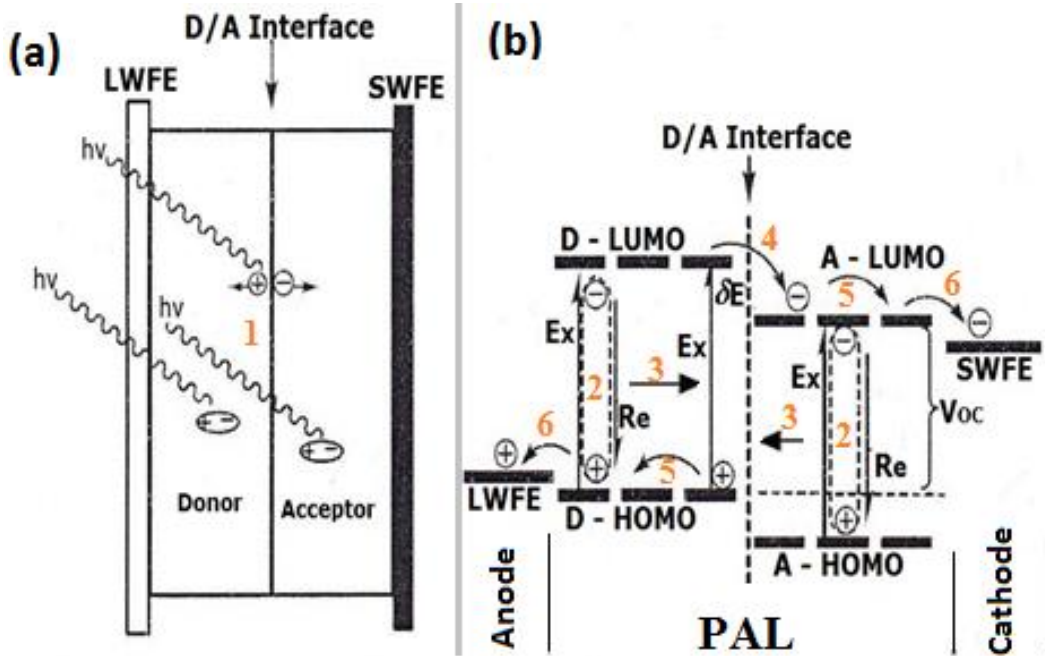


Figure 2.6 Mechanistic operational steps for the photo-generation, transportation and collection of free charge carriers in BHJ organic solar cell structures.<sup>[58]</sup>

In order to guarantee OPV effect, as long as excitons annihilation via recombination processes (the *Re* step in Figure 2.7) do not occur, the exciton-pairs must diffuse inside the solid-state photoactive layers to reach the D/A (MDMO-PPV/PCBM) interfaces. At the MDMO-PPV/PCBM interfaces, exciton-pairs are dissociated (step 4 of Figure 2.7) to form weakly bound pairs of charge transfer complexes known as polaron-pairs.<sup>[154]</sup>

#### 2.2.2.2.2 Difference between OPV and Inorganic Solar Cells

Unlike inorganic semiconductors (c-Si, a-Si, CdTe, CIGS and group III-V compounds), in which the photo-generated exciton-pairs are easily dissociated and

separated into free electrons and holes,<sup>[1]</sup> organic excitons are strongly bound with energies of  $\sim 0.4$  eV.<sup>[155]</sup> Such energy values are strong: of the order of between 0.5 and 2 eV higher than the thermal energy at room temperature.<sup>[156-159]</sup> As a result, the organic exciton pairs are not easily separated into completely free charge carriers. Instead, at the D/A interfaces, the exciton pairs dissociate into short lived, weakly bound polaron pairs.<sup>[154]</sup> As mentioned earlier, this is why the photoactive layers are made generally of interpenetrating blends with phase segregated electron donor and electron acceptor materials. This reduces the separated domain sizes of the photoactive layers, thus increasing the exciton pairs mean free-path lengths.<sup>[160-162]</sup>

Note that, electrons and holes in the polaron pairs are still bound together weakly by coulombic forces. Therefore, in order for OPV effect to occur, there must be further mechanisms to separate the polaron pairs into free-charge carriers. While excitonic dissociation and polaronic recombination have been shown to depend significantly on the nature of the D/A interfaces, the polaron pair separation, transportation and extraction of free-charges at the electrodes are strongly determined by the local internal and external electric fields along with the ambient conditions, such as temperature.<sup>[154]</sup> This suggests the role of the differences between the work-functions of the two electrodes at the anode and cathode ends of organic solar cell systems. It also indicates the importance of local morphological configuration of donor and acceptor materials, after phase segregation through controlled thermal treatments of the photoactive solid-state layer.<sup>[14,163]</sup>

In the case where contributions of the electric field from external electrodes and local photoactive layer domains assisted internal electric fields are sufficiently large; the polaron pairs most likely will separate into free electrons and holes, before they are

transported for collection.<sup>[164]</sup> The separated electrons and holes can still, however, annihilate each other by recombination during migration to their respective electrodes (step 5 in Fig. 2.7). Furthermore, provided there are no traps (such as impurities/defects, re-organization of polymeric chains and significant variations in the degree of crystallinity, which hinder charge carrier mobility,<sup>[165]</sup> the transportation of free charge carriers is believed to depend largely on the morphology of blended donor and acceptor photoactive solid-state layer.

In BHJ organic solar cell systems, the transportation phenomenon of free charge carriers is known to occur primarily by hopping movements through the bi-continuous percolation paths within the photoactive layer.<sup>[58,166,167]</sup> This movement depends also on the quality of the internal and external electric field of the system. The magnitude of the electric field is determined largely by the difference between the work functions of anode and cathode, that are attached on the terminals of the BHJ organic solar cell systems.<sup>[154]</sup>

Finally, after reaching their respective electrodes, the electrons at the cathode and holes at the anode can either recombine or become extracted through drift-diffusion (DD) processes.<sup>[154]</sup> The extracted carriers, after collection at the electrodes, result in the open-circuit voltage,  $V_{OC}$ , of the organic solar cell system. The  $V_{OC}$  can then be used to create photoelectric current, which circulate the external circuitry to generate useful photoelectric power for consumption.

Therefore, apart from formation of exciton pairs, organic solar cell PCEs depend significantly on the exciton and/or polaron pairs dissociation, separation, recombination as well as collection of free-charge carriers at the respective electrodes. This suggests the importance of appropriateness in matching of the two-electrode work functions. It also

suggests the importance of interfacial adhesion and contacts for the design of organic PV systems.<sup>[163,168]</sup> These issues are investigated generally using BHJ organic solar cell structures with photoactive organic baseline materials, that use polymer-fullerene,<sup>[162]</sup> polymer-polymer<sup>[138,169]</sup> or polymer-nanoparticle blends.<sup>[170]</sup>

#### **2.2.2.2.3 BHJ Organic PV Solar Cell Structure: How it Works?**

As shown in Figures 2.3 and 2.7, organic solar cells are activated, using sunlight from the anode sides of BHJ structures. This is in opposite to the injection conditions of OLEDs, the first broad area of application of organic electronics and opto-electronic devices,<sup>[171,172]</sup> such as flat panel displays<sup>[173]</sup> and other electroluminescence devices.<sup>[174]</sup> The conditions needed to optimize the photo-generation, transportation and collection of charges at the electrodes of organic solar cells are:  $(E_F)_{Cathode} < (E_{LUMO})_{Acceptor}$  and  $(E_F)_{Anode} > (E_{HOMO})_{Donor}$ .<sup>[58]</sup>

Subsequently, the PCE of an organic solar cell is estimated generally from the collective contributions from efficiencies of separate individual mechanistic steps of the solar cell operation processes (Figure 2.7). A comprehensive physics of organic solar cells can be cited from the work by Wolfgang<sup>[56]</sup> while the contemporary overview of the historical development and operation mechanisms of organic PV solar cell systems can be found in References.<sup>[1,7,9]</sup>

### **2.3 Transparent Conducting Oxides in OPV Systems**

As mentioned above, the operation of solar cells requires illumination, which upon absorption by the electron donor materials generates free-charge carriers.<sup>[10]</sup> In organic solar cells, illumination is made through the anode side of BHJ structure (Figures 2.3 and 2.7). This requires that the anode side of the BHJ structure must be transparent

enough to allow sufficient photons to enter the photoactive layers of organic solar cell systems. In addition, the transparent anode materials must conform to the other organic solar cell operation requirements. These include high electrical conductivities and reasonable electronic work functions.<sup>[154]</sup>

The most useful solar cell anode materials include thin films of transparent semiconducting oxides.<sup>[68]</sup> Such oxides materials possess wide bandgap energies, which minimize their optical losses by absorption. This gives them high optical transparencies in the visible and near infrared wave length range of the solar spectrum.<sup>[74,175]</sup> They also have relatively high electrical conductivities, associated with their native defects, depending on how they are prepared. These two factors leave them with appropriate quantitative and qualitative figures of merit (low specific sheet resistance combined with low absorption/reflection of visible light) as anodes or TE materials.<sup>[68,74,75]</sup>

Generally, TCO films are used in a vast number of electronics and opto-electronic applications.<sup>[68]</sup> These include applications in layered structures, such as memory devices,<sup>[91]</sup> solar cells, liquid crystal displays and light emitting devices.<sup>[68,74]</sup> Also, due to good electro-optical properties, ITO has dominated the TCO materials for most electronic and optoelectronic applications.<sup>[176]</sup> However, as mentioned earlier, indium is a rare earth element. This makes ITO expensive for application in large area solar cell devices.<sup>[69,177]</sup> Furthermore, the market demand of indium as principal material in various optoelectronic devices and components has been increasing. These include applications in Copper-Indium-Gallium-Diselenide (CIGS) solar cells,<sup>[22]</sup> indium phosphide (InP) for semiconductor devices<sup>[178,179]</sup> and ITO thin film coatings for applications in liquid crystal

displays.<sup>[103,105,107]</sup> As a result, ITO has become increasingly scarce and expensive. This makes it not readily available for large scale industrial applications.<sup>[74,101,102]</sup>

Note that, the notion of organic PVs for potential application as cost-effective source of clean energy is being reviewed periodically. However, there are still so many numbers of challenges facing the development of organic electronics and PV technologies in general. Among these challenges facing the PV industry, is the fundamental resolution of cost problems that are associated to the use of ITO-coated transparent substrates in organic electronics and many other optoelectronic devices. This has been and remains an open issue until adequate cost-effective TCO materials (with low resistivities and reasonable visible spectra transparencies) can be found.

Furthermore, although ITO-coated TCO is the widely used anode or TE material, its optoelectronic performance has been shown to be inadequate<sup>[103]</sup> for applications in some of the most sophisticated organic and inorganic devices, that require TE materials with very low electrical resistivities. This has increased recent research efforts to develop other TCOs (with much lower resistivities) that can compete with and replace the indium-based TEs in future applications.<sup>[74,75,110]</sup> So far, good efforts have been invested in a number of material systems<sup>[68,74,75,86-111,180-183]</sup> that have potentials for applications in TEs. These have been investigated by use of the oxide doping or composite technology, i.e. sandwiching thin layers of highly conducting metals between thin films of traditional TCO materials.

### **2.3.1 Doped Transparent Conducting Oxides**

The structural, electrical and optical properties of doped and undoped single layered thin films of TCOs have been widely studied.<sup>[92-98,184]</sup> These efforts have

improved the transparent conductive properties of tin, zinc and indium oxides to high levels.<sup>[68]</sup> For example, maximum solar visible T spectra between ~ 85% – 95% and associated electrical sheet resistivities, as low as  $\sim 3 \times 10^{-4} \Omega \text{ cm}$ , have been reported in ZnO thin films doped with Al.<sup>[98]</sup> Note that these values compare favourably to the electro-optical properties of the standard substrates coated with ITO thin films, for which resistivities of  $\sim 1 \times 10^{-4} \Omega \text{ cm}$  and Ts as high as ~ 80% in the visible region of the solar spectrum have been reported.<sup>[75,89]</sup> However, single TCOs with nano-scale thicknesses have been shown to have limited applications.<sup>[74,100]</sup> This is due partly to high ionized impurity scattering, which limit their optical and electrical properties.<sup>[74]</sup> It is also due to their chemical and thermal instabilities in various environments.<sup>[100]</sup>

## **2.3.2 Multilayered Transparent Conducting Films**

### **2.3.2.1 ITO-based Multilayered Films**

In an effort to address some of the challenges above inherently transpiring in single-layered doped and undoped TCO coatings, the family of multilayered TCO/metal/TCO composite films have been recently proposed as good candidates for applications in TE coatings.<sup>[74,75,90,107]</sup> Furthermore, since ITO is the most widely used TCO,<sup>[68,74]</sup> the immediate approach that has been proposed is the use of IMI systems in the enhancement of electrical conductivity at reasonable optical T.<sup>[102-108]</sup> The IMI structures have been shown to have better durability than single layered metallic films.<sup>[103,108]</sup> The IMI films have also been revealed to have practical and stable electro-optical properties at lower thicknesses than single layered ITO coatings.<sup>[103,108]</sup> Some researchers<sup>[101,103,105]</sup> have suggested that the high transparent conductive properties and the low thicknesses of IMI multilayers may enable these structures to surpass ITO in

overall performance. The structures are also potentially less expensive than conventional single layered ITO-coated transparent electrodes.<sup>[101]</sup>

Fahland *et al.*<sup>[105]</sup> have investigated the electrical and optical characteristics of IMI structures that were fabricated on flexible polymer substrates. They reported multilayered IMI thin film composite structures with sheet resistance of  $\sim 16\Omega/sq.$  and solar Ts as high as  $\sim 80\%$  in the visible region of the spectrum.<sup>[105]</sup> The high sheet resistance value obtained was attributed to various limitations associated with the polymeric flexible substrates that were used. The substrate prohibited the use of rigorous post-deposition high temperature (above  $200^\circ\text{C}$ ) during annealing treatments of the IMI films. Nevertheless, it was shown that, the overall thicknesses that were needed to attain optimum electro-optical properties that are comparable to those of single layered ITO were significantly smaller than the thicknesses that are needed in the latter films. Note that the use of thinner thicknesses in the multilayered IMI films minimizes the usage of indium, thus reducing the overall costs of the IMI TE coatings.

Choi *et al.*<sup>[103]</sup> have also reported on the properties of transparent conductive multilayered IMI thin films with intermediate nanolayers of metallic silver. They obtained composite thin film electrodes with best sheet resistance of  $\sim 4\text{ ohm/sq.}$  and average visible T as high as  $\sim 90\%$ . These were obtained for the multilayered IMI thin film structure with optimum Ag intermediate layer thickness of 14 nm and ITO double-layer thicknesses ranging between 55 – 60 nm each. Their results also show that, the transparent conductive properties of the multilayered thin films depend strongly on the conditions that were used for the deposition of ITO and intermediate silver layers.

Similar ITO/Ag/ITO thin film composite stacks have recently been investigated by Kloppel *et al.*<sup>[104]</sup> They produced IMI TCEs with sheet resistance as low as  $\sim 4.7 \text{ ohm/sq.}$  for the Ag mid-layer thickness of  $\sim 10 \text{ nm.}$  These authors<sup>[104]</sup> showed that the crystallinity, microstructure, post-deposition treatment and purity of the deposition environment have significant influence on the electro-optical performances of the multilayered thin film TCEs. The best multilayered IMI TCE (with lowest electrical sheet resistance and highest optical transparency) was obtained when the upper and lower ITO layers were deposited under optimum stoichiometric conditions followed with post-deposition annealing in vacuum environments.

The influence of substrate temperature and deposition pressure on the electro-optical properties of multilayered IMI based on ITO/Ag/indium-cerium oxide thin film structures was also investigated by Kloppel *et al.*<sup>[106]</sup>. In agreement with Fahland *et al.*,<sup>[105]</sup> they showed that the multilayered IMI thin film composite structures can be tailored to have very low sheet resistances and high  $T_s$  at relatively low thicknesses that are smaller than those of single nano-layered TCO films. It was also revealed that multilayered IMI thin films are more stable than single-layered TCO films in various environments.

Masato *et al.*<sup>[107]</sup> have investigated the characteristics of ITO/Ag/ITO sandwiches for potential applications in liquid crystal displays (LCDs). They showed that, integration of the multilayered IMI thin films (with optimum mid-layer Ag thickness of  $\sim 15 \text{ nm}$  and ITO thicknesses of  $\sim 40 \text{ nm}$ ) with a liquid crystal display system results in an improved optoelectronic performance of the systems. The LCD devices with multilayered IMI thin film electrodes were shown to lead to a reduction in crosstalk levels, in the range of

between ~ 27 – 48% better than conventional LCD systems that were fabricated using single ITO-coated thin film electrodes.<sup>[107]</sup>

Other researchers<sup>[102,108]</sup> have investigated the dependence of electro-optical properties of multilayered IMI thin film structures on composition, interlayer thicknesses and post-deposition thermal treatments. Additionally, the work of Bender *et al.*<sup>[102]</sup> reported on the electro-optical characteristics of ITO double-layers with intermediate layers of AgCu alloys. In this case, multilayered thin film electrodes with sheet resistances as low as ~ 5.7 ohm/sq. and average optical Ts as high as ~ 83% were obtained by these authors.<sup>[102]</sup> Note that, the electro-optical results obtained in multilayered thin film structures with mid-layer AgCu alloy are relatively poor, compared to those obtained in multilayered thin film stacks with mid-layer of pure metallic Ag. This suggests that alloying of metals for applications as intermediate conductive layers does not necessarily improve the electro-optical performances of multilayered thin film composite electrodes.

A study by Jung *et al.*<sup>[108]</sup> investigated the influence of thermal treatments on the electro-optical properties of IMI structures. They also demonstrated the differences between the transparent conductive properties of ITO/Ag/ITO and ITO/Ag-alloy/ITO multilayered thin film composite structures. It was shown by these authors<sup>[108]</sup> that, annealing and other post-deposition treatments of the multilayered IMI thin film composite structures can greatly improve the electro-optical properties of the TCEs that are deposited at given preparation conditions (such as the deposition pressure, deposition rate and deposition substrate temperature).

Furthermore, a shift in solar T spectra was observed in their work.<sup>[108]</sup> This was attributed to changes in refractive indices of the layers within the multilayered thin film composite structures as a result of thermal annealing. Thermal annealing was also shown to influence the degree of crystallinity of the multilayered IMI thin film composite structures.<sup>[108]</sup> It was also shown in the work of Jung *et al.*<sup>[108]</sup> that, the use of silver alloys in between the upper and lower ITO layers, resulted in multilayered IMI thin film composite structures with higher resistivity values than those of multilayered IMI thin composite structures that were fabricated with pure Ag mid-layers.

It is important to note here that, the reported high optical T values in the visible region of the solar spectrum as well as the very low resistivities of multilayered IMI thin film composite structures are generally desirable in TCOs for applications such as transparent anodes in organic solar cells and in other passive and active organic electronics, optoelectronic devices and their components. Therefore, insertion of nano-layers of highly conductive metals between the ITO layers improves their transparent conductive figures of merit. Note also that, the characteristically low thicknesses of ITO in the multilayered IMI thin film composite structures make these structures potentially less expensive than conventional ITO-coated TEs.<sup>[101]</sup>

However, due mainly to the large demand for optoelectronic devices along with the increasing need and problems associated with the scarceness of indium,<sup>[69]</sup> ITO has become increasingly expensive. This has also increased recent interest for the search of other host transparent conducting materials (with lower resistivities and reasonable visible spectra Ts) alternatives to ITO-based TCOs. In recent years, the main emphasis has been put generally on the realization of indium free multilayered thin film composite

structures. The composite films are tailored in a way that enhances electrical sheet resistances or resistivities at practical optical transparencies in the visible region of the solar spectrum. The performances of the multilayered thin film composite structures are controlled to have electro-optical properties that are comparable to the performance characteristics of ITO or the multilayered IMI thin film composite anodes that are used currently in solar cells and light emitting devices.<sup>[74,75,100]</sup>

### **2.3.2.2 Multilayered ZmZ Film Composite Electrodes**

Major improvements in TCO materials have involved modification of electrical and optical properties in the oxide thin films of indium, zinc and tin.<sup>[68]</sup> As discussed in the previous sections, ZnO is one of the promising TCO materials that can be tailored to meet both low electrical resistivities and high Ts that are needed in the operation of organic and inorganic electronic devices and components. Hence, ZnO has been widely explored, in recent years, as one of the host materials alternatives to ITO-coated TCOs.<sup>[88,89]</sup> Multilayered ZmZ thin film stacks have also been suggested as alternatives to IMI systems<sup>[74,90]</sup> that contain costly indium, which is not as readily available as ZnO.<sup>[69]</sup> The multilayered ZmZ thin film composite structures are also environmentally benign and they are not difficult to produce. In this section, representative results on multilayered ZmZ thin film composite structures cited from recent literature are presented, before discussing their implications for the design of transparent ZAZ thin film composite electrodes.

#### **2.3.2.2.1 Design of Multilayered ZmZ Thin Film Composites**

The general knowledge on multilayered ZmZ thin film composite structures for applications in TE in various optoelectronic devices exists. ZnO-based multilayered thin

film composite structures that were fabricated with different intermediate layers of highly conductive metals<sup>[185]</sup> have already been produced.<sup>[74,109,111]</sup> Also, their potentials for applications in TEs have been tested for some device technologies.<sup>[74,90,111]</sup> The multilayered ZmZ thin film composite structures have been produced by sandwiching a thin layer of a highly conductive metal between the layers of ZnO.

The commonly used intermediate metals include gold (Au),<sup>[74]</sup> silver (Ag)<sup>[75,90,101,110]</sup> and copper (Cu).<sup>[109,111]</sup> These metals are being investigated as ultra-thin transparent conductive ZmZ mid-layers, due to their low electrical resistivities.<sup>[74,185]</sup> Al is the next metal to copper in terms of low resistivity (see Table 2.1).<sup>[185]</sup> It also has adequately low resistivity values ( $\sim 26.3$  n $\Omega$  meters)<sup>[185]</sup> for applications in multilayered ZmZ thin film composite structures. Compared to Ag and Au, which are precious, Al is cheap.<sup>[186]</sup> Al has also been shown to result in good transparent conductive properties, when used as an n-type dopant in ZnO.<sup>[89,180-183,187]</sup> There is, therefore, great interest in the development and understanding of multilayered ZmZ with special emphasis on ZAZ thin film composite structures. These are explored for applications in TEs in large area solar cells, light emitting diodes and other optoelectronic devices and components.

Table 2.1: Electrical resistivity values for the highly conductive metals.<sup>[185]</sup>

Metal	Silver	Copper	Gold	Aluminium
Resistivity (ohm meters)	$1.47 \times 10^{-8}$	$1.72 \times 10^{-8}$	$2.44 \times 10^{-8}$	$2.63 \times 10^{-8}$

### 2.3.2.2.2 Prior Work on Multilayered ZmZ Thin Film Composites

Despite the need to develop TE materials alternatives to ITO-coated TCOs, which are produced from scarce and expensive reserves of indium, there are relatively very few

reports of multilayered ZnZ thin film composite structures in the literature. These are mainly as results of works by Sahu *et al.*<sup>[101]</sup> and Alford *et al.*<sup>[74]</sup>

In 2005, Sahu *et al.*<sup>[90]</sup> reported multilayered ZnO/Ag/ZnO thin film composite structures that were produced using RF MS. It was shown by these authors<sup>[90]</sup> that the properties of multilayered thin film composite structures (as function of interlayer silver thicknesses) changed mainly with the properties of mid-layer Ag as opposed to the characteristics of the upper and lower ZnO layers. These authors<sup>[90]</sup> also showed that multilayered ZnO/Ag/ZnO thin film composite electrodes with optimum solar T of ~ 90% (in the visible range of the spectrum) and sheet resistances as low as ~ 3 *ohm/sq.* can be produced provided that the thicknesses of the layers are carefully optimized. The good transparent conductive properties observed in the multilayered ZnO/Ag/ZnO thin film composite structures were adequate enough for application of the multilayered ZnZ thin film composite TEs in dye sensitized solar cell systems.

In another work by Sahu and coworkers<sup>[110]</sup> that, critical mid-layer metal thicknesses at which the multilayered thin film sandwiches attain the lowest resistivity values while maintaining reasonable optical transparencies were determined. For example, at the mid-layer Ag thickness of ~ 6 nm, multilayered ZnO/Ag/ZnO thin film composite structures with sheet resistances as low as ~ 3 *ohm/sq.* were obtained.<sup>[110]</sup> For the mid-layer Ag thicknesses that were relatively thicker than the critical thickness of ~ 6 nm, the electrical properties became generally steady with increasing mid-layer Ag thickness.<sup>[110]</sup> They demonstrated the electro-optical and morphological characteristics of the multilayered ZnO/Ag/ZnO thin film sandwiches in comparison with the properties of single nano layers of Ag and ZnO thin films. In a later study with similar multilayered

ZnO/Ag/ZnO thin film composite structures, Sahu and coworkers<sup>[110]</sup> have also proposed some experimental procedures for establishment of possible interlayer film thicknesses that can be used in the design of transparent conducting multilayered ZnO/Ag/ZnO thin film composite structures.

An important phenomenon was suggested by the studies above.<sup>[90,110]</sup> This involved the optimum T and sheet resistance values that were observed to occur generally in the same mid-layer Ag thickness ranges between ~ 4 – 8 nm. This observation is generally important for the design of multilayered ZnO transparent thin film composite electrodes. It enables the use of one property (either optical or electrical) to predict the other. Ultimately, this allows easiness in the prediction of the interlayer thicknesses for the design of ZnO-based multilayered thin film composite systems, with intermediate nanolayers of highly conductive metals. This observation suggests the basis for the numerical simulations and analysis of multilayered ZnO thin film composite structures with special accent on prediction of possible ranges of the intermediate metal layer thicknesses. It remains, however, to be seen whether these important milestones hold only for multilayered thin film composite structures with mid-Ag layer or applies for all ZnO-based multilayered film composites with any metallic nano-layers such as Au, Cu and Al.

Multilayered thin film composite structures with double-layers of ZnO and conductive nanolayers of copper were investigated by Sahu *et al.*<sup>[109,111]</sup> They demonstrated the dependence of electro-optical properties of multilayered ZnO/Cu/ZnO thin film composite structures on mid-layer Cu thickness (as functions of processing conditions, such as substrate temperature, annealing treatments and crystal structure). It

was shown by these authors<sup>[109,111]</sup> that, the deposition conditions have significant influence on the physical and opto-electronic performances of the transparent multilayered ZnZ thin film composite structures. It was also shown that the multilayered ZnO/Cu/ZnO thin film composite stacks with sheet resistances as low as  $\sim 10 \text{ ohm/sq.}$  and average T as high as  $\sim 85\%$  in the visible region of the solar spectrum could be produced for structures with mid-layer Cu thicknesses ranging between  $\sim 4 - 6 \text{ nm.}$

Note that the reported mid-Cu optimum thickness range ( $\sim 4 - 6 \text{ nm}$ ) is generally in agreement with that of between  $4 - 8 \text{ nm}$  for multilayered thin film composite structures with mid-Ag layers.<sup>[90,110]</sup> However, the differences between the electro-optical properties for multilayered thin film composite structures with mid-Cu and those with mid-Ag layers are possibly due to the differences in their optical constants.<sup>[188]</sup> This could also occur as results of differences between the electrical resistivities (Table 2.1)<sup>[185]</sup> of Cu<sup>[109,111]</sup> and Ag,<sup>[90,110]</sup> that were used by the authors. For example, the average visible solar T of  $\sim 85\%$  was obtained in multilayered ZnZ thin film composite structures with mid-Cu layers while visible solar T values as high as  $\sim 90\%$  could be achieved in multilayered ZnO/Ag/ZnO thin film composite structures. Similarly, the optimum electrical sheet resistance increased from  $\sim 3 \text{ ohm/sq.}$  for multilayered ZnZ thin film composite structures with mid-Ag layers to  $\sim 10 \text{ ohm/sq.}$  in multilayered ZnZ thin film composite structures with mid-Cu layers.

It is important to note here that, the trends reported above of electro-optical properties in ZnO-based multilayered thin film stacks (with Cu<sup>[109,111]</sup> and Ag<sup>[90,110]</sup> nanolayers) suggest another important phenomenon for the design of transparent multilayered ZnZ thin film composite electrodes. The discrepancies that were observed

in the electro-optical data, suggest that the electro-optical properties, as well as the overall performance of the multilayered ZnZ thin film composite structures are controlled mainly by physical mechanistic interactions as opposed to chemical interactions between the interlayered ZnO and metallic materials. This is clearly seen by comparing the electro-optical properties of multilayered ZnZ thin film composite structures with Cu<sup>[109,111]</sup> and those with Ag<sup>[90,110]</sup> intermediate layers.

Thus, the use of mid-Cu<sup>[109,111]</sup> nanolayers between ZnO films resulted to multilayered ZnZ thin film composite structures with relatively higher sheet resistance values than those of multilayered thin film composite stacks that were produced with mid-Ag<sup>[90,110]</sup> nanolayers. Furthermore, thick intermediate Cu<sup>[109,111]</sup> layers that are thicker than mid-layer Ag<sup>[90,110]</sup> thicknesses were necessary to produced ZnO/Cu/ZnO film composite structures with reasonable electrical properties. This can be associated to the high electrical resistivity of copper that is higher than that of silver (Table 2.1).<sup>[185]</sup>

Recently, the electro-optical properties of multilayered ZnO/Au/ZnO thin film composite stacks that were produced by RF MS have been investigated by Sivaramakrishnan *et al.*<sup>[74]</sup> Multilayered ZnO/Au/ZnO thin film composite structures with high electrical conductivities and good visible spectra Ts (between ~ 75 – 85%) were produced in the work of Sivaramakrishnan *et al.*<sup>[74]</sup> These authors<sup>[74]</sup> showed that multilayered ZnZ thin film composite structures with intermediate nanolayers of gold can be tailored to have room temperature electro-optical properties, that surpasses those of commercially available ITO thin film coated substrates.

All these studies suggest that ZnO-based multilayered thin film composite structures can be engineered to have electro-optical properties that are needed as TEs in

organic solar cells and many other optoelectronic structures. They also suggest that the multilayered ZnZ thin film composite stacks are potentially good TE material candidates alternatives to the conventionally used ITO-coated TCO substrates or the multilayered IMI thin film composite structures that are currently used to improve the transparent conductive properties of indium based TE materials, for applications in organic solar cell systems and other layered electronics and optoelectronic devices and components. However, although these multilayered ZnZ structures exhibit good electro-optical properties, one may still question their robustness since they are very thin structures.

Some researchers<sup>[99]</sup> have investigated the stabilities of multilayered ZnO/Ag/ZnO and Al-doped ZnO /Ag/Al-doped ZnO thin film composite structures for applications in various environments. They<sup>[99]</sup> found that, the insertion of mid-Ag layers between the upper and lower layers of ZnO can enhance the moisture resistance of ZnO films. This was attributed to the decrease in the internal stresses in the thin films of ZnO, as a result of the mid-Ag layers that were embedded between them. For multilayered ZnZ thin films with Al-doped ZnO /Ag/Al-doped ZnO composite structures, the establishment of optimum dopant levels (Al contents) was very crucial. Increasing the Al concentration above a certain critical content resulted in fast moisture degradation of the multilayered thin film composite structures. In the high doping concentration regime, the multilayered Al-doped ZnO /Ag/Al-doped ZnO thin film composite structures exhibited unfavourable morphological properties that were characterized by foggy features.<sup>[99]</sup>

The increased degradations above were attributed to the increase in the hydration of the multilayered thin film stacks as results of the possible chemical reactions between moisture and the excess Al, thus leading to fast degradation mechanism rates.<sup>[99]</sup> This

suggests that the use of doped ZnO in the multilayered thin film composite structures does not improved either the transparent conductive properties or the environmental stability of the multilayered ZnZ thin film composite electrodes. The multilayered ZnZ thin film composite structures with undoped ZnO layers are therefore more stable than the traditional single nanolayers of silver and/or single nanolayers of doped and undoped thin films of ZnO.

### **2.3.2.2.3 Multilayered ZnO/Al /ZnO Thin Film Composite Structures**

Recently, typical multilayered ZAZ thin film composite structures that were prepared by thermal evaporation technique have been investigated by Al-Kuhaili *et al.*<sup>[80]</sup> They reported multilayered ZAZ thin film composite structures with optimum average visible solar T spectra of ~ 75% and electrical resistivities as low as  $\sim 2.9 \times 10^{-3} \Omega \text{ cm}$ . However, these authors found significant differences between the measured solar T values and resistivities of the multilayered ZAZ thin film composite stacks (as function of annealing temperature).<sup>[80]</sup> In addition, the stoichiometry of ZnO and the homogeneity of the mid-Al layers may be better controlled in the multilayered ZAZ thin film composite structures that are prepared by other fabrication techniques such as RF MS<sup>[68]</sup> with a range of possible mid-layer Al thicknesses.

It is, therefore, of great interest to study the influence of mid-layer Al thickness on the electro-optical properties of multilayered ZAZ thin film composite stacks, that have potential for applications as cost-effective transparent electrode coatings in large area electronic structures/devices and layered optoelectronic components such as organic solar cells and organic light emitting diodes.

# 3. Chapter Three

## Numerical Modeling of Multilayered ZAZ Thin Film Composite Structures

### 3.1 Introduction

As discussed in chapter 2, some studies have shown that the sandwiching of the nanolayers of a highly conducting metal such as Ag, Cu, Au and Al between ZnO films can significantly promote the electrical conductivity of ZnO at reasonable optical transparencies that are needed for applications in solar cells and optoelectronic devices. One of the challenges in the experimental design of such transparent conducting multilayered ZnO thin film composite structures is the selection of possible optimum metal thickness ranges such as those of mid-Al layer in multilayered ZAZ thin film composite structures. Therefore, this chapter attempts to overcome this limitation by investigating how mid-layer Al thickness affects the optical properties of multilayered ZAZ thin film composite structures. To do this, a modified variable-optical software package was used to efficiently model the thicknesses of mid-Al nanolayers embedded in the double-layers of ZnO thin films. Numerical simulations were used to study the influence of mid-Al with nanolayer thicknesses on the optical T, reflectance, R, and absorbance, A, properties of multilayered ZAZ thin film composite structures with mid-Al and ZnO layer thicknesses that were varied between  $\sim 1 - 100$  nm.

The multilayered ZAZ thin film composite structures with mid-layer Al thicknesses between  $\sim 1 - 10$  nm are shown to have average optical solar T spectra between  $\sim 75 - 90\%$ , which decreased further to  $\sim 35$  and  $15\%$  for the mid-layer Al thicknesses of 50 and 100 nm, respectively. Variations in the thickness of ZnO layers

between  $\sim 10 - 100$  nm are shown to have little effects on the optical characteristics of the multilayered ZAZ thin film composite structures, for a given mid-layer Al thickness. The optimum thicknesses for the ZnO and mid-Al layers are predicted and discussed for possible applications in the experimental design of transparent conducting multilayered ZAZ thin film composite electrodes.

## 3.2 Numerical Methods

### 3.2.1 Theory of Light Absorption

The phenomenology of light transport in multilayered thin film composite structures is predicted generally from combined considerations of Maxwell's equations and the conditions of continuity at the interfaces of given multilayered thin film composite structures.<sup>[189]</sup> In this case, one starts with the form of an exponentially damped light wave traveling in the positive  $z$  direction (Figure 3.1). For an absorbing material, the refractive index,  $N$ , is a complex quantity. It is given by:

$$N = n - ik \quad (3.1)$$

where  $n$  is the real quantity of refractive index and  $k$  is the extinction coefficient.

The solution for the classical wave equation<sup>[190]</sup> can now be readily obtained when the phase vector in the classically well-known wave equation is assumed to be zero.<sup>[190]</sup> Such a solution is given by:

$$\mathbf{E} = E_0 \exp \left[ i\omega \left( t - \frac{Nz}{c} \right) \right] \quad (3.2)$$

where  $\mathbf{E}$  is the electric field vector of the traveling light wave,  $t$  is the time,  $c$  and  $\omega$  are the respective velocity and the angular frequency of light wave.

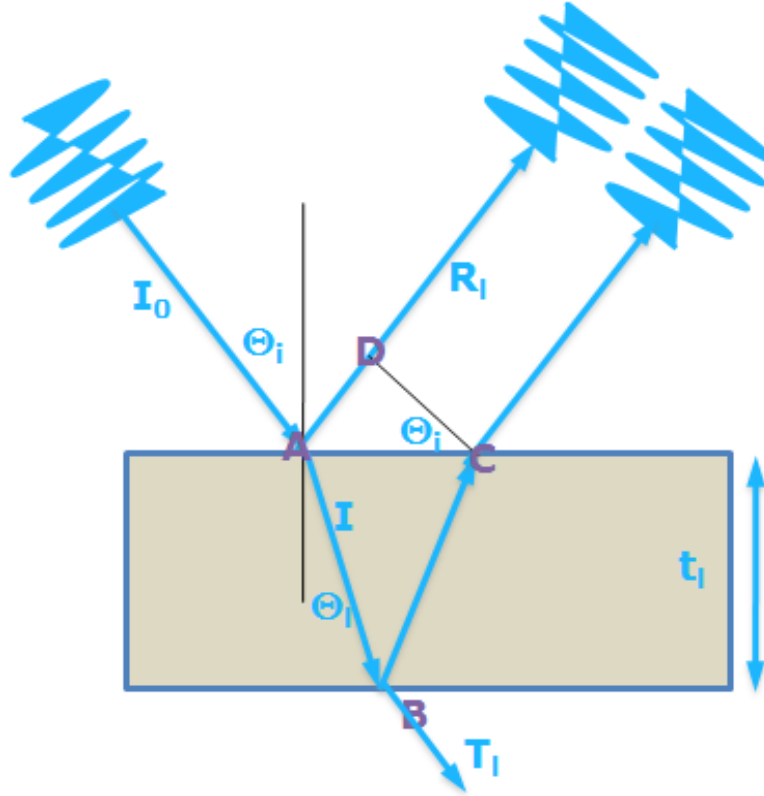


Figure 3.1: Schematic illustration of thin film interference. Light wave of intensity,  $I_0$ , traveling from a layer of lower refractive index to the layer of higher refractive index automatically undergoes a phase shift of  $\pi$  radians upon reflection. The optical path difference (OPD) and wave length,  $\lambda$ , of light in a layer,  $l$ , of refractive index,  $n_l$ , and thickness,  $t_l$ , at an angle of refraction,  $\theta_l$ , are given by:  $OPD = 2n_l t_l \cos \theta_l$  and  $\lambda_l = \lambda_{\text{vacuum}}/n_l$ , respectively.

Accordingly, from the solution (equation 3.2) above, the amplitude,  $|\mathbf{E}|$ , of the light wave, which is associated with the depth,  $z$ , from the interface inside the multilayered thin film composite structure can be deduced. This is given by:<sup>[190]</sup>

$$|\mathbf{E}| = E_0 \exp\left(-\frac{2\pi k z}{\lambda}\right) \quad (3.3)$$

where  $\lambda$  is the wave length of light wave in vacuum. The light intensity, which is proportional to the square of the amplitude, is thus exponentially damped by the absorbing material within the multilayered thin film composite structures.

The absorption coefficient of the absorbing material of a given layer,  $l$ , inside the multilayered thin film structures is given by:

$$\alpha_l = \frac{4\pi k}{\lambda} \quad (3.4a)$$

This is obtained as the reciprocal of the distance below an interface at which the amplitude of the wave falls to  $e^{-1}$  of its value at the interface. Accordingly, when photons traverse a layer of the absorbing film of thickness,  $t_l$ , inside the multilayered thin film composite structure, the amplitude of light wave decreases with increasing interlayer film thickness by the factor,  $\delta$ . This is obtained from equation (3.3) by taking the ratio of  $|\mathbf{E}|$  to  $E_0$ . It is, therefore, given by:

$$\delta = \exp\left(-\frac{2\pi k t_l}{\lambda}\right) \quad (3.4b)$$

This is simplified further by combining equations (3.4a) and (3.4b), to arrive at:

$$\delta = \exp\left(-\frac{\alpha_l t_l}{2}\right) \quad (3.4c)$$

### 3.2.2 Light Reflection and Transmission Model

This model is based on the combined considerations of the classical optical transmission and reflection characteristics, in which the incident light wave splits into a transmitted and a reflected part at the interfaces of a given multilayered thin film composite stack.<sup>[189]</sup> For non-absorbing materials, the perpendicular,  $R_s$ , and parallel,  $R_p$ , intensity reflection coefficients are obtained by simply squaring the classically well-

known respective Fresnel perpendicular,  $r_s$ , and parallel,  $r_p$ , amplitudes of reflection coefficients. These are given by:

$$r_s = \frac{n_m \cos \theta_m - n_{m+1} \cos \theta_{m+1}}{n_m \cos \theta_m + n_{m+1} \cos \theta_{m+1}} \quad (3.5a)$$

and

$$r_p = \frac{n_{m+1} \cos \theta_m - n_m \cos \theta_{m+1}}{n_{m+1} \cos \theta_m + n_m \cos \theta_{m+1}} \quad (3.5b)$$

where  $R_s = |r_s|^2$  and  $R_p = |r_p|^2$ ,  $n_m$  is the refractive index of the glass substrate on which the transparent multilayered thin film composite structure is designed,  $n_{m+l}$  represents the consecutive refractive indices of the materials for the given stack of layers,  $l = 1, 2, \dots$  on top of the glass substrate. Subsequently, the total reflection coefficient,  $R_{s,p}$ , of multilayered thin film composite structures with perpendicular (s) and parallel (p) components is deduced from:

$$R_{s,p} = \frac{(R_s + R_p)}{2} \quad (3.6a)$$

Note that, for the combined transmission coefficient,  $T_{s,p}$ , and reflection coefficient,  $R_{s,p}$ , of multilayered thin film composite structures, the quantity  $\xi$  is known to be strongly dependent on  $k$ .<sup>[191]</sup> It is given by:

$$\xi = \frac{T_{s,p}}{1 - R_{s,p}} \quad (3.6b)$$

Furthermore, in actual multilayered thin film composite structures, the light wave is transmitted through a slab of combined absorbing and non-absorbing materials. This causes the light wave to undergo complex multiple reflections, absorptions and interference effects. In this situation, the Fresnel definition is of limited usefulness. However, the transmitted part of the incident light,  $T_{\text{sample}}$ , of a slab with non-absorbing

materials can be calculated from an optical model of the modified form of Fresnel equation. Equation (3.6b) is readily modified from the Airy equation.<sup>[190]</sup> This leads to:<sup>[192]</sup>

$$T_{sample} = \left[ 1 + \left[ \frac{4R_{s,p}}{(1-R_{s,p})^2} \right] \sin^2 \frac{2\pi n_{sample} d_{sample} \cos \theta}{\lambda} \right]^{-1} \quad (3.7)$$

where  $\theta$  is the angle of refraction and  $d_{sample}$  is the thickness of the multilayered thin film composite structure.

Note that for a given material refractive index and angle of incidence, equation (3.7) suggests that the transmission characteristics of multilayered thin film composite structures can be made to vary between a maximum value of  $\sim 1$  and a minimum value of  $\sim T_{min}$  given by:

$$T_{min} = \frac{(1-R_{s,p})^2}{(1+R_{s,p})^2} \quad (3.8)$$

These minimum and maximum T values can be attained mainly by changes in the wave length of light wave,  $\lambda$ , and/or the thicknesses of the layers within the multilayered thin film composite structures. This implies that the thicknesses of multilayered thin film composite structures and their interlayer materials properties can be controlled to obtain multilayered thin film composite structures with reasonable visible T spectra that are needed for applications in TE coatings in electronics and optoelectronic devices.

However, in the case where an absorbing layer, such as Al is inserted in the multilayered ZAZ thin film composite structure, the refractive index of the multilayer film becomes a complex quantity. In this scenario, different approaches have been proposed.<sup>[190]</sup> One of these involves the use of effective refractive indices in which both, the perpendicular and parallel refractive indices are complex. These are written according

to Berning's method, in which the respective perpendicular (s) and parallel (p) refractive indices of a given layer,  $l$ , are considered separately. These are given by:<sup>[190]</sup>

$$N_{ls} = N_l \cos \theta_l \quad (3.8a)$$

and

$$N_{lp} = \frac{N_l}{\cos \theta_l} \quad (3.8b)$$

where  $N_l$  is a complex refractive index of a material (equation 3.1) for a given absorbing layer,  $l$ , within the multilayered thin film composite structure,

$$\cos \theta_l = \left[ \frac{(\tau_l^2 + \beta_l^2)^{1/2} + \tau_l}{2} \right]^{1/2} - i \left[ \frac{(\tau_l^2 + \beta_l^2)^{1/2} - \tau_l}{2} \right]^{1/2} \quad (3.8c)$$

$$\tau_l = 1 + \left( \frac{n_{l-1} \sin \theta_{l-1}}{n_l^2 + k_l^2} \right)^2 (k_l^2 - n_l^2) \quad (3.8d)$$

and

$$\beta_l = -2n_l k_l \left( \frac{n_{l-1} \sin \theta_{l-1}}{n_l^2 + k_l^2} \right)^2 \quad (3.8e)$$

Note here that, by combining equations (3.6 – 3.8) one can readily substitute, the effects of multiple absorptions and reflections in a particular direction into the optical characteristics to obtain a regular absorption-reflection-transmission model for the multilayered thin film composite structures.

### 3.2.3 Numerical Modeling Tool and Procedure

#### 3.2.3.1 The Modeling Tool

The numerical simulations of the multilayered ZAZ thin film composite structures were carried out using the optical software package, edition 0.1.8 (CENTURIONI Emanuele, CNR – IMM, Bologna, Italy).<sup>[193]</sup> This was used to predict the thicknesses and their corresponding effects on the optical transparencies of the multilayered ZAZ thin

film composite structures. The variable-optical 0.1.8 software derives the characteristics of multilayered thin film composite structures mainly from the refractive indices of the materials and the thicknesses of the layers.

The multilayered ZAZ thin film composite model that was used in this study assumed multilayered thin film structures with ZnO and mid-Al layers with planar-interfaces. It also assumed, that the transmitted part of the incident light wave from the sample multilayered ZAZ thin film structure is not oscillating with photon wave length,  $\lambda$ .<sup>[191]</sup> The multilayered ZAZ thin film composite model assumed further that there are no chemical interactions at the interfaces between the ZnO and mid-Al layers. Hence, within the optical program, the phenomenology of light transport (A, R and T) in the multilayered ZAZ thin film composite systems is derived mainly by linking equations (3.1 – 3.8), together with the photon of wave length,  $\lambda$ , to generate the regular transmission-absorption-reflection model.<sup>[190]</sup>

### **3.2.3.2 Numerical Procedure**

In an effort to estimate the layer thicknesses of the multilayered ZAZ thin film composite structures with the optical software package, the layer dimensions and the associated optical properties were simulated. This was done by building discrete models of ZnO and mid-Al nanolayers within the multilayered ZAZ thin film composite structures. The refractive indices of the layers were then incorporated into the optical simulations, within the optical software program, which searches for extinction coefficient,  $k$  values that satisfy the multilayered thin film composite refractive index equation (3.1).

The close similarity between the optical properties of bulk and thin film materials<sup>[188,194]</sup> enabled the application of the existing Al and ZnO optical constants to the multilayered ZAZ thin film composite structures. In this study, the wave length-refractive indices file of Al was modified using an optical index-wave length database that was created earlier by Schubert.<sup>[195]</sup> The wave length-refractive indices data file of ZnO layers was modified to have refractive indices fixed at 2.02.<sup>[79]</sup> The thicknesses of the layers were then varied between ~ 1 – 100 nm (for Al), and between 10 – 100 nm for the upper and lower ZnO layers.

### **3.3 Results and Discussion**

#### **3.3.1 Effects of Al Thickness on the Optical Properties of ZAZ Film**

The results obtained from the simulations of the optical properties of multilayered ZAZ thin film composite structures are presented in Figures 3.2 – 3.4. These show the dependence of T, A and R on mid-layer Al thicknesses. The results show the effects of intermediate Al nanolayers on the optical properties of the multilayered ZAZ thin film composite structures, for mid-layer Al thicknesses between ~ 1 – 100 nm.

From the optical profiles (Figures 3.2 – 3.4), it is clearly observed that, for wave lengths above the ultra-violet (UV) region (~350 nm) of the solar spectrum, the multilayered ZAZ thin film composite structures with Al interlayer thickness of ~ 10 nm have Ts between ~ 68 and 89%, an average of ~ 75%. Furthermore, high spectra Ts between ~ 88 and 91%, an average of ~ 90% were achieved (by simulations) in multilayered ZAZ thin film composite structures with mid-layer Al thickness of ~ 1 nm. This implies that, in order to avoid absorbing (Figure 3.3) and reflecting (Figure 3.4)

most of the incident photons, it is necessary to use Al interlayers with ultra-thin thicknesses.

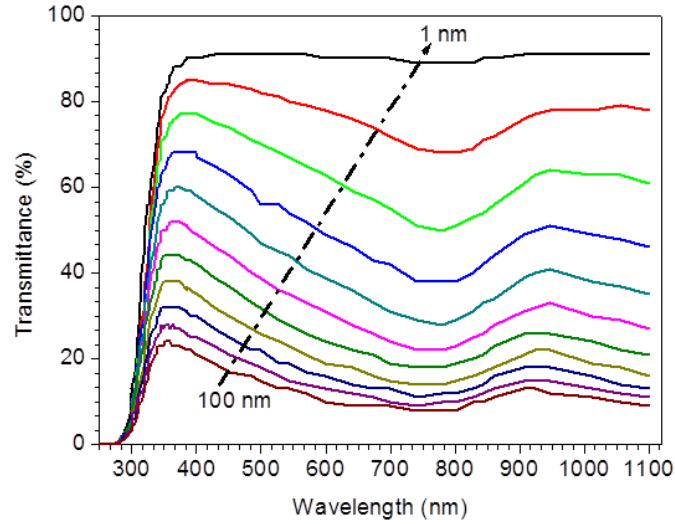


Figure 3.2: Optical T of ZAZ multilayer films with different mid-Al thicknesses between 1 – 100 nm and ZnO double-layers of 50 nm each on transparent glass substrates.

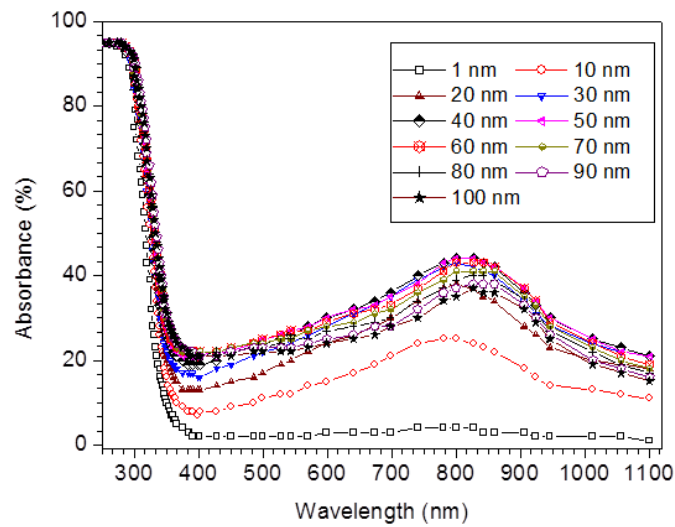


Figure 3.3: Simulated optical A of multilayered ZAZ thin film composite structures with different captioned mid-layer Al thicknesses and ZnO layers of 50 nm thick each.

However, the design of the transparent conducting multilayered thin film composite structures requires a balance between  $T$ , conductivity and thickness. Therefore, in order to avoid major electrical property limitations, which may arise due to discontinuous ultra-thin metallic thin films that generally form on oxides,<sup>[74,75,103,111]</sup> the mid-Al layers must be sufficiently thick to ensure continuous thin film structures. Hence, no further numerical investigation was carried out, in this study, to simulate Al interlayer thicknesses below  $\sim 1$  nm.

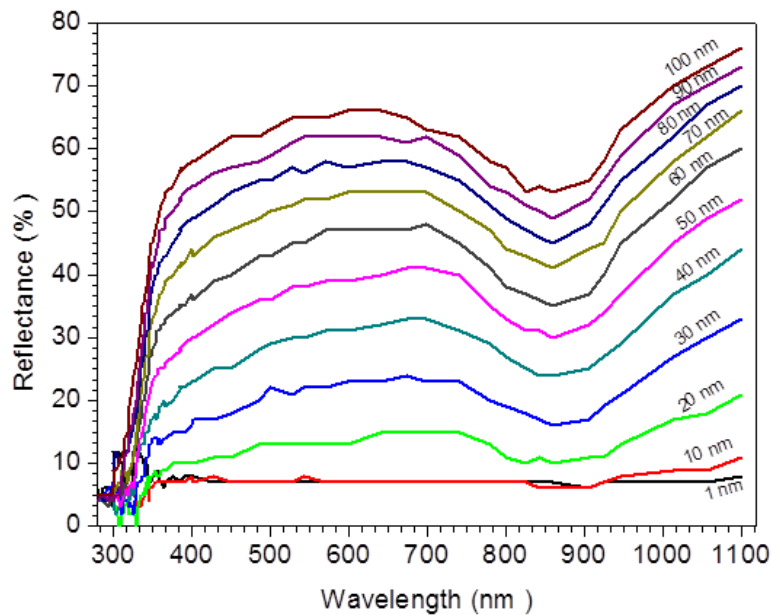


Figure 3.4: Simulations illustrating the dependence of the optical  $R$  of multilayered thin film structures with fixed upper and lower ZnO thicknesses of 50 nm and different mid-Al layer thicknesses captioned on each curve.

The results of the optical simulations obtained from multilayered ZAZ thin film composite structures with mid-layer Al thickness greater than 10 nm are also presented in Figures 3.2 – 3.4. These show the dependence of optical properties of the multilayered

ZAZ thin film composite structures on Al interlayer thicknesses with upper and lower ZnO film layer thicknesses of 50 nm. The results show that, with further increase in Al interlayer thicknesses, the T decreases strongly. This can be attributed to the high absorptive and reflective nature of metallic Al. Further increase in the thickness of mid-Al layer leads to increased values of A (Figure 3.3) and R (Figure 3.4). Hence, at higher Al interlayer thicknesses above 10 nm, increasing Al mid-layer thicknesses results in a serious deterioration of the effective multilayered ZAZ thin film transmission quality (Figure 3.2).

However, as shown in Figures 3.3 and 3.4, for mid-layer Al thicknesses of  $\sim 1 - 10$  nm, the R and A values are low. Also, in this mid-layer Al thickness range, the visible A and R values (not shown in this section) were less significantly affected by changes in mid-Al layer thicknesses. This suggests that, minimum mid-Al layer thicknesses between  $\sim 1$  nm and 10 nm are of major importance for the effective optical designs of layered thin film composites. These are required for the optimum optical performance of the multilayered ZAZ thin film sandwiches in TE coatings. Within this range, the minimum and maximum visible spectra Ts of the model multilayered ZAZ thin film structures are between 68 and 91% of the incident photons.

### **3.3.2 Effects of ZnO Thickness on the Optical Properties of ZAZ Film**

The dependence of the optical properties of multilayered ZAZ thin film composite stacks on the thickness of the ZnO layers is presented in Figure 3.5. The results show that the optical T, A and R values of the multilayered ZAZ thin film composite structures are not significantly affected by the thickness of the ZnO layers between  $\sim 10 - 100$  nm. In

this range, for multilayered ZAZ thin film composite structures with fixed mid-layer Al thickness of 5 nm, the transmission output characteristics are almost independent of ZnO layer thickness between  $\sim 10 - 100$  nm (Figure 3.5). These can be attributed to the characteristically lower absorption and reflection coefficients of ZnO, compared to those of Al,<sup>[196]</sup> and based on equations (3.4) and (3.7). This leads to the observed low absorption and reflection characteristics with increasing ZnO-layer thicknesses between 10 and 100 nm.

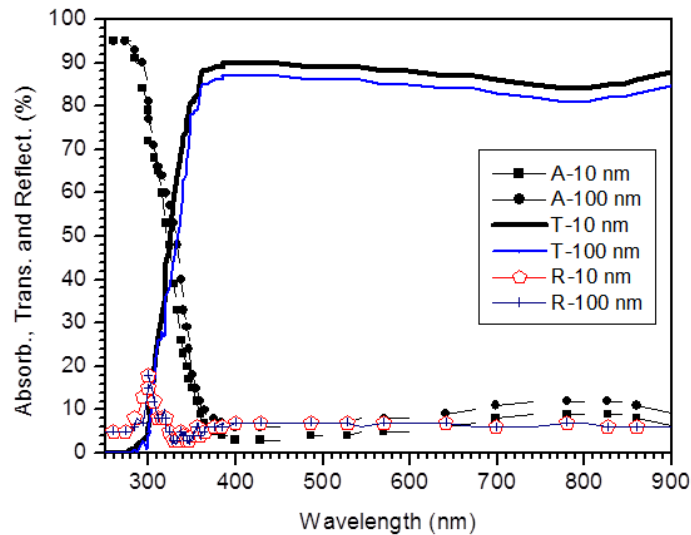


Figure 3.5: Simulations illustrating the effects of ZnO layer thicknesses between 10 – 100 nm on the optical characteristics of multilayered ZAZ thin film composite structures. Each of the lower and upper ZnO layer thicknesses were varied between 10 – 100 nm with mid-Al layer thickness fixed at 5 nm.

### 3.3.3 Average Optical Properties of Model Multilayered ZAZ Films

For each Al interlayer thickness that was embedded between ZnO layers (Figures 3.2 – 3.4), the average optical Ts, As and Rs in the visible region of the solar spectrum

were determined (note that upper and lower ZnO layers had thicknesses of 50 nm). The results are presented in Figure 3.6. These prove further that only ultra-thin mid-layer Al thicknesses are of major importance for the effective optical performance of multilayered ZAZ thin film composite stacks in TE coatings. For multilayered ZAZ thin film composite structures with mid-layer Al thickness between  $\sim 1 - 10$  nm, the predicted average visible solar T spectra are between  $\sim 75 - 90\%$ . Furthermore, Figures 3.2 – 3.6 suggest that, the optical properties of the multilayered ZAZ thin film composite stacks are largely determined by the optical constants of the Al interlayer, instead of those of the embedding ZnO layers.

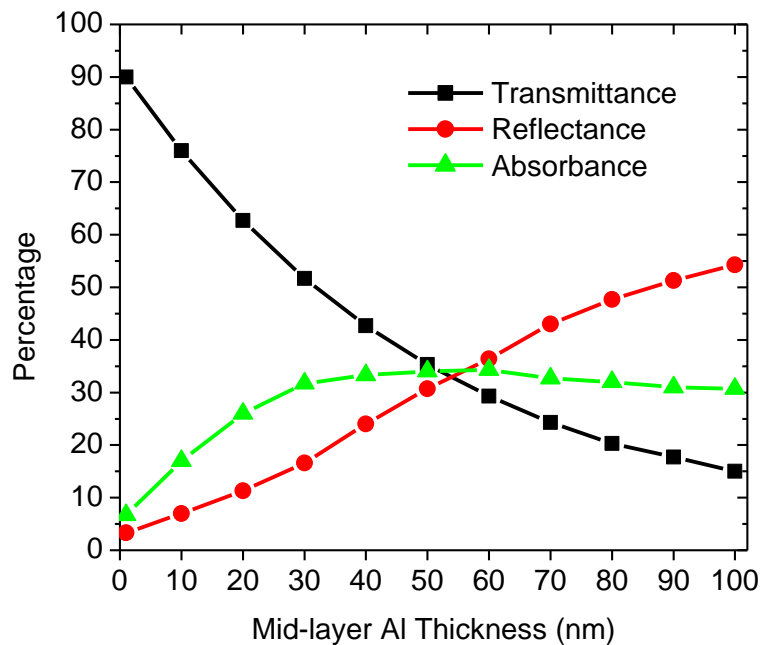


Figure 3.6: Percentage averages of optical A, R and T of multilayered ZAZ thin film composite structures with ZnO double-layers with thicknesses of 50 nm each and mid-layer Al thicknesses varying between  $\sim 1 - 100$  nm.

### 3.4 Concluding Remark

This chapter presents the results of the numerical simulations of the optical properties of multilayered ZAZ thin film composite structures on transparent glass substrates. Optical simulations were carried out for composite structures with ZnO and Al interlayer thicknesses between  $\sim 1 - 100$  nm. The results suggest that lower thicknesses of Al intermediate layer result in improved spectral Ts of the model multilayered ZAZ thin film composite structures. Multilayered ZAZ thin film composite structures with optimal ranges of mid-layer Al thicknesses between  $\sim 1 - 10$  nm are shown to have average visible T spectra between  $\sim 75 - 90\%$ . These values are within the desirable visible optical T spectra ranges that are needed in TE coatings for applications in organic solar cells, light emitting diodes and other electronics and optoelectronic devices. It is clear that the optical T increases as the thickness of the mid-Al layer decreases. However, the need for reasonable electrical conductivity of the ZAZ composite requires a non-zero thickness for the Al layer. An optimal value for this thickness that gives a high value for both the optical transmission T and the electrical conductivity still need to be determined.

Furthermore, experimental work is clearly needed to ascertain the optical and electrical characteristic performances of the real multilayered ZAZ thin film composite stacks. Such actual multilayered ZAZ thin film composite structures with appropriate numerically predicted optimum mid-Al layer thicknesses between  $\sim 1 - 10$  nm should be prepared on rigid transparent glass substrates before testing their optical and electrical characteristics.

# **4. Chapter Four**

## **Optical and Electrical Properties of Multilayered ZAZ Thin Film Composites for Applications in Transparent Electrode Coatings**

### **4.1 Introduction**

The numerical equations that govern the phenomenology of light transport and the simulations of the optical properties of multilayered ZAZ thin film composite stacks were discussed in chapter 3. These were also used to establish the optimum mid-layer Al thickness range at which the multilayered ZAZ thin film composite structures can attain practical visible solar T spectra, that are sufficiently high for applications in TEs in solar cells and light emitting devices. However, the numerical simulations cannot be used to ascertain how the optical and electrical properties of actual multilayered ZAZ thin film composite structures will change when the distinct ZnO and Al layers are put together in physical interactive contacts. It is also curious to test the reproducibility and validity of the optical properties and the interlayer thicknesses of the multilayered ZAZ thin film composite structures that were predicted by numerical modeling and simulations (chapter 3). Furthermore, it is important to check the reliabilities of the material parameters and the numerical conditions that were assumed in the models and simulations of multilayered ZAZ thin film composite structures.

Therefore, this chapter presents the results of a combined experimental, numerical and theoretical study of multilayered ZAZ thin film composite stacks. For this purpose, the structural, optical and electrical properties of multilayered ZAZ thin film composite

structures are investigated. First, the numerical study is used to clarify the role of mid-layer Al (with optimum thickness ranging between  $\sim 1 - 10$  nm) in a multilayered ZAZ thin film composite stack with fixed upper and lower ZnO-layer thicknesses of 25 nm. The simulation results obtained are then compared with experimental measurements in actual multilayered ZAZ thin film composite structures produced with similar mid-Al and ZnO interlayer thicknesses.

The transparent electrode characteristics of actual multilayered ZAZ thin film structures are presented. These include the structural, electrical and optical measurements, which showed that the multilayered ZAZ thin film composite stacks with optimum mid-Al layer thicknesses, between  $\sim 1$  and 10 nm, have resistivities as low as  $\sim 362 \mu\Omega \text{ cm}$  and high average Ts between  $\sim 85$  and 90% (in the visible region of the solar spectrum). In addition, the highest Haacke figure of merit of  $4.72 \times 10^{-3} \Omega^{-1}$  was obtained in a ZAZ thin film composite structure with mid-layer Al thickness of 8 nm.

The effective optical bandgap energies of the multilayered ZAZ thin film composite structures increased by  $\sim 0.60 \text{ eV}$  for mid-layer Al thicknesses between  $\sim 1 - 10$  nm. The observed shifts in the optical absorption edges to shorter wave lengths of the solar spectrum are shown to be in agreement with the Moss-Burstein effect.<sup>[197]</sup> The electrical and optical properties of multilayered ZAZ thin film composite structures produced are also shown to be comparable to the optoelectronic performance characteristics of the conventionally standard ITO-coated TCO substrates.

## 4.2 Methods

### 4.2.1 Simulations of ZAZ with Ultra-thin Mid-Al Layer Thicknesses

For the simulations of multilayered ZAZ thin film composite structures with optimal mid-Al layer thicknesses, the numerical method in chapter 3 was used in this chapter. While the thicknesses of the upper and lower ZnO layers were each purposely set to be 25 nm, the thickness of mid-layer Al was controlled to be very thin between ~ 1 – 10 nm. The latter thicknesses were selected based on the optimum visible solar T spectra results suggested by the optical simulations in chapter 3.

### 4.2.2 Experimental

#### 4.2.2.1 Experimental Procedure

The multilayered ZAZ thin film composite structures were fabricated on rigid transparent substrates ( $2.5 \times 2.5 \text{ cm}^2$  glass slides) that were procured by Mark Optics Inc., Santa Ana, CA, USA. These were thoroughly washed with dilute DeCON 90 neutral liquid detergent, rinsed in de-ionized water, ultrasonically cleaned in acetone and isopropyl alcohol (IPA) and blow-dried in nitrogen. The thoroughly cleaned substrates were then transferred to the RF MS deposition chamber of a dual-cathode Edwards Auto 306 MS system with a RF generator of 13.56 MHz (Edwards Limited, Crawley, Sussex, UK). All of the multilayered ZAZ thin film composite structures were fabricated from a ZnO ceramic target (99.9% purity) and Al metallic target (99.999% purity, Target materials Inc., Columbus, Ohio, USA), each with a diameter of 10 cm.

The two cathodes were adequately isolated to avoid cross contaminations. Before deposition and prior to the introduction of argon (Ar), the RF MS chamber was pumped down to below  $3 \times 10^{-5} \text{ Torr}$ . Sequential RF MS deposition was then carried out in a

pure argon atmosphere (at pressures between  $\sim 6.0 - 7.5 \text{ mTorr}$ ) to achieve multilayered ZAZ thin film composite structures. All depositions were done at room temperature ( $\sim 25^\circ\text{C}$ ). There was no external heating of substrates during the deposition process. Furthermore, the metal back-plate on the substrate was externally cooled using a Grant 3000G recirculating water chiller with the temperature set at  $25^\circ\text{C}$ .

First, the reliability of the set-up and RF MS deposition parameters was investigated by depositing multilayered ZAZ thin film composite stacks with identical thicknesses. This was achieved using different RF MS generator power levels between  $\sim 50 - 100 \text{ Watts}$  and  $\sim 100 - 500 \text{ Watts}$ , for ZnO and mid-Al layers, respectively. Preliminary x-ray diffraction (XRD) analyses revealed that all of the multilayered ZAZ thin film composite structures produced were amorphous at room temperature.

In order to improve the properties of the multilayered ZAZ thin film composite structures, a detailed post-deposition treatment of the samples was undertaken. This involved thermal annealing of the multilayered ZAZ thin film composite structures at temperatures of  $\sim 250 - 400^\circ\text{C}$  and for durations between  $\sim 1 - 4$  hours. Annealing at temperatures greater than  $300^\circ\text{C}$  resulted in the formation of the preferred Wurtzite c-axis (002) oriented ZnO crystallites. As shown in Figure 4.1, the best crystalline structure was observed in multilayered ZAZ thin film composite structures that were deposited using power densities of  $2.27 \text{ W cm}^{-2}$  (100 W) and  $5.10 \text{ W cm}^{-2}$  (400 W) for the ZnO and the mid-Al layers, respectively, and annealed at  $400^\circ\text{C}$  for 90 minutes in air. The optimum process parameters are summarized in Table 4.1.

Subsequently, for all of the multilayered ZAZ thin film composite structures that were examined, the RF MS process parameters given in Table 4.1 were chosen for the

deposition and post-deposition treatment. The reproducibility of the results was also investigated in order to examine the effect of the optimum mid-layer Al thickness on the TE properties of the multilayered ZAZ thin film composite structures. The mid-layer Al thickness was varied between  $\sim 1 - 10$  nm in accordance with optimal visible solar transmittance spectra results suggested by the numerical simulations of chapter 3.

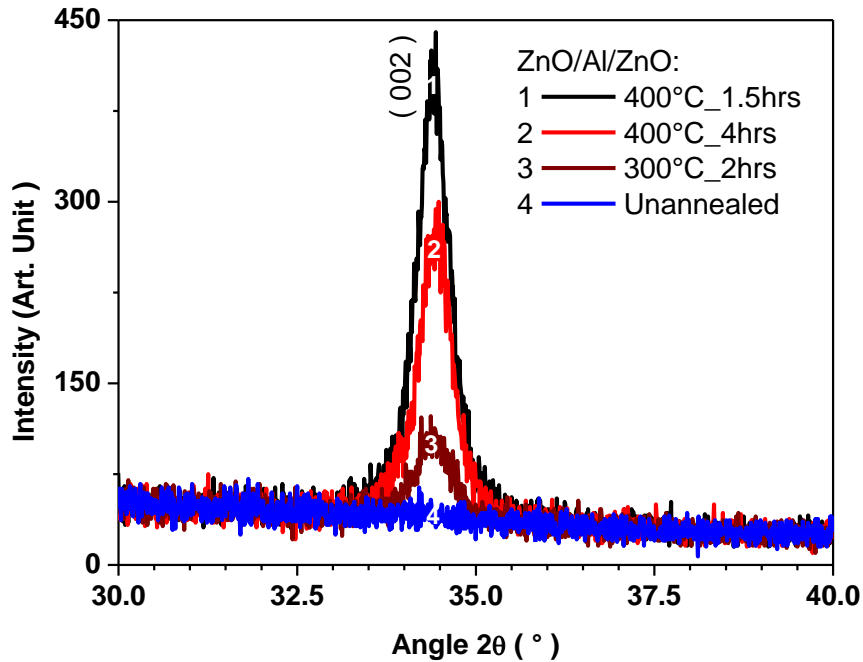


Figure 4.1: XRD patterns demonstrating the dependence of crystallinity on thermal annealing conditions for a multilayered ZnO(25 nm)/Al(3 nm)/ZnO(25 nm) thin film composite structures. These were obtained using RF MS deposition power densities of  $2.27 \text{ Wcm}^{-2}$  and  $5.10 \text{ Wcm}^{-2}$  for ZnO and mid-Al layers, respectively.

The deposition rates and the effective layer thicknesses of the multilayered ZAZ thin film composite structures were measured *in-situ* (during the deposition) using an Inficon thin film deposition controller. Subsequently, after deposition, all multilayered

ZAZ thin film composite samples were annealed at 400°C for 90 minutes in a Carbolite tubular furnace (Carbolite Ltd., Model CTF, HV, UK). After annealing, the thicknesses of the multilayered ZAZ thin film composite structures were checked and confirmed by profilometry measurements with a Veeco Dektak 150 Stylus surface profiler (Bruker Instruments, Santa Barbara, California, USA). The surface roughness of the resulting multilayered ZAZ thin film composite structures was also tested with a Hysiton T-750Ubi Nano-indenter in the scanning probe microscope (SPM) mode and also using the above surface profilometry measurements.

Table 4.1: Process parameters for the deposition of ZAZ multilayer Film stacks

Parameter	ZnO	Al
Purity	99.9%	99.999%
Layer Thicknesses	25 nm	1 – 10 nm
Residual pressure	$(2.3 - 3.0) \times 10^{-5}$ Torr	
Deposition Pressure	6.0 – 7.5 mTorr	
RF power	100 W	400 W
Power density	1.27 Wcm <sup>-2</sup>	5.10 Wcm <sup>-2</sup>
Substrate temperature	25 – 60°C	25 – 65°C
Target-substrate distance	3.5 cm	3.5 cm
Annealing process	400°C for 90 minutes	

#### 4.2.2.2 Characterization Techniques

##### 4.2.2.2.1 The Crystalline Structure of the Obtained ZAZ Multilayer Films

Prior to electro-optical characterization, the structural properties of the multilayered ZAZ thin film composite stacks obtained were studied with the XRD technique. The XRD, which uses a collimated beam of x-rays<sup>[198]</sup> presents a powerful scientific tool for structural analyses and characterization of materials. The XRD systems

contain sources of monochromatic x-rays. During operation, the monochromatic x-rays are made to irradiate and interact with the sample before they are diffracted at the characteristic atomic planes of the crystalline phases of the material sample under analysis. The diffracted beam of x-rays containing the structural characteristics and the other physical information of the material are then detected for further analyses.

The monochromatic x-rays are electromagnetic (EM) waves with characteristic wavelength  $\lambda$  in the range of very small fractions of nanometres between  $\sim 0.5 - 2 \text{ \AA}$ .<sup>[198]</sup> Note that these  $\lambda$  values are very small and comparable to the inter-planar spacing of different material crystals. This makes XRD a very powerful and widely used technique for determination of crystal structures and other physical characteristics of materials. Some of the typical applications of the XRD technique include: identification of phase composition, distribution of polycrystalline and/or amorphous phases and materials purity analyses. XRD measurement is also a widely used technique for lattice constant analyses, strain measurements, determination of film thicknesses, probing of sample concentration profiles, detection of degree of crystallinity, analyses of epitaxial and atomic arrangements in amorphous and/or multilayered materials.<sup>[198]</sup>

In terms of its working principle, the XRD system uses Bragg's diffraction condition (equation 4.1) to capture the structural and physical information in the crystals of materials (Figure 4.2). At first, the x-ray beams (from the x-ray tube inside the XRD systems) are made to pass through a monochromator, before penetrating and interacting with the sample. The portion of these monochromatic EM (x-ray) waves is reflected at each plane of atoms in the crystals of the material under test. The reflected waves (from different planes) are then made to interact with each other. During the interactions, any

constructive interferences that occur results to diffracted beams occurring at well-defined angles,  $2\theta$  (Figures 4.2 and 4.3).

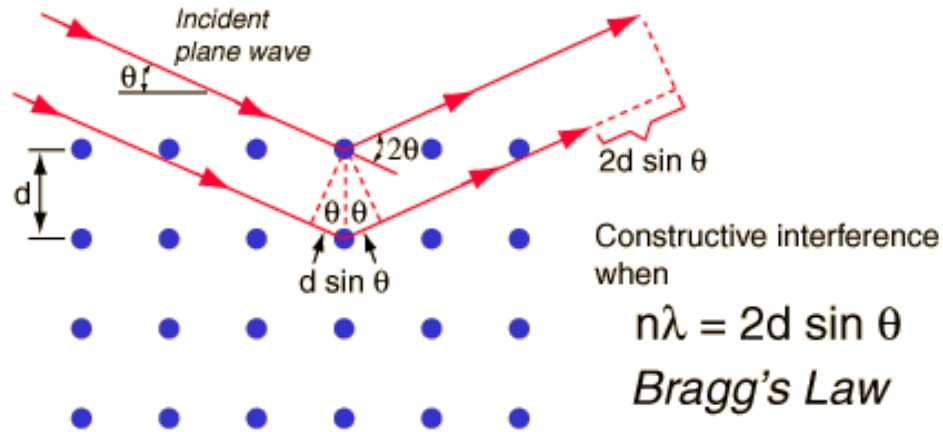


Figure 4.2: Condition (path-length difference) for the maximum (preferred crystal-orientations) intensity contained in the Bragg's law. The angle of diffraction of x-rays by the crystalline atomic planes gives the structural characteristics of the crystal while the intensity of the scattered radiation signifies the characteristic information or the atomic composition of the crystalline material.

After diffraction, the diffraction angle,  $2\theta$ , the wave length of the x-ray radiations,  $\lambda$ , and the inter-planar separation,  $d$ , between the atomic diffraction planes of the crystals inside the material are all related through the Bragg diffraction criterion. This is given by:<sup>[198]</sup>

$$m\lambda = 2d\sin\theta \quad (4.1)$$

where  $m$  is the order of diffraction. Subsequently, from the Bragg's diffraction condition (equation 4.1), the different structural and physical properties such as the different phases that are present in a particular specimen of materials can be deduced and displayed depending on the operational mechanism of a given XRD system.

In this study, the XRD experiments were carried out using a Xpert-Pro MPD XRD system (PANalytical BV., Almelo, Netherlands) with a  $Cu K_{\alpha 1}$  anode radiation ( $\lambda \sim 0.1541$  nm), in the grazing incidence mode. The XRD was used for the determination of phase purity and crystallinity of the synthesized multilayered ZAZ thin film composite stacks. The experimental conditions for an applied voltage and current were set to 45 kV and 40 mA, respectively. The XRD measurements were taken for a conventional scan with fixed angle of incidence of  $5^\circ$  and  $2\theta$  angle varying between  $10 - 95^\circ$ .

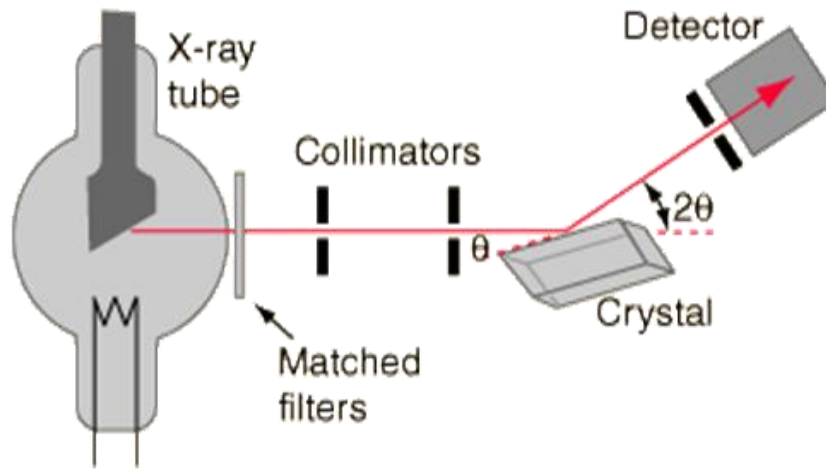


Figure 4.3: Schematic diagram illustrating the operation principle of XRD system.<sup>[198]</sup> As long as the wave length of the x-rays impinging upon the crystal is known, the obtained XRD data allow for the determination of the material crystal structure. If the crystal structure is known, the XRD information allows the identification of the phase composition of a given material.

#### 4.2.2.2.2 Optical Characterization

The dependence of optical T and R spectra of the multilayered ZAZ thin film composite structures on the mid-layer Al thickness were studied by spectrophotometry

measurements. The optical spectrophotometers are designed to use light transport theories (equations 3.1 – 3.8) to measure the optical properties (A, R and T) of materials. In this study, the optical T and R spectra of the multilayered ZAZ thin film composite stacks produced were investigated. This was done as function of wave length in the range of up to ~ 1200 nm. The optical measurements were achieved using an Avantes UV-Vis optical spectrophotometer (Avantes Inc., Broomfield, USA).

#### 4.2.2.2.3 Electrical Characterization

The electrical characteristics of the multilayered ZAZ thin film composite structures (with optimum mid-layer Al thicknesses between ~ 1 – 10 nm) were measured using a Signatone 4-point probe system having a Keithley 2400 source measure unit (Keithley Instruments Inc., Cleveland, OH, USA). In terms of operation principle, the Signatone system contains four equally spaced pins (Figure 4.4). These were used to probe the surface of the ZAZ thin film composite structures. The contacts between the probes and the surface of the multilayered ZAZ thin film composite samples were adequately secured to ensure non-rectifying *Ohmic contacts* (with linear current–voltage characteristics) between the probes and the surface of the multilayered ZAZ thin film composite structures.

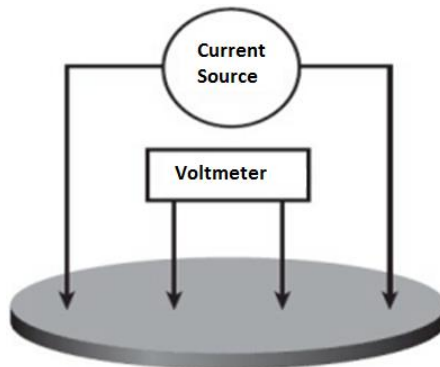


Figure 4.4: Schematics illustrating the head of a Signatone four-point probe system.

During operation, a current source unit produces a fixed current,  $I$ . As shown in Figure 4.4, this current is then made to flow through the two outer pins. The potential difference,  $V$ , created by the flow of the current is measured across the two inner pins (Figure 4.4). The flow of the current inside the sample follows generally a spherical path, such that the resistivity,  $\rho$ , of a given specimen can readily be deduced. This is given by:

$$\rho = 2\pi s \frac{V}{I} \quad (4.2)$$

where  $s$  is the spacing between the probing pins of the Signatone four-point probe system.

However, for thin film materials the thickness,  $t$  of the sample is generally very small compared to the spacing between the probing pins,  $s$ , of a four-point system. This makes the current flowing from the two outer probes to assume circular paths (Figure 4.5) instead of the spherical paths. This implies that, the electrical properties of thin film samples do not necessarily depend on the spacing,  $s$ , between the probes of the 4-point equipment. Thin film electrical properties are, thus, determined merely by the thicknesses of the thin film samples under test. Therefore, for thin film materials, the resistivity equation (4.2) can be modified using the thickness of the thin film sample. This leads to:

$$\rho = \frac{\pi t}{\ln 2} \left( \frac{V}{I} \right) \quad (4.3a)$$

Equivalently, taking the inverse of resistivity (equation 4.3a), the conductivity,  $\sigma$ , of thin film samples is obtained. This is given by:

$$\sigma = \frac{\ln 2}{\pi t} \left( \frac{I}{V} \right) \quad (4.3b)$$

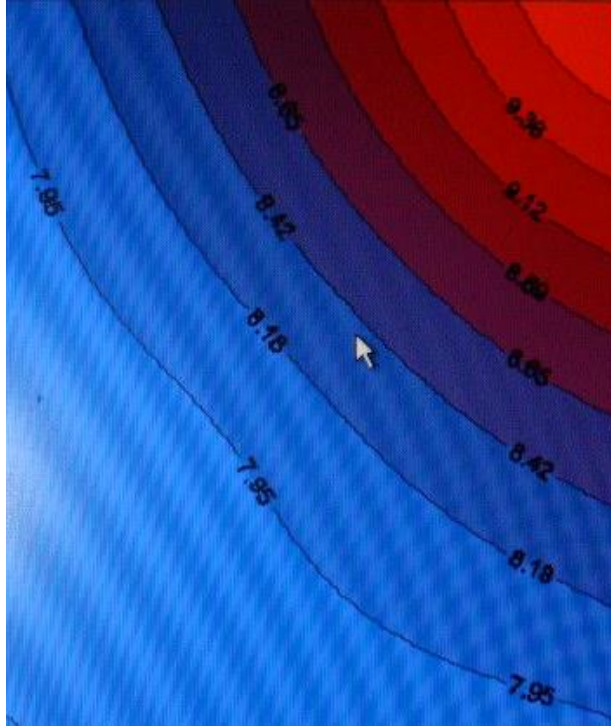


Figure 4.5: Snapshot of a computer screen showing the cross section of a 2D contour map for sheet resistance of a multilayered ZAZ thin film composite structure with mid-Al layer thickness of 9 nm and ZnO double-layer thickness of 25 nm each.

Similarly, the electrical sheet resistance ( $R_s$ ) can be used for the characterization of the electrical properties of multilayered ZAZ thin film composite structures. This is calculated from a ratio of sheet resistivity (equation 4.3a) to the thickness of the multilayered ZAZ thin film composite sample that is being characterized. The sheet resistance of thin film samples is, therefore, given by:

$$R_s = \frac{\pi}{\ln 2} \left( \frac{V}{I} \right) \quad (4.3c)$$

#### 4.2.2.2.4 Effective Electrical Properties of ZAZ Multilayer Films

The effective electrical properties of the multilayered ZAZ thin film composite structures were determined largely by the conductive characteristics of the mid-Al layer.

This forms a combined effective parallel sheet resistance with the upper and lower ZnO layers. The parallel circuitry was accomplished when the pins of the 4-point probe system were secure enough to penetrate through and touch all the layers of the multilayered thin film composite structure.<sup>[104]</sup> This made the entire multilayered ZAZ thin film composite structure equivalently to an electric circuitry of three different (two ZnO layers and the mid-Al layer) resistors connected in parallel. This is illustrated in Figure 4.6.

Hence, assuming a multilayered ZAZ thin film composite structure with planar-interfaces and pure physical interactions (ignoring any form of chemical interferences) between ZnO and mid-Al layers, the combined sheet resistance,  $R_s^M$ , of the multilayered ZAZ thin film composite stacks was theoretically predicted. This was obtained from:

$$R_s^M = \frac{R_s^Z R_s^A}{2R_s^A + R_s^Z} \quad (4.4a)$$

Since the sheet resistance,  $R_s^A$  of the mid-Al layer was very small, compared with the sheet resistance,  $R_s^Z$  of the ZnO layers, the overall sheet resistance,  $R_s^M$  of the multilayered ZAZ thin film composite structure was largely dominated by the  $R_s^A$ . Thus,

$$R_s^M = \frac{R_s^Z R_s^A}{2R_s^A + R_s^Z} \underset{R_s^Z \gg R_s^A}{\approx} R_s^A \quad (4.4b)$$

Equivalently, the effective electrical resistivity of the multilayered film structures can be readily deduced from the sheet resistance of the multilayer structures above (equation 4.4b). The theoretical derivation of effective resistivities of multilayered film structures as function of the respective interlayer thicknesses was reported earlier by Kloppel and coworkers.<sup>[104]</sup>

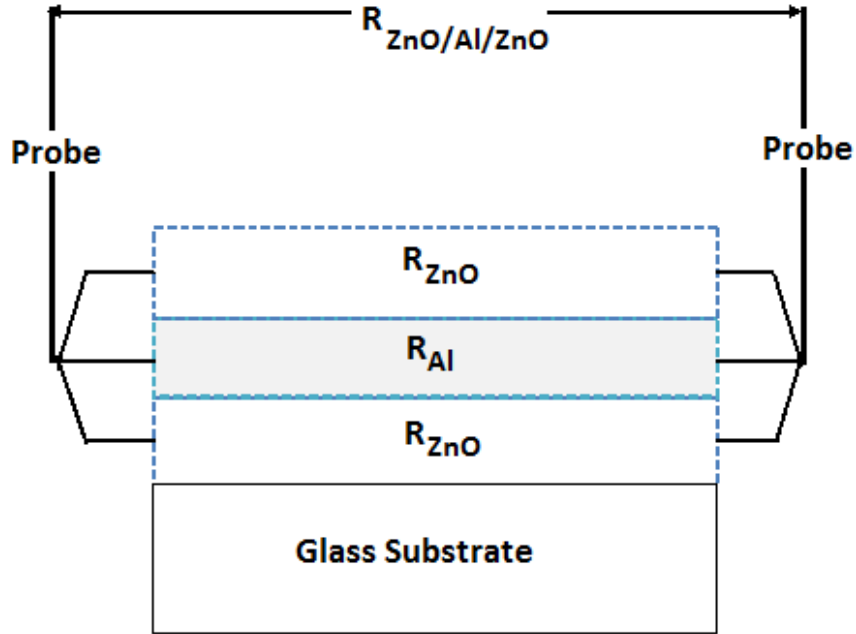


Figure 4.6: Schematics of the multilayered ZAZ thin film composite structure with effective sheet resistance,  $R_s$  ( $R_{ZnO/Al/ZnO}$ ), represented as a parallel combination of sheet resistances of the discrete layers of ZnO and mid-Al in an electric circuitry.

Note that, equation (4.4b) suggests that the thicknesses of mid-Al and ZnO layers (within the multilayered ZAZ thin film composite stacks) can be controlled to result in multilayered ZAZ thin film composite structures with effective sheet resistance values that are comparable to those of the mid-Al layers. This partly explains why the different multilayered ZnZ thin film composite systems have been with good optoelectronic figure of merit values that are better than those of single nanolayers of doped transparent ZnO or ultra-thin transparent metallic thin films.<sup>[99,101]</sup> This also explains the improvements of electrical properties that have been observed in other multilayered composite thin film stacks such as those that are based on IMI systems.<sup>[102-108]</sup>

The thicknesses of multilayered ZAZ thin film composite samples produced in this study were obtained from profilometry measurements. The effective thicknesses of

most of the multilayered ZAZ thin film composite structures produced were between  $\sim 52.5 - 62.5 \text{ nm}$ . Consequently, the resistivities of the multilayered ZAZ thin film composite structures were readily analyzed with a model 4200 SCS Keithley Signatone 4-point probe system (Keithley Instruments Inc., Cleveland, OH, USA).

## **4.3 Results and Discussion**

### **4.3.1 Crystal Properties of ZAZ Multilayer Film Composites**

Figure 4.7 presents the XRD patterns of the annealed multilayered ZAZ thin film composite stacks with different mid-layer Al thicknesses between 3 – 8 nm. The results show that the multilayered thin film composite structures are multi-crystalline. This is in good agreement with the published crystalline structure of a c-axis (002) oriented hexagonal Wurtzite XRD patterns for ZnO thin films,<sup>[76,86,90,110]</sup> without the mid-layer Al phase. The XRD technique was, therefore, not able to resolve the mid-Al layers (between  $\sim 1 - 10 \text{ nm}$  thick) as the secondary phases. For comparison, the XRD pattern obtained from a single layered 50 nm thick ZnO film (after annealing at the same temperature and dwelling time) is also shown in Figure 4.8 (a). These show the effect of mid-layer Al thickness ranging between  $\sim 1 - 10 \text{ nm}$ . These are sandwiched between the upper and lower ZnO layers (each with a thickness of 25 nm). The results suggest that the mid-Al layer (in the range of  $\sim 1 - 10 \text{ nm}$ ) is too thin to be resolved by the XRD.

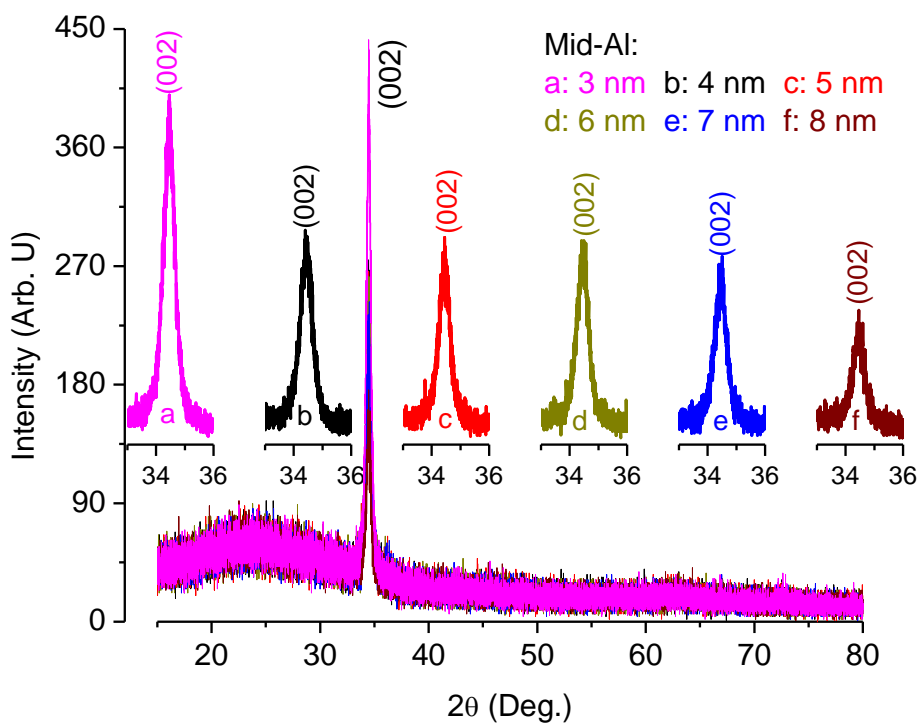


Figure 4.7: XRD patterns of multilayered ZAZ thin film composite structures with ZnO double-layer thicknesses of 25 nm. The inserts indicate the relative dependence of the preferred (002) oriented peak intensity on the different mid-Al layer based on the captioned thicknesses. These patterns were obtained after annealing the multilayered ZAZ thin film composite structures for 90 minutes at 400°C in air.

However, as the mid-layer Al thickness increases between  $\sim 1 - 10$  nm, the peak height of the preferred (002) orientation decreases. As shown in Figure 4.7 (for the multilayered ZAZ thin film composite structures with mid-Al layer thicknesses between 3 – 8 nm), a decrease of the preferred (002) oriented peak intensity was observed, with increasing mid-layer Al thickness. This change in the relative intensity of the c-axis XRD peak, by the introduction of mid-Al layers implies that the crystallinity of the multilayered ZAZ thin film composite structures decreases as the mid-layer Al thickness increases. It also suggests that the electro-optical properties of the multilayered ZAZ thin

film stacks are increasingly altered<sup>[199]</sup> by the introduction of thicker Al interlayers. Figures 4.8 (a) and 4.8 (b) show the respective XRD structure and optical transmission of a single layered 50 nm thick ZnO on glass. Clearly, the introduction of mid-Al layers led to decrease in the crystallinity as well as slight decrease in the optical transmission of the ZnO.

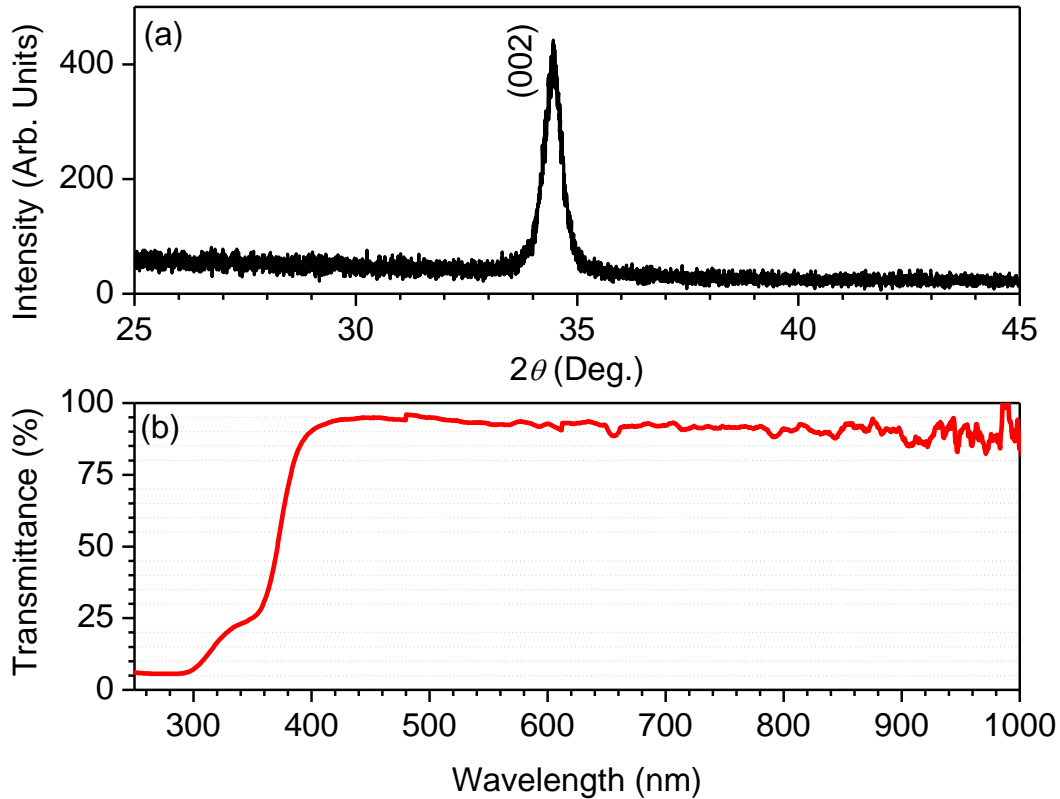


Figure 4.8: (a) XRD pattern and (b) optical T profile of a 50 nm thick ZnO thin film deposited on rigid transparent glass after annealing for 90 minutes at 400°C in air.

The observed decrease in the crystallinity of multilayered ZAZ thin film stack (with increasing mid-layer Al thickness) can be attributed to changes in the physical and the electronic structure of the multilayered ZAZ thin film composite stacks, which lead to

the deviation of ZnO from stoichiometry. This can occur due to the defects that influence the crystal structure of materials. Such defects may be due to excess charge carrier concentration from mid-Al layer, since the charge carrier mobility in the multilayered ZAZ thin film composite structure is lower than that in the corresponding bulk materials.<sup>[80]</sup> In the case of the conventionally Al doped ZnO thin films that are produced by combining known moles of ZnO and Al, the defect structure and the associated non-stoichiometric oxides that are formed can readily be predicted.<sup>[68]</sup>

However, contrary to the conventionally doped TCO thin films, the exact nature of the defect structure and non-stoichiometric oxides formed by thermal treatments of the multilayered thin film composite structures have not yet established. Hence, an acceptable quantitative determination for the observed decrease in crystallinity of multilayered ZAZ thin film composite stack with increasing mid-layer Al thickness (at a fixed annealing temperature of 400°C) is uncertain. This suggests the need for a simultaneous study of structural and electrical properties of multilayered ZAZ thin film composite structures. Such studies should explore the dependence of n-type charge carrier (electron) density and mobility on the annealing temperature, mid-Al layer metallurgical, and the physical and optical properties of the multilayered ZAZ thin film composite stacks with different ranges of ZnO and Al interlayer thicknesses.

## **4.3.2 Optical Properties of Model ZAZ Multilayer Film**

### **4.3.2.1 Transmittance of ZAZ Multilayer Thin Film Stacks**

The optical properties of the multilayered ZAZ thin film composite structures were measured as a function of the mid-layer Al thickness between ~ 1 – 10 nm. The solar T spectra (in the visible region for the multilayered ZAZ thin film composite stacks

with different mid-layer Al thicknesses) are presented in Figures 4.9 (a) – 4.9 (d). For comparison, the solar T profile obtained from a single layered 50 nm thick ZnO film (after annealing in air at 400°C for 90 minutes) is also presented in Figure 4.8 (b). Increasing the mid-layer Al thickness between ~ 1 – 10 nm had only a slight effect on the T spectra characteristics of the multilayered ZAZ thin film composite structures.

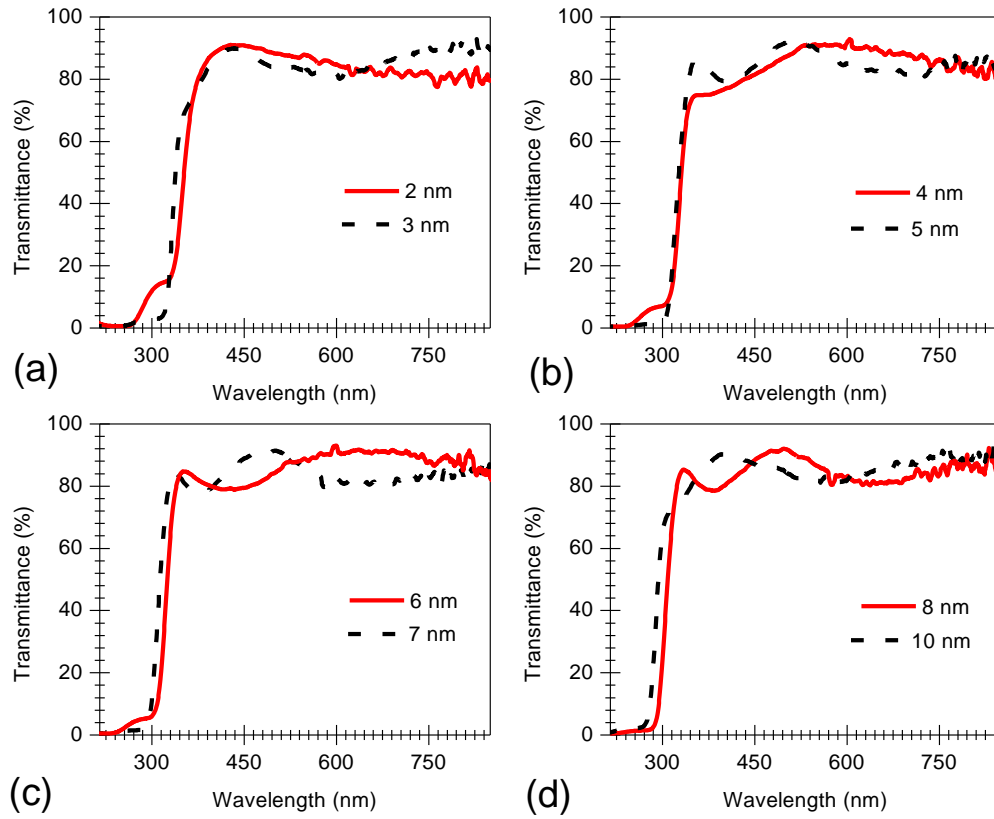


Figure 4.9: Solar T curves in the visible region of the spectrum obtained from annealed multilayered ZAZ thin film composite structures with upper and lower ZnO layers, with 25 nm each and mid-Al layer thicknesses captioned in the plots.

The observed decrease in the optical T spectra of the multilayered ZAZ thin film composite structure (with increasing mid-layer Al thicknesses) can be attributed to

several factors. These include reflection losses that comprise both diffuse and specular scattering phenomena that arise mainly from interlayer surface roughness and interfacial defects. These defects arise from reacted and/or unreacted chemical species, including other oxide phases, trapped gases and some impurities or inclusion atoms generated during the non-ideal processing of the multilayered ZAZ thin film composite structures.

#### **4.3.2.2 Reflectance of Multilayered ZAZ Thin Film Stacks**

Figure 4.10 presents the visible solar R profiles obtained from the multilayered ZAZ thin film composite structures. The result shows the other important causes of the decrease in T spectra of multilayered ZAZ thin film composite structures. The decrease depends on the thickness of mid-Al layer, as a result of its reflective nature and the multiple interference phenomena which require that the averages of the visible solar T spectra must be taken by the spectrophotometer used.<sup>[190]</sup> Furthermore, the T in the multilayered ZAZ thin film composite structures is decreased by multiple light absorptions, which may occur primarily due to the increasing free charge-carrier density<sup>[80]</sup> from the mid-Al layer.

Nevertheless, the average transmitted fraction of the incident photons in the multilayered ZAZ thin film composite structures (with mid-layer Al thickness ranging between ~ 2 – 10 nm) is generally very good, that is between ~ 85 and 90% in the visible region of the solar spectrum with wave lengths between ~ 400 – 900 nm (Figure 4.9). These high T values (in the visible region of the solar spectrum) are generally desirable for the optical performance of TCE coatings. They are attributed to the reductions in optical reflection (Figure 4.10) and optical absorption by the ultra-thin mid-Al layers that were sandwiched between the highly visible spectra transmitting layers of ZnO films.<sup>[80]</sup>

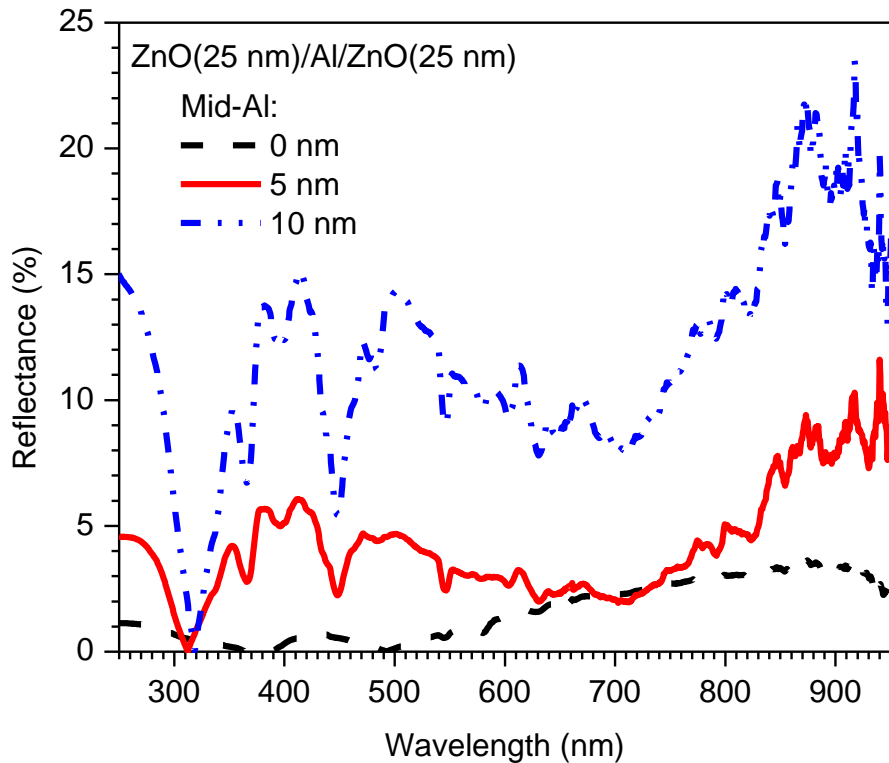


Figure 4.10: Visible R spectra for the annealed multilayered ZAZ thin film composite structures with ZnO layers of 25 nm thick each and mid-layer Al thicknesses based on 0, 5 and 10 nm.

Furthermore, the observed high T spectra in multilayered ZAZ thin film composite structures with relatively thick mid-Al layers (between  $\sim 6 - 10$  nm) can be attributed to the crystal characteristics of the multilayered ZAZ thin film composite structures shown in Figure 4.7. Clearly, with increasing mid-layer Al thickness, the light wave was less scattered because of the decreasing crystalline structure of the multilayered ZAZ thin film composite stacks. This resulted in higher solar Ts in the visible region of the spectra. Figure 4.9 also shows that, with increasing mid-layer Al thickness, the absorption limits of multilayered ZAZ thin film composite stacks are shifted to shorter

wave lengths. All of the absorption limits lie within the ultra-violet (UV) region of the solar spectrum.

### 4.3.2.3 Comparison of Multilayer ZAZ Simulations with Experiments

The numerical simulations of the optical properties and predictions of the optimal thicknesses for the design of multilayered ZAZ thin film composite structures were successfully demonstrated in chapter 3. In order to compare the numerical and experimental results, simulations were performed again on multilayered ZAZ thin film composite structures with ZnO double-layers with thicknesses of 25 nm each and Al interlayer thicknesses between  $\sim 1 - 10$  nm. Within this range, the numerical T results obtained (Figure 4.11) were compared with experimental solar T spectra of Figure 4.9 that were obtained from multilayered ZAZ thin film composite structures having similar ZnO and optimum Al interlayer thicknesses as in chapter 3.

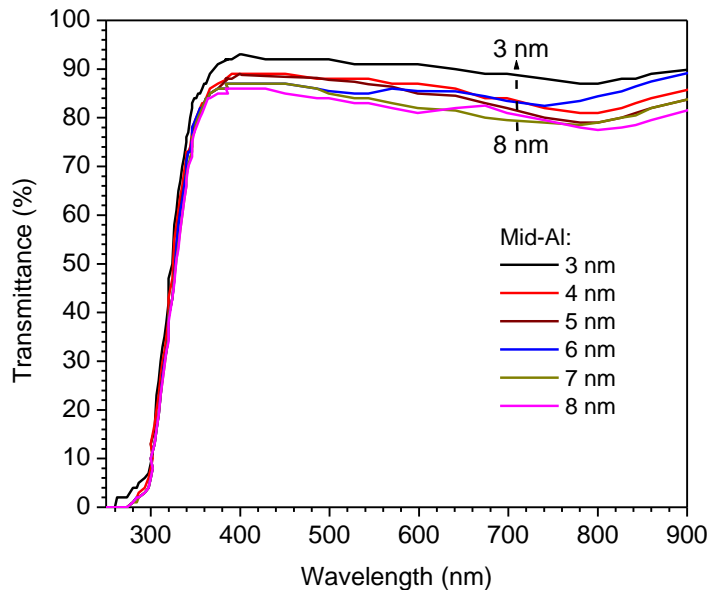


Figure 4.11: Simulated T curves illustrating the dependence of ZnO(25nm)/Al/ZnO(25 nm) multilayered thin film on the thickness of Al interlayer between 3 – 8 nm.

The simulated and experimental T spectra (in the wave length range of 250 – 900 nm for multilayered ZAZ thin film composite structures with different thicknesses of mid-Al layers between 3 and 8 nm) are presented in Figure 4.12. In this range, the average values of simulated and experimental solar Ts (in the visible region of the solar spectrum) are between ~ 80% and 85% (Figure 4.13). Note that, in agreement with the numerical simulations (Figures 3.2 and 4.11), the experimental Ts decreased slightly with increasing mid-layer Al thickness between ~ 1 – 10 nm (Figures 4.9 and 4.12). From Figure 4.11, it is observed that, for Al interlayer thicknesses between ~ 3 and 8 nm, the multilayer transmission efficiency is not significantly affected by changes in mid-Al layer thickness. For comparison, the T profile obtained from a 50 nm single layered thin film of ZnO on glass is reported in Figure 4.12 (a).

As shown in Figures 4.12 (a) – 4.12 (f), the correlation between the fits of numerical simulations to the experimental T profiles are generally very good. The slight differences observed in the high wave length regime (above 360 nm) are due the experimental minima and maxima in the T spectra. These are attributed to the effects of light oscillations at interfaces within the multilayered ZAZ thin film composite structures.<sup>[190]</sup> As discussed earlier, these can also occur as results of experimental artifacts and/or defects<sup>[190]</sup> in the multilayered ZAZ thin film composite samples due to the non-ideal deposition or post-deposition conditions used along with the unavoidable environmental interventions, since the multilayered ZAZ thin film composite structures were prepared in air.

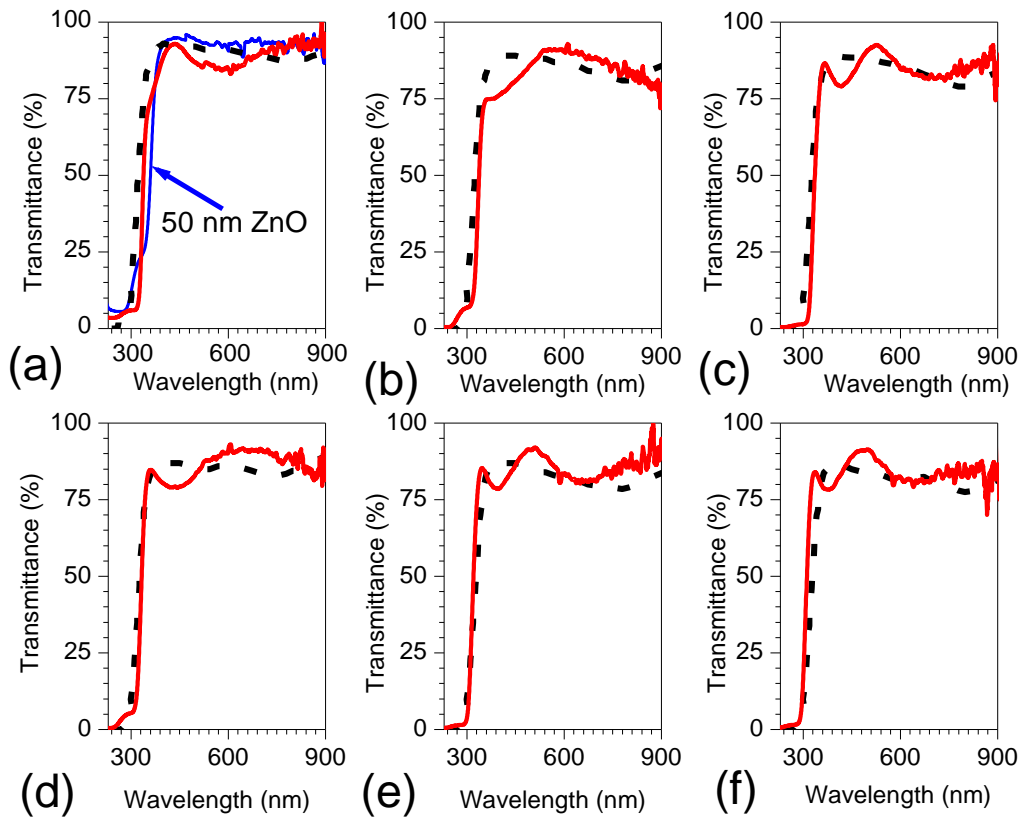


Figure 4.12: Experimental (solid) and simulated (dash) profiles illustrating the dependence of visible solar T spectra of the multilayered ZnO (25 nm)/Al/ZnO (25 nm) thin film composite structure on different Al interlayer thicknesses based on (a) 3 nm, (b) 4 nm, (c) 5 nm, (d) 6 nm, (e) 7 nm and (f) 8 nm. For comparison, the experimental T spectrum of a 50 nm ZnO film (without mid-layer Al) prepared on glass substrate is also shown as the blue curve in (a).

Consequently, due to experimental artifacts, defects and interventions from the ambient, the optical constants of the actual ZAZ interlayers may vary slightly from those of the stoichiometric ZnO and Al perfect crystal that were assumed in the model and the simulations of the multilayered ZAZ thin film sandwiches. The actual interfaces between

the ZnO and mid-Al layers may also vary slightly from the simulated planar-interfaces that were assumed for the multilayered ZAZ thin film composite stacks. Nevertheless, the predicted and experimental visible solar T spectra (Figure 4.12) were generally in excellent agreement across the entire range of wave lengths that was examined (for the multilayered ZAZ thin film composite stacks with ZnO double-layers with thicknesses of 25 nm each and Al interlayer thicknesses between  $\sim 1 - 10$  nm).

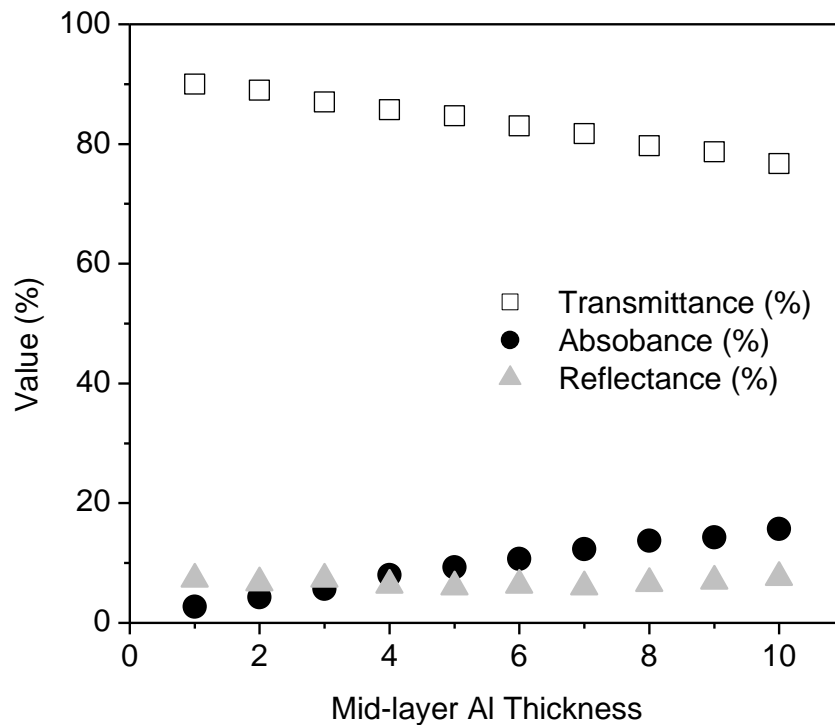


Figure 4.13: Average optical properties of ZAZ multilayer film stacks with ZnO double-layers with thicknesses of 25 nm and optimum mid-Al thickness between 1 – 10 nm.

The excellent agreement between the plots of experimental and numerical optical T spectra above, suggests that the actual experimental conditions were close to those assumed in the models and the simulations of multilayered ZAZ thin film composite

structures. Furthermore, due to large direct optical bandgap energy of ZnO (between  $\sim 3.2 - 3.4$  eV),<sup>80</sup> the ZnO layers are highly transmitting in the visible region of the solar spectrum.<sup>[80]</sup> This determines, ultimately, the shape of the transmission profiles and maintains high visible solar T values for the multilayered ZAZ thin film composite stacks (with thinner mid-layer Al thicknesses between 3 – 8 nm). In this range, the average values of simulated and measured visible T spectra are between  $\sim 80 - 85\%$  (Figure 4.13).

#### 4.3.2.3.1 Effects of Al Thickness on the Optical Bandgap of ZnO Films

Apart from high values of optical T spectra, the other factors that govern the performances of transparent conductors include their electrical properties and optical bandgap energies.<sup>[68]</sup> The optical bandgap energies,  $E_0$ , of thin film samples are estimated generally from:<sup>[74,80]</sup>

$$\alpha_{\lambda}(hv) = Y(hv - E_0)^{1/2} \quad (4.5)$$

where  $hv$  is the photon energy and  $Y$  is a constant. The absorption coefficient,  $\alpha_{\lambda}$ , which is a function of photon wave length,  $\lambda$  (equation 3.4a), is obtained from the approximate spectrophotometry quadratic equation. This is given by:<sup>[200,201]</sup>

$$T = \frac{(1-R)^2 e^{-\alpha_{\lambda}t}}{1 - R^2 e^{-2\alpha_{\lambda}t}} \quad (4.6)$$

where  $t$  the multilayered ZAZ thin film thickness is obtained using surface profilometry measurement so that the absorption coefficient is readily determined by solving the quadratic equation above (equation 4.6). This leads to:

$$e^{-\alpha_{\lambda}t} = \frac{-(1-R)^2 \pm [(1-R)^4 + 4T^2R^2]^{1/2}}{2TR^2} \quad (4.7a)$$

or equivalently simplified to:

$$\alpha_{\lambda} = -\frac{1}{t} \ln \frac{1}{R^2} \left[ \frac{-(1-R)^2}{2T} + \left( \frac{(1-R)^4}{4T^2} + R^2 \right)^{1/2} \right] \quad (4.7b)$$

$R$  and  $T$  represent the respective experimental reflectance and transmittance values of the multilayered ZAZ thin film composite stacks.

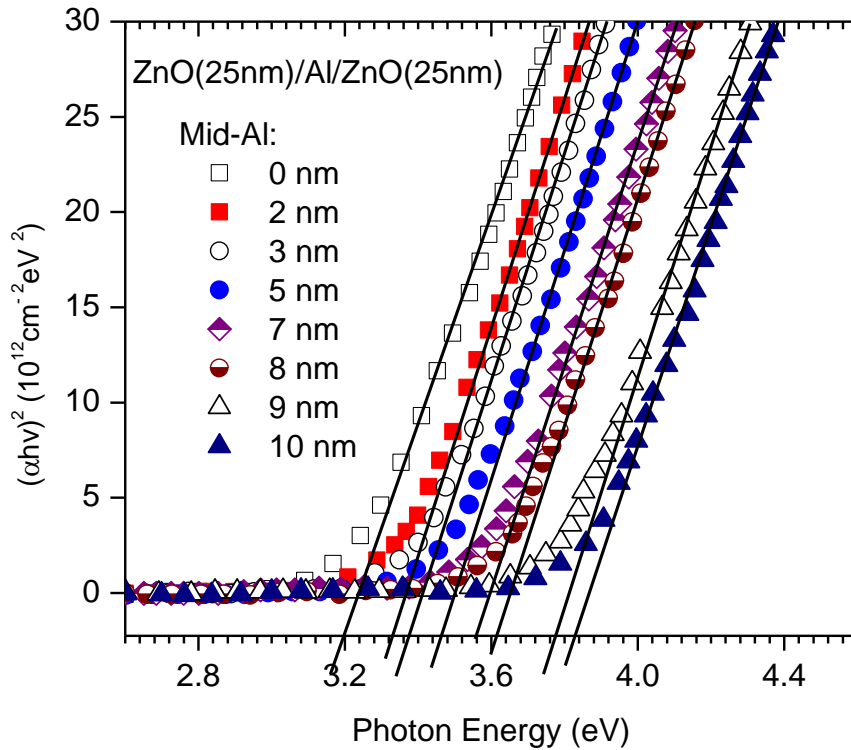


Figure 4.14: Plots of  $(\alpha_{\lambda}hv)^2$  as function of photon energy,  $hv$ , illustrating the dependence of optical bandgap energy of multilayered ZnO (25 nm)/Al/ZnO (25 nm) thin film composite structures on the captioned mid-layer Al thicknesses.

The dependence of the  $(\alpha_{\lambda}hv)^2$  on the thickness of the mid-layer Al (as a function of photon energy,  $hv$ ) is presented in Figure 4.14. This was used to estimate the apparent optical bandgap energies for the multilayered ZAZ thin film composite

structures. We extrapolated the  $(\alpha_{\lambda}h\nu)^2$  curves to obtain the photon energy-intercepts at  $(\alpha_{\lambda}h\nu)^2 = 0$ . The apparent optical bandgap energies of the multilayered ZAZ thin film composite structures are obtained at the intercepts. With increasing mid-layer Al thickness (from  $\sim 0$  to 10 nm), the result shows a spectacular increase of the apparent optical bandgap energy of the multilayered ZAZ thin film composite stack from  $\sim 3.26$  to 3.85 eV, a range of  $\sim 0.60$  eV (Figures 4.14 and 4.15, and Table 4.2).

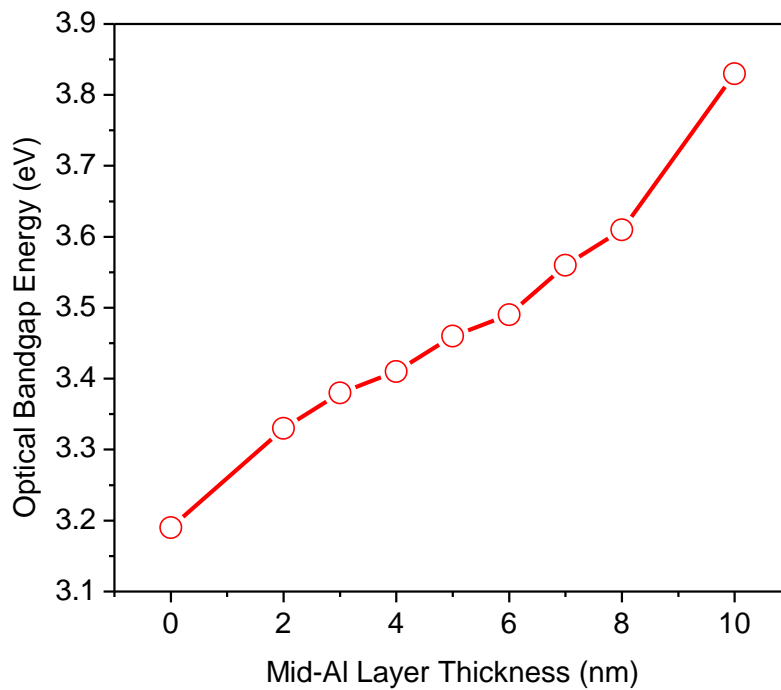


Figure 4.15: Dependence of optical bandgap energy of ZnO (25 nm)/Al/ZnO (25 nm) on the mid-Al thickness between 0 and 10 nm.

The observed increase in the optical bandgap energy,  $E_0$ , of the multilayered ZAZ thin film composite structure with increasing mid-layer Al thickness (Figure 4.14) is attributed to the Moss-Burstein effect.<sup>[197]</sup> The Moss-Burstein effect occurred in multilayered ZAZ thin film composite structures due mainly to the increase in charge

carrier density with increasing mid-layer Al thickness. This increased the charge carriers in the ZnO films. The extra charge carriers (from the increasing mid-layer Al thickness) then fill the states at the bottom of the conduction band of ZnO, in accordance to the Moss-Burstein effect.<sup>[197]</sup> This resulted in the widening of the optical bandgap energy,  $E_0$ , of the multilayered ZAZ thin film composite structure (Figures 4.14 and 4.15).

Table 4.2: List of intermediate layer Al thicknesses used for the RF MS deposition of ZnO (25 nm)/Al/ZnO (25 nm) multilayer thin film composite structures and the corresponding electrical sheet resistances, effective resistivities and HFoMs for structures with conductive nanolayers of Al and Au.

ZAZ (from this study)					ZnO/Au/ZnO <sup>[74]</sup>	
Mid-Al (nm)	$R_s$ ( $\Omega/sq.$ )	$\rho$ ( $\Omega cm$ )	HFoM ( $\Omega^{-1}$ )	$E_0$ (eV)	Mid-Au (nm)	HFoM ( $\Omega^{-1}$ )
0	-	-	-	3.19	-	-
2	$1.73 \times 10^5$	1.74	$2.75 \times 10^{-7}$	3.33	2	$1.14 \times 10^{-7}$
3	$7.44 \times 10^4$	$2.98 \times 10^{-1}$	$5.88 \times 10^{-7}$	3.38	3	$1.59 \times 10^{-5}$
4	$1.88 \times 10^4$	$5.65 \times 10^{-2}$	$1.30 \times 10^{-6}$	3.41	4	$1.2 \times 10^{-3}$
5	$2.67 \times 10^3$	$5.34 \times 10^{-3}$	$1.38 \times 10^{-5}$	3.46	-	-
6	$1.54 \times 10^3$	$4.65 \times 10^{-3}$	$2.41 \times 10^{-5}$	3.49	6	$8.3 \times 10^{-3}$
7	$1.62 \times 10^1$	$8.07 \times 10^{-4}$	$1.25 \times 10^{-3}$	3.56	-	-
8	9.83	$4.91 \times 10^{-4}$	$4.72 \times 10^{-3}$	3.61	9	$13.8 \times 10^{-3}$
10	7.25	$3.62 \times 10^{-4}$	$4.52 \times 10^{-3}$	3.83	12	$15.1 \times 10^{-3}$

The interpretation of the optical bandgap energy results, based on the Moss-Burstein effect,<sup>[197]</sup> assumes a sharp parabolic conduction band curvature, such that the shift in Fermi level position,  $\Delta E$ , for a given free charge carrier density,  $N$ , can be obtained. This is given by:<sup>[68]</sup>

$$\Delta E = \frac{h^2}{8m^*} \left( \frac{3N}{\pi} \right)^{2/3} \quad (4.8)$$

where  $m^*$  is the carrier effective mass. Subsequently, the widening of the optical bandgap energy is obtained from:<sup>[197]</sup>

$$E_0 = E_G + \Delta E \quad (4.9)$$

where  $E_G$  is the intrinsic minimum bandgap energy of ZnO.

### 4.3.3 Electrical Properties of ZAZ Multilayer Film Structures

The observed widening of the optical bandgap energy and high T spectra in multilayered ZAZ thin film composite structures with mid-layer Al thickness between  $\sim 1 - 10$  nm are generally desirable for the improved optical performance of layered composite transparent films. However, the ultra-thin mid-layer Al thicknesses might have detrimental effects on the electrical properties of the transparent multilayered ZAZ thin film composite electrodes. In order to test the electrical performance of the model multilayered ZAZ thin film composite structures, electrical data were obtained from the multilayered ZAZ thin film composite stacks with double layers of ZnO with 25 nm each and mid-Al thicknesses that were varied between  $\sim 1 - 10$  nm.

The effective average values of resistivity and sheet resistance obtained from the optically optimized multilayered ZAZ thin film composite structures (with ZnO double-layers of 25 nm each and mid-layer Al thicknesses between  $\sim 1 - 10$  nm) are presented in Table 4.2 and Figure 4.16. The electrical properties of single nano-layered ZnO films (without mid-Al nanolayers) could not be measured due to their extremely high sheet resistance values. The latter were greater than the sensitivity limit of the four-point probe system that was used (4200 SCS Signatone, Keithley Instruments Inc., Cleveland, OH,

USA). As shown in Figure 4.16, when the thickness of Al mid-layer was increased, both electrical sheet resistance and the effective resistivity of the multilayered ZAZ thin film composite structures were enhanced significantly.

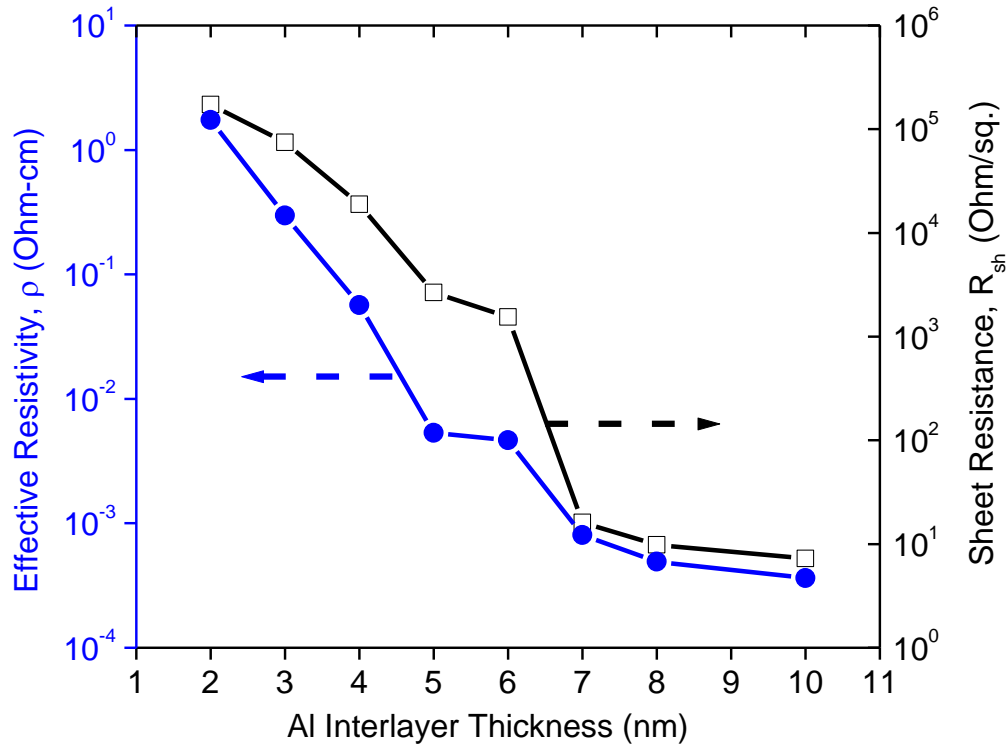


Figure 4.16: Dependence of the sheet resistance and the effective resistivity of the model multilayered ZAZ thin film composite stack with ZnO-layer thicknesses of 25 nm on the optimum mid-layer Al thicknesses between 1 – 10 nm.

The resistivity decreased rapidly from  $1.74$  to  $5.65 \times 10^{-2} \Omega cm$  ( $\sim 97\%$ ), as the mid-layer Al thickness increased from 2 to 4 nm. Furthermore, the resistivity of the multilayered ZAZ thin film composite structure decreased gradually to a value of  $\sim 8.07 \times 10^{-4} \Omega cm$ , for an Al mid-layer thickness of 7 nm. A further slight decrease of

resistivity to  $\sim 3.63 \times 10^{-4} \Omega \text{ cm}$  was observed at an Al interlayer thickness of 10 nm. As shown in Figure 4.16, the corresponding sheet resistance of the model multilayered ZAZ thin film composite structures was improved spectacularly. The sheet resistance dropped from  $\sim 1.73 \times 10^5 \Omega/\text{sq}$ . (for an Al interlayer thickness of 2 nm) to  $\sim 7.25 \Omega/\text{sq}$ . for an Al mid-layer thickness of 10 nm (Table 4.2).

### 4.3.4 Comparison of Model ZAZ with other Multilayer Films

#### 4.3.4.1 Other Multilayered ZAZ Thin Film Stacks

The transparent conductive properties presented in this study are largely in agreement with the earlier results for similar multilayered ZAZ thin film structures that were fabricated by Al-Kuhaili *et al.*<sup>[80]</sup> The work by Al-Kuhaili *et al.*<sup>[80]</sup> demonstrated the effects of annealing temperature on the transparent conductive properties of a multilayered ZAZ thin film stack with fixed mid-layer Al thickness of  $\sim 20$  nm and ZnO layer thicknesses of  $\sim 200$  nm. It was shown by these authors<sup>[80]</sup> that the thicknesses, structural and electro-optical properties of the composite ZAZ thin film structures depend significantly on the post-deposition treatments. The best multilayered ZAZ thin film electrode with average visible spectra Ts of  $\sim 75\%$  and electrical sheet resistivity as low as  $\sim 2.9 \text{ m}\Omega \text{ cm}$  were obtained at an optimal annealing temperature of  $300^\circ\text{C}$  in the work of Al-Kuhaili *et al.*<sup>[80]</sup>

While the work of Al-Kuhaili *et al.*<sup>[80]</sup> was based on a fixed thickness of ZnO and mid-Al layer, the experimental transparent conductive properties of the multilayered ZAZ thin film structures presented in the this study include the effects of different mid-layer Al thicknesses between  $\sim 1 - 10$  nm. In comparison, the electro-optical properties obtained by Al-Kuhaili *et al.*<sup>[80]</sup> are largely in agreement with the results obtained in this

study. However, the differences between our results and those of Al-Kuhaili *et al.*<sup>[80]</sup> are very likely due to differences in the fabrication techniques (thermal evaporation versus RF MS) that were used. In addition, the initial form of raw materials (ZnO and Al pellets<sup>[80]</sup> versus ZnO ceramic and Al metallic circular targets), the deposition rates and the post-deposition thermal treatments of the multilayered ZAZ thin film stacks were also different along with the thicker ZnO (~ 200 nm) and mid-Al (~ 20 nm) layers used in the study by Al-Kuhaili *et al.*<sup>[80]</sup>

#### **4.3.4.2 Effects of Mid-Al on the Electrical Properties of ZAZ Film**

The observed trends in the electrical properties of the multilayered ZAZ thin film stacks have been attributed to the increase in the n-type free charge-carrier (electron) density<sup>[80]</sup> and charge carrier mobility in the multilayered thin film stacks. As shown in Figures 4.14 and 4.15, the charge carrier increased with increasing mid-layer Al thickness, thus resulting to the observed widening of the optical bandgap energy in accordance with Moss-Burstein effect.<sup>[197]</sup> However, during deposition by RF MS, the ultra-thin metallic layers are known to form discontinuous films on top of the oxides.<sup>[74,75,103,111]</sup> These films result in high combined resistivities of multilayered ZAZ thin film structures, which decrease (Figure 4.16) significantly as the mid-layer Al becomes thicker. It has been clearly shown in Ref.<sup>[75]</sup> that the metallic mid-layers become continuous with increasing thickness of the layers.

Thus, it is certain that the effective resistivity decreases as the metallic mid-layer becomes more continuous. With further increase in the thickness, the mid-layer Al gradually changes from discontinuous to continuous, after reaching a critical transition thickness ( $t_c$ ). At their  $t_c$ , the multilayered thin film stacks are known to adopt different

charge-carrier transport mechanisms.<sup>[74]</sup> This leads to the observed gradual decrease in electrical properties of multilayered ZAZ thin film structures with increasing mid-layer Al thickness between  $\sim 7 - 10$  nm. Further evidence of the onset of the mid-layer Al discontinuous-continuous transition phenomena is presented in Table 4.2 and Figures 4.7, 4.14 and 4.16.

The filling of the states near the bottom of the conduction band (as a result of the increasing mid-layer Al thickness) is associated with an increase in free charge-carrier (electron) density and mobility. This is further attributed to the widening of the optical bandgap energy (Figure 4.14), and results in an increase in the electrical conductivity in the multilayered ZAZ thin film structure (Table 4.2 and Figure 4.16). The sharp increase in apparent optical bandgap energy was observed for mid-layer Al thicknesses between  $\sim 8 - 10$  nm (Figure 4.14). This suggests the onset of ZnO – Al charge-carrier density and conductivity transitions, resulting mainly from the merging of the lower and upper ZnO layers with the continuous mid-Al for the thicker layers than  $t_c$ .

Furthermore, the two sharp transitions in the XRD patterns at the mid-layer Al thicknesses between  $\sim 2 - 5$  nm and  $6 - 8$  nm (Figure 4.7) are also revealed in the electrical properties of the multilayered ZAZ thin film structures (Figure 4.16). While the first transition (at mid-Al of between  $\sim 2 - 5$  nm thick) can be associated to substantial mid-layer Al thicknesses, the second transition at mid-Al  $\sim 6 - 8$  nm suggests the onset of the critical mid-Al layer thickness,  $t_c$ . In this thickness regime, the merging of the lower and upper ZnO layers with the continuous mid-Al layer leads to increase in free charge-carrier density and hence the observed high conductivity values in multilayered ZAZ thin film stacks with mid-Al layer thickness between  $\sim 7 - 10$  nm (Table 4.2 and Figure 4.16).

However, as shown in Figure 4.7, as the mid-layer Al thickness increases, the crystallinity of the multilayered ZAZ thin film stacks decreases. The decrease in crystallinity (with increasing mid-layer Al thickness) implies that the mobility of free-charge carriers decreased.<sup>[80,199]</sup> This indicates that, in multilayered ZAZ thin film stacks with thick Al intermediate layers (that were relatively thicker than the  $t_c$ ), some charge carriers were bound in the short range by the increasing non-uniform amorphous structures. This is partly the reason for the bulk resistivity values, which are generally steady (Figure 4.16) with increasing mid-layer Al thickness, for thicker Al mid-layers between  $\sim 7 - 10$  nm. This trend, which has also been observed in earlier studies<sup>[74,111]</sup> occurs for other multilayered TCO/metal/TCO thin film structures.<sup>[75]</sup>

### 4.3.5 Performance of Model ZAZ Multilayer Films

The choice of TE coatings is based generally on combined considerations of sheet resistance and T, for given TE material systems. This has led to the definition of the Haacke Figure of Merit, HFoM<sup>[68]</sup> for the evaluation of the performance of transparent conductors.<sup>[80]</sup> This is given by:<sup>[68,74,75]</sup>

$$HFoM = \frac{T_{av}^{10}}{R_s} \quad (4.10)$$

where  $T_{av}$  and  $R_s$  are the respective measured average T and sheet resistance of a given TE coating system. This was used to obtain the HFoM for each of the multilayered ZAZ thin film stacks produced.

The HFoM results obtained (Table 4.2) for the multilayered ZAZ thin film structures with mid-layer Al thicknesses between  $\sim 1 - 10$  nm ranges from  $\sim 2.75 \times 10^{-7} \Omega^{-1}$  for the thinner Al thicknesses to  $\sim 4.72 \times 10^{-3} \Omega^{-1}$  for the thicker mid-Al layers. These compare with published Haacke figures of merit for other multilayered ZnO

thin film structures with intermediate nanolayers of gold (Figure 4.17), in which HFoM between  $\sim 8.3 \times 10^{-3}$  and  $15.1 \times 10^{-3} \Omega^{-1}$  at the mid-layer Au thickness between 6 – 12 nm have been reported.<sup>[74]</sup> For mid-layer Al thicknesses in the range of  $\sim 7 – 10$  nm, high HFoM between  $\sim 1.25 \times 10^{-3}$  and  $4.72 \times 10^{-3} \Omega^{-1}$  were obtained in this study (Table 4.2). These values are also very close to those reported earlier for ITO-coated transparent conducting substrates that have HFoM values between  $\sim 2.07 \times 10^{-3}$  and  $3.82 \times 10^{-2} \Omega^{-1}$ .<sup>[202]</sup>

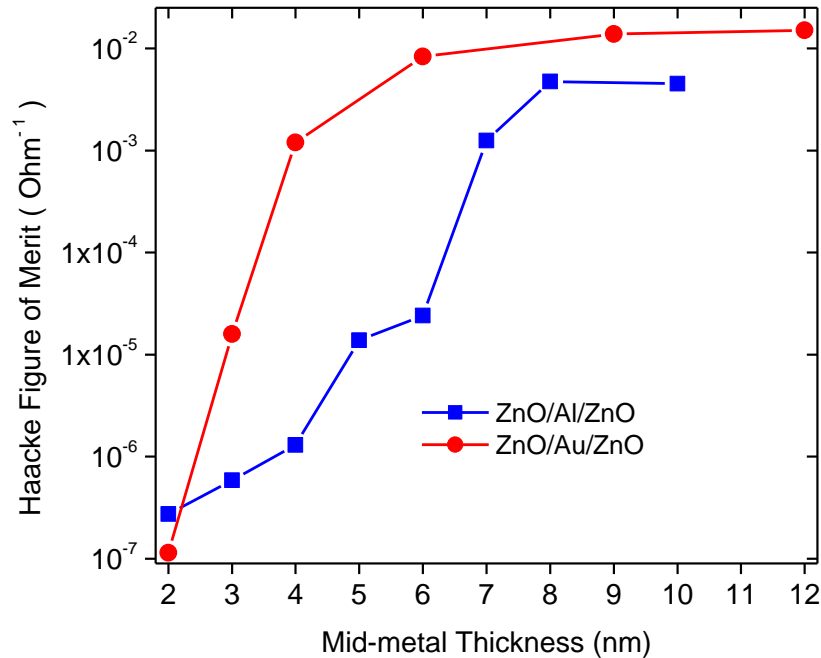


Figure 4.17: Comparison between the Haacke figures of merits for the multilayered ZnO films with mid-layer Al (the ZAZ produced in this work) and those with nanolayers of Au obtained from Ref.<sup>[74]</sup>

## 4.4 Concluding Remarks

This Chapter presents the results of a combined theoretical, experimental and numerical study of transparent conductive properties of multilayered ZAZ thin film stacks on rigid transparent glass substrates. The numerical simulations of multilayered ZAZ thin film composite structures were based on very thin mid-layer Al thickness ranging between  $\sim 1 - 10$  nm. These were selected based on the optimum visible solar T results suggested by the earlier numerical simulations (chapter 3). Within this range, the results were validated by the experimental optical Ts that were obtained from multilayered ZAZ thin film structures with similar ZnO and mid-Al layer thicknesses. Sharp transitions in the XRD patterns (Figure 4.7), and the apparent optical bandgap energy (Figure 4.14), as well as in the electrical properties (Figure 4.16) were observed in multilayered ZAZ thin film structures with mid-layer Al thicknesses between  $\sim 6 - 9$  nm. These were attributed to the important thickness range for the onset of continuous mid-Al layer. This results to the zinc oxide – aluminum free charge-carrier density and electrical property transitions, which enhances the conductivity of the multilayered ZAZ thin film composite electrode, at reasonable visible solar transparencies for applications in TE coatings in organic solar cells and other optoelectronic components.

# 5. Chapter Five

## Prospects of Non-ideal Interfacial/Interlayer Contacts in Polymer: Fullerene BHJ Solar Cells

### 5.1 Introduction

Interfacial and interlayer contact processes are part of the critical charge transport and solar cell efficiency limiting issues in the operation of BHJ OSCs and other organic electronic devices.<sup>[203]</sup> Therefore, the work in this chapter, examines the prospects of those contact issues between the anode and the photoactive layers of a newly produced OPV device with poly[2-methoxy-5-(3', 7'-dimethyloctyloxy)-p-phenylene-vinylene]:[6,6]-phenyl C<sub>61</sub>-butyric acid methyl ester (OC<sub>1</sub>C<sub>10</sub>-PPV: PCBM) structure, with a 1:4 ratio (by weight). To do this, a modified BHJ device model<sup>[126]</sup> is used to efficiently simulate the photo-current-density versus voltage (J-V) characteristics of an OSC with planar interface between the transparent anode and the photoactive layers.

The results obtained are shown to have favorable correlation between the simulations and the earlier reported experimental J-V curves of the same organic solar cell structure.<sup>[126]</sup> Additionally, in this study, the effects of non-ideal photoactive/anode interfacial contacts on the J-V curves of the OSC are explored. These effects, which are associated with the partial contact lengths and the contact heights, are shown to affect the J-V characteristics of organic solar cell with OC<sub>1</sub>C<sub>10</sub>-PPV: PCBM structures. The existence of partial contacts (due to voids at the interface) between the transparent anode and the photoactive organic layers is shown to decrease greatly the overall PCEs of OSCs with BHJ structures.

The effects of non-ideal contacts are further associated with the increase in series resistances of BHJ OSCs. These are shown to occur as a result of the decreasing planar contact length and/or the increasing partial contact height at the interface between the transparent anode and the photoactive layer. This led to a drop in the short-circuit current, the fill factor and hence deterioration of the efficiency and the overall performance of OPV devices with BHJ structures. The implications of the results are discussed for the design of pressure-assisted electronic processes for the fabrication of OSCs with enhanced power conversion efficiencies.<sup>[203]</sup>

## **5.2 Overview of Organic Solar Cell Models**

As discussed in prior chapters, OPV devices with BHJ structures show greater promises for the development of cost effective and efficient polymer solar cell systems.<sup>[1,126]</sup> As mentioned earlier, also, the key technical issues that make organic based PV systems attractive include their potential for large-area device processing. Furthermore, the OSC lamination processes are achieved using fast and low temperature roll-to-roll techniques. These involve spin coating or printing on low-cost substrates.<sup>[155]</sup> OPV technology, also, involves lesser usage of flexible polymeric materials and fewer low cost fabrication steps<sup>[54]</sup> using wet solution or dry thermal evaporation of the active organic constituents.<sup>[128]</sup> In fact, lightweight OPV solar cell modules with high efficiencies between  $\sim 7 - 10\%$ <sup>[7]</sup> have recently been reported.<sup>[54]</sup> There is also great potential for the large scale development of OPV modules, currently, with a single mass production line of organic solar cells based on the printing of large areas that are estimated to exceed  $1000 \text{ m}^2/\text{hour}$ .<sup>[54]</sup>

However, still there are significant numbers of practical challenges that must be overcome prior to the anticipated widespread use of OPV modules.<sup>[1]</sup> These include the non-ideal interlayer contact-limiting processes, which interfere adversely with charge transport and collection, thus affecting the efficiencies and overall performances of OPV device detrimentally.<sup>[1]</sup> Furthermore, the phenomenology of diffusion, dissociation and separation of excitons into EHPs as well as the recombination, transport and collection of the photo-generated free charge carriers are directly dependent on the interfacial and/or interlayer contacts of the OPV solar cell systems and their ingredients.

Hence, the influence of contact-limiting processes on the performance of OPV devices is of great interest. Accordingly, effective fabrication of BHJ OSC structures often requires carefully engineered interfacial and interlayer contacts. This must be done in order to maximize the interfacial-contact area to improve the free charge carrier generation and their migration towards respective electrodes for the enhancement of the PV effect and improvement of OPV device efficiencies.<sup>[204]</sup> These contact-limited issues occur usually as a result of defects (such as voids or dust particles) that are present due to impurities in the clean room environments and non-ideal production processes that are used for the fabrication of OSCs.<sup>[203]</sup> Such defects create partial contacts at the interfaces of the OSC elements, thus interfering with the fluxes of free charge carriers throughout the organic solar cell systems and their interlayers. This, ultimately, inhibits the efficiency and lowers the overall performance of OPV BHJ devices.

Therefore, besides engineering of new polymeric functional materials and their corresponding OPV device structures, electrical models are increasingly being developed to ascertain the dependency of OSCs efficiencies on their structural and materials

properties. These models are developed generally based on one-dimensional geometry (1DG) solar cell electrical systems and concepts.<sup>[126,205-210]</sup> Recently, however, a number of research groups<sup>[25,57,211-214]</sup> have also applied a two-dimensional geometry (2DG) modeling approach to study the properties of BHJ OSC structures. These can be used to probe the very sensitive performance issues in the operation of OSC systems. These include the influence of D/A interfaces on the transport of excitons and the generated free charge carriers. They can also be used to determine impacts of active layer morphological factors on the electrical performances and their associated limits on the efficiency of OPV devices.<sup>[215]</sup> There is, therefore, a great interest in the development of new and/or modified electrical models that can be used to explain precisely some of the non-ideal interlayer/interfacial contacts issues and how these affect the performance of BHJ OPV devices.

### **5.3 Characterization of Solar Cells via Numerical Modeling**

For solar cells and PV modules in general, the J-V characteristics (Figure 6.1) of a given device system enable examination of their important metric performance parameters. As shown in Figure 6.1, such parameters include the fill factor (FF), short circuit current density ( $J_{SC}$ ), open circuit voltage ( $V_{OC}$ ), the maximum theoretical power point (MTPP), voltage ( $V_{MPP}$ ) and current density ( $J_{MPP}$ ) at the maximum power point (MPP). Ultimately, these quantities are used in the evaluation of PCEs and other functionality of different PV solar cell systems. Moreover, in cases where the PV solar cell is described within relevant regime and with appropriate models/mechanism, the J-V characteristics of an illuminated device are known to provide an excellent diagnostic for the most of solar cell limiting features.<sup>[58]</sup>

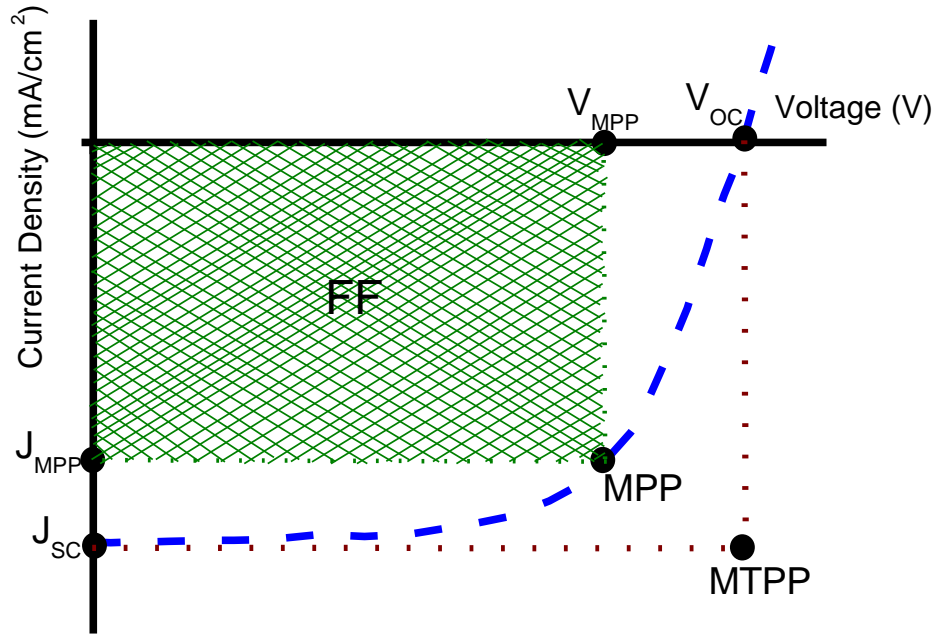


Figure 5.1: Schematics of typical current-voltage (J-V) characteristics of an illuminated PV solar cell system.

The electrical properties of BHJ OPV devices, for example, can similarly be investigated based on the evolution of their J-V characteristics. This is, essentially, the most important method that is widely used in the evaluation of the overall PCEs for PV systems and light emitting devices. The efficiency of a PV solar cell, for example is derived simply from the ratio of its output power to the input power. This is given by:

$$\eta_c = \frac{P_{max}}{P_{in}} = \frac{V_{oc}J_{sc}FF}{P_{in}} \quad (5.1)$$

where  $\eta_c$  is the overall PCE of a solar cell,  $P_{max}$  is the maximum power produced by the solar cell,  $V_{oc}$  (open circuit voltage) is the maximum possible photo-voltage across the solar cell,  $J_{sc}$  (short circuit current density) is the maximum photo-current density generated by the solar cell under zero bias,  $FF$  (the fill factor of a solar cell) is the ratio of the actual maximum power output ( $V_{MPP}J_{MPP}$ ) to the theoretical power output

( $V_{oc}J_{sc}$ ) and the  $P_{in}$  ( $\sim 100 \text{ mW/cm}^2$ ) is the standard incident power per unit area of the solar cell. This incident power is obtained generally as the sum of all wavelengths under the AM1.5 standard solar spectral illuminations.

Note that, despite the need to focus only on the few aspects of the solar cell devices (i.e. neglecting some of the indispensable parameters as a result of the inexplicabilities of most numerical models), the 2DG models of J-V characteristics<sup>[57,213]</sup> are widely being used to obtain detailed insightful information about the operational mechanisms, by simulating the electronics and kinetic processes of BHJ OPV devices. Such models have been used to describe explicitly the dependence of OSC efficiencies on the mobility of charge carriers.<sup>[213]</sup> The 2DG models of photoactive layers are also another useful and increasingly approach for exploring the electronic properties of OPV solar cell devices. For example, this has been used to examine the effects of interfacial morphology on the efficiencies,<sup>[25,211,212,214]</sup> as well as the evaluation of the different factors and processes<sup>[57]</sup> that limit the overall performances of BHJ OSC structures.

Considering the potentials of BHJ OSC depicted above, it is of high curiosity to develop detailed electrical OSC models. These are particularly needed to ascertain the different OSC interfacial and interlayer contact issues, as well as numerating on the prospects of contact imperfectness on the physicality and performance of OPV solar cell devices. So far, in the past years, several electrical models<sup>[215]</sup> that are based on the drift-diffusion (DD) equations<sup>[126,205-210,216]</sup> have been reported. These are usually coupled with band-to-band and/or tail states recombination<sup>[126,217]</sup> models to describe the characteristics of polymer: fullerene BHJ OSCs (with planar interface structures). Such models<sup>[126,215]</sup> and several other analytical and/or numerical simulation concepts<sup>[154,155,218]</sup> have been

shown to have great exploratory capacity for probing some of the critical factors, that limit the efficiencies and overall performance of OPV devices.

However, significant research efforts are still needed to examine fully the interfacial/interlayer electronic processes to further improve the design and performance of OSC systems. In particular, the planar interlayer interfaces that are being assumed in the numerical models above are not necessarily representative of the charge carrier transfer interfaces in the actual BHJ OSC structures. Clearly, the interfacial/interlayer contact is a vital efficiency limiting factor that has not been explicitly considered in the modeling of BHJ OPV devices until now. This feature is particularly important due to the strong detrimental effects of partial interfacial contacts, which limit charge carrier generation, transportation and collection at the electrodes. As noted earlier, there is also a great interest in the development of the operational, design, production and commercialization of BHJ OPV solar cell systems with improved interfacial/interlayer contacts and hence high PCEs. Hence, there is a great need to extend the existing organic solar cell DD J-V models to include effects of interfacial and/or interlayer contacts.

Novel electrical models are, therefore, needed to enable the investigation of the non-ideal interfacial/interlayer contact phenomena and the charge transfer interfaces that are relevant to organic electronic structures and devices.<sup>[219-221]</sup> Hence, this chapter attempts to investigate the prospects of the OSC PCE contact-limiting processes. A 2DG J–V numerical approach is used in this study. For simplicity, the modeling was purposely limited to interfaces between the photoactive organic layer and the transparent anode of BHJ OPV system with OC<sub>1</sub>C<sub>10</sub>-PPV: PCBM structure. This was chosen to make it consistent with the 1DG model that was developed earlier by Koster *et al.*<sup>[126]</sup> for a

similar OSC structure with planar interlayer interfaces with OC<sub>1</sub>C<sub>10</sub>-PPV: PCBM photoactive materials.

However, the important aspect of our numerical study is the extension of the 1DG drift-diffusion model<sup>[126]</sup> to 2DG models. Our 2DG model is expanded further to include features for the inspection of influences of interfacial/interlayer contacts on the J-V characteristics of BHJ organic semiconductor PV systems. This is achieved by including explicitly the effects of non-ideal interfaces with partial interlayer contacts (voids) in the earlier reported BHJ OSC drift-diffusion model.<sup>[126,217]</sup> The results obtained reveal spectacular detrimental effects on the short-circuit current density, fill factor, as well as on the overall performance of OSCs as function of contact (void) length ( $L_C$ ) and contact (void) height ( $H_C$ ) at the interface between the photoactive layer and the transparent anode of BHJ organic solar cells.

Furthermore, the results obtained highlight the clear prospects on interfacial/interlayer contacts on the performances of BHJ OSCs. The results also show clearly how far the perfectly planar interlayer contacts that are implicitly assumed in the modeling of the electronics and kinetics of OSCs can be physically misleading in mimicking of actual non-ideal contacts in OPV and OLED devices. The ability of the 2DG DD model to gauge on how partial contacts translate directly into an evolution of the solar cell J-V characteristics (as function of contact length,  $L_C$ , and contact height,  $H_C$ ) are presented and discussed, before discussing the implications of the results for the design of OPV solar cell systems and other electronic semiconductor devices with improved interfacial/interlayer contacts and hence the overall device performances.

## 5.4 Solar Cell Numerical Modeling Approach

So far, the FDM drift-diffusion models<sup>[25,57,126,205-214]</sup> have widely been developed and implemented to study the electronics and kinetic processes of OSC systems. In this case, some of the processes that have been widely studied (using FDM DD models) include the multiple organic electronic steps that are relevant in the operation of BHJ OSCs. These include: photo-generation, dissociation and separation of excitons at the D/A interfaces as well as recombination, transportation and extraction of electrons and holes<sup>[126]</sup> at the respective electrodes of OSC systems. Note also that, the FDM DD electrical models<sup>[25,57,126,205-214]</sup> are, in principle, useful for organic and inorganic solar cell systems, as well as organic and inorganic light-emitting diodes and other semiconductor devices.<sup>[215]</sup> This is due mainly to the driving forces for charge carriers in electronic semiconductor structures and device components. These have been shown to be closely similar for organic and inorganic electronic semiconductor materials.<sup>[222,223]</sup>

In this chapter, the FDM DD continuum model is first derived from the charge-carriers (electrons and holes) drift and diffusion current equations. This is a combined Poisson's and current continuity equations model. Secondly, in an effort to estimate the electronic properties of BHJ OPV solar cell devices using the above basic DD continuum formulation, the J-V characteristics of an OSC with a photoactive blend of OC<sub>1</sub>C<sub>10</sub>-PPV:PCBM was simulated. This was achieved by building very small discrete of continuous gridded charge-transport models for electrons and holes, with FDM within the organic solar cell structure. The model was then solved iteratively with appropriate self-consistent boundary conditions (BC) at front and backside electrodes. The numerical results obtained are compared with experimental results that were reported earlier by Koster *et*

*al.*<sup>[126]</sup> Good agreement was achieved between the simulations and the experimental results. This confirms the suggestions that the continuum electrical DD numerical method can be used as reasonably simulation tools for studying the qualitative and quantitative physical and electronic properties of BHJ OSC structures intuitively.

## 5.4.1 Basic Drift Diffusion Equations

The basic drift-diffusion type equations that are used in the writing of the drift-diffusion continuum models for simulation of OSCs and other semiconductor devices were contemporary discussed by Koster *et al.*<sup>[126]</sup> and XinYan *et al.*<sup>[215]</sup> These include:

### 5.4.1.1 The Poisson's equation

The Poisson's equation relates the position dependent electrostatic potential,  $\Psi$ , to the charge carrier densities (electron,  $n$ ) and (hole,  $p$ ), which are also function of position within the solar cell device. In a 2D space coordinate system, the Poisson's equation is given by:

$$\nabla^2\Psi = -\frac{q}{\varepsilon}(p - n) \quad (5.2)$$

where the dielectric constant,  $\varepsilon$ , is given by  $\varepsilon = \varepsilon_r\varepsilon_0$  and  $q$  is the elementary charge.

### 5.4.1.2 Current Continuity Equations

For simplicity, the respective current continuity equations for electrons of density  $n$  and holes of density  $p$  are often written and solved under steady state condition. These are given in a 2D space coordinate by:

$$\nabla J_n = -q(G - R_n) \quad (5.3)$$

and

$$\nabla J_p = -q(R_p - G) \quad (5.4)$$

where  $J_n$  and  $J_p$  are electron and hole current densities,  $R_n$  and  $R_p$  are the respective electron and hole recombination rates and  $G$  is the generation rate of the charge carriers.

It is important to note here that in solar cells both electrons and holes contribute to the photo-current of the device. This has led to the definition of series of postulates for the evaluation of the performance of PV devices, based on the current densities, for electrons and holes. These are written in a way that relates the electron and hole current densities to the electrostatic potential, which is also related to the electric field strength of the solar cell system. The current density equations, therefore, combine both drift and diffusion characteristic transport of charge carriers. In a typical OSC device (a system with weak electric field strength), the respective 2DG drift-diffusion current densities, for electron and hole densities are given by:

$$J_n = q(n\mu_n \mathbf{F} + D_n \nabla n) \quad (5.5)$$

and

$$J_p = q(p\mu_p \mathbf{F} - D_p \nabla p) \quad (5.6)$$

where  $\mathbf{F}$ , the electric field is given by  $\mathbf{F} = -\nabla\psi$ ,  $\mu_n$  and  $\mu_p$  are respective mobilities for electron and hole, and  $D_n$  and  $D_p$  are diffusivities of electron and hole, respectively.

These diffusivities are defined from the Einstein relation<sup>[126]</sup> so that:

$$\frac{D_p}{\mu_p} = \frac{D_n}{\mu_n} = \frac{k_B T}{q} = V_T \quad (5.7)$$

where  $k_B$  is the Boltzmann constant and  $V_T$  is the thermal voltage relating the ambient temperature,  $T$ , to the elementary electronic charge,  $q$ . This results in:

$$J_n = q\mu_n(-n\nabla\psi + V_T \nabla n) \quad (5.8)$$

and

$$J_p = q\mu_p(-p\nabla\psi - V_T \nabla p) \quad (5.9)$$

### 5.4.1.3 Boundary Conditions

To obtain the solution of the drift-diffusion equations, the entire device must be discretized into a finite number of discrete grid units. This is done using either forward or backward difference approximation method.<sup>[224]</sup> Assuming Ohmic contacts,<sup>[126]</sup> the equations above were discretized and solved iteratively with appropriate anode ( $y = 0$ ) and cathode ( $y = t$ ) boundary conditions (BCs). In this study, the BCs were set as below for the electron (n) and hole (p) densities:<sup>[126,205,206,209]</sup>

$$n(0) = N_C \exp\left(-\frac{E_g}{k_B T}\right), \quad n(t) = N_C \quad (5.10)$$

and

$$p(0) = N_V, \quad p(t) = N_V \exp\left(-\frac{E_g}{k_B T}\right) \quad (5.11)$$

where  $N_C$  and  $N_V$  are the respective electron and hole effective density of states and  $t$  is the thickness of the device. The BC for the potential is given:<sup>[126]</sup>

$$\Psi(t) - \Psi(0) = E_g - V_a \quad (5.12)$$

where  $V_a$  is the applied potential voltage.

### 5.4.2 Generation-Recombination of Excitons and EHPs

The production of excitons is induced by the absorption of photons inside the active semiconductor materials of the organic solar cells. Immediately, after their production, excitons must diffuse to the D/A interfaces for their dissociation. The contemporary description of the exciton diffusion process in BHJ OSCs can be found in Ref.<sup>[164]</sup> Note that, the photogenerated organic excitons are only capable of diffusing across a certain distance,  $L$ , called organic exciton diffusion length or the exciton mean free path. This is given by:<sup>[215]</sup>

$$L = \sqrt{D\tau} \quad (5.13)$$

where  $D$  is the exciton diffusivity and  $\tau$  is the exciton mean lifetime. However, the distances between the D/A interfaces and the excitons in BHJ OSCs are generally very short,<sup>[215]</sup> in the order of the organic exciton diffusion length. Generally, this makes the typical exciton diffusion efficiency in BHJ OPV devices to be considerably effective, very close to 100%.<sup>[1]</sup> This consideration enabled the disregarding of the excitonic diffusion processes<sup>[215]</sup> in the modeling of BHJ OSC, using electrical DD models.<sup>[126]</sup>

Hence, at steady-state condition, the dissociation and recombination processes of excitons at the D/A interface are usually combined to describe the net photo-generation of EHP density. This is given by:<sup>[126,225]</sup>

$$G_X - k_f X - k_s X + R = 0 \quad (5.14)$$

where  $G_X$  is the exciton dissociation rate. Note that, after excitation of donor polymers, the resulting charge carriers may recombine promptly and/or excitation may result to the formation of stable exciton pairs. The former occurs with a decay rate constant,  $k_f$ , while the dissociation of the latter at the D/A interfaces produces the electron-hole pairs of density,  $X$ , commonly known as polaron pairs. Furthermore, the polaron pairs that are formed may either recombine with a rate constant,  $R$ , and/or separate with a rate constant,  $k_s$ , to produce free electrons and holes. The photo-generated free charge-carriers are then migrated through drift-diffusion transport mechanisms towards their respective electrodes, whereupon contribute to the PV effects of organic solar cells.

### 5.4.3 Generation and Recombination of Charge Carriers

There are several theories that have been developed to describe the generation, recombination and separation of the electrostatically bound EHPs into free-charge

carriers in organic-like amorphous semiconductors.<sup>[126,215]</sup> These include: the Langevin recombination,<sup>[226]</sup> the Onsager's geminate generation-recombination model<sup>[226,227]</sup> and its successful refinement by Braun.<sup>[228]</sup> In the Onsager–Braun approach, a probability, P, for the separation of EHPs is written as function of the distance,  $x$ , between the electron and hole, that forms an exciton or a polaron pair. The probability, P, is also a function of the electric field strength, F, as well as the ambient temperature, T. This is given by:<sup>[126,228]</sup>

$$P(x, T, F) = \frac{k_s(x, T, F)}{k_s(x, T, F) + k_f} \quad (5.15)$$

The Onsager's geminate recombination model<sup>[227]</sup> applies generally to cases like organic solar cell electronic systems in which there are weak electrolytes.<sup>[215]</sup> This was further refined by Braun<sup>[228]</sup> to derive the field-dependent separation rate constant theory. The Onsager-Braun's theory relates the field-dependent separation rate constant,  $k_s$ , with the EHP binding energy,  $E_B$ . This is given by:<sup>[228]</sup>

$$k_s(x, T, F) = \frac{3R}{4\pi x^3} e^{-E_B/k_B T} J_1((2\sqrt{-2b})/\sqrt{-2b}) \quad (5.16)$$

or equivalently by:<sup>[126]</sup>

$$k_s(x, T, F) = \frac{3R}{4\pi x^3} e^{-E_B/k_B T} J_1(1 + b + b^2/3 + \dots) \quad (5.17)$$

where  $J_1$  is the Bessel function of order 1,  $b$  the field-temperature dependent parameter given by  $b = q^3 F / (8\pi\epsilon k_B^2 T^2)$  and R is the bimolecular recombination rate. In the case of disordered polymer: fullerene solar cell systems, the distance between electron and hole within the exciton or polaron pair is known not to be constant throughout the device.<sup>[229]</sup> Hence, the probability of EHP separation, P is obtained generally as an integral over the spherical averaged Gaussian distribution of electron-hole pair separation distances. This is given by:<sup>[126]</sup>

$$P(a, F, T) = \frac{4}{\sqrt{\pi a^3}} \int_0^\infty P(x, F, T) x^2 e^{-x^2/a^2} dx \quad (5.18)$$

It is important to note here that, after separation of charge carriers, during transportation of holes and electrons to their respective electrodes, they may still suffer losses due to different factors. These factors may include: the Shockley-Read-Hall,<sup>[230-232]</sup> the trap-assisted,<sup>[232,233]</sup> the surface<sup>[234,235]</sup> and the bimolecular<sup>[236,237]</sup> recombination mechanisms of free-charge carriers. However, while the trap-assisted recombination has been shown to occur dominantly in organic solar cells with polymer: polymer structures,<sup>[232]</sup> they do not play significant effects in OPV devices with polymer: fullerene structures.<sup>[215]</sup> The trap-assisted recombination can, therefore, be neglected in the modeling of organic solar cells with polymer: fullerene structures.<sup>[126]</sup> This implies that, during transportation of carriers, the dominant loss mechanisms of electrons and holes occur generally by bimolecular recombination, which transpires with a recombination rate constant,  $R$ . This is given by:<sup>[126]</sup>

$$R = \gamma(np - n_{int}^2) \quad (5.19)$$

where  $n_{int}$  is the intrinsic charge-carriers density and  $\gamma$  is the Langevin-Braun recombination rate constant for BHJ semiconductor systems.<sup>[228,238]</sup> It is given by:<sup>[126,215]</sup>

$$\gamma = \frac{q}{\langle \varepsilon \rangle} \langle \mu \rangle \quad (5.20)$$

where  $\langle \varepsilon \rangle$  and  $\langle \mu \rangle = \langle \mu_n + \mu_p \rangle$  are the respective spatially averages of the dielectric constant and the sum of charge carriers mobilities.

The bimolecular recombination rate constant equations (5.19 and 5.20) were used, in a modified form initially by Koster *et al.*<sup>[126]</sup> They<sup>[126]</sup> refined the recombination constant in order to account for the charge carrier density gradients that occur generally in BHJ amorphous organic semiconductor devices. It was revealed by these authors<sup>[126]</sup>

that the dominant bimolecular recombination rate, in OSCs is determined mainly by the type of charge carriers with minimum mobility, generally the hole. The bimolecular recombination rate model was extended further by Deibel *et al.*<sup>[239,240]</sup> to describe the generally observed experimental recombination rates in OSCs that are often lower than the Langevin recombination rate. Their modification was achieved by introducing, to the Langevin recombination rate, a non-dimensional parameter,  $\xi$ . This led, ultimately, to the description of the bimolecular recombination rate constant for the OPV solar cell devices. It is given by:<sup>[139,240]</sup>

$$R = \xi\gamma(np - n_{int}^2) \quad (5.21)$$

and

$$\xi = \beta^2 e^{-\beta} (1 - e^{-\beta})^{-2} \quad (5.22)$$

where  $\beta = \ln(N_C/n_{an}) = \ln(N_V/p_{ca})$  with  $n_{an}$  and  $p_{ca}$  representing the electron and hole densities at the anode and cathode, respectively. By combining the generation and bimolecular recombination rate equations above, for electrons and holes, the net expression for the generation/recombination rate, GU, of charge carriers is readily obtained. It is given by:<sup>[126]</sup>

$$GU = PG_x - (1 - P)R \quad (5.23)$$

## 5.4.4 Solving the 2DG Drift-Diffusion Model

### 5.4.4.1 Iteration Scheme

To obtain the solution of the drift-diffusion model, the basic Poisson and continuity equations above were solved based on Gummel iteration scheme.<sup>[241]</sup> This was chosen due mainly to its simplicity as compared to the other commonly used iteration based on Newton scheme.<sup>[251]</sup> While the latter is a kind of coupling method that solves

the basic drift-diffusion equations synchronously, thus making it complicated.<sup>[215]</sup> The Gummel iteration scheme<sup>[241]</sup> is an uncoupling method that solves the basic DD equations by sequence and hence a relatively simple iteration method.<sup>[215]</sup>

Note also that, the values of the original parameters ( $n$ ,  $p$  and  $\Psi$ ), that are used in the basic DD equations above, might be relatively large. The equations were, therefore, normalized and the model was operated with reduced variables with inflections (equation 5.24). This was done by defining the equation variables as follows:

$$\tilde{\Psi} = \frac{\Psi}{V_T}; \quad \tilde{p} = \frac{p}{N_s}; \quad \tilde{n} = \frac{n}{N_s}; \quad \tilde{\nabla}^2 = \frac{1}{l^2} \nabla^2 \quad (5.24)$$

where  $N_s$  and  $l$  are the carrier density and the differential operator scaling factors, respectively. Hence, the Poisson's equation, for example, was rewritten in a reduced form. This led to:

$$\frac{V_T}{l^2} \tilde{\nabla}^2 \tilde{\Psi} = -\frac{q}{\epsilon} N_s (\tilde{p} - \tilde{n}) \quad (5.25)$$

Equation (5.25), can be further simplified by defining the differential operator scaling factor,  $l$ . In this study, it was defined by:

$$l^2 = \left( \frac{q N_s}{V_T \epsilon} \right) \quad (5.26)$$

So that the normalized Poisson's equation is simply given by:

$$\tilde{\nabla}^2 \tilde{\Psi} = \tilde{n} - \tilde{p} \quad (5.27)$$

The current continuity equations were equally normalized using a similar approach above. The flow chart of the Gummel iteration simulation program that was used is shown in Figure 5.1. This was based on the 1DG simulation work of Koster *et al.*<sup>[126]</sup>, with a difference that, our model is based on 2D space geometry and includes simulations of the interfacial/interlayer contact features. In solving the DD model, first a

zero applied potential was used to calculate the initial equilibrium values of the charge carrier densities ( $n$  and  $p$ ). Secondly, a guess was made for the non-zero potential and used to solve the Poisson's equation.

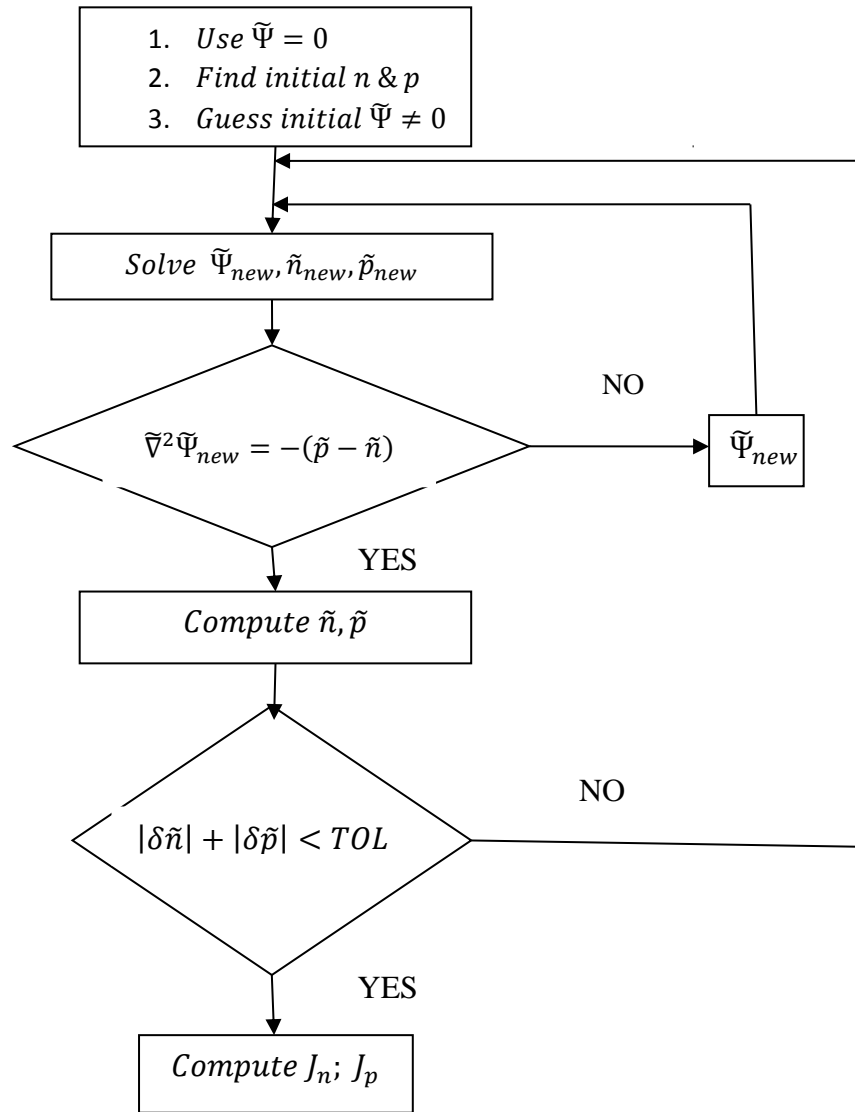


Figure 5.2: Schematics of iterative flow diagram for solving the basic continuum drift-diffusion equations model.

With the above guessed value of potential and using the initial equilibrium charge carrier densities (obtained at zero applied potential), a correction potential factor,  $\delta\Psi$ , to the guessed non-zero potential was computed from Poisson's equation. Subsequently, a

new potential was calculated using the value of the correction factor, so that ( $\Psi_{\text{new}} = \Psi_{\text{old}} + \delta\Psi$ ). The new potential obtained was then used to re-calculate the charge carrier densities from continuity equations. As shown in Figure 5.2, this numerical procedure was repeated iteratively until a convergence of the numerical drift-diffusion computer program code was attained.

### 5.4.5 Discretization of the OSC Device

To solve the DD equations with Gummel iteration scheme, the first step that has to be taken is to replace the continuous solar cell system with discrete finite difference grid points.<sup>[224]</sup> Thus, before solving the basic drift-diffusion equations, the entire OPV solar cell system was discretized into finite number of grids. This was done based on the finite difference representation of the OPV solar cell device. It enabled solving of the basic derivative DD equations at finite number of points within meshed OSC solar cell. A 2DG grid representation of the OPV device system that was used in the modeling and simulations J-V characteristics is shown in Figure 5.3. The grids were introduced by replacing all the derivatives of a function,  $f(i, j)$ , using a well-known forward (equation 5.28) or backward (equation 5.29) finite difference approximation. These equations are obtained by differences between grid points.<sup>[224]</sup> Thus,

$$\frac{\partial f_{i,j}}{\partial x} \approx \frac{f_{i+1,j} - f_{i,j}}{dx} \quad (5.28a)$$

and

$$\frac{\partial f_{i,j}}{\partial y} \approx \frac{f_{i,j+1} - f_{i,j}}{dy} \quad (5.28b)$$

or

$$\frac{\partial f_{i,j}}{\partial x} \approx \frac{f_{i,j} - f_{i-1,j}}{dx} \quad (5.28c)$$

and

$$\frac{\partial f_{i,j}}{\partial y} \approx \frac{f_{i,j} - f_{i,j-1}}{dy} \quad (5.28d)$$

where  $i$  and  $j$  are the respective  $x$  and  $y$  space coordinate indices of a given point in the grid. As shown in Figure 5.2, a regular mesh was formed by sets of these grid points. This resulted to a continuous mesh with intervals between the points that are specified by  $dx = (x_{i+1} - x_i)$  and  $dy = (y_{i+1} - y_i)$  for the  $x$  and  $y$  space coordinate indices, respectively.

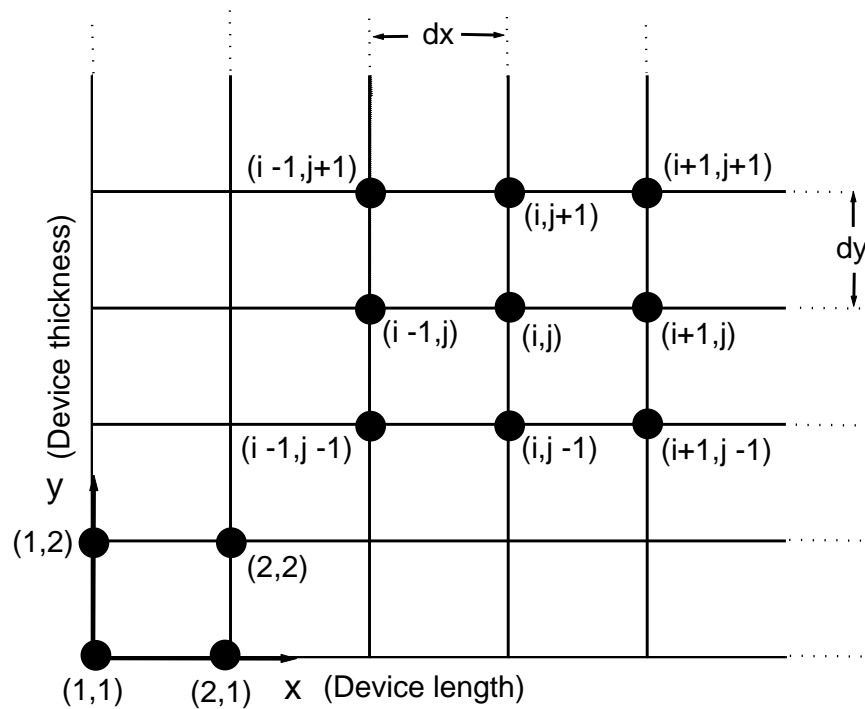


Figure 5.3: Typical 2D finite difference discretization of the OPV solar cell device

#### 5.4.5.1 Discretization of Poisson's Equation

The Poisson's equation (5.2) was first expanded using the forward difference approximation, equation (5.28). This led to:

$$\frac{a_x\psi_{i+1,j}-b_x\psi_{i,j}+c_x\psi_{i-1,j}}{(dx)^2} + \frac{a_y\psi_{i,j+1}-b_y\psi_{i,j}+c_y\psi_{i,j-1}}{(dy)^2} = RHS \quad (5.29a)$$

or equivalently to:

$$\frac{a_x\psi_{i+1,j}+c_x\psi_{i-1,j}}{(dx)^2} + \frac{a_y\psi_{i,j+1}+c_y\psi_{i,j-1}}{(dy)^2} - RHS = \frac{b_x\psi_{i,j}}{(dx)^2} + \frac{b_y\psi_{i,j}}{(dy)^2} \quad (5.29b)$$

where the right hand side term is given by  $RHS = -q(p - n)$  and the dielectric constant variables for the space coordinates x and y are given by:

$$a_x = \varepsilon_{i+1/2,j} \quad (5.30a) \quad a_y = \varepsilon_{i,j+1/2} \quad (5.30d)$$

$$b_x = \varepsilon_{i+1/2,j} + \varepsilon_{i-1/2,j} \quad (5.30b) \quad b_y = \varepsilon_{i,j+1/2} + \varepsilon_{i,j-1/2} \quad (5.30e)$$

$$c_x = \varepsilon_{i-1/2,j} \quad (5.30c) \quad c_y = \varepsilon_{i,j-1/2} \quad (5.30f)$$

One can now readily solve for the new potential,  $\psi_{i,j}$ , at a given grid point  $(i,j)$  from equations (5.29) and (5.30). This is given by:

$$\psi_{i,j} = \frac{\frac{a_x\psi_{i+1,j}+c_x\psi_{i-1,j}}{(dx)^2} + \frac{a_y\psi_{i,j+1}+c_y\psi_{i,j-1}}{(dy)^2} - RHS}{\frac{b_x}{(dx)^2} + \frac{b_y}{(dy)^2}} \quad (5.31)$$

#### 5.4.5.2 Discretization of Current Densities

The 2DG current densities for electron and hole are presented in equations (5.5) and (5.6), respectively. In 1DG, the equation for the electron, for example, can be rewritten as follows:

$$J = nq\mu_n \mathbf{F}_n + qD_n \frac{\partial n}{\partial x} \quad (5.32)$$

Using equation (5.7), equation (5.32) is readily modified. This modification gives:

$$J_{i+1/2} = n_{i+1/2}q\mu_{i+1/2}\mathbf{F}_{1+1/2} + kT\mu_{i+1/2}\frac{\partial n}{\partial x} \quad (5.33a)$$

or simply as,

$$a - n = \frac{kT}{qF} \frac{\partial n}{\partial x} \quad (5.33b)$$

where

$$a = \frac{J}{q\mu F} \quad (5.33c)$$

Note that the space index dependence of variables is sometimes purposely dropped for notational convenience. Rearrangement and subsequent integration of equation (5.33) gives:

$$\frac{qF}{kT} dx = -\ln \left( \frac{a-n_{i+1}}{a-n_i} \right) \quad (5.34a)$$

or equivalently written as:

$$a = \frac{n_{i+1}-n_i e^{-\lambda}}{1-e^{-\lambda}} \quad (5.34b)$$

where

$$\lambda = \frac{qF dx}{kT} \quad (5.34c)$$

Combining equations (5.33c) and (5.34b), one gets:

$$J = \frac{\mu kT}{dx} (n_{i+1} B_e(-\lambda) - n_i B_e(\lambda)) \quad (5.35)$$

where  $B_e$  the Bernoulli's function is given by:

$$B_e(z) = \frac{z}{e^z - 1} \quad (5.36)$$

Note also that the factor,  $\lambda$ , in equation (5.35) is related to the thermal energy,  $kT$ , by equation (5.34c). It can, therefore, be coupled with the thermal voltage,  $V_T$ . This is done based on the Einstein's equation (5.7), so that one arrives at:

$$\lambda = \frac{F_{i+1/2} dx}{V_T} \quad (5.37)$$

Furthermore, since the electric field strength,  $F$ , is given by:  $F = -\nabla\psi$ . Its forward difference approximation in 1DG gives:

$$F_{i+1/2} = -\left( \frac{\psi_{i+1} - \psi_i}{dx} \right) \quad (5.38)$$

Combining equations (5.37) and (5.38) leads to:

$$\lambda = -\left(\frac{\psi_{i+1}-\psi_i}{V_T}\right) \quad (5.39)$$

Inserting equation (5.39) into equation (5.35) results to the expression for the discretized current density for the electron in 1DG. It is given by:

$$J_{i+1/2} = \frac{\mu_{i+1/2}kT}{dx} \left[ n_{i+1}B_e \left( \frac{\psi_{i+1}-\psi_i}{V_T} \right) - n_iB_e \left( \frac{\psi_i-\psi_{i+1}}{V_T} \right) \right] \quad (5.40)$$

In 2DG, equation (5.40) is equivalently rewritten to give:

$$[J_n^x]_{i+1/2,j} = \frac{[\mu_n^x]_{i+1/2,j}kT}{dx} \left[ n_{i+1,j}B_e \left( \frac{\psi_{i+1,j}-\psi_{i,j}}{V_T} \right) - n_{i,j}B_e \left( \frac{\psi_{i,j}-\psi_{i+1,j}}{V_T} \right) \right] \quad (5.41a)$$

$$[J_n^y]_{i,j+1/2} = \frac{[\mu_n^y]_{i,j+1/2}kT}{dy} \left[ n_{i,j+1}B_e \left( \frac{\psi_{i,j+1}-\psi_{i,j}}{V_T} \right) - n_{i,j}B_e \left( \frac{\psi_{i,j}-\psi_{i,j+1}}{V_T} \right) \right] \quad (5.41b)$$

Similarly, the discretized current density equations for the hole in 2D space geometry can be obtained. These are given by:

$$[J_p^x]_{i+1/2,j} = \frac{[\mu_p^x]_{i+1/2,j}kT}{dx} \left[ p_{i,j}B_e \left( \frac{\psi_{i+1,j}-\psi_{i,j}}{V_T} \right) - p_{i+1,j}B_e \left( \frac{\psi_{i,j}-\psi_{i+1,j}}{V_T} \right) \right] \quad (5.42a)$$

and

$$[J_p^y]_{i,j+1/2} = \frac{[\mu_p^y]_{i,j+1/2}kT}{dy} \left[ p_{i,j}B_e \left( \frac{\psi_{i,j+1}-\psi_{i,j}}{V_T} \right) - p_{i,j+1}B_e \left( \frac{\psi_{i,j}-\psi_{i,j+1}}{V_T} \right) \right] \quad (5.42b)$$

### 5.4.5.3 Discretized Equations for Charge Carrier Densities

Starting with the current continuity equations (5.3) and (5.4), the discretization for the respective electron and hole densities were derived. The 2D space geometry derivative of the current density for electrons, for example, is given by:

$$\frac{\partial J_n^x}{\partial x} + \frac{\partial J_n^y}{\partial y} = -q(G - R_n) \quad (5.43)$$

This was expanded using the forward difference approximation. The expansion led to:

$$\frac{[J_n^x]_{i+1/2,j} - [J_n^x]_{i-1/2,j}}{dx} + \frac{[J_n^y]_{i,j+1/2} - [J_n^y]_{i,j-1/2}}{dy} = -q(G - R_n) \quad (5.44)$$

Hence, the discretized equation for the electron density was readily obtained by simply combining equations (5.41) and (5.44) to obtain:

$$n_{i,j} = \frac{e_{n1}n_{i+1,j}B_e(d_{n1})+e_{n2}n_{i-1,j}B_e(d_{n2})+e_{n3}n_{i,j+1}B_e(d_{n3})+e_{n4}n_{i,j-1}B_e(d_{n4})+GU_n}{e_{n1}B_e(-d_{n1})+e_{n2}B_e(-d_{n2})+e_{n3}B_e(-d_{n3})+e_{n4}B_e(-d_{n4})} \quad (5.45)$$

where  $GU_n$  is the generation-recombination rate for electrons and the other terms for charge carrier mobilities and potential at different grid points are defined by:

$$e_{n1} = \frac{\mu_{i+1/2,j}^n}{(dx)^2} \quad (5.46a) \quad d_{n1} = \frac{\psi_{i+1,j}-\psi_{i,j}}{V_T} \quad (5.46e)$$

$$e_{n2} = \frac{\mu_{i-1/2,j}^n}{(dx)^2} \quad (5.46b) \quad d_{n2} = \frac{\psi_{i-1,j}-\psi_{i,j}}{V_T} \quad (5.46f)$$

$$e_{n3} = \frac{\mu_{i,j+1/2}^n}{(dy)^2} \quad (5.46c) \quad d_{n3} = \frac{\psi_{i,j+1}-\psi_{i,j}}{V_T} \quad (5.46g)$$

$$e_{n4} = \frac{\mu_{i,j-1/2}^n}{(dy)^2} \quad (5.46d) \quad d_{n4} = \frac{\psi_{i,j-1}-\psi_{i,j}}{V_T} \quad (5.46h)$$

Similarly, the discretized equation for the hole density can be deduced. This is given by:

$$p_{i,j} = \frac{e_{p1}p_{i+1,j}B_e(d_{p1})+e_{p2}p_{i-1,j}B_e(d_{p2})+e_{p3}p_{i,j+1}B_e(d_{p3})+e_{p4}p_{i,j-1}B_e(d_{p4})+GU_p}{e_{p1}B_e(-d_{p1})+e_{p2}B_e(-d_{p2})+e_{p3}B_e(-d_{p3})+e_{p4}B_e(-d_{p4})} \quad (5.47)$$

where charge carrier mobilities and potential terms are now defined as:

$$e_{p1} = \frac{\mu_{i+1/2,j}^p}{(dx)^2} \quad (5.48a) \quad d_{p1} = \frac{\psi_{i,j}-\psi_{i+1,j}}{V_T} \quad (5.48e)$$

$$e_{p2} = \frac{\mu_{i-1/2,j}^p}{(dx)^2} \quad (5.48b) \quad d_{p2} = \frac{\psi_{i,j}-\psi_{i-1,j}}{V_T} \quad (5.48f)$$

$$e_{p3} = \frac{\mu_{i,j+1/2}^p}{(dy)^2} \quad (5.48c) \quad d_{p3} = \frac{\psi_{i,j}-\psi_{i,j+1}}{V_T} \quad (5.48g)$$

$$e_{p4} = \frac{\mu_{i,j-1/2}^p}{(dy)^2} \quad (5.48d) \quad d_{p4} = \frac{\psi_{i,j}-\psi_{i,j-1}}{V_T} \quad (5.48h)$$

## 5.4.6 Modeling of Non-ideal Photoactive-Anode Contacts

In an effort to investigate the effects of partial contacts on the performance of BJJ OSC systems, non-ideal contact features, with characteristics of voids (an ideal insulator layer) were assumed. These were then successfully introduced at the interface

between the transparent anode and the photoactive layers of the OPV solar cell system. As shown in the program code (Appendix A), the 2DG model enabled the incorporation of partial contacts (voids) at the interface with reasonable ranges of partial contact heights and contact lengths. This is illustrated further in Figure 5.4 for the simulated generation rate of the organic solar cell device.

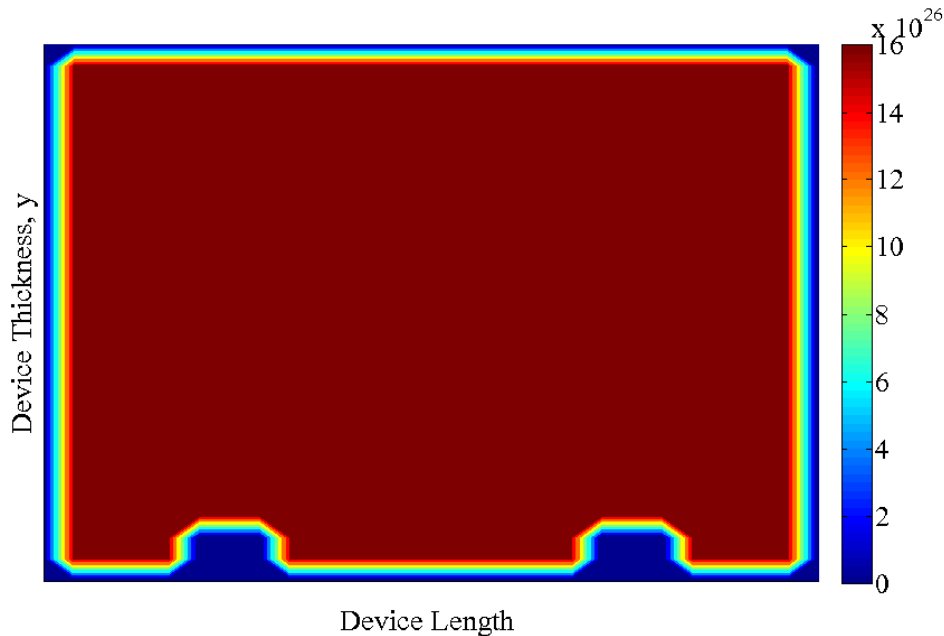


Figure 5.4: Generation rate demonstrating non-ideal contact of arbitrary  $L_c$  and  $H_c$

An ideal metal insulator semiconductor electronic configuration was assumed. In this consideration, the conductance of the void film between the transparent electrode and the photoactive organic semiconducting materials was set to be zero (the value for ideal insulation). The J-V characteristics of the solar cell were then simulated for the BHJ OPV device with perfectly planar interfacial/interlayer contacts, before simulation of the same OSC system with different carefully selected partial interlayer contacts. The simulation of OSC device with perfect planar contact was compared with the experimental J-V results of the same device, before varying the contact length,  $L_c$  between 10 – 80%. The partial

contact height,  $H_c$  was also changed between 0.1 – 0.5% of the device thickness of  $\sim 100$  nm<sup>[126]</sup> for each of the contact lengths that were investigated. This was done to mimic the effect of pressure<sup>[203]</sup> that is usually applied to reduce the adverse effects associated with partial contacts between the interlayers of organic electronic structures.

## 5.5 Results and Discussion

### 5.5.1 Effects of contact on the J-V characteristics

Figures 5.5 – 5.9 present the results obtained from the numerical modeling of the J-V characteristics of an OSC system with OC<sub>1</sub>C<sub>10</sub>-PPV:PCBM material structure. These show the dependence of open-circuit voltage,  $V_{OC}$  and short-circuit current density,  $J_{SC}$  on the different partial contacts at the interface between the photoactive organic materials and the transparent electrode. In order to test the effects of partial contacts on the performance of the solar cell, J-V curves based on different solar cell contact lengths and heights were simulated. The results obtained from the simulations for a device with perfect planar interface were compared to the experimental and numerical results of similar BHJ organic solar cell structure that were reported earlier by Koster and coworkers.<sup>[126]</sup>

Generally, the results show that only the  $J_{SC}$  of the OSC is significantly affected by the partial contacts at the photoactive/anode interfaces. The  $V_{OC}$  of the OSC system was steady, not influenced by the partial interfacial-contact phenomena. This can be attributed to the fact that the partial contacts between the transparent anode and the photoactive layer interface of BHJ OSC result to increases of series resistances,  $r_s$ . In agreement with the modeling results obtained, the changes in the  $r_s$  of solar cells have been shown to affect only the  $J_{SC}$  instead of the  $V_{OC}$  of organic PV devices.<sup>[155]</sup>

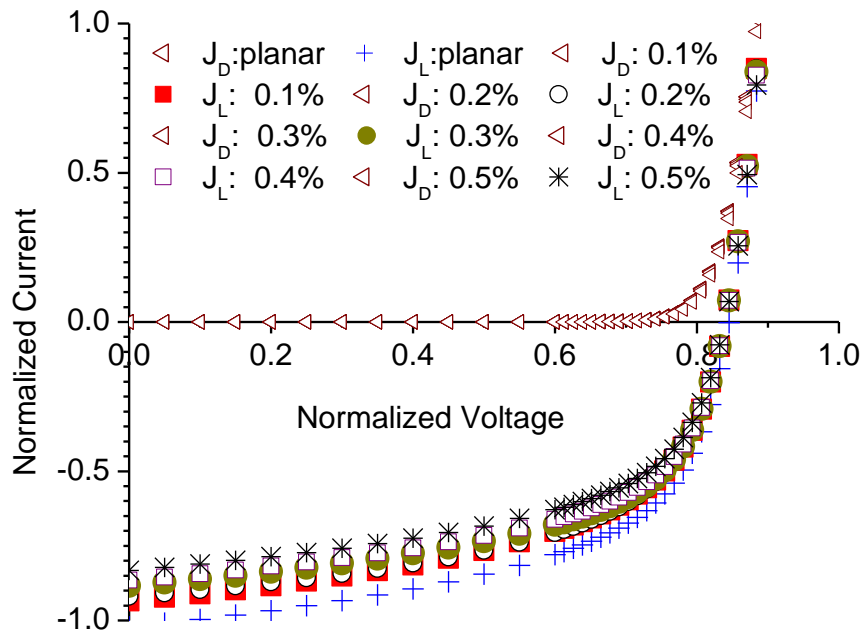


Figure 5.5: Influence of  $H_c$  on J-V curves of a BHJ OSC with  $L_c$  of 80%.

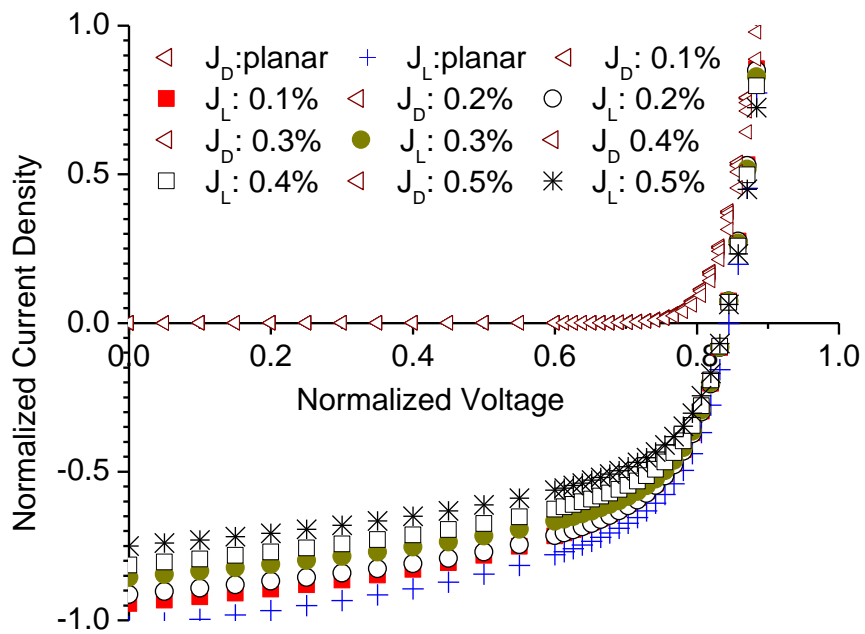


Figure 5.6: Influence of  $H_c$  on the J-V curves of a BHJ OSC with  $L_c$  of 60%.

Figure 5.5 shows the simulated J-V profiles of an OPV BHJ solar cell device as function of partial contact heights for the device with a fixed contact length of 80%. From the J-V characteristics, it is clear that the partial contact at the interface between the photoactive layer and the TE layer decreases the fill factor of the solar cells. The partial contact height due to void was increased arbitrary in the range of  $\sim 0.1 - 0.5\%$  of the device thickness of  $\sim 100$  nm.<sup>[126]</sup> The result shows that an increase in partial contact height affects only the illuminated current density of the device but not the dark current density. As mentioned above, it is clear from the plot that the effects of partial contacts dominated the short current as opposed to open circuit voltage of the solar cell J-V characteristics.

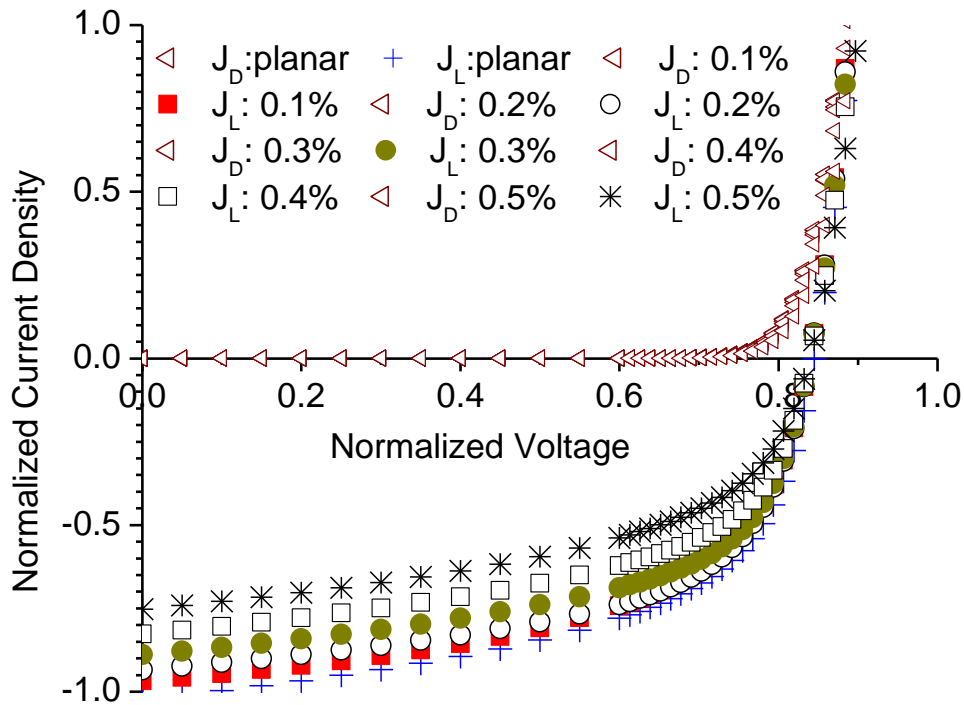


Figure 5.7: Influence of  $H_c$  on the J-V curves of a BHJ OSC with  $L_C$  of 40%.

The results of the J-V simulations obtained from an OSC device with contact lengths less than 80% are presented in Figures 5.6 – 5.9. These also show the dependence of electrical characteristics of organic BHJ solar cell systems on interfacial contacts as function of partial contact with heights between 0.1 – 0.5% of the device thickness. The results show that, with further decrease in planar contact length, down to between ~ 60-20%, the plots are more or less similar to that of an organic solar cell system with perfect planar structure with a difference that, values of short-circuit current and hence the FF of the solar cell are reduced strongly, with increasing partial contact lengths and heights at the interface between the photoactive organic layer and the transparent electrode layer.

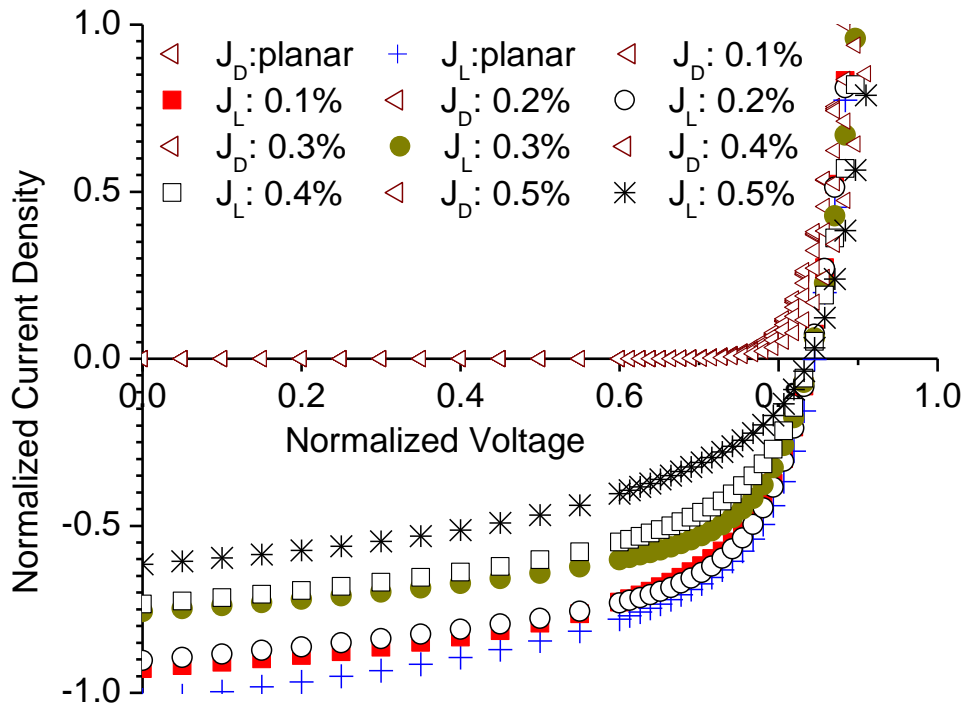


Figure 5.8: Influence of  $H_c$  on the J-V curves of a BHJ OSC with  $L_C$  of 20%.

The observed decrease in the  $J_{SC}$  and the FF of the OSC system are attributed to the increase in series resistance of the solar cell as a result of increasing partial contacts between the photoactive material and the transparent anode layers. Further increase in partial contacts stops some of the photo-generated free charge carriers from reaching the electrodes, for collection. Note that the ideal metal insulator semiconductor configuration was assumed in the modeling of charge carrier transport. However, for the very thin layer of the insulator (void) that were inserted between the photoactive and the transparent electrode layers, some basic charge transport phenomena such as tunneling and thermionic emissions may still prevail.

The charge transport mechanisms above, however, decrease strongly with increasing thickness of the partial contacts in terms of length and height. This effect explains the observed trends of the current density versus voltage, which decreased with increasing partial contact heights and lengths. Furthermore, the decrease in solar cell fill factor reflects the formation of space charges at the proximity of the void layer that were introduced at the interface between the photoactive and TE layers. Such space charges, once formed, act in a way that opposes the flux of free charge carriers from the device to the electrode for collection. Hence, at high partial contact lengths and heights, most of the free-charge carriers are most likely hindered from contributing to the PV effects, since they are congested by the space charge potential before being corrected at the terminals of the solar cells or wasted.

Furthermore, for the illuminated solar cells, the formation of space charges above is known to accelerate the rate of bimolecular recombination.<sup>[58]</sup> In this case, the observed decreases in the FF and  $J_{sc}$  are very likely due to the limitations arising from the space

charge density. The congested charge carriers due to partial contact will ultimately be destroyed by the accelerated bimolecular recombination rates, since all the free charge carriers that cannot be extracted from the devices are annihilated by recombination, the FF and  $J_{SC}$  of OSCs are expected to degrade with increasing partial contact lengths and heights as in Figures 5.5 to 5.8. This suggests that, in order to prepare efficient BHJ organic solar cells, interfaces must be carefully engineered to have planar contacts. The interfaces should be well controlled to have contact lengths between  $\sim 80$  (Figure 5.5) and 100% (the perfect planar device structure). This important in order to lower the associated interfacial series resistance, resulting from partial contacts, such voids. The series resistance should ideal be low enough to enable the dissipation of the photocurrent produced by the solar cell into the external circuit via the electrodes.

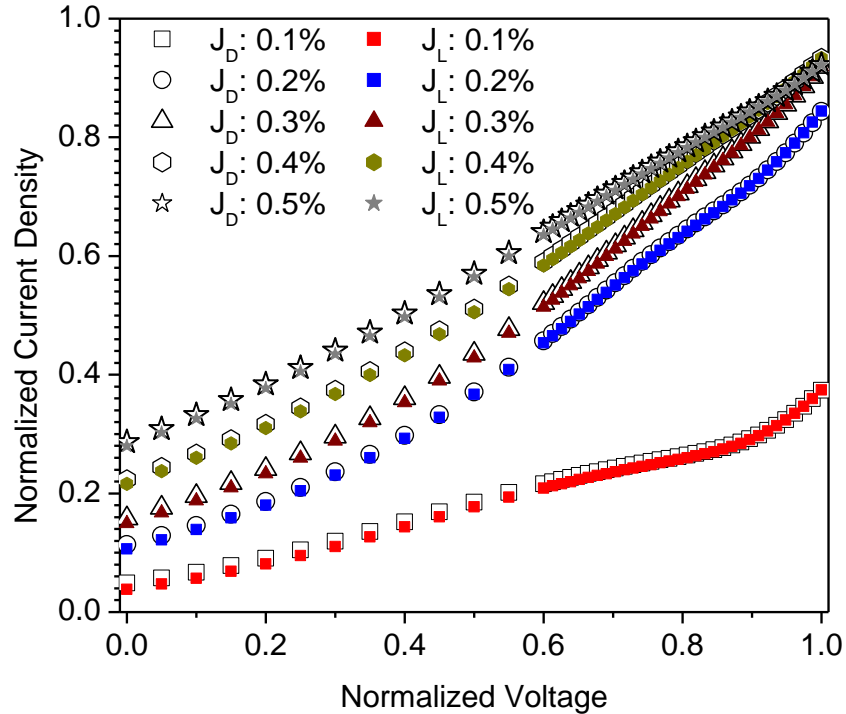


Figure 5.9: Influence of contact height,  $H_c$  on the J-V curves a BHJ OSC with  $L_c$  of 10%.

Figure 5.9 shows the simulated J-V characteristics of an organic BHJ solar cell with a contact length of ~ 10% and different heights. The result shows clearly that with further decrease in the planarity of interlayer/interfacial contacts, the PV device lost all of its solar cell J-V characteristics. It evolved from solar cell to an almost conversional Ohmic resistor with nearly a linear J-V profile. This can be explaining the similar mechanism of charge congestion and their successful annihilation as a result of increasing interfacial/interlayer partial contacts. Owing to the additional space charge limited transportation of photogenerated electrons and holes, there appears an associated increase in series resistance. This led to distortion of the device characteristics changing it from solar cell to a resistor-like system. Thus, since at high partial contact lengths and heights majority of free charge carriers are prevented from reaching the electrodes for proper collection, the PV effects are completely dampened.

### 5.5.2 Influence of contact on potential and carrier distributions

Modeling calculations were also used to explore the potential of BHJ organic solar cell systems. The potential distribution,  $\psi$ , in a given dielectric system is related to its energy distribution, E by:

$$E = -q\psi \quad (5.49)$$

In OSC systems, therefore, the potential plays a key role in influencing the nature of the local hetero-junction structures that are formed between the donor and acceptor molecules. According to the modeling results (Figure 5.10), it is observed that in the whole range of contact lengths (between 80 – 10%) that were explored, the potential increased with decreasing planar contact length. Furthermore, for partial contact height (between 0.1 – 0.5% of the 100 nm solar cell thickness), the  $\psi$  also increases with partial

contact height at the interface between photoactive material and the transparent anode layers of OSC systems.

For the 80% contact length, however, all the heights ( $\sim 0.1 - 0.5\%$  of the device thickness) have their potential distributions slightly different, but very close to the potential of the OSC structures with perfectly planar interfaces. This is in agreement with Figure 5.5 in which the J-V characteristics are shown to resemble closely the characteristics of an organic solar cell with perfectly planar contact length. This suggests further the likely optimum contact lengths to be between 80 and 100%. On the contrary, for organic BHJ solar cell with contact lengths below 80%,  $\psi$  increases spectacularly with the partial contact height at the photoactive/transparent electrode interface of the device.

The trend observed in the J-V characteristics of an OSC structure with different partial interfacial contacts could also be attributed to the formation of fully developed space charge potential, around the interfacial insulating (void) layers that were introduced. These potentials due to space charges at the interface act in a way that opposes the flow of photogenerated free charge carriers. Such counter effects that occur from space charges are also known to cause sub-linear dependence of short-circuit current on the light intensity, thus reducing PCEs of PV solar cell system.<sup>[242]</sup> This confirms the pattern of the J-V characteristic profiles as function of partial contact lengths and heights as shown clearly in Figures 5.5 – 5.9.

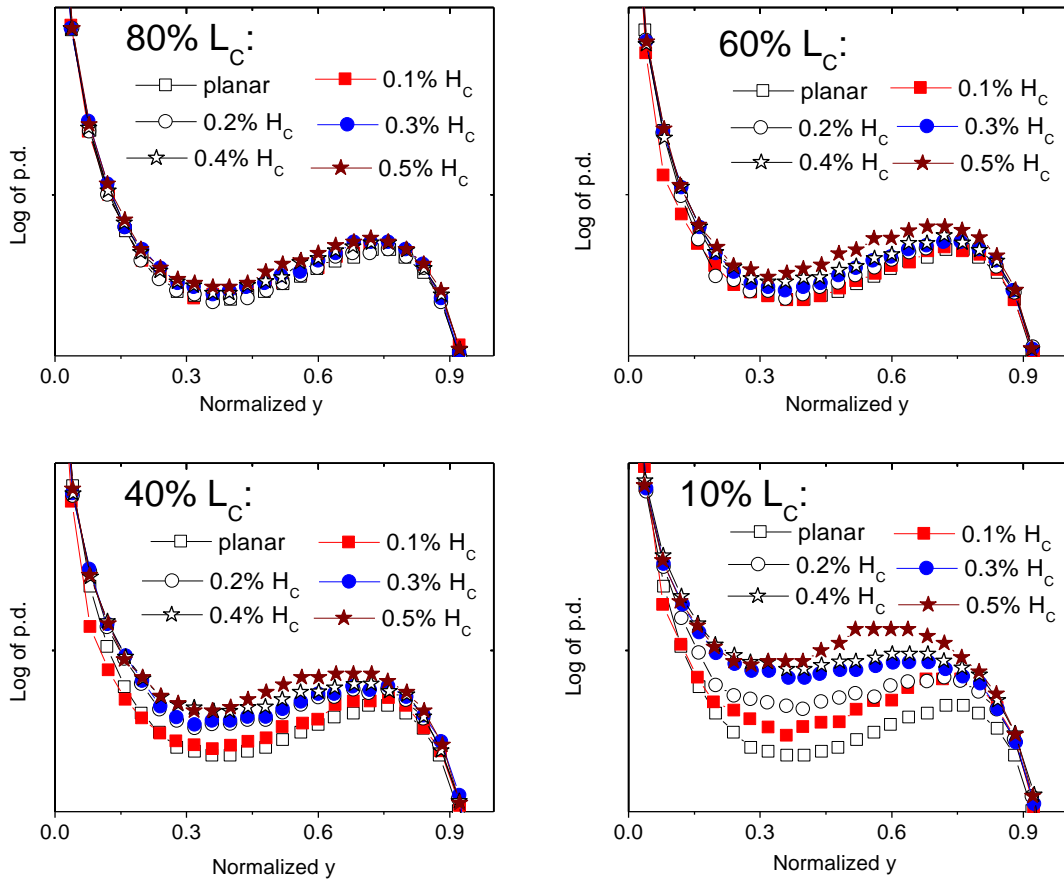


Figure 5.10: Evolution of p.d with different contact lengths,  $L_c$ , and partial contact,  $H_c$ , captioned.

Figure 5.11 illustrates the dependence of charge carrier distribution on the interlayer contacts between the photoactive material and the transparent anode with different contact lengths and different partial contact (void) heights. The result shows clearly that the carrier density trend is more or less similar to that of inorganic solar cell systems with a difference that, the value of equality  $np = n_i^2$  was not clearly maintained at both ends ( $y=0$  and  $y=t$ ) of the OSC structure. The result shows also that the

distribution of charge carrier densities, within BHJ organic solar cells is not significantly affected by the partial contact features, due to voids that were introduced at the interface between photoactive organics and TE layers.

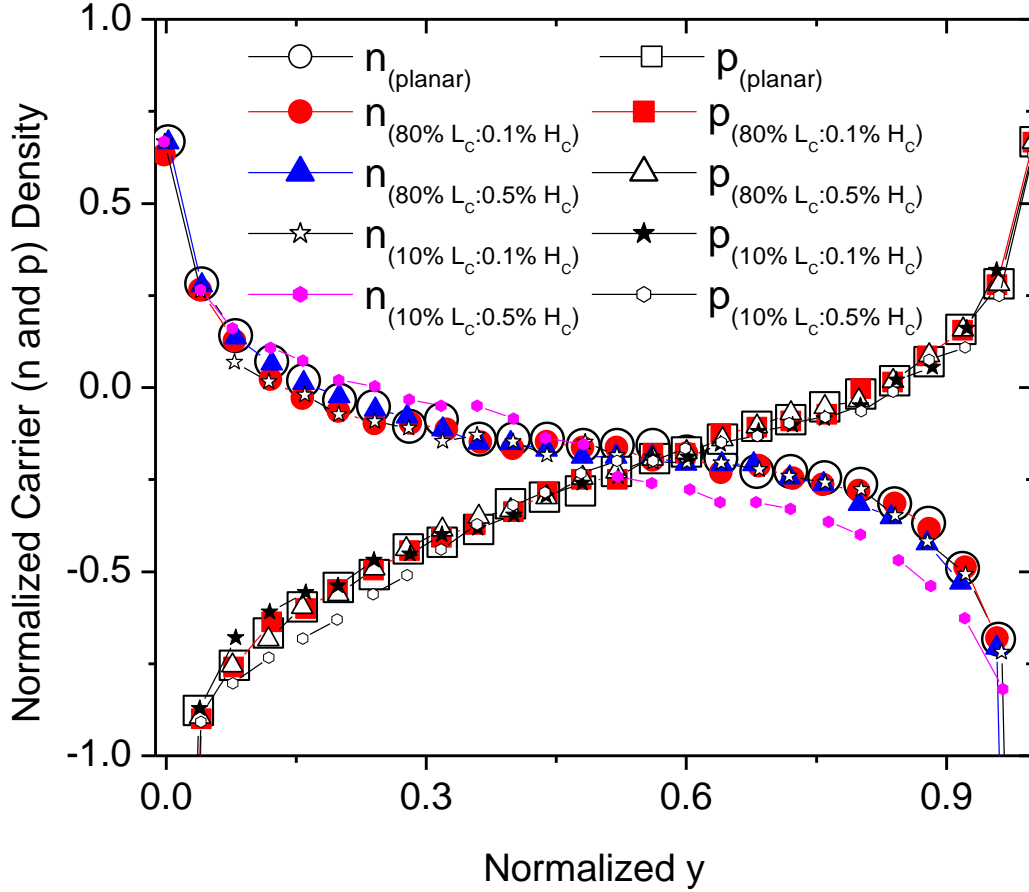


Figure 5.11: Evolution of charge carrier (p and n) densities with contact length and partial contact height at the photoactive/transparent anode of a BHJ OSC.

### 5.5.3 Evaluation of the Numerical Results

In order to test the reliability of the numerical results above, simulations were performed on similar organic BHJ solar cell structure with perfectly planar interlayer

contacts. The modeling results were then compared with experimental and numerical J-V characteristics that were obtained earlier by Koster *et al.*<sup>[126]</sup> for similar organic BHJ solar cell structures. The experimental<sup>[126]</sup> and simulated J-V characteristics are shown in Figure 5.12. It observed that, the fits of the model to the experimental profiles are in good agreement with the data that were obtained for both dark and illuminated organic solar cell. This suggests that the conditions that were assumed in the models and the numerical simulations of an organic solar cell with perfectly planar and partial contacts are closely mimicking the actual charge carrier transfer interfaces in the actual structures of BHJ OSC systems.

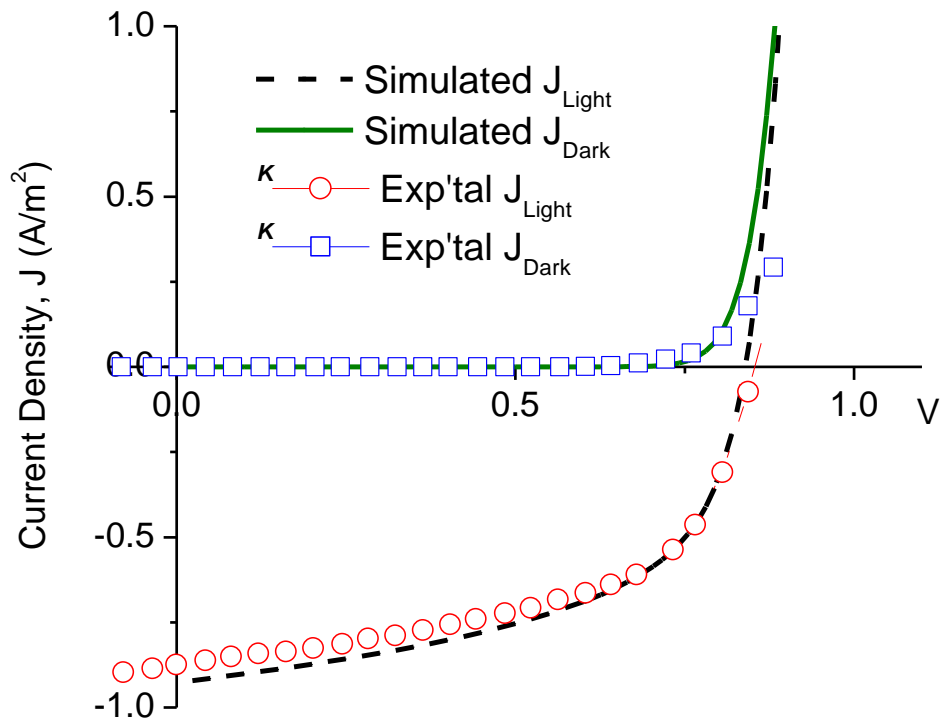


Figure 5.12: Comparison of J-V characteristics of an OPV solar cell system with perfect planar interface with experimental profiles (<sup>K</sup>) adapted from Koster *et al.*<sup>[126]</sup>

## 5.5.4 Implications and Concluding Remarks

The two-dimensional modeling and simulations of interfacial/interlayer contacts presented in this chapter revealed salient implications that are relevant to the design of BHJ OPV solar cell systems and other organic electronic devices. Some of these implications, as well as some concluding remarks arising from the organic solar cell modeling work are presented below:

- i. The results obtained showed clearly that, the transportation and collection of the photogenerated charge carriers across the interface between photoactive organics and the transparent anode layers of organic PV devices are significantly affected by partial contacts at the interfaces. Furthermore, the model showed that the interfacial/interlayer partial contact effects can reach appreciable levels, under certain critical partial contact lengths and heights, at which the OPV devices become completely malfunctioned. This suggests that, keen engineering efforts are greatly need to control any possible causes of partial contacts between the material components of PV devices and other electronic devices and optoelectronic systems. Generally, this can be achieved, in actual devices, using clean environments (glove boxes) along with well-controlled applied pressure to compress the voids and other defects at the interfaces of the solar cell systems.<sup>[203]</sup>
- ii. Also, the J-V characteristic results have shown that partial contacts at the photoactive/anode interface of BHJ organic solar cell systems lead to series resistance, which increases with decreasing contact lengths and increasing partial contact heights. Higher series resistance is undesirable for better performance of OPV BHJ solar cells. This led to the decrease in the short-circuit current and reduced the

fill-factor of the OPV solar cell. The model showed that the OPV solar cell open-circuit voltage characteristics are independent of the partial contact lengths and heights that were simulated. This suggests that, either the shunt resistance of the solar cell is unaffected by the photoactive/transparent anode interface or the 2DG model used in this study is inadequate to probe the influence of interface features on the shunt resistance of BHJ OPV solar cell systems.

- iii. Considering the latter suggestion in number ii above and the reality in fabrication of the BHJ OPV solar cell devices, further work is clearly needed to further modify and refine the 2DG drift-diffusion models in a way that can make them more broad to address the most complex interfacial/interlayer optoelectronic processes and dimensional morphological issues that influence the operation mechanisms of polymer BHJ solar cells. Such efforts to extend the 2DG DD models should attempt to include within the non-ideal partial (void/insulator) layer the possible forms of charge carrier transports, such as thermionic emission and the different quantum charge tunneling.
- iv. Since the J-V results showed that the OPV BHJ solar cell PCE is greatly deteriorated by interfacial/interlayer partial contacts, which worsened further with increasing partial photoactive/anode interlayer contact height, one could consider extending the 2DG DD model, presented in this study, to take into account the effects of applying well-controlled pressure to curb systematically the observed effects of partial contact heights, using reasonable numerical modeling and simulation approaches, as well as with actual experimental studies.

# 6. Chapter Six

## Implications, Concluding Remarks and Suggestions for Future Work

### 6.1 Implications of the Study

The practical implications of the results presented in this dissertation are quite significant. First, the Haacke Figures of Merit obtained for the model multilayered ZAZ thin film composite electrodes are comparable to those reported earlier for the conventional ITO-based electrodes that have HFoM values between  $\sim 2.07 \times 10^{-3}$  and  $3.82 \times 10^{-2} \Omega^{-1}$ .<sup>[202]</sup> This suggests that the multilayered ZAZ thin film composite structures have the potential to compete with and replace ITO-coated TCO substrates in future TEs and anodes in solar cells, light emitting devices and other electronics and optoelectronic components. The attractive combinations of optical and electrical properties are also promising for potential applications of the model multilayered ZAZ thin film composite TEs in organic solar cells and organic light emitting devices.

The experimental mid-layer Al thicknesses corresponding to the low resistivities were generally in good agreement with predicted optimum transmittance spectra in thinner mid-Al films ( $\sim 1 - 10$  nm), for solar spectrum with wavelengths of between  $\sim 300 - 900$  nm. This suggests that the numerical simulations captured the essential physics of the multilayered ZAZ thin film composite structures, as transparent electrodes. Hence, for this particular ZAZ thin film composite system and the other highly conductive metals such as gold, silver and copper with known optical constants,<sup>[188]</sup> the numerical method presented in this study can be used to obtain reasonable predictions of optical Ts

and the associated ZnO and intermediate metallic layer thicknesses for the design of transparent nano-film composite electrodes. Also, the measured electrical properties revealed realistic transparent electrode sheet resistances and resistivities, in agreement with those reported earlier for the substrates coated with standard ITO TCO thin films that have resistivities in the range of  $\sim 1 \times 10^{-4} - 3.03 \times 10^{-3} \Omega cm$ .<sup>[89,111,202]</sup>

Furthermore, since the working principles of organic solar cells, organic light emitting diodes and other organic electronics and optoelectronic devices require electric fields<sup>[9]</sup> for the dissociation (in solar cells) or recombination (in light emitting diodes) of free electrons and holes, layered sandwich organic solar cells and organic light emitting device structures<sup>[1,9]</sup> with electronically photoactive organic semiconducting materials are usually integrated with electrodes with large and small work functions such as ITO and Al, whose work functions are between  $\sim 4.6 - 4.7 eV$ <sup>[9,72]</sup> and  $4.28 eV$ ,<sup>[73]</sup> respectively. In comparison, ZnO has an effective work function of  $\sim 4.45 eV$ ,<sup>[73]</sup> which is sufficiently large comparable to that of ITO-coated TCO substrates.

Also, numerical modeling of charge transport was successfully used to investigate some of partial and planar contact phenomena that are relevant in a photoactive/anode layer interface of organic solar cells. The effect of partial contacts is detrimental to the short-circuit current and the fill-factor of organic solar cells. The findings also show that the open-circuit voltage are not influenced by partial contact features at the photoactive/anode layer interface of OPV solar cell devices. The model was also used to capture the evolutions of electric potential, and carrier density (holes and electrons) distributions within the BHJ organic solar cell, as function of contact lengths and partial contact heights. The distribution of carrier densities across the device was not

significantly affected by the partial contact features. The potential, however, increased with increasing partial contact height at the photoactive/transparent electrode interface of the device, while exhibiting more or less insignificant changes with increasing interlayer contact length of the device. These can be used to guide the design and fabrication of organic solar cells with improved interfacial/interlayer contacts and device PCEs.

## **6.2 Summary and Concluding Remarks**

This work has introduced an important study towards the development of layered composite thin films for cost-efficient transparent organic solar cell electrodes. It consequently presents the combined experimental, numerical and theoretical results of the transparent conductive properties of multilayered composite ZAZ thin film structures. These structures have the potential for applications as improved anodes and transparent electrodes in layered organic solar cells and other active and passive optoelectronic devices and components. Optical simulations were carried out for structures with Al interlayer thicknesses between  $\sim 1 - 100$  nm. The numerical results suggest that lower thicknesses (between  $\sim 1 - 10$  nm) of mid-layer Al result in improved spectral Ts of the model multilayered ZAZ thin film composites stacks.

Within this range of optimum intermediate layer Al thicknesses, the numerical optical results compare favorably with the experimental optical property measurements obtained from the model multilayered ZAZ thin film composite structures with similar interlayer thicknesses. High transparent conductive properties were achieved in the annealed multilayered ZAZ thin film sandwiches deposited on glass substrates by RF magnetron sputtering method. The multilayered ZAZ thin film composite structures were characterized by examining the effects of Al mid-layer thicknesses between  $\sim 1 - 10$  nm

on the structural, optical and electrical properties. The multilayered ZAZ thin film composite stacks annealed at 400°C for 90 minutes exhibited high crystalline structures which decreased with increasing Al mid-layer thickness.

The average numerical and experimental visible solar T spectra of the model multilayered ZAZ thin film composite structures obtained were between ~ 75 – 90%. The electrical resistivity and sheet resistance of the model multilayered ZAZ thin film composite structures decreased with increasing mid-Al layer thickness between ~ 1 – 10 nm. The corresponding apparent optical bandgap energy increased with increasing mid-Al layer thickness. The multilayered ZAZ thin film composite structures with mid-layer Al thicknesses in the range of ~ 7 – 10 nm had low resistivity values between  $3.62 \times 10^{-4} - 8.07 \times 10^{-4} \Omega cm$ . Within this range, the model multilayered ZAZ thin film composite electrodes had optical bandgap energies of between ~ 3.6 – 3.84 eV and average solar Ts that were above 85% in the visible region of the solar spectrum.

For the mid-layer Al thickness of ~ 8 nm, the model multilayered ZAZ thin film composite structures exhibited the best Haacke figure of merit of ~  $4.72 \times 10^{-3} \Omega^{-1}$  and an electrical resistivity of  $4.91 \times 10^{-4} \Omega cm$ . This resistivity values as well as the lowest experimental sheet resistance values of ~ 7.25  $\Omega/sq$ . that were achieved compare favorably to the transparent conductive properties of commercially available ITO-coated substrates, for which resistivities of ~  $1 \times 10^{-4} \Omega cm$  have been reported.<sup>[89]</sup> This suggests that the optoelectronic properties of multilayered ZAZ thin film composite electrodes synthesized compare well to those of ITO-coated TCOs that are used currently in organic solar cells and light emitting devices. It also indicate that the model multilayered ZAZ thin film composite electrodes are potentially good candidates as cost-

effective materials alternatives to costly transparent ITO or ITO/metal/ITO anodes for applications in large area solar cells, light emitting diodes and other electronics and optoelectronic devices with active and/or passive technologies.

Furthermore, a precise 2DG drift-diffusion model for modeling and simulations of BHJ organic PV solar cells is described. Among the significance of the modeling method presented, is the simplicity of the computer code that was developed in a Matlab software package. This enabled easy modifications and implementation of the program source code on simple computer systems, such as moderate laptops, with improved iteration scheme convergence, high level of accuracy and preciseness attained.

Also, the model was successfully used to investigate some of the partial and planar phenomena in photoactive/transparent anode layer interfaces of BHJ organic PV structures. While the  $V_{OC}$  of the OSC was shown to remain steady with changing partial contact lengths and heights, the results show that the  $J_{SC}$  of OSCs is significantly affected by the partial contacts at the photoactive/anode interface of the OPV devices. The numerical results were tested and validated with experimental solar cell data from literature.<sup>[126]</sup> Comparably, good agreements were achieved between the numerical and experimental J-V characteristic curves of BHJ organic solar cells with  $OC_1C_{10}$ -PPV/PCBM materials with perfect planar-interface BHJ solar cell structures.

### **6.3 Suggestions for Future Work**

The research of transparent electrodes is obviously very far from being exhausted. The search for cost-effective TCO materials that could compete with and replace indium based TCO-coated substrate must neither be restricted to the traditional TCOs (oxide thin films of In, Sn and Zn) nor to their conventionally doped oxide films. The final goal of

this project is, therefore, to develop an organic solar cell TE system based mainly on multilayered ZnO thin film composite structures with highly conducting transparent intermediate nanolayers of aluminum. Despite the results and fresh insights obtained on the course of this study, which fulfill clearly some of the performance characteristics of transparent organic solar cell electrodes, there is still the need for further research to prepare the composite electrodes for future applications. This includes research that addresses the following open issues:

### **6.3.1 The Multilayered ZAZ Thin Film Composite Electrodes**

The crystalline structure of multilayered ZAZ thin film composite structures has been described and shown to affect both the electrical and optical performances, at the optimum mid-layer Al thickness between  $\sim 1 - 10$  nm. However, further studies must be done to refine the design of multilayered ZAZ thin film structures in a way that can resolve the observed decrease in the crystallinity of the multilayered ZAZ thin film stacks associated with incorporated intermediate nanolayer of Al. Some experimentally-coupled calculations should also be developed to determine appropriately the non-stoichiometric ZnO defect structures that are formed during heat treatment of the multilayered ZAZ thin film composite structures at reasonable ranges of annealing temperature and dwelling durations. These might include investigations of efficient physical and opto-electronic methods for the fabrication and optimization of prototype ZnO and mid-Al layers, to verify the performance properties of model multilayered thin film electrodes.

These will ultimately improve the effective charge and light transport across the model multilayered ZAZ thin film composite electrodes. There is, therefore, a need to explore further the simultaneous effects of the different deposition techniques, deposition

conditions, annealing temperatures and mid-layer Al thicknesses on the crystal structure, morphology, charge and light transport in multilayered ZAZ thin film composite structures.

### **6.3.2 The Organic Solar Cell**

Since the multilayered ZAZ thin film composite electrodes produced in this study are proposed for efficiency optimization of BHJ organic solar cell systems, there is a need to study their use in actual organic solar cells. Therefore, the use of multilayered ZAZ thin film TCEs alternatives to ITO-coated substrates remains the final goal to reduce further the cost of potentially cheap organic PV systems. For that purpose, the integration and implementation of the multilayered ZAZ thin film composite electrodes with a BHJ organic solar cell structures should be studied and tested accordingly. A dedicated work is required to test the performance of the composite TCEs in actual organic solar cell systems and organic light emitting devices.

Such work should explore the current-voltage J-V characteristics; fill factors, power conversion and external quantum efficiencies, degradation mechanisms and the long term overall performance characteristics of organic solar cells and organic light emitting devices fabricated with multilayered ZAZ thin film composite electrodes on rigid transparent glass substrates. These are clearly some of the challenges and opportunities for future work. Such work is particularly important due to the limited abundance and availability of indium (used in ITO thin film coated substrates) for the wide range of applications in active and passive electronics and optoelectronic structures and components.

In addition to the the realization and implementation of the multilayered ZAZ thin film composite electrodes with organic solar cell systems, efficient operation of OPV solar cell devices will require an accurately synchronized operation of the interface of the materials and interlayers of the OSC structures. Well controlled interfacial/interlayer strategy should, therefore, be developed to ensure an efficient, reliable and secure engineering of contacts in BHJ OSC structures. The proposed interfacial/interlayer 2DG DD contact model developed in this study, for improving PCEs of BHJ OSC systems needs to be experimentally implemented and evaluated. BHJ OSC structures with similar materials used in the 2DG modeling need to be produced with or without controlled pressure to mimic the simulated planar and partial contacts and evaluation of the pressure effects on the overall performance of the OPV solar cell devices.

Furthermore, the development, search and/or appropriate modifications of the existing semiconductor devices and/or solar cell models to explain the J-V characteristics of OPV solar cell systems is far from being exhausted. The modeling of organic semiconductor devices and OSCs is neither restricted to the 1DG DD models, in the literature nor to the 2DG model suggested in this dissertation. However, these two models are the widely studied and the most promising models for the investigation of organics and inorganic semiconductor devices. An attempt can, therefore, be made to expand the presented 2DG drift-diffusion model of BHJ OSCs in a three-dimensional (3D) space modeling and simulation geometry. This could likely lead to the broadly extended, more comprehensive modeling tools that can enable analyses of the broad complex 3D features found inherently in organic PV and other organic electronic materials and organic semiconductor devices. These may include the analysis of the active

layer polymer morphological and non-uniformity nature of the entire BHJ OPV solar cell and other organic electronic structures.

The extension of the 2DG DD model in a 3D geometry and modeling approach could also enable direct accounting for the effects of applied pressure on the evolution of the J-V characteristics of OPV solar cell systems and their components. This can then be used to estimate the possible pressure ranges, based on the compliances and robustnesses of a given OPV material parameters, before testing and confirming them in the actual laboratories with actual organic solar cell specimens, fabricated with or without such predicted values of the applied pressure.

In addition, the prospects of contacts at the photoactive/transparent anode interfaces of BHJ OPV systems, can as well be studied using other simulations and modeling tools. These may include modeling of organic solar cell with other modeling techniques such as Monte-Carlo simulations and finite element models. Comparisons of the results obtained from those modeling techniques could then be made with the J-V results presented in this study and also with the actual experimental results of organic PV solar cells and their electronic components.

The combination of modeling and experimental results above would lead, ultimately, to a more comprehensive conclusion about the effects and prospects of non-ideal interfacial/interlayer contacts in Polymer: Fullerene BHJ solar cell systems. They could also lead to a very insightful benchmark for the development of organic solar cell systems their appropriate components with improved interlayer contacts, as well as the possible technical suggestions to address some of the open issues that have been identified in the course of this dissertation work.

# References

- [1]. N. Grossiord, M. J. Kroon, R. Andriessen and M. W. P. Blom: Degradation Mechanisms in Organic Photovoltaic Devices. *Organic Electronics* **13**, 432–456, 2012.
- [2]. T. Ameri, G. Dennler, C. Lungenschmied and J. C. Brabec: Organic Tandem Solar Cells: A Review. *Energy Environ. Sci.* **2**, 347–363, 2009.
- [3]. S. N. Lewis, G. Crabtree and others: Basic Research Needs for Solar Energy Utilization: Report of the Basic Energy Sciences Workshop on Solar Energy Utilization," [http://www.sc.doe.gov/bes/reports/files/SEU\\_rpt.pdf](http://www.sc.doe.gov/bes/reports/files/SEU_rpt.pdf) , (U.S.), 2005.
- [4]. Z. Sun, R. K. Zhang, H. H. Xie, M. Liang, R. H. Du and S. Xue: Influence of 4-N,N-dimethylaminopyridine on the Photovoltaic Performance of Dye-sensitized Solar cells with Poly(ethyleneoxide)/oligo(ethylene glycol) Blend Electrolytes. *Electrochimica Acta* **56**, 7555–7562, 2011.
- [5]. R. H. Bossert, C. J. J. Tool, J. A. M. van Roosmalen, C. H. M. Wentink and M. M. J. Vaan de: Thin-film solar cells - Technology Evaluation and Perspectives, 2000.
- [6]. S. E. Shaheen, D. S. Ginley and G. E. Jabbour: Organic-Based Photovoltaics: Towards Low-Cost Power Generation. *MRS Bull.* **30**, 10-19, 2005.
- [7]. P. Kumar and S. Chand: Recent Progress and Future Aspects of Organic Solar Cells. *Prog. Photovolt: Res. Appl.* **20**, 377–415, 2012.
- [8]. A. Goetzberger, C. Hebling and H. W. Schock: Photovoltaic Materials, History, Status and Outlook. *Materials Science and Engineering R* **40**, 1–46, 2003.
- [9]. H. Spanggaard and C. F. Krebs: A Brief History of the Development of Organic and Polymeric Photovoltaics. *Solar Energy Materials & Solar Cells* **83**, 125–146, 2004.
- [10]. S. O. Kasap, *Principles of Electronic Materials and Devices*, 3rd ed., New York: Mc Graw Hill, 1997, pp. 473-554.
- [11]. US EIA - Energy Information Administration: International Energy Outlook 2013. 25 July 2013. [Online]. Available: <http://www.eia.gov/forecasts/ieo/world.cfm>. [Accessed 16 June 2014].
- [12]. S. Olz, R. Sims and N. Kirchner: Contribution of Renewables to Energy Security," International Energy Agency (IEA Information Paper), OECD, 2007.
- [13]. WE Council: Survey of energy Resources, World Energy Council, 2004. [Online]. Available: [www.worldenergy.org](http://www.worldenergy.org). [Accessed 28 January 2013].
- [14]. T. M. Tong and W. O. Soboyejo: Adhesion and Interfacial Fracture: From Organic Light Emitting Devices and Photovoltaic Cells to Solar Lanterns for Developing Regions. Dissertation: Princeton University, NY, September 2012.
- [15]. IE Agency: Key World Energy Statistics 2005, International Energy Agency, 2005. [Online]. Available: [www.iea.org](http://www.iea.org). [Accessed 28 January 2014].
- [16]. WE Council: Global Energy Scenario to 2050 and Beyond, World Energy Council, July 2004. [Online]. Available: [www.Worldenergy.org](http://www.Worldenergy.org).

- [17]. IUCN, The World Conservation Union and the World Bank Group. Large Dams: Learning from the Past, Looking at the Future; Workshop Proceeding, " IUCN, Gland, Switzerland and Cambridge, UK and the World Bank Group, Washington, DC. v. + 145, pp 41-102, July 1997.
- [18]. D. Weisser, M. Howells and H.-H. Rogner: Nuclear Power and Post-2012 Energy and Climate Change Policies. *Environmental Science & Policy* **11**, 467-477, 2008.
- [19]. M. D. S. Hossain, N. Amin, M. A. Matin, M. M. Aliyu, T. Razykov and K. Sopian: A Numerical Study on the Prospects of High Efficiency Ultra Thin ZnxCd1-xS/CdTe Solar Cell. *Chalcogenide Letters* **8** (3), 263-272, 2011.
- [20]. EU-Directive 2002/95/EC: Restriction of the Use of Certain Hazardous Substances in Electrical and Electronic Equipment (RoHS). *Official J. European Union* **46** (L37), 19-23, 2003.
- [21]. EU-Directive 2002/96/EC: Waste Electrical and Electronic Equipment (WEEE). *Official J. European Union* **46** (L37), 24-38, 2003.
- [22]. H. W. Schock and R. Noufi: CIGS-based Solar Cell for the Next Millennium. *Prog. Photovolt. Appl.* **8**, 151-160, 2000.
- [23]. R. A. Murphy, M. J. Jean and M. J. Fréchet: Organic Semiconducting Oligomers for Use in Thin Film Transistors. *Chem. Rev.* **107**, 1066-1096, 2007.
- [24]. K. R. Choudhury, J. Subbiah, S. Chen, P. M. Beaujuge, C. M. Amb, J. R. Reynolds and F. So: Understanding the Performance and Loss-mechanisms in Donor–acceptor Polymer Based SolarCells: Photocurrent Generation, Charge Separation and Carrier Transport. *Solar Energy Materials & SolarCells* **95**, 2502–2510, 2011.
- [25]. J. Williams and A. B. Walker: Two-dimensional Simulations of Bulk Heterojunction Solar Cell Characteristics. *Nanotechnology* **19**, 424011, 2008.
- [26]. B. Verreet, S. Schols, D. Cheyns, B. P. Rand, H. Gommans, T. Aernouts, P. Heremans and J. Genoe: The Characterization of Chloroboron (III) Subnaphthalocyanine Thin Films and Their Application as a Donor Material for Organic Solar Cells. *J. Mater. Chem.* **19**, 5295–5297, 2009.
- [27]. G. Dennler, M. C. Scharber and C. J. Brabec: Polymer-Fullerene Bulk-Heterojunction Solar Cells. *Adv. Mater.* **21**, 1323–1338, 2009.
- [28]. J. Jung, D. L. Kim, S. H. Oh and H. J. Kim: Stability Enhancement of Organic Solar Cells with Solution-processed Nickel Oxide Thin Films as Hole Transport Layers. *Solar Energy Materials & Solar Cells* **102**, 103–108, 2012.
- [29]. M. Riede, T. Mueller, W. Tress, R. Schueppel and K. Leo: Small-molecule Solar Cells—status and Perspectives. *Nanotechnology* **19**, 424001, 2008.
- [30]. V. A. Kostyanovsky, D. K. Susarova, A. S. Peregudov and P. A. Troshin: Polymerizable Fullerene-based Material for Organic Solar Cells. *Thin Solid Films*, **519**, 4119–4122, 2011.
- [31]. H. Do, M. Reinhard, H. Vogeler, A. Puetz, M. F. G. Klein, W. Schabel, A. Colsmann and U. Lemmer: Polymeric Anodes from Poly(3,4-ethylenedioxythiophene):

- Poly(styrenesulfonate) for 3.5% Efficient Organic Solar Cells. *Thin Solid Films* **517**, 5900–5902, 2009.
- [32]. A. Geisera, B. Fan, H. Benmansour, F. Castro, J. Heier, B. Keller, K. E. Mayerhofer, F. Nüesch and R. Hany: Poly(3-hexylthiophene)/C<sub>60</sub> Heterojunction Solar Cells: Implication of Morphology on Performance and Ambipolar Charge Collection. *Solar Energy Materials & Solar Cells* **92**, 464–473, 2008.
- [33]. L. Yan, H. Yan-Bing, H. J. Jin, S. Quan-Min, Y. W. Wang and F. Zhi-Hui: Photovoltaic Properties of MEH-PPV/TiO<sub>2</sub> Nanocomposites. *Chinese Science Bull.* **53**, 2743-2747, 2008.
- [34]. B. J. Kim, Y. Miyamoto, B. Ma and J. M. J. Fréchet: Photocrosslinkable Polythiophenes for Efficient, Thermally Stable, Organic Photovoltaics. *Adv. Funct. Mater.* **19**, 2273–2281, 2009.
- [35]. A. J. Moulè and K. Meerholz: Intensity-dependent Photocurrent Generation at the Anode in Bulk-heterojunction Solar Cells. *Appl. Phys. B* **92**, 209–218, 2008.
- [36]. M. S. Ryu, H. J. Cha and J. Jang: Improvement of Operation Lifetime for Conjugated Polymer:Fullerene Organic Solar Cells by Introducing a UV Absorbing Film. *Solar Energy Materials & Solar Cells* **94**, 152–156, 2010.
- [37]. F. Qiao, A. Liu, Z. Hu, Y. Liu, S. Yu and Z. Zhou: Improved Photovoltaic Properties of Solar Cells Based on Poly[9, 90-dioctyl-fluorene-co-bithiophene] and a Soluble Fullerene by Microwave Annealing. *J Mater Sci.* **44**, 3462–3465, 2009.
- [38]. D. Gupta, S. Mukhopadhyay and K. S. Narayan: Fill Factor in Organic Solar Cells. *Solar Energy Materials & Solar Cells* **94**, 1309–1313, 2010.
- [39]. P. E. Shaw, A. Ruseckas and I. D. W. Samuel: Exciton Diffusion Measurements in Poly(3-hexylthiophene). *Adv. Mater.* **20**, 3516–3520, 2008.
- [40]. F. Qiao, A. Liu, Y. Xiao, Y. P. Ouc, J. Zhang and Y. C. Sang: Enhanced Photovoltaic Characteristics of Solar Cells Based on n-type Triphenodioxazine Derivative. *Microelectronics* **39**, 1568–1571, 2008.
- [41]. S. Isoda: Energy Conversion Efficiency in Exciton Process for Single and Bulk Heterojunction Organic Solar Cells. *Japanese Journal of Applied Physics* **47**, 8859–8867, 2008.
- [42]. K. H. Yim, Z. Zheng, Z. Liang, R. H. Friend, W. T. S. Huck and J. S. Kim: Efficient Conjugated-Polymer Optoelectronic Devices Fabricated by Thin-Film Transfer-Printing Technique. *Adv. Funct. Mater.* **18**, 1012–1019, 2008.
- [43]. G. D. Sharma, J. A. Mikroyannidis and S. P. Singh: Efficient Bulk Heterojunction Solar Cells Based on D-A Copolymers as Electron Donors and PC<sub>70</sub>BM as Electron Acceptor. *Materials Chemistry and Physics* **135**, 25-31, 2012.
- [44]. G. D. Sharma, P. B. Raju and M. S. Roy: Effect of Functional Groups of Acceptor Material on Photovoltaic Response of Bulk Hetero-junction Organic Devices Based on Tin Phthalocyanine (SnPc). *Solar Energy Materials & Solar Cells* **92**, 261–272, 2008.

- [45]. D. Kekuda, J. S. Huang, M. Velusamy, J. T. Lin and C. W. Chu: Dibenzo[f,h]thieno[3,4-b] Quinoxaline–fullerene Heterojunction Bilayer Solar Cells with Complementary Spectrum Coverage. *Solar Energy Materials & Solar Cells* **94**, 1767–1771, 2010.
- [46]. M. G. Varnamkhasti, H. R. Fallah, M. Mostajaboddavati, R. Ghasemi and A. Hassanzadeh: Comparison of Metal Oxides as Anode Buffer Layer for Small Molecule Organic Photovoltaic Cells. *Solar Energy Materials & Solar Cells* **98**, 379–384, 2012.
- [47]. G. D. Sharma, P. Balraju, S. K. Sharma and M. S. Roy: Charge Conduction Process and Photoelectrical Properties of Bulk Heterojunction Device Based on Sulphonated Nickel Phthalocyanine and Rose Bengal. *Journal of Physics and Chemistry of Solids* **70**, 1422–1431, 2009.
- [48]. A. T. Mallajosyula, N. Srivastava, S. S. K. Iyer and B. Mazhari: Characterization of Matrix and Isolated Organic Solar Cells. *Solar Energy Materials & Solar Cells* **94**, 1319–1323, 2010.
- [49]. F. Qiao, A. Liu, Y. Zhou, Y. Xiao and P. O. Yang: Bulk Heterojunction Organic Solar Cell Based on a Novel Fluorescent Fluorine–boron Complex. *J Mater Sci.* **44**, 1283–1286, 2009.
- [50]. Y. M. Nam, J. Huh and W. H. Jo: A computational Study on Optimal Design for Organic Tandem Solar Cells. *Solar Energy Materials & Solar Cells* **95**, 1095–1101, 2011.
- [51]. L. H. Chan, S. Y. Juang, M. C. Chen and Y. J. Lin: A New Series of Random Conjugated Copolymers Containing 3,4-diphenylmal-eimide and Thiophene Units for Organic Photovoltaic Cell Applications. *Polymer* **53**, 2334–2346, 2012.
- [52]. K. M. Coakley and M. D. McGehee: Conjugated Polymer Photovoltaic Cells. *Chem. Mater.* **16**, 4533–4542, 2004.
- [53]. J. R. Kline and D. M. McGehee: Morphology and Charge Transport in Conjugated Polymers. *J. Macromol. Sc., Part C: Pol. Rev.* **46** (1), 27–45, 2006.
- [54]. F. C. Krebs: ALTERNATIVE PV: Large Scale Organic Photovoltaics. *Refocus* **6**, 38–39, 2005.
- [55]. Y. Zang, J. Huang, H. Li, J. Yu and Y. Jiang: Effect of Molybdenum Oxide Anode Buffer Layer on the Performance of Inverted Small Molecular Organic Solar Cells. *Energy Procedia* **12**, 513 – 518, 2011.
- [56]. T. Wolfgang: *Device Physics of Organic Solar cells*. 2011.
- [57]. T. Kirchartz, K. Taretto and U. Rau: Efficiency Limits of Organic Bulk Heterojunction Solar Cells. *J. Phys. Chem.* **113** (41), 17958–17966, 2009.
- [58]. A. Moliton and J.-M. Nunzi: How to Model the Behaviour of Organic Photovoltaic Cells. *Polymer International* **55**, 583–600, 2006.

- [59]. M. A. Green, K. Emery, Y. Hishikawa, W. Warta and E. D. Dunlop: Solar Cell Efficiency Tables (version 39). *Progress in Photovoltaics, Research and Applications* **20** (1), 12–20, 2012.
- [60]. L. Kazmerski: Best Research Cell Efficiencies. [Online]. Available: <http://upload.wikimedia.org/wikipedia/commons/1/16/PVeff%28rev110901%29.jpg>. [Accessed 16 March 2014].
- [61]. K. Norrman and F. C. Krebs: Photodegradation of Poly(ether sulphone) Part 2. Wavelength and Atmosphere Dependence. *Surface and Interface Analysis* **36** (12) 1542–1549, 2004.
- [62]. M. Jørgensen, K. Norrman and F. C. Krebs: Stability/Degradation of Polymer Solar Cells. *Solar Energy Materials and Solar Cells* **92** (7) 686–714, 2008.
- [63]. K. Norrman, N. B. Larsen and F. C. Krebs: Lifetimes of Organic Photovoltaics: Combining Chemical and Physical Characterisation Techniques to Study Degradation Mechanisms. *Solar Energy Materials and Solar Cells* **90** (17) 2793 – 2814, 2006.
- [64]. F. C. Krebs: Analysis of the Failure Mechanism for a Stable Organic Photovoltaic During 10000 Hours of Testing. *Progress in Photovoltaics: Research and Applications* **15** (8), 697, 2007.
- [65]. J. A. Hauch, P. Schilinsky, S. A. Choulis, R. Childers, M. Biele and C. J. Brabec: Flexible Organic P3HT:PCBM Bulk-heterojunction Modules with More Than 1 Year Outdoor Lifetime. *Solar Energy Materials and Solar Cells* **92** (7) 727-731, 2008.
- [66]. V. Shrotriya, G. Li, Y. Yao, C. C. W. Chih-Wei and Y. Yang-Yang: Transition Metal Oxides as the Buffer Layer for Polymer Photovoltaic Cells. *Appl. Phys. Lett.* **88**, 073508, 2006.
- [67]. S. K. Hau, H.-L. Yip, N. S. Baek, J. Zou, K. O'Malley and A. K.-Y. Jen: Air-stable Inverted Flexible Polymer Solar Cells Using Zinc Oxide Nanoparticles as an Electron Selective Layer. *Applied Physics Letters* **92** (25), 253301–253303.
- [68]. K. L. Chopra, S. Major and D. K. Pandya: Transparent Conductors--A Status Review. *Thin Solid Films: Electronics and Optics* **102**, 1- 46, 1983.
- [69]. A. Feltrin and A. Freundlich: Material Considerations for Terawatt Level Deployment of Photovoltaics. *Renewable Energy* **33**, 180–185, 2008.
- [70]. B. Zimmermann, H. F. Schleiermacher, M. Niggemann and U. Würfel: ITO-free Flexible Inverted Organic Solar Cell Modules with High Fill Factor Prepared by Slot Die Coating. *Solar Energy Materials & Solar Cells* **95**, 1587–1589, 2011.
- [71]. B. Zimmermann, M. Glatthaara, M. B. Niggemann, M. K. Riedea, A. Hinsch and A. Gombert: ITO-free Wrap Through Organic Solar Cells – A Module Concept for Cost-efficient Reel-to-Reel Production. *Solar Energy Materials & Solar Cells* **91**, 374–378, 2007.
- [72]. Y. Park, V. Choong, Y. Gao, R. B. Hsieh and W. C. Tang: Work Function of Indium Tin Oxide Transparent Conductor Measured by Photoelectron Spectroscopy. *Appl. Phys. Lett.* **68**, 2699-2701, 1996.

- [73]. S. Ju, S. Kim, S. Mohammadi, B. D. Janes, H. G.-Y. Young-Geun, A. Facchetti and J. T. Marks: Interface Studies of ZnO Nanowire Transistors Using Low-frequency Noise and Temperature-dependent I-V Measurements. **92**, 022104, 2008.
- [74]. K. Sivaramakrishnan and T. L. Alford: Conduction and Transmission Analysis in Gold Nanolayers Embedded in Zinc Oxide for Flexible Electronics. *Appl. Phys. Lett.* **96**, 201109, 2010.
- [75]. A. Dhar and T. L. Alford: High Quality Transparent TiO<sub>2</sub>/Ag/TiO<sub>2</sub> Composite Electrode Films Deposited on Flexible Substrate at Room Temperature by Sputtering. *APL materials* **1**, 012102, 2013.
- [76]. H. Morkoç and Ü. Özgür: ZnO Oxide Fundamentals, Materials and Device Technology, Weinheim: WILEY-VCH Verlag GmbH & Co. KGaA, 2009.
- [77]. Forsch Material [Online]. Available: [www.emg.tu-bs.de/forsch/material/mat\\_half\\_de.htm](http://www.emg.tu-bs.de/forsch/material/mat_half_de.htm). [Accessed 6 April 2014].
- [78]. A. Onodera, N. Tamaki, K. Jin and H. Yamashita: Ferroelectric Properties in Piezoelectric Semiconductor Zn<sub>1-x</sub>M<sub>x</sub>O (M=Li, Mg). *J. Appl. Phys.* **36**, 6008-6011, 1997.
- [79]. S. J. Pearton, D. P. Norton, Y. W. Heo and T. Steiner: Recent Progress in Processing and Properties of ZnO. *Progress in Materials Science* **50**, 293–340, 2005.
- [80]. M. F. Al-Kuhaili, M. A. Al-Maghrabi, S. M. A. Durrani and I. A. Bakhtiari: Investigation of ZnO/Al/ZnO Multilayers as Transparent Conducting Coatings. *J. Phys. D: Appl. Phys.* **41**, 215302, 2008.
- [81]. Dhananjay, J. Nagaraju and Krupenidh: Off-centered Polarization and Ferroelectric Phase Transition in Li-doped ZnO thin Films Grown by Pulsed-laser ablation. *Appl. Phys.* **101**, 104104, 2007.
- [82]. W. Xudong, S. Jinhui, L. Jin and W. L. Zhong: Direct-Current Nanogenerator Driven by Ultrasonic Waves. *Science* **316**, 102, 2007.
- [83]. C. Y. Yang, C. Song, F. Zeng and F. Pan: Giant Piezoelectric d<sub>33</sub> Coefficient in Ferroelectric Vanadium Doped ZnO Films. *Appl. Phys. Lett.* **90**, 242903, 2008.
- [84]. C. Y. Yang, C. Song, F. Zeng and F. Pan: V<sup>5+</sup> Ionic Displacement Induced Ferroelectric Behavior in V-doped ZnO Films. *Appl. Phys. Lett.* **90**, 242903, 2007.
- [85]. A. Onodera, N. Tamaki, Y. T. Kawamura, K. J. Sawada and H. Yamashita: Dielectric Activity and Ferroelectricity in Piezoelectric Semiconductor Li-Doped ZnO. *J. Appl. Phys.* **35**, 5160-5162, 1996.
- [86]. D. Song, A. G. Aberle and J. Xia: Optimisation of ZnO:Al Films by Change of Sputter Gas Pressure for Solar Cell Application. *Applied Surface Science* **195**, 291-296, 2002.
- [87]. S. S. Lin, J. L. Huang and D. F. Lii: Effect of Substrate Temperature on the Properties of Ti-doped ZnO Films by Simultaneous RF and DC Magnetron Sputtering. *Materials Chemistry and Physics* **90**, 22–30, 2005.

- [88]. Q. Huang, Y. Wang, S. Wang, D. Zhang, Y. Zhao and X. Zhang: Transparent Conductive ZnO:B Films Deposited by Magnetron Sputtering. *Thin Solid Films* **520**, 5960–5964, 2012.
- [89]. G. Luka, T. A. Krajewski, B. S. Witkowski, G. Wisz, I. S. Virt, E. Guziewicz and M. Godlewski: Aluminum-doped Zinc Oxide Films Grown by Atomic Layer Deposition for Transparent Electrode Applications. *J Mater Sci: Mater Electron* **22**, 1810–1815, 2011.
- [90]. D. R. Sahu, S.-Y. Lin and J.-L. Huang: ZnO/Ag/ZnO Multilayer Films for the Application of a Very Low Resistance Transparent Electrode. *Applied Surface Science* **252**, 7509-7514, 2006.
- [91]. F. Pan, S. Gao, C. Chen, C. Song and F. Zeng: Recent Progress in Resistive Random Access Memories: Materials, Switching Mechanisms, and Performance. *Materials Science and Engineering R* **83**, 1-59, 2014.
- [92]. J. Tsujino, N. Hommaa, S. Tomoaki, S. Isao and A. Yoshihiko: Preparation of Al-doped ZnO Thin Films by RF Thermal Plasma Evaporation. *Thin Solid Films* **407**, 86–91, 2002.
- [93]. A. F. Aktaruzzaman, G. L. Sharma and L. K. Mahgotra: Electrical, Optical and Annealing Characteristics of ZnO:Al Films Prepared by Spray Pyrolysis. *Thin Solid Films* **198**, 1991.
- [94]. T. Nakada, O. Yukiyasu, M. Naoki and K. Akio: Transparent Conducting Boron-Doped Zinc Oxide Films Deposited by DC-Magnetron Sputtering in B<sub>2</sub>H<sub>6</sub>-Ar Mixture. *Appl. Phys.* **34**, 3623-3627, 1995.
- [95]. H. A. Gomez, J. P.-G. Maldonado, R. Asomoza, E. P. Zironi, J. Canetas-Ortega and J. Palacios-Gomez: Characterization of Indium-Doped Zinc Oxide Films Deposited by Pyrolytic Spray with Different Indium Compounds as Dopants: *Thin Solid Films* **293**, 117-123, 1997.
- [96]. A. Tiburcio-Silver, A. Sanchez-Juarez and A. Avila-Garcia: Properties of Gallium-Doped ZnO Deposited onto Glass by Spray Pyrolysis. *Sol. Energy Mater.Sol. Cells* **55**, 3, 1998.
- [97]. R. Saad, S. A. Mohamed, C. Abdelouahad, B. T. Hachemi and D. Abdou: Elaboration of Transparent Undoped ZnO and Al-Doped ZnO Thin Films by Spray Pyrolysis and Their Properties. *Plasma Process. Polym.* **4**, S356–S358, 2007.
- [98]. B. Szyszka: Transparent and Conductive Aluminum Doped Zinc Oxide Films Prepared by Mid-frequency Reactive Magnetron Sputtering. *Thin Solid Films* **351**, 164-169, 1999.
- [99]. E. Ando and M. Miyazaki: Moisture Resistance of the Low-emissivity Coatings with a Layer Structure of Al-doped ZnO/Ag/Al-doped ZnO. *Thin Solid Films* **392**, 289-293, 2001.

- [100]. S.-H. Park, H.-M. Kim, B.-R. Rhee, E.-Y. Ko and S.-H. Shon: Effects of Oxygen Concentration on Characteristics of RF-Sputtered In<sub>2</sub>O<sub>3</sub>-ZnO Thin Films. *Jpn. J. Appl. Phys.* **40**, 1429-1430, 2001.
- [101]. D. R. Sahu and J.-L. Huang: Design of ZnO/Ag/ZnO Multilayer Transparent Conductive Films. *Materials Science and Engineering B* **130**, 295–299, 2006.
- [102]. M. Bender, W. Seelig, C. Daube, H. Frankenberger, B. Ocker and J. Stollenwerk: Dependence of Film Composition and Thicknesses on Optical and Electrical Properties of ITO–metal–ITO Multilayers. *Thin Solid Films* **326**, 67–71, 1998.
- [103]. K. H. Choi, J. Y. Kim, Y. S. Lee and H. J. Kim: ITO/Ag/ITO Multilayer Films for the Application of a Very Low Resistance Transparent Electrode. *Thin Solid Films* **341**, 152-155, 1999.
- [104]. A. Klöppel, W. Kriegseis, B. K. Meyer, A. Scharmann, C. Daube, J. Stollenwerk and J. Trube: Dependence of the Electrical and Optical Behaviour of ITO-silver-ITO Multilayers on the Silver Properties. *Thin Solid Films* **365**, 139-146, 2000.
- [105]. M. Fahland, P. Karlsson and C. Charton: Low Resisitivity Transparent Electrodes for Displays on Polymer Substrates. *Thin Solid Films* **392**, 334-337, 2001.
- [106]. A. Klöppel, B. Meyer and J. Trube: Influence of Substrate Temperature and Sputtering Atmosphere on Electrical and Optical Properties of Double Silver Layer Systems. *Thin Solid Films* **392**, 311-314, 2001.
- [107]. M. Sawada, M. Higuchi, S. Kondo and H. Saka: Characteristics of Indium-Tin-Oxide/Silver/Indium-Tin-Oxide Sandwich Films and Their Application to Simple Liquid-Crystal Displays. *Jpn. J. Appl. Phys.* **40**, 3332-3336, 2001.
- [108]. Y. S. Jung, Y. W. Choi, H. C. Lee and D. W. Lee: Effects of Thermal Treatment on the Electrical and Optical Properties of Silver-based Indium Tin Oxide/Metal/Indium Tin Oxide Structures. *Thin Solid Films* **440**, 278–284, 2003.
- [109]. D. R. Sahu and J. L. Huang: Dependence of Film Thickness on the Electrical and Optical Properties of ZnO-Cu-ZnO Multilayers. *Applied Surface Science* **253**, 915-918, 2006.
- [110]. D. R. Sahu and J. L. Huang: High Quality Transparent Conductive ZnO/Ag/ZnO Multilayer Films Deposited at Room Temperature. *Thin Solid Films* **515**, 876-879, 2006.
- [111]. D. R. Sahu and J. L. Huang: Characteristics of ZnO-Cu-ZnO Multilayer Films on Copper Layer Properties. *Applied Surface Science* **253**, 827-832, 2006.
- [112]. M. A. Green: *High Efficiency Silicon Solar Cells*. Trans Tech Publications, 1987.
- [113]. A. E. Becquerel: Mémoire Sur Les Effets Electriques Produits Sous L'fluence Ds Ryons Slaires. *Compt. Rend. Acad. Sci.* **9**, 561-567, 1839.
- [114]. C. M. Haanyika: Rural Electrification Policy and Institutional Linkages. *Energy Policy* **34**, 2977-2993, 2006.

- [115]. S. John, O. Stephen, C. David, B. Rita, G. David, B. Marilyn, B. Eldon, M. Kathryn, C. David, D. Stephen, K. Gerald and P. L. Denholm: Energy Options for the Future. *Journal of Fusion Energy* **23** (2), 63, 2004.
- [116]. J. K. Kaldellis and D. Zafrakis: Present Situation and Future Prospects of Electricity Generation in Aegean Archipelago Islands. *Energy Policy* **35**, 4623-4639, 2007.
- [117]. G. Tamulaitis: LEDs in Developing World. *International Journal of High Speed Electronics and Systems* **20** (2), 343-358, 2011.
- [118]. M. O. Abdullah, V. C. Yung, M. Anyi, A. K. Othman, K. B. A. Hamid and J. Tarawe: Review and Comparison Study of Hybrid Diesel/Solar/Hydro/Fuel Cell Energy Schemes for a Rural ICT Telecenter. *Energy* **35**, 639-646, 2010.
- [119]. D. Egge and J. C. Milewski: The Diversity of Hydropower Projects. *Energy Policy* **30**, 1225-1230, 2002.
- [120]. R. M. Shrestha and G. B. Bhattarai: Electricity Planning with Demand-side Management in Nepal: Economics and Environmental Implications. *Energy Policy*, 757-767, 1993.
- [121]. C. R. Henderson, J. F. Manwell and J. G. McGowan: A Wind/Diesel Hybrid System with Desalination for Star Island, NH: Feasibility Study Results. *Desalination* **237**, 318–329, 2009.
- [122]. Sirte: Hydropower Resource Assessment of Africa, in Ministerial Conference on Water for Agriculture and Energy in Africa: The Challenges of Climate Change, Libyan Arab Jamahiriya, 15-17 December 2008.
- [123]. R. T. Kivaisi: Installation and Use of a 3 kWp PV Plant at Umbuji Village in Zanzibar. *Renewable Energy* **19**, 457-472, 2000.
- [124]. M. L. Chabinye and L. Yueh-lin: Semiconducting Polymers for Thin-Film Electronics. *J. Macromolecular Sci., Part C: Pol. Rev.* **46** (1), 1-5, 2006.
- [125]. S. M. Casseiro, F. Thomazi, L. S. Roman, A. Marletta and L. Akcelrud: Effect of Conjugation Length on Photophysical Properties of a Conjugated-non-Conjugated Multiblock Copolymer. *Synthetic Metals* **159**, 1975-1982, 2009.
- [126]. L. J. A. Koster, E. C. P. Smits, V. D. Mihailetschi and P. W. M. Blom: Device Model for the Operation of Polymer/Fullerene Bulk Heterojunction Solar Cells. *Physical Review B* **72**, 085205-(1-9), 2005.
- [127]. Physics Institute – V. School of Mathematics and Science - Institute of Physics. University of Oldenburg, 5 March 2014. [Online]. Available: <http://www.uni-oldenburg.de/en/physics/research/ehf/ohpv/research/>. [Accessed 27 June 2014].
- [128]. H. Hoppe and N. S. Sariciftci: Organic Solar Cells: An Overview. *J. Mater. Res.* **19**, 1924–1944, 2004.
- [129]. W. Guang-Feng, X.-M. Tao and R.-X. Wang: Flexible Organic Light-emitting Diodes with a Polymeric Nanocomposite Anode. *Nanotechnology* **19**, 145201, 2008.

- [130]. Konarka : Power Plastic Products. [Online]. Available: <http://www.konarka.com/index.php/power-plastic/power-plastic-products>. [Accessed 14 September 2013].
- [131]. A. Hagfeldt and M. Gratzel: Molecular Photovoltaics. *Acc. Chem. Res.* **33**, 269-277, 2000.
- [132]. G. A. Chamberlain: Organic Solar Cells: A Review. *Solar Cells* **8**, 47 – 83, 1983.
- [133]. P. Peumans, V. Bulovic and S. R. Forrest: Efficient Photon Harvesting at High Optical Intensities in Ultrathin Organic Double-heterostructure Photovoltaic Diodes. *Appl. Phys. Lett.* **76**, 2650, 2000.
- [134]. B. A. Gregg: Bilayer Molecular Solar Cells on Spin-coated TiO<sub>2</sub> Substrates. *Chem. Phys. Lett.* **258**, 376, 1996.
- [135]. S. A. Jenekhe and S. Yi: Efficient Photovoltaic Cells from Semiconducting Polymer Heterojunctions. *Appl. Phys. Lett.* **77**, 2635, 2000.
- [136]. C. W. Tang: Two-layer Organic Photovoltaic Cell. *Applied Physics Letters* **48** (2), 183–185, 1986.
- [137]. S. E. Shaheen, C. J. Brabec, N. S. Sariciftci, F. Padinger, T. Fromherz and J. C. Hummelen: 2.5% Efficient Organic Plastic Solar Cells. *Applied Physics Letters* **78**, 841-843, 2001.
- [138]. J. J. M. Halls, N. C. Walsh, E. A. Greenham, E. A. Marseglia, R. H. Friend, S. C. Moratti and A. B. Holmes: Efficient Photodiodes from Interpenetrating Polymer Networks. *Nature* **376**, 498–500, 1995.
- [139]. G. Yu, J. Gao, J. C. Hummelen, F. Wudl and A. J. Heeger: Polymer Photovoltaic Cells: Enhanced Efficiencies Via a Network of Internal Donor-acceptor Heterojunctions. *Science* **270** (5243), 1789, 1995.
- [140]. W. U. Huynh, J. J. Dittmer and A. P. Alivisatos: Hybrid Nanorod-Polymer Solar Cells. *Science* **295**, 2425-2427, 2001.
- [141]. M. Hiramoto, H. Fujiwara and M. Yokoyama: Three-layered Organic Solar Cell with a Photoactive Interlayer of Codeposited Pigments. *Applied Physics Letters* **58** (10), 1062–1064, 1991.
- [142]. S. J. Fonash: *Solar Cell Device Physics*, 2nd ed., Acad. Press, Elsevier.
- [143]. R. A. Marsh, J. M. Hodgkiss, S. Albert-Seifried and R. H. Friend: Effect of Annealing on P3HT:PCBM Charge Transfer and Nanoscale Morphology Probed by Ultrafast Spectroscopy. *Nano Letters* **10** (3), 923-930, 2010.
- [144]. S. R. Scully and M. D. McGehee: Effects of Optical Interference and Energy Transfer on Exciton Diffusion Length Measurements in Organic Semiconductors. *Journal of Applied Physics* **100** (3), 034907, 2006.
- [145]. O. Oklobia and T. S. Shafai: Correlation Between Charge Carriers Mobility and Nanomorphology in a Blend of P3HT/PCBM Bulk Heterojunction Solar Cell: Impact on Recombination Mechanisms. *Solar Energy Materials & Solar Cells* **122**, 158–163, 2014.

- [146]. F. I. CalLab: Tandem Solar Cell by Heliatek with an Efficiency of 9.8 % on an Area of 1.1 Square Centimeters, Freiburg, 2011.
- [147]. A. J. Mozer, P. Denk, M. C. Scharber, H. Neugebauer, N. S. Sariciftci, P. Wagner, L. Lutsen and D. Venderzande: Novel Regiospecific MDMO-PPV Copolymer with Improved Charge Transport for Bulk Heterojunction Solar Cells. *Journal of Physical Chemistry B* **108** (17), 5235–5242, 2004.
- [148]. J. Roncali: Conjugated Poly(thiophenes): Synthesis, Functionalization and Applications. *Chemical Reviews* **92** (4), 711–738, 1992.
- [149]. R. D. McCullough: The Chemistry of Conducting Polythiophenes. *Advanced Materials* **10** (2), 93–116, 1998.
- [150]. S.-C. Chuang, C.-W. Chiu, S.-C. Chien, C.-W. Chu and F.-C. Chen: 1-(3-Methoxycarbonyl)propyl-2-selenyl-[6,6]-methanofullerene as a n-Type Material for Organic Solar Cells. *Synthetic Metals* **161**, 1264–1269, 2011.
- [151]. K. K. Kim, J. Liu, M. Namboothiry and D. L. Carroll: The Roles of Donor and Acceptor Nanodomains in 6% Efficient Thermally Annealed Photovoltaic Devices. *Applied Physics Letters* **90**, 2007.
- [152]. P. Vanlaeke, A. Swinnen, I. Haeldermans, G. Vanhoyland, T. Aernouts, D. D. Cheyns, C. Deibel, J. D'Haen, P. Heremans, J. Poortmans and J. V. Manca: P3HT/PCBM Bulk Heterojunction Solar Cells: Relation Between Morphology and Electro-optical Characteristics. *Solar Energy Materials and Solar Cells* **90** (14) 2150–2158, 2006.
- [153]. S. M. Liu, Y.-H. Niu, L. J. Jingdong, C. B. Baoquan, K. T.-D. Tae-Dong, J. Bardecker and K.-Y. A. Jen: Material and Interface Engineering for Highly Efficient Polymer Light Emitting Diodes. *J. Macromol. Sci., Part C: Pol. Rev.* **46** (1), 7-26, 2006.
- [154]. B. Mazhari: An Improved Solar Cell Circuit Model for Organic Solar Cell. *Solar Energy & Solar Cells* **90**, 1021-1033, 2006.
- [155]. A. Jain and A. Kapoor: A New Approach to Study Organic Solar Cell Using Lambert W-function. *Solar Energy Materials & Solar Cells* **86**, 197-205, 2005.
- [156]. I. G. Hill, A. Kahn, Z. G. Soos and R. A. J. Pascal: Charge-separation Energy in Films for TT-conjugated Organic Molecules. *Chemical Physics Letters* **327** (3) 181–188, 2000.
- [157]. S. F. Alvarado, P. F. Seidler, D. G. Lidzey and D. D. C. Bradley: Direct Determination of the Exciton Binding Energy of Conjugated Polymers Using a Scanning Tunneling Microscope. *Physical Review Letters* **81** (5), 1082–1085, 1998.
- [158]. M. Knupfer, J. Fink, E. Zojer, G. Leising, U. Scherf and K. Müllen: Localized and Delocalized Singlet Excitons in Ladder-type Poly(paraphenylene). *Physical Review B* **57** (8), R4202–R4205, 1998.
- [159]. S. Barth and H. Bässler: Intrinsic Photoconduction in PPV-Type Conjugated Polymers. *Physical Review Letters* **79** (22), 4445–4448, 1997.

- [160]. C. J. Brabec, N. S. Sariciftci and J. C. Hummelen: Plastic Solar Cells. *Advanced Functional Materials* **11** (1), 15–26, 2001.
- [161]. C. J. Brabec, G. Zerza, G. Cerullo, S. D. Silvestri, S. Luzzati, J. C. Hummelen and S. Sariciftci: Tracing Photoinduced Electron Transfer Process in Conjugated Polymer/Fullerene Bulk Heterojunctions in Real Time. *Chemical Physics Letters* **240**, 232-236, 2001.
- [162]. N. S. Sariciftci, L. Smilowitz, A. J. Heeger and F. Wudl: Photoinduced Electron Transfer from a Conducting Polymer to Buckminsterfullerene. *Science* **258** (5087), 1474–1476, 1992.
- [163]. V. D. Mihailetschi, L. J. A. Koster and P. W. M. Blom: Effect of Metal Electrodes on the Performance of Polymer:Fullerene Bulk Heterojunction Solar Cells. *Applied Physics Letters* **85**, 970–972, 2004.
- [164]. P. Peumans, A. Yakimov and S. R. Forrest: Small Molecular Weight Organic Thin-film Photodetectors and Solar Cells. *J. Appl. Phys.* **93**, 3693, 2003.
- [165]. V. Coropceanu, J. Cornil, D. A. da Silva Filho, Y. Olivier, R. Silbey and J.-L. Brédas: Charge Transport in Organic Semiconductors. *Chemical Reviews* **107** (4) 926–952, 2007.
- [166]. H. Hoppe, T. Glatzel, M. Niggeman, M. Schwinger, F. Schaeffler, A. Hinsch, M. C. Lux-Steiner and N. S. Sariciftci: Efficiency Limiting Morphological Factors of MDMO-PPV:PCBM Plastic Solar Cells. *Thin Solid Films* **511–512**, 587, 2006.
- [167]. H. Hoppe and N. S. J. Sariciftci: Morphology of Polymer/Fullerene Bulk Heterojunction Solar Cells. *Journal of Materials Chemistry* **16**, 45–61, 2006.
- [168]. J. Hwang, A. Wan and A. Kahn: Energetics of Metal-Organic Interfaces: New Experiments and Assessment of the Field. *Materials Science and Engineering Reports* **64** (1-2), 1–31, 2009.
- [169]. G. Yu and A. J. Heeger: Charge Separation and Photovoltaic Conversion in Polymer Composites with Internal Donor/Acceptor Heterojunctions. *Journal of Applied Physics* **78**, 4510–4515, 1995.
- [170]. B. R. Saunders and M. L. Turner: Nanoparticle-Polymer Photovoltaic Cells. *Advances in Colloid and Interface Science* **138** (1), 1–23, 2008.
- [171]. C. W. Tang and S. A. VanSlyke: Organic Electroluminescent Diodes. *Applied Physics Letters* **51**, 30–32, 1987.
- [172]. J. H. Burroughes, D. D. C. Bradley, A. R. Brown, R. N. Marks, K. Mackay, R. H. Friend, P. L. Burns and A. B. Holmes: Light-emitting Diodes Based on Conjugated Polymers. *Nature* **347** (6293), 539–541, 1990.
- [173]. OLED Info, 10 February 2014. [Online]. Available: <http://www.oled-info.com>.
- [174]. S. Reineke, F. Lindner, G. Schwartz, N. Seidler, K. Walzer, B. Lussem and K. Leo: White Organic Light-emitting Diodes with Fluorescent Tube Efficiency. *Nature* **459** (7244), 234–238, 2009.

- [175]. M. A. Martinez, J. Herrero and M. T. Gutierrez: Deposition of Transparent and Conductive Al doped ZnO Thin Films for Photovoltaic Solar Cells. *Sol. Energy Mater. Sol. Cells* **45**, 75-86, 1997.
- [176]. F.-L. Kuo, Y. Li, M. Solomon, J. Du and D. N. Stepher: Workfunction Tuning of Zinc Oxide Films by Argon Sputtering and Oxygen Plasma: An Experimental and Computational Study. *J. Phys. D: Appl. Phys.* **45**, 065301, 2012.
- [177]. [Online]. Available: <http://geology.com/articles/indium.shtml>. [Accessed 1 March 2014].
- [178]. P. Mushonga, M. O. Onani, A. M. Madiehe and M. Meyer: Indium Phosphide-Based Semiconductor Nanocrystals and Their Applications. *Journal of Nanomaterials* **2012**, 1-11, 2012.
- [179]. A. K. Nedoluha: Technology and Application of Indium Phosphide and Related Semiconductors. *Electronic Material Sciences*, NOCS, San Diego, California 92152-5000, March 1989.
- [180]. J. H. Lee: Effects of Sputtering Pressure and Thickness on Properties of ZnO:Al Films Deposited on Polymer Substrates. *J Electroceram* **23**, 512–518, 2009.
- [181]. Y. K. Moon, B. Bang, S. H. Kim, C. O. Jeong and J. W. Park: Effects of Working Pressure on the Electrical and Optical Properties of Aluminum-doped Zinc Oxide Thin Films. *J Mater Sci: Mater Electron* **19**, 528–532, 2008.
- [182]. S.-N. Bai and T.-Y. Tseng: Electrical and Optical Properties of ZnO:Al Thin Films Grown by Magnetron Sputtering. *J. Mater Sci: Mater Electron* **20**, 253–256, 2009.
- [183]. H. Wang, J. Xu, M. Ren and L. Yang: Room Temperature Deposition and Properties of ZnO:Al Thin Films by Nonreactive DC Magnetron Sputtering. *J. Mater Sci: Mater Electron* **19**, 1135–1139, 2008.
- [184]. I. Yasuhiro and K. Hirokazu: Argon Gas Pressure Dependence of the Properties of Transparent Conducting ZnO:Al Films Deposited on Glass Substrates. *Applied Surface Science* **169-170**, 508-511, 2001.
- [185]. A. Halpern and E. Erlbach, Chapter 5: Simple Electric Circuits, in *Theory and Problems of Beginning Physics II Waves, Electromagnetism, Optics, and Modern Physics*, McGraw-Hill, 1998, p. 141.
- [186]. Sleepless Media: Current Metal Prices. *Mining Journal ICMJ*, 2009. [Online]. Available: <http://www.icmj.com/current-metal-prices.php>. [Accessed 7 March 2014].
- [187]. Y. Bouzmit, Y. Beggah and K. Djessas: RF Magnetron Sputtering of ZnO and Al-doped ZnO Films from Ceramic and Nanopowder Targets: A Comparative Study. *J. Sol-Gel Sci Technol.* **61**, 449–454, 2012.
- [188]. P. B. Johnson and R. W. Christy: Optical Constants of the Noble Metals. *Physical review B* **6** (12), 4370-4379, 1972.

- [189]. D. P. Gruber, G. Meinhardt and W. Papousek: Modelling the Light Absorption in Organic Photovoltaic Devices. *Solar Energy Materials & Solar Cells* **87**, 215–223, 2005.
- [190]. J. M. Bennett: Polarization, in *Hand book of Optics: Fundamentals, Techniques and Design*, 2nd ed., vol. I, McGraw-Hill, 1995, p. Chapter 5.
- [191]. C. Summonte: A Quasi-Exact Invertible Equation for Absorption Coefficient from Reflectance and Transmittance Measurements. *MRS* **297**, 395-400, 1993.
- [192]. J. A. Berning and P. H. Berning: Thin Films Calculations Using the IBM 650 Electronic Calculator. *J. Opt. Soc. Am.* **50**, 813-813, 1960.
- [193]. E. Centurioni: Generalized Matrix Method for Calculation of Internal Light Energy Flux in Mixed Coherent and Incoherent Multilayers. *Applied Optics* **44**, 7532-7539, 2005.
- [194]. C. Reale: Optical Constants of Vacuum Deposited Thin Metal Films in the Near Infrared. *Infrared Physics* **10**, 173-181, 1970.
- [195]. E. F. Schubert, 2004. [Online]. Available: <http://homepages.rpi.edu/~schubert/Educational-resources/Materials-Refractive-index-and-extinction-coefficient.pdf>. [Accessed 11 February 2014].
- [196]. J. A. Dobrowolski: Optical Properties of Films and Coatings, Institute for Microstructural Sciences National Research Council of Canada, Part 11, Chapter 42, Page 14, Ottawa, Ontario, Canada. [Online]. Available: [http://photonics.intec.ugent.be/education/IVPV/res\\_handbook/v1ch42.pdf](http://photonics.intec.ugent.be/education/IVPV/res_handbook/v1ch42.pdf). [Accessed 30 October 2014].
- [197]. E. Burstein: Anomalous Optical Absorption Limit in InSb. *Phys. Rev.* **93**, 632–633, 1954.
- [198]. C. R. Brundle, C. A. Evans, S. Wilson and L. E. Fitzpatrick: *Encyclopedia of Materials Characterization - Surfaces, Interfaces, Thin Films*, 3 Lewis Street, Greenwich, CT 06830, USA: Manning Publications Co., 1992.
- [199]. M. Zhu, H. Huang, J. Gong, C. Sun and X. Jiang: Role of Oxygen Desorption During Vacuum Annealing in the Improvement of Electrical Properties of Aluminum Doped Zinc Oxide Films Synthesized by Sol Gel Method. *J. Appl. Phys.* (102), 043106, 2007.
- [200]. K. L. Chopra, S. K. Bahl: Structural, Electrical and Optical Properties of Amorphous Germanium Films. *Phys. Rev. B.* **1**, 2545-2556, 1970.
- [201]. V. V. Filippov and B. G. Shulitskii: Optical Modeling and Optimization of Multilayer Organic Photovoltaic Cells. *J. Appl. Spect.* **77** (2), 266-272, 2010.
- [202]. N. M. Khusayfan and M. M. El-Nahass: Study of Structure and Electro-Optical Characteristics of Indium Tin Oxide Thin Films. *Advances in Condensed Matter Physics* **2013**, p. 5, 2013.

- [203]. J. Du, V. C. Anye, E. O. Vodah, T. Tong, M. G. Zebaze-Kana and W. O. Soboyejo: Pressure- assisted fabrication of organic light emitting diodes with MoO<sub>3</sub> hole-injection layer materials. *J. Appl. Phys.* **115**, 233703, 2014.
- [204]. D. Yu, O. K. Oyewole, D. Kwabi, T. Tong, A. V. C, J. Asare, E. Rwenyagila, A. Fashina, O. Akogwu, J. Du and W. O. Soboyejo: Adhesion in Flexible Organic and Hybrid Organic/Inorganic Light Emitting Device and Solar Cells. *J. Appl. Phys.* **116**, 074506, 2014.
- [205]. D. W. Sievers, V. Shrotriya and Y. Yang: Modeling optical effects and thickness dependent current in polymer bulk-heterojunction solar cells. *J. Appl. Phys.* **100**, 114509, 2006.
- [206]. H. H. P. Gommans, M. Kemerink, J. M. Kramer and R. A. J. Janssen: Field and temperature dependence of the photocurrent in polymer/fullene bulk heterojunction solar cells. *Appl. Phys. Lett.* **87**, 122104, 2005.
- [207]. C. Deibel, A. Baumann and V. Dyakonov: Polaron pair dissociation and polaron recombination in polymer:fullerene solar cells. *Mater. Res. Soc. Symp. Proc.* **H09-21**, 1031E, 2008.
- [208]. T. Kirchartz, B. E. Pieters, K. Taretto and U. Rau: Electro-optical modeling of bulk heterojunction solar cells. *J. Appl. Phys.* **104**, 094513 , 2008.
- [209]. S. Lacic and O. Inganäs: Modeling electrical transport in blend heterojunction organic solar cells. *J. Appl. Phys.* **97**, 124901 , 2005.
- [210]. M. Glatthaar, M. Riede, N. Keegan, K. Sylvester-Hvid, B. Zimmermann, M. Niggemann, A. Hinsch and A. Gombert: Efficiency limiting factors of organic bulk heterojunction solar cells identified by electrical impedance spectroscopy. *Sol. Energy Mater. Sol. Cells* **91**, 390-393, 2007.
- [211]. G. A. Buxton and N. Clarke: Predicting structure and property relations in polymeric photovoltaic devices. *Phys. Rev. B* **74**, 085207, 2006.
- [212]. C. M. Martin, V. M. Burlakov, H. E. Assender and D. A. R. Barkhouse: A numerical model for explaining the role of the interface morphology in composite solar cells. *J. Appl. Phys.* **102**, 104506, 2007.
- [213]. T. Kirchartz, B. E. Pieters, K. Taretto and U. Rau: Mobility dependent efficiencies of organic bulk heterojunction solar cells: Surface recombination and charge transfer state distribution. *Phys. Rev. B* **80**, 035334, 2009.
- [214]. G. A. Buxton and N. Clarke: Computer simulation of polymer solar cells. *Model. Simul. Mater. Sci. Eng.* **15**, 13-26, 2007.
- [215]. Z. XinYan, M. BaoXiu, G. ZhiQiang and H. Wei: Recent progress in the numerical modeling for organic thin film solar cells. *Science China: Physics, Mechanics & Astronomy* **54**, 375–387, 2011.
- [216]. J. D. Kotlarski, P. W. M. Blom, L. J. A. Koster, M. Lenes and L. H. Slooff: Combined Optical and Electrical Modeling of Polymer:Fullerene Bulk Heterojunction Solar Cell. *J. Appl. Phys.* **103**, 084502, 2008.

- [217]. M. Soldera, K. Taretto and T. Kirchartz: Comparison of Device Models for Organic Solar Cells: Band-to-band vs. Tail States Recombination. *Phys. Status Solidi A* **209**, 207–215, 2012.
- [218]. A. Cheknane, H. S. Hilal, F. Djeflal, B. Benyoucef and J.-P. Charles: An Equivalent Circuit Approach to Organic Solar Cell Modelling. *Microelectronics* **39**, 1173-1180, 2008.
- [219]. C. Kim, P. E. Burrows and S. R. Forrest: Micropatterning of organic electronic devices by cold-welding. *Science* **288**, 831, 2000.
- [220]. J. W. P. Hsu: Soft lithography contacts to organics. *Mater. Today* **8**, 42, 2005.
- [221]. S. F. Lim, L. Ke, W. wang and S. J. Chua: Correlation between dark spot growth and pinhole size in organic light-emitting diodes. *Appl. Phys. Lett.* **78**, 2116, 2001.
- [222]. B. A. Gregg and M. C. Hanna: Comparing organic to inorganic photovoltaic cells: Theory, experiment, and simulation. *J. Appl. Phys.* **93**, 3605-3614, 2003.
- [223]. B. Ruhstaller, T. Flatz, D. Rezzonico, M. Moos, N. Reinke, E. Huber, R. Haeusermann and B. Perucco: Comprehensive simulation of light-emitting and light-harvesting organic devices. *Organ Light Emitting Mater Devices XII* **7051**, 70510J , 2008.
- [224]. T. A. Osswald and J. P. Hernandez-Ortiz: *Polymer Processing: Modeling and Simulation - Chapter 8*, Munich: Hanser Publishers, 2006.
- [225]. J. A. Barker, C. M. Ramsdale and N. C. Greenham: Modeling the current-voltage characteristics of bilayer polymer photovoltaic devices. *Phys. Rev. B* **67**, 075205, 2003.
- [226]. J. Mort: Geminate and non-geminate recombination in amorphous semiconductors. *J. de Physique* **42**, c4-433 - c4-441, 1981.
- [227]. L. Onsager: Initial recombination of ions. *Phys. Rev.* **54**, 554-557, 1938.
- [228]. C. L. Braun: Electric field assisted dissociation of charge transfer states as a mechanism of photocarrier production. *J. Phys. Chem.* **80**, 4157–4161, 1984.
- [229]. T. E. Goliber and J. H. Perlstein: Analysis of photogeneration in doped polymer system in terms of a kinetic model for electric-field-assisted dissociation of charge-transfer states. *J. Chem. Phys.* **80**, 4162, 1984.
- [230]. W. Shockley and W. T. Reed: Statistics of the recombinations of holes and electrons. *Phys. Rev.* **87**, 835–842 , 1952.
- [231]. R. N. Hall: Electron-hole recombination in germanium. *Phys. Rev.* **87**, 387-388, 1952.
- [232]. M. M. Mandoc, W. Veurman, L. J. A. Koster, B. deBoer and P. W. M. Blom: Origin of the reduced fill factor and photocurrent in MDMO-PPV:PCNEPV all-polymer solar cells. *Adv. Func. Mater.* **17**, 2167–2173, 2007.
- [233]. J. Schafferhans, A. Baumann, C. Deibel and V. Dyakonov: Trap distribution and the impact of oxygen-induced traps on the charge transport in poly(3-hexylthiophene). *Appl. Phys. Lett.* **93**, 093303, 2008.

- [234]. J. C. Scott and G. G. Malliaras: Charge injection and recombination at the metal-organic interface. *Chem. Phys. Lett.* **299**, 115-119, 1999.
- [235]. Z. E. Ooi, R. Jin, J. Huang, Y. F. Loo, A. Sellinger and J. C. deMello: On the pseudo-symmetric current-voltage response of bulk heterojunction solar cells. *Mater. Chem.* **18**, 1605-1651, 2008.
- [236]. A. Pivrikas, Sariciftci, N. S, G. Juška and R. Österbacka: A review of charge transport and recombination in polymer/fullerene organic solar cells: *Prog. Photovolt: Res. Applic.* **15**, 677-696, 2007.
- [237]. A. Pivrikas, G. Juška, A. J. Mozer, M. Scharber, K. Arlauskas, N. S. Sariciftci, H. Stubb and R. Österbacka: Bimolecular recombination coefficient as a sensitive testing parameter for low-mobility solar-cell materials. *Phys. Rev. Lett.* **94**, 176806, 2005.
- [238]. L. P. Ann: Recombinaison et mobilités des ions dans les gaz. *Chim. Phys.* **28**, 433-452, 1903.
- [239]. C. Deibel, A. Wagenpfahl and V. Dyakonov: Influence of charge carrier mobility on the performance of organic solar cells. *Phys. Stat. Sol.* **2**, 175-177, 2008.
- [240]. C. Deibel, A. Wagenpfahl and V. Dyakonov: Origin of reduced polaron recombination in organic semiconductor devices. *Phys. Rev. B* **80**, 075203, 2009.
- [241]. H. K. Gummel: A self-consistent iterative scheme for one-dimensional steady state transistor calculations. *IEEE Trans Electron Devices* **ED-11**, 455-465, 1964.
- [242]. V. D. Mihailetschi, L. J. A. Koster and H. Xie: Origin of the light intensity dependence of the short-circuit current of polymer/fullerene solar cells. *Appl. Phys. Lett.* **87**, 203502, 2005.

# APPENDIX A

## Program Source Code

```
clear all
global q kB T VT Nx Ny dy2 dx2 V N Ly coeff
global ni epsr C w maxDoping nx ny eps0
global m dy maxT w
global VU debye nim coeffnim %nim=ni/maxT
global GRate % Generation rate
global kf % rate of decay to D--A ground state
global a %e-h Pair distance
global anorm
global ni munsc mupsc gamma
global tov4pi dCoul
global N1 N2
global aa b1 b2 b3 b4
global sc
format longE
fid=fopen('JV.out','w');
sc=0.00 ; % scale the mobilities
dddd=1.0
w=1.0
Nc=2.5e25;
Egap=1.34;
%%%%%%%%%% Parameters for the G-U Generation-Recombination Term
%%%%%%%%%%
GRate=2.7e27; % Illuminated
GRate=0.0 % In the dark
kf=1.5e6
a=1.3e-9 %0.5 nm
anorm = 2.256758334191025/a^3; % 4/(a^3*sqrt(pi))
tov4pi=0.238732414637843 % 3/4pi
dCoul= 1.439805929292076e-09 % q/4pi\epsilon_0
%%%%%%%%%% End Parameters for the G-U Generation-Recombination Term
%%%%%%%%%%
m=9.10938188e-31
eps0= 8.854187e-12 % dielectric constant of vacuum
epsr= 3.0e-11/eps0; % relative dielectric constant 3 for organics
dCoul = dCoul/epsr;
q=1.602e-19 % electronic charge
kB=1.38e-23 %kB
T=298.15e0 %near room temperature
VT=kB*T/q
munsc = 2.5e-7; % electron mobility for organics
```

```

mupsc = 3.0e-8; % hole mobility for organics
gamma = q*(munsc+mupsc)/(eps0*epsr)
% For BHJ
ni=(Nc*Nc*exp(-Egap/VT))^0.5
% End For BHJ
maxDoping=0.0
% Choose dimension
Lx=48e-9; % 12 nm
Ly=100e-9 % 100 nm
% Choose ny:
ny=20
% With this choice of ny (and Ly), we calculate debye length as:
debye = Ly/ny
% and nx as:
nx=round(Lx*ny/Ly)+1
nx=20
% next, choose nx and ny to be about 1.2times the original choice (so
% that dx and dy will be both smaller than the debye length
ny=round(1.2*ny)+1;
nx=round(1.2*nx)+1;
% we make ny even :
if mod(ny,2) ==0
    ny=ny
else
    ny=ny+1
end
% we make nx even also:
if mod(nx,2) ==0
    nx=nx
else
    nx=nx+1
end
nx
ny
% Calculate maxT
maxT = eps0*kB*T/(q*debye)^2
nim = ni/maxT
coeff=debye*debye/(VT*maxT)/dddd;
coeff2=kB*T*maxT/debye;
coeffnim=2.0*nim
Nx=nx-2;
Ny=ny-2;
N=Nx*Ny;
N1=2*(Nx+2-1);
N2=2*(Ny+2-1);
% We define contact length and partial contact height

```

```

%Perfect planar device
aa=1.0/N2 % fractional height (y-direction of defect)
b1=1.0/N1 % fractional start (x-direction of 1st defect)
b2=1.0/N1 % fractional end (x-direction of 2nd defect)
b3=1.0/N1 % fractional start (x-direction of 1st defect)
b4=1.0/N1 % fractional start (x-direction of 1st defect)
%Partially planar device
aa=0.5 % fractional height (y-direction of defect)
b1=0.2 % fractional start (x-direction of 1st defect)
b2=0.3 % fractional end (x-direction of 2nd defect)
b3=0.7 % fractional start (x-direction of 1st defect)
b4=0.8 % fractional end (x-direction of 2nd defect)

dx=Lx/(nx-1);
dy=Ly/(ny-1); % must be many times smaller than the Debye Length
% Make Lx and Ly now to be in units of the debye length
Lx=Lx/debye;
Ly=Ly/debye;
dx=dx/debye
dy=dy/debye
dx2=dx*dx;
dy2=dy*dy;
%Percentage Tolerance
TOL1=0.001 % ==> maximum 0.1%
TOL=(1.0e-8*N)^2
TOL2=(1.0e-8)^2
%Initialize doping profile
Gam=zeros(nx,ny);
Gam=doping(nx,ny);
Vnew=zeros(nx,ny);
%initialize relative dielectric
er=zeros(2*nx-1,2*ny-1);
er=epsr*ones(2*nx-1,2*ny-1); % Eddited on 28.3.14
er=diel(epsr,2*nx-1,2*ny-1); % assume relative dielectric is not constant
%initialize electron mobility
mun=zeros(2*nx-1,2*ny-1);
mun=elecmob(munsc/dddd,2*nx-1,2*ny-1,Vnew); % assume mobility is not constant
%initialize electron mobility
mup=zeros(2*nx-1,2*ny-1);
mup=holemob(mupsc/dddd,2*nx-1,2*ny-1,Vnew); % assume mobility is not constant
%To Plot: Uncomment if you want to plot
%[X,Y] = meshgrid(0:dx:Lx, 0:dy:Ly);
%[x,y]=meshgrid(dx:dx:Lx,dy:dy:Ly);
rnp=linspace(0,1,ny)*Ly;
r=linspace(0,1,ny-1)*Ly;
%initialize electron concentration

```

```

n=zeros(nx,ny);
n= 0.5*(Gam + (Gam.*Gam +4.0*ni^2*ones(nx,ny)).^0.5);
%initialize hole concentration
p=zeros(nx,ny);
p= 0.5*(-Gam + (Gam.*Gam +4.0*ni^2*ones(nx,ny)).^0.5);
p=p/maxT; n=n/maxT; Gam=Gam/maxT;
%Special case for system (BHJ) at hand
n(:,1)=nim*exp(0.5*Egap/VT)*ones(nx,1);
n(:,ny)=nim*exp(-0.5*Egap/VT)*ones(nx,1);
p(:,ny)=nim*exp(0.5*Egap/VT)*ones(nx,1);
p(:,1)=nim*exp(-0.5*Egap/VT)*ones(nx,1);
%End Special case for system (BHJ) at hand
nL=n(:,1)
nU=n(1,ny)
pL=p(:,1)
pU=p(1,ny)
[X,Y] = meshgrid(1:1:nx, 1:1:ny);
contourf(X,Y,n');
colorbar
title('ElectronDensity0');
%pause(10)
%initialize array for currents
Jny=zeros(nx-1, ny-1);
Jpy=zeros(nx-1, ny-1);
%Initialize V
Vnew=zeros(nx,ny); % eddited on 28.3.14
for i=1:nx
for j=1:ny
if(p(i,j)~= 0.0 && n(i,j)~=0.0)
Vnew(i,j) = 0.5*(-log(p(i,j)/nim) + log(n(i,j)/nim));
end% endif
end
end
Vnew(1,:)=Vnew(3,:);
Vnew(nx,:)=Vnew(nx-2,:);
VL=Vnew(:,1);
VU=Vnew(1,ny);
[X,Y] = meshgrid(1:1:nx, 1:1:ny);
contourf(X,Y,Vnew');
colorbar
title('Potential0');
%pause(10)
mun=elecmob(munsc/dddd,2*nx-1,2*ny-1,Vnew); % assume mobility is not constant
%initialize electron mobility
mup=holemob(mupsc/dddd,2*nx-1,2*ny-1,Vnew); % assume mobility is not constant
plot(rnp,Vnew(1,:),'-or')

```

```

title('rn-p versus potential');
%pause(5)
%First, we solve for the equilibrium (J=0, Vapp=0) case:
%This will help us find our initial guess for the non-equilibrium
%case(s) (J!=0, Vapp!=0)
Vold = Vnew;
d2=1.0e200
while d2 > TOL
[Vnew] = GSV0(Vold,er,Gam,VL);
Vnew(1,:)=Vnew(3,:);
Vnew(nx,:)=Vnew(nx-2,:);
%d2=norm(Vnew-Vold,'fro')/sqrt(nx*ny);
d2=norm(Vnew-Vold,'fro')
Vold=Vnew;
%plot(rnp,Vnew(1,:),'-r')
%title('Pot');
%pause(3)
end
contourf(X,Y,Vnew');
colorbar
title('Potential0');
pause(2)
Vnew(:,1)
mun=elecmob(munsc/dddd,2*nx-1,2*ny-1,Vnew); % assume mobility is not constant
%initialize electron mobility
mup=holemob(mupsc/dddd,2*nx-1,2*ny-1,Vnew); % assume mobility is not constant
n=nim*exp(Vnew);
p=nim*exp(-Vnew);
%Create Defects
%p=defect(p)
%n=defect(n)
p
n
%p-n
nL=n(:,1);
nU=n(1,ny);
pL=p(:,1);
pU=p(1,ny);
% Vnew = 0.5*(-log(p/nim) + log(n/nim));
[X,Y] = meshgrid(1:1:nx, 1:1:ny);
contourf(X,Y,Vnew');
colorbar
title('Potential');
pause(5)
contourf(X,Y,n');
colorbar

```

```

title('ElectronDensity');
pause(5)
contourf(X,Y,p');
colorbar
title('HoleDensity');
pause(5)
plot(rnp,Vnew(1,:),'x-r')
title('Pot');
%pause(3)
hold off
plot(rnp,n(1,:),'o-b')
hold on
plot(rnp,p(1,:),'-r')
title('n(blue), p(red)')
%pause(5)
hold off
NV=12;
Vmin=0.0;
Vmax=0.6;
Vapp1=linspace(Vmin/VT, Vmax/VT, NV+1);
ik=round(0.4/(0.5*VT))+1
Vapp2=linspace(0.6/VT, 1.0/VT,ik);
Vapp=[ Vapp1 Vapp2]
for iV=1:size(Vapp,2)
%Initialize V
Vnew(:,ny) = Vnew(:,1) - Egap/VT +Vapp(iV)*ones(nx,1); %forward bias
%BC:
Vnew(1,:)=Vnew(3,:);
Vnew(nx,:)=Vnew(nx-2,:);
VL=Vnew(:,1);
VU=Vnew(1,ny);
mun=elecmob(munsc/dddd,2*nx-1,2*ny-1,Vnew); % assume mobility is not constant
%initialize electron mobility
mup=holemob(mupsc/dddd,2*nx-1,2*ny-1,Vnew); % assume mobility is not constant
diffPoisson=1.0e200;
Vold = Vnew;
while diffPoisson > TOL2
%contourf(X,Y,Vnew');
%colorbar
%title('Potential1');
%pause(2)
% Solve the Poisson Equation
diffPot=1.0e200;
[Vnew] = GSV2(Vold,er,p,n,Gam,VL,VU); %Ideally, I should iterate until
Vnew(1,:)=Vnew(3,:); % Vold=Vnew, but ... at the end
Vnew(nx,:)=Vnew(nx-2,:); %it works out via the global iteration

```

```

diffPot= max(max(abs(Vnew-Vold)))
Vold = Vnew;
contourf(X,Y,Vnew');
colorbar
title('PotentialUUU');
pause(2)
% now solve the continuity + drift equation
nold=n;
pold=p;
diffn=1.0e200;
[n] = GSn(nold,Vnew,mun,mup,pold,nL,nU);
%for x=0 edge and x=L edge:
n(1,:)=n(3,:);
n(nx,:)=n(nx-2,:);
diffn= max(max(abs(n-nold)))
nold=n;
contourf(X,Y,n');
colorbar
title('ElectronDensity');
pause(2)
diffp=1.0e200;
[p] = GSp(pold,Vnew,mun,mup,nold,pL,pU);
%for x=0 edge and x=L edge:
p(1,:)=p(3,:);
p(nx,:)=p(nx-2,:);
diffp= max(max(abs(p-pold)))
pold = p;
contourf(X,Y,p');
colorbar
title('HoleDensity');
pause(2)
if diffn < TOL1 && diffp < TOL1 && diffPot < TOL1
    diffPoisson = TOL2/10.0
end
end% end outermost while loop
for i=1:nx-1
for j=1:ny-1
d1=(Vnew(i,j+1)-Vnew(i,j));
Jny(i,j)=dddd*mun(2*i,2*j-1)*(n(i,j+1)*be(d1)-n(i,j)*be(-d1));
Jpy(i,j)=dddd*mup(2*i,2*j-1)*(p(i,j)*be(d1)-p(i,j+1)*be(-d1));
end
end
plot(rnp,log(n(1,:)))
hold on
plot(rnp,log(p(1:)),'-r')
pause(2)

```

```

hold off
plot(rnp,Vnew(1,:),'-r')
%pause(2)
plot(r,-(coeff2/dy)*Jny(1,:))
hold on
plot(r,-(coeff2/dy)*Jpy(1,:),'-r')
hold on
plot(r,-(coeff2/dy)*(Jpy(1,:)+Jny(1,:)),'-g')
title('Jpy(red), Jny(blue) Sum(green) ')
%pause(10)
hold off
Jytot= -((coeff2/dy)*sum(sum(Jny+Jpy))/(nx-1)/(ny-1))/260 % normalized using 260
fprintf(fid,'%e %e \n',Vapp(iV)*VT,Jytot);
% fflush(fid); undefined function error so commented out
disp('*****');
[r1,r2] = meshgrid(1:1:nx-1, 1:1:ny-1);
contourf(r1,r2,((Jpy'+Jny')/260)*(coeff2/dy)); % normalize using 260
colorbar
title('Current Density');
pause(5)
(Jpy+Jny)*(coeff2/dy)
% fflush(stdout)
% fflush(stderr)
% fflush(fid)
end% end voltage loop

```

## Electron Mobility

```

function temp = elecmob(munsc,N1,N2,Vnew)
%electron mobility
%Modify as suits you
global dy q m VT debye
global aa b1 b2 b3 b4
global sc
q2=q*debye*debye/VT; % debye length added
temp = munsc*ones(N1,N2);
mu=sc*munsc;
for I=int32(b1*N1):int32(b2*N1)
    temp(I,1)=mu;
end
for I=(1+int32(b3*N1)):(1+int32(b4*N1))
    temp(I,1)=mu;
end
%copy and paste from holemob

```

```

% FIRST DEFECT
% If J is even
for J = 2:int32(aa*N2)
if(mod(J,2)==0) % if J is even
for I=int32(b1*N1):int32(b2*N1)
if(mod(I,2)==1) %if I is odd
    i=(I+1)/2;
    j=(J+2)/2; % J+2 was J+1 before
    etemp=-(Vnew(i,j)-Vnew(i,j-1))/dy;
    Pot=0.5*(Vnew(i,j)+Vnew(i,j-1))-Vnew(i,1);
if (Pot==0.0)
    temp(I,J)=mu;
else
    temp(I,J)= mu;
end
end
if(mod(I,2)==0) %if I is even
    i=I/2;
    j=J/2;
    Pot1=(Vnew(i,j)+Vnew(i+1,j))/2;
    Pot2=(Vnew(i,j+1)+Vnew(i+1,j+1))/2;
    Pot=0.5*(Pot2+Pot1)-(Vnew(i,1)+Vnew(i+1,1))/2.0;
    etemp=-(Pot2-Pot1)/dy;
if(Pot==0.0)
    temp(I,J)=mu;
else
    temp(I,J)=mu;
end
end
end
end
% If J is Odd
for J = 2:int32(aa*N2)
if(mod(J,2)==1) % if J is odd
for I=int32(b1*N1):int32(b2*N1)
if(mod(I,2)==1) %if I is odd
    i=(I+1)/2;
    j=(J+1)/2;
    etemp=-(Vnew(i,j+1)-Vnew(i,j-1))/(2*dy);
    Pot=Vnew(i,j)-Vnew(i,1);
if (Pot==0.0)
    temp(I,J)=mu;
else
    temp(I,J)=mu;
end
end
end
end

```

```

end
if(mod(I,2)==0) %if I is even
    i=I/2;
    j=(J+1)/2;
    Pot=(Vnew(i,j)+Vnew(i+1,j))/2 - (Vnew(i,1)+Vnew(i+1,1))/2;
    etemp1=Vnew(i,j-1)+Vnew(i+1,j-1);
    etemp2=Vnew(i,j+1)+Vnew(i+1,j+1);
    etemp=(etemp2-etemp1)/(2*dy);
if(Pot==0.0)
    temp(I,J)=mu;
else
    temp(I,J)=mu;
end
end
end
end
end
% SECOND DEFECT
% If J is even
for J = 2:int32(aa*N2)
if(mod(J,2)==0) % if J is even
for I=(1+int32(b3*N1)):(1+int32(b4*N1))
if(mod(I,2)==1) %if I is odd
    i=(I+1)/2;
    j=(J+2)/2;
    etemp=-(Vnew(i,j)-Vnew(i,j-1))/dy;
    Pot=0.5*(Vnew(i,j)+Vnew(i,j-1))-Vnew(i,1) ;
if (Pot==0.0)
    temp(I,J)=mu;
else
    temp(I,J)=mu;
end
end
if(mod(I,2)==0) %if I is even
    i=I/2;
    j=J/2;
    Pot1=(Vnew(i,j)+Vnew(i+1,j))/2;
    Pot2=(Vnew(i,j+1)+Vnew(i+1,j+1))/2;
    Pot=0.5*(Pot2+Pot1)-(Vnew(i,1)+Vnew(i+1,1))/2.0;
    etemp=-(Pot2-Pot1)/dy;
if(Pot==0.0)
    temp(I,J)=mu;
else
    temp(I,J)=mu;
end
end
end

```

```

end
end
end
%If J is Odd
for J = 2:int32(aa*N2)
if(mod(J,2)==1) % if J is odd
for I=(1+int32(b3*N1)):(1+int32(b4*N1))

if(mod(I,2)==1) %if I is odd
    i=(I+1)/2;
    j=(J+1)/2;
    etemp=-(Vnew(i,j+1)-Vnew(i,j-1))/(2*dy);
    Pot=Vnew(i,j)-Vnew(i,1);
if (Pot==0.0)
    temp(I,J)=mu;
else
    temp(I,J)=mu;
end
end
if(mod(I,2)==0) %if I is even
    i=I/2;
    j=(J+1)/2;
    Pot=(Vnew(i,j)+Vnew(i+1,j))/2-(Vnew(i,1)+Vnew(i+1,1))/2;
    etemp1=Vnew(i,j-1)+Vnew(i+1,j-1);
    etemp2=Vnew(i,j+1)+Vnew(i+1,j+1);
    etemp=(etemp2-etemp1)/(2*dy);
if(Pot==0.0)
temp(I,J)=mu;
else
    temp(I,J)=mu;
end
end
end
end
[X,Y] = meshgrid(1:1:N1,1:1:N2);
contourf(X,Y,temp')
colorbar;
title('Electron Mobility')
xlabel('DEVICE LENGTH')
ylabel('DEVICE THICKNESS')
pause(1);
end

```

## Hole Mobility

```
function temp = holemob(mupsc,N1,N2,Vnew)
%Hole mobility
%Modify as suits you
global dy q m VT debye
global aa b1 b2 b3 b4
global sc
q2=q*debye*debye/VT; % debye length added
temp = mupsc*ones(N1,N2);
mu=sc*mupsc;
for I=int32(b1*N1):int32(b2*N1)
    temp(I,1)=mu;
end
for I=(1+int32(b3*N1)):(1+int32(b4*N1))
    temp(I,1)=mu;
end
% [ b1*N1 int32(b1*N1)]
% [b2*N1 int32(b2*N1)]
% [ b3*N1 int32(b3*N1)]
% [b4*N1 int32(b4*N1)]
%N1
% 1:1:N1
%exit();
% FIRST DEFECT
%If J is even
for J = 2:int32(aa*N2)
if(mod(J,2)==0) % if J is even
for I=int32(b1*N1):int32(b2*N1)

if(mod(I,2)==1) %if I is odd
    i=(I+1)/2;
    j=(J+2)/2; % J+2 was J+1 before
    etemp=-(Vnew(i,j)-Vnew(i,j-1))/dy;
    Pot=0.5*(Vnew(i,j)+Vnew(i,j-1))-Vnew(i,1);
if (Pot==0.0)
        temp(I,J)=mu;
else
        temp(I,J)=mu;
end
end
if(mod(I,2)==0) %if I is even
    i=I/2;
    j=J/2;
    Pot1=(Vnew(i,j)+Vnew(i+1,j))/2;
    Pot2=(Vnew(i,j+1)+Vnew(i+1,j+1))/2;
```

```

        Pot=0.5*(Pot2+Pot1)-(Vnew(i,1)+Vnew(i+1,1))/2.0;
        etemp=- (Pot2-Pot1)/dy;
if(Pot==0.0)
        temp(I,J)=mu;
else
        temp(I,J)=mu;
end
end
end
end
end
%If J is Odd
for J = 2:int32(aa*N2)
if(mod(J,2)==1) % if J is odd
for I=int32(b1*N1):int32(b2*N1)
if(mod(I,2)==1) %if I is odd
        i=(I+1)/2;
        j=(J+1)/2;
        etemp=- (Vnew(i,j+1)-Vnew(i,j-1))/(2*dy);
        Pot=Vnew(i,j)-Vnew(i,1);
if (Pot==0.0)
        temp(I,J)=mu;
else
        temp(I,J)=mu;
end
end
if(mod(I,2)==0) %if I is even
        i=I/2;
        j=(J+1)/2;
        Pot=(Vnew(i,j)+Vnew(i+1,j))/2- (Vnew(i,1)+Vnew(i+1,1))/2;
        etemp1=Vnew(i,j-1)+Vnew(i+1,j-1);
        etemp2=Vnew(i,j+1)+Vnew(i+1,j+1);
        etemp=(etemp2-etemp1)/(2*dy);
if(Pot==0.0)
        temp(I,J)=mu;
else
        temp(I,J)=mu;
end
end
end
end
end
% SECOND DEFECT
%If J is even
for J = 2:int32(aa*N2)
if(mod(J,2)==0) % if J is even

```

```

for I=1+int32(b3*N1):(1+int32(b4*N1))
if(mod(I,2)==1) %if I is odd
    i=(I+1)/2;
    j=(J+2)/2;
    etemp=-(Vnew(i,j)-Vnew(i,j-1))/dy;
    Pot=0.5*(Vnew(i,j)+Vnew(i,j-1))-Vnew(i,1);
if (Pot==0.0)
    temp(I,J)=mu;
else
    temp(I,J)=mu;
end
end
if(mod(I,2)==0) %if I is even
    i=I/2;
    j=J/2;
    Pot1=(Vnew(i,j)+Vnew(i+1,j))/2;
    Pot2=(Vnew(i,j+1)+Vnew(i+1,j+1))/2;
    Pot=0.5*(Pot2+Pot1)-(Vnew(i,1)+Vnew(i+1,1))/2.0;
    etemp=-(Pot2-Pot1)/dy;
if(Pot==0.0)
    temp(I,J)=mu;
else
    temp(I,J)=mu;
end
end
end
end
end
%If J is Odd
for J = 2:int32(aa*N2)
if(mod(J,2)==1) % if J is odd
for I=(1+int32(b3*N1):(1+int32(b4*N1))
if(mod(I,2)==1) %if I is odd
    i=(I+1)/2;
    j=(J+1)/2;
    etemp=-(Vnew(i,j+1)-Vnew(i,j-1))/(2*dy);
    Pot=Vnew(i,j)-Vnew(i,1);
if (Pot==0.0)
    temp(I,J)=mu;
else
    temp(I,J)=mu;
end
end
if(mod(I,2)==0) %if I is even
    i=I/2;
    j=(J+1)/2;

```

```

        Pot=(Vnew(i,j)+Vnew(i+1,j))/2-(Vnew(i,1)+Vnew(i+1,1))/2;
        etemp1=Vnew(i,j-1)+Vnew(i+1,j-1);
        etemp2=Vnew(i,j+1)+Vnew(i+1,j+1);
        etemp=(etemp2-etemp1)/(2*dy);
if(Pot==0.0)
        temp(I,J)=mu;
else
        temp(I,J)=mu;
end
end
end
end
end
[X,Y] = meshgrid(1:1:(N1),1:1:(N2));
contourf(X,Y,temp')
colorbar;
title('Hole Mobility');
xlabel('DEVICE LENGTH')
ylabel('DEVICE THICKNESS')
pause(1);
end

```